Synchronization Algorithms and Architectures for Wireless OFDM Systems

Sedki Younis

School of Electrical, Electronic and Computer Engineering

Faculty of Science, Agriculture and Engineering

Newcastle University

Newcastle upon Tyne, UK.

A thesis submitted for the degree of

Doctor of Philosophy

March 2012

To my loving parents and sisters, for their support and encouragement.

Declaration

I declare that this thesis is my own work and it has not been previously submitted, either by me or by anyone else, for a degree or diploma at any educational institute, school or university. To the best of my knowledge, this thesis does not contain any previously published work, except where another person's work used has been cited and included in the list of references

Acknowledgements

First, I would like to thank my supervisors for their support and advice throughout the duration of my study at Newcastle University. Without the lengthy discussions and meetings we had and without their constant encouragement and guidance, this thesis would not be the same. I am extremely grateful to Dr. Arafat Al-Dweik, for sharing his outstanding expertise and knowledge about synchronization problems in digital communication receivers, Dr. Charalampos Tsimenidis, from whom I learned a lot in the field of signal processing and digital communications, and Prof. Bayan Sharif, who accepted me to pursue PhD at Newcastle University and offered me all kinds of support. I thank them all for being patient and continuously offering advices and help.

I wish to thank Dr. Ali Hazmi, from Tampere University in Finland, for the valuable comments and helpful discussions about practical communication systems. I would also like to thank my friends and colleagues at Newcastle University, Maher, Emad, Mohammed, Anas, Salah, Muayad and Ammar. I would like to acknowledge the financial support of Ministry of Higher Education and Scientific Research (MOHSR) of Iraq through their scholarship.

Last but by no means least, I thank my parents and my sisters. I would like to express my deepest gratitude to my parents whom this work is dedicated to. Without your unconditional support, your kind words, and your sound advice, I would not be the person I am today.

Abstract

Orthogonal frequency division multiplexing (OFDM) is a multicarrier modulation technique that has become a viable method for wireless communication systems due to the high spectral efficiency, immunity to multipath distortion, and being flexible to integrate with other techniques. However, the high-peak-to-average power ratio and sensitivity to synchronization errors are the major drawbacks for OFDM systems.

The algorithms and architectures for symbol timing and frequency synchronization have been addressed in this thesis because of their critical requirements in the development and implementation of wireless OFDM systems. For the frequency synchronization, two efficient carrier frequency offset (CFO) estimation methods based on the power and phase difference measurements between the subcarriers in consecutive OFDM symbols have been presented and the power difference measurement technique is mapped onto reconfigurable hardware architecture. The performance of the considered CFO estimators is investigated in the presence of timing uncertainty conditions. The power difference measurements approach is further investigated for timing synchronization in OFDM systems with constant modulus constellation. A new symbol timing estimator has been proposed by measuring the power difference either between adjacent subcarriers or the same subcarrier in consecutive OFDM symbols. The proposed timing metric has been realized in feedforward and feedback configurations, and different implementation strategies have been considered to enhance the performance and reduce the complexity. Recently, multiple-input multiple-output (MIMO) wireless communication systems have received considerable attention. Therefore, the proposed algorithms have also been extended for timing recovery and frequency synchronization in MIMO-OFDM systems.

Unlike other techniques, the proposed timing and frequency synchronization architectures are totally blind in the sense that they do not require any information about the transmitted data, the channel state or the signal-to-noise-ratio (SNR). The proposed frequency synchronization architecture has low complexity because it can be implemented efficiently using the three points parameter estimation approach. The simulation results confirmed that the proposed algorithms provide accurate estimates for the synchronization parameters using a short observation window. In addition, the proposed synchronization techniques have demonstrated robust performance over frequency selective fading channels that significantly outperform other well-established methods which will in turn benefit the overall OFDM system performance.

Furthermore, an architectural exploration for mapping the proposed frequency synchronization algorithm, in particular the CFO estimation based on the power difference measurements, on reconfigurable computing architecture has been investigated. The proposed reconfigurable parallel and multiplexed-stream architectures with different implementation alternatives have been simulated, verified and compared for field programmable gate array (FPGA) implementation using the Xilinx's DSP design flow.

Contents

List of Figures

List of Tables

Nomenclature

Roman Symbols

$P_{lock-in}$ Probability of Lock-in

ADSL Asymmetric Digital Subscriber Lines

ASIC Application Specific Integrated Circuit

AWGN Additive White Gaussian Noise

BER Bit Error Rate

BRAM Block RAM

CFO Carrier Frequency Offset

CIR Channel Impulse Response

CM Constant Modulus

CORDIC Coordinate Rotational Digital Computer

CP Cyclic Prefix

CPE Cyclic Prefix Estimator

CS Cyclostationary

DA Data-Aided

DAB Digital Audio Broadcasting

DAC Digital-to-Analogue Converter

DDS Direct Digital Synthesizer

DFT Discrete Fourier Transform

DSP Digital Signal Processing

DSR Deviation from the Safe Region

DVB-T Digital Video Broadcasting-Terrestrial

ELG Early Late Gate

EM Electromagnetic

FDM Frequency Division Multiplexing

FEQ Frequency Domain Equalization

FFT Fast Fourier Transform

FPGA Field Programmable Gate Array

GPP General Purpose Processor

GSM Global System for Mobile communications

HDL Hardware Description Languages

HF High Frequency

I/O Input/Output

ICI Inter-Carrier Interference

IDFT Inverse Discrete Fourier Transform

IGVAV Iterative Generalized Viterbi and Viterbi Estimator

IIR Infinite Impulse Response

IP Intellectual Property

ISI Inter-Symbol Interference

JMLE Joint Maximum Likelihood Estimator

KBE Kurtosis Based Estimator

LMMSE Linear Minimum Mean Square Error

LO Local Oscillator

LPF Low Pass Filter

LS Least-Squares

LTE Long Term Evolution

LTI Linear Time Invariant

LUT Look-UP Table

M-PSK M-ary Phase Shift Keying

M-QAM M-order Quadrature Amplitude Modulation

MBWA Mobile Broadband Wireless Access

MCSPS Minimizing the Components of the Signal Power Spectrum

MIMO Multi-Input Multi-Output

MISO Multi-Input Single-Output

ML Maximum Likelihood

MLE-TER Maximum Likelihood Estimator-Timing Error Robust

MSA Multiplexed Stream Architecture

MSE Mean Squared Error

MVE Minimum Variance Estimator

NDA Non Data-Aided

NSC Null Subcarriers

OFDM Orthogonal Frequency Division Multiplexing

OSTBC Orthogonal Space Time Block Coding

PAPR Peak-to-Average Power Ratio

PDE-F Power Difference Estimator-Frequency

PDE-T Power Difference Estimator-Time

PEs Processing Elements

PSA Parallel Stream Architecture

QPSK Quadrature Phase Shift Keying

RF Radio Frequency

Rx Receiver

SDR Software Defined Ratio

SFDR Spurious Free Dynamic Range

SINR Signal to Interference-plus-Noise Ratio

SM Subcarrier Multiplexed

SNR Signal-to-Noise Ratio

SO Subcarrier Orthogonal

SR Safe-Region

SRL Shift Register Look-up table

ST Symbol Timing

STC Space-Time Coding

STO Symbol Timing Offset

SUI Stanford University Interim

TM Time Multiplexed

TO Time Orthogonal

Tx Transmitter

UWB Ultra Wideband

VHDSL Very High-speed Digital Subscriber Lines

VLSI Very Large Scale Integration

VS Virtual Subcarriers

WiMAX Worldwide Interoperability for Microwave Access

WLAN Wireless Local Area Networks

WMAN Wireless Metropolitan Area Networks

XSG Xilinx System Generator

ZMLE Zeng Maximum Likelihood Estimator

List of Symbols

n	Sub-carrier
τ_p	Delay of the pth delay
$h(t, \tau)$	Channel impulse response
L_h	Channel order
$\varphi(\tau)$	Autocorrelation function of the channel
E	statistical expectation
τ_{rms}	Channel delay spread
B_{coh}	Channel coherence bandwidth
P_i	Received power of ith multipath component
T_s	OFDM symbol duration
B_{signal}	Bandwidth of the signal
T_{coh}	Coherence time of the channel
B_d	Doppler spread
N	Number of subcarriers
B	System bandwidth
f_n	Frequency of the nth subcarrier
Δf	Subcarrier spacing
l	OFDM symbol index
$\mathbf{d}$	Complex data sequence
$\mathbf{x}$	Time domain OFDM sequence
M	Constellation size
$\mathbf{W}$	Normalized DFT matrix
N_{CP}	Length of the cyclic prefix
$\bar{\mathbf{x}}$	Transmitted OFDM block after adding the cyclic prefix
N_t	Length of OFDM block after adding the cyclic prefix
f_c	Carrier frequency

I	In-phase component of the received baseband signal
Q	Quadrature component of the received baseband signal
$\bar{\mathbf{y}}$	Received OFDM block before removing the cyclic prefix
$\mathbf{y}$	Received OFDM block after removing the cyclic prefix
c_i	The ith cyclic prefix samples
$\bar{\mathbf{H}}(\mathbf{l})$	Channel matrix during the lth OFDM block
h_p	Discrete-time channel impulse response sample
$\mathbf{H}$	Channel frequency response
$\mathbf{s}$	Received frequency domain samples
$\hat{\mathbf{H}}$	Estimated channel frequency response
f_ϵ	Frequency offset of the carrier in Hz
ϵ	Normalized frequency error by the subcarrier spacing
K_n	Null subcarriers in the OFDM symbol
K_a	Modulated subcarriers in the OFDM symbol
$\hat{\epsilon}$	Estimated normalized frequency offset
δ	Symbol timing offset in samples
$\bar{\mathbf{W}}$	Null subspace of the DFT matrix
$\hat{\delta}$	Estimated timing offset
P_L	Length of the repeated pattern in the training symbol
N_t	Length of OFDM symbol including the cyclic prefix
M_T	Number of transmit antennas
M_R	Number of receive antennas
$\mathbf{D}^{(M)}$	Block diagonal matrix with M diagonal blocks
β	Desired signal component
I	Additive ICI and ISI disturbance in addition to the noise
$H_{mn}^k(l)$	Channel response of the kth subcarrier on the m,nth antenna
$p_n^k(j)$	Total power of kth subcarrier on the nth receive antenna
L	Averaging factor
γ	Trial value of the symbol timing offset δ
μ	Trial value of the carrier frequency offset ϵ
Ψ_n^k	ICI induced additional noise
f_d	Maximum Doppler shift
B_L	Normalized loop bandwidth

ς	Damping factor
ω_n	Natural frequency
$L(z)$	Loop transfer function in the z-domain
e_δ	Loop error signal
τ_δ	Time shift relative to the timing offset δ
D	Delay in samples
$\check{\mathbf{H}}$	Toeplitz channel matrix
$\overrightarrow{c}$	CP samples from the next OFDM symbol
$\overrightarrow{y}$	Data samples from the next OFDM symbol
$\overleftarrow{c}$	CP samples from the previous OFDM symbol
$\overleftarrow{y}$	Data samples from the previous OFDM symbol
$\mathbf{v}$	Sequence within the FFT window
$\check{H}_i$	Channel frequency response combined with the phase rotation
α_δ	Attenuation due to the missing data samples
ϕ	Phase rotation due to timing error with the safe region
$M\tilde{S}E$	MSE degradation
$\epsilon_{\max}$	Maximum CFO that can be estimated
K_i	Modulation removal factor
I_i	Number of iteration for the VAV
SNR_e	Effective SNR
b_l	Arbitrary filter function
$F(\cdot)$	Arbitrary real nonlinearity
$\bar{\mathbf{h}}$	Channel impulse response embedded with timing uncertainty
$\mathbf{W}_{L_h+1}$	Matrix containing the first $L_h + 1$ columns of DFT matrix
$\tilde{\epsilon}$	Estimation error of the CFO
$\mathbf{C}(\epsilon)$	Accumulated phase shift caused by the CFO

Chapter 1

Introduction

In wireless digital communication systems, data is transmitted in the form of electromagnetic (EM) waves through the wireless channel that represents the propagation media between transmit and receiver antennas. The receiver gathers and processes the EM waves to detect the transmitted information. The spectrum allocation and bandwidth are important parameters in wireless communication systems because the frequency spectrum is limited. Several studies have been conducted to maximize the system spectral efficiency for a given allocated spectrum or bandwidth and to improve the signal detection by mitigating the impact of various impairments of the wireless link.

Many wireless technologies had large evolution and low cost consumer systems have been developed to support not only low rate services but also high rate applications. Global system for mobile communications (GSM), bluetooth, and wireless local area networks (WLAN) are some examples for the wireless evolution in the last two decades. Nowadays, there has been a tremendous demand for more applications to become wireless. However, meeting the high data rate requirements of current applications has added more challenges to the design of wireless systems.

High data rate transmission is a major challenge for wireless communication systems due to the requirement of wide bandwidth. The wireless channel, also referred to as wideband channel, has frequency selective fading characteristics which introduces inter-symbol interference (ISI) to the received signal due to the multipath echoes. To combat the effect of ISI, channel equalization has to be employed, however, since the multipath usually spans multiple symbols, the channel equalization is becoming more complicated. In addition, complex adaptive equalizers with feed-

back loops have to be used to track the channel variations. Orthogonal frequency division multiplexing (OFDM) is a parallel data transmission technique that can efficiently mitigate the effects of multipath distortions. Basically, OFDM converts the wideband channel into multiple narrowband subchannels where each subchannel experiences flat fading thus offering several advantages over conventional modulation techniques.

1.1 OFDM Systems: Past and Present

The principle of multitone (multicarrier) modulation by means of frequency division multiplexing (FDM) has been employed for some applications since the 1960s where it was first used in military high frequency (HF) radios. In OFDM, the multicarriers overlap in frequency domain. In this sense, it can be considered as an optimal version of multicarrier transmission. However, OFDM implementation requires a bank of sinusoidal generators and demodulators with precise phasing to maintain minimum crosstalk between the subchannels. In addition, the process of coherent demodulation becomes bulky and expensive as the number of subchannels increases.

A digital implementation for OFDM system was first suggested by Weinstein and Ebert [4] in 1971 to replace the array of sinusoidal generators with inverse discrete Fourier transform (IDFT) and DFT to perform modulation and demodulation, respectively. Because the DFT uses a set of harmonically related sinusoidal and cosinusoidal functions with frequency of integer multiple of the basis frequency, it can be used to generate the orthogonal subcarriers required by the OFDM modem. In addition, more efficient digital realization can be implemented using fast Fourier transform (FFT) algorithm, especially when the number of subchannels is large [5].

After years of slow progress, multicarrier modulation has gained considerable interest by the research community and industry. Consequently, OFDM has become a mature technology and found space in many wired and wireless communication applications and standards. For instance, it has been employed for broadband communication using asymmetric digital subscriber lines (ADSL) and very high-speed digital subscriber lines (VHDSL) [5]. Moreover, it has been integrated in several other applications such as digital audio broadcasting (DAB) and digital terrestrial video broadcasting (DVB-T) in Europe and Japan [6, 7]. More recently, there has been an emerging use for OFDM in various commercial applications and standards such

as WLANs IEEE 802.11a/g/n [8], wireless metropolitan area networks (WMANs) IEEE 802.16 [9], ultra wideband (UWB) radios IEEE 802.15, mobile broadband wireless access (MBWA) IEEE 802.20, 3GPP LTE and 4G LTE-Advanced [10, 11].

1.2 Thesis Scope

Recently, OFDM has been adopted in a wide variety of high data rate communication systems because of the high spectral efficiency and robustness to multipath fading distortions and narrowband interferences. On the other hand, there are some limitations associated with OFDM systems that impair their performance significantly. The peak-to-average power ratio (PAPR) of OFDM signal is significantly higher than that of single carrier systems, which is a serious problem when nonlinear amplifiers are used [12]. The other major problem, which is the main focus of this thesis, is that OFDM systems are very sensitive to synchronization imperfections between the transmitter and receiver. The carrier frequency offset (CFO) and symbol timing jitter destroy the orthogonality of the subchannels which result in considerable performance degradation due to the provoked interferences between successive symbols and adjacent subcarriers, i.e. ISI and inter-carrier interference (ICI). Therefore, OFDM systems require precise synchronization and this has been the subject of extensive research over the past few years.

Depending on whether the receiver has some pre-knowledge about the transmitted data or not, the synchronization schemes can be generally classified into two broad categories: data-aided (DA) and non data-aided (NDA). Data-aided techniques require the insertion of known data sequences, most often take the form of either repeated OFDM data symbols, pilot subcarriers or tones, in the transmitted signal which are used to assist the synchronization at the receiving side [13–15]. The synchronization information can be extracted, and then used for correction, from the correlation between the repeated symbols or among the pilot tones. These methods are advantageous, because they are capable of producing consistent estimates for the synchronization parameters with low computational complexity. However, they suffer from low power and bandwidth efficiencies, since a portion of the transmission must be used for the training or pilot data. On the other hand, non data-aided, also referred to as blind [16], synchronization techniques have been proposed in the literature to regain the lost transmission efficiency of data-aided synchronization.

Blind synchronization methods take advantage of the existing OFDM transmission structure or exploit some statistical information to estimate the synchronization parameters without requiring the overhead of training data. Hence, they are more power and bandwidth efficient than data-aided techniques.

Due to their bandwidth efficiency, blind techniques to estimate the synchronization parameters in OFDM systems have been addressed in the literature and significant advancement been achieved. Although, some of the methods estimate the synchronization parameters in a non data-aided manner such as [17], [18], [19] and [20], however, information about the signal-to-noise ratio (SNR) and/or channel impulse response (CIR) might be required. Thus, they can not be considered as totally blind synchronization systems. In addition, the accuracy of blind approaches is not as high as data-aided estimators and they might produce inconsistent estimates [17, 21]. Moreover, non data-aided estimators usually have high computational complexity and require a long observation window for convergence, i.e. the number of symbols required to produce reliable estimates, over which the synchronization parameters can not be tracked. Since the OFDM technique is the preferable choice for transmission in multipath fading channels, the estimation of synchronization parameters should be resilient to multipath impairments as well. Otherwise, the main benefit of using OFDM will be diminished. Unfortunately, a common problem for most blind synchronization techniques is that they are not robust to multipath distortion and most of them experience significant performance deterioration in frequency selective fading channels such as the estimators reported in [17], [22], [23], [24], and [25].

1.3 Contributions of the Thesis

The aim of this thesis is to develop totally blind and robust symbol timing and frequency synchronization architecture for OFDM systems that can provide accurate estimate for the synchronization parameters over frequency selective fading channels using short observation window. For the frequency synchronization, two robust CFO estimators are presented and the effect of timing errors on their performance is investigated. The first estimator is derived from power difference measurements among the subcarriers of constant modulus constellations in consecutive OFDM symbols based on the assumption of approximate channel response over them. While

the other CFO estimator utilizes the phase difference measurements between the subcarriers in consecutive OFDM symbols. In contrast to other blind frequency synchronization techniques, a closed-form estimate is provided which reduces the computational complexity significantly. Most of the CFO estimators are based on the assumption of perfect timing synchronization. Therefore, the considered CFO estimators are evaluated in more realistic scenarios with various timing uncertainty conditions and compared with other timing error robust CFO estimator.

Moreover, an efficient blind symbol timing estimator for OFDM systems is proposed. The power difference measurements approach is exploited to deduce a new timing synchronization metric. In addition, two different realizations for the proposed timing estimator, feedforward and feedback configurations, are presented. For both configurations, some implementation aspects are discussed to enhance the synchronization performance and to reduce the computational complexity of the proposed timing estimator. Furthermore, the proposed power difference estimator is extended to multi-input multi-output OFDM (MIMO-OFDM) systems. The adoption of the proposed synchronization metric for symbol timing recovery and frequency synchronization in MIMO-OFDM systems employing orthogonal space-time coding (STC) and spatial stream multiplexing over frequency selective fading channels is discussed. The performance of the proposed synchronization techniques is assessed over fading channels with different frequency selectivity conditions. The proposed techniques have shown superior performance that outperform other well-established methods in the literature.

Additionally, two architectures are presented for mapping the proposed frequency synchronization algorithm, in particular the power difference estimator for CFO synchronization, on reconfigurable hardware platforms. The design parameters of the proposed architectures are tuned to produce efficient hardware module in terms of resource utilization with marginal deterioration in the estimation accuracy. In summary, the following points indicate the contributions of the work:

1. Design and performance evaluation of robust blind CFO estimators for OFDM systems based on power and phase difference measurements in the presence of timing uncertainty conditions.

2. Introduction of the power difference measurements approach to symbol timing synchronization problem in OFDM receivers.

3. Introduction of a new performance assessment metric for timing synchronization algorithms denoted as deviation from the safe region (DSR).

4. A low complexity realization for the feedforward structure of the proposed timing estimator.

5. A novel self-noise free realization for the proposed timing estimator using early-late gate (ELG) structure.

6. A robust symbol timing and frequency synchronization methods for MIMO-OFDM systems employing orthogonal space-time coding using the power difference measurements approach and its adoption for spatial stream multiplexing systems.

7. Architectural exploration and design alternatives to map the power difference estimator for frequency synchronization on reconfigurable platforms.

1.4 Publications Arising From This Research

1. S. Younis, B. Sharif, C. Tsimenidis, A. Al-Dweik, and A. Hazmi, "Blind Scheme for Carrier Frequency Offset Estimation in MIMO-OFDM Systems," in *Proc. IEEE ISSPIT*, Ajman, UAE, Dec. 2009.

2. S. Younis, A. AL-Dweik, A. Hazmi, B. S. Sharif, and C. Tsimenidis, "Blind CFO Estimator for MIMO-OFDM Systems over Frequency Selective Fading Channels," *IET Com.*, vol. 4, pp. 990-999, May. 2010.

3. S. Younis, A. Al-Dweik, A. Hazmi, C. Tsimenidis, and B. Sharif, "Symbol Timing Offset Estimation Scheme for OFDM systems based on Power Difference Measurements," in *Proc. IEEE PIMRC*, Istanbul, Turkey, Sept. 2010.

4. S. Younis, A. Al-Dweik, C. Tsimenidis, B. Sharif, and A. Hazmi, "Robust Early-Late Gate System for Symbol Timing Recovery in MIMO-OFDM Systems," in *Proc. IEEE WiMob*, Shanghai, China, Oct. 2011.

5. S. Younis, A. Al-Dweik, C. Tsimenidis, B. Sharif, and A. Hazmi, "The Effect of Timing Errors on Frequency Offset Estimation in OFDM Systems," in *Proc. IEEE ISSPIT*, Bilbao, Spain, Dec. 2011.

6. S. Younis, A. Al-Dweik, C. Tsimenidis, B. Sharif, and A. Hazmi, "CORDIC based Architecture for Blind CFO Estimation in OFDM Systems," in *Proc. IEEE ISSPIT*, Bilbao, Spain, Dec. 2011.

7. A. Al-Dweik, S. Younis, A. Hazmi, C. Tsimenidis, and B. Sharif, "Efficient Timing Estimator for OFDM systems using Power Difference Measurements," Accepted for Publication in *IEEE Trans. Veh. Technol.*.

1.5 Thesis Outline

The thesis is organised as follows:

Chapter 2 presents the baseband channel model that will be used to evaluate the performance of the proposed synchronization techniques. It also outlines the system model for OFDM systems and discusses the effect of synchronization impairments on the performance. Moreover, the chapter also provides details of the synchronization requirements of OFDM systems and highlights a number of synchronization techniques available in the literature.

Chapter 3 covers basic architectures of some common components used in the hardware implementation of synchronization systems. The increasing role of reconfigurable computing in the implementation of signal processing algorithms is discussed and an overview of field programmable gate array (FPGA) structure is given. The chapter also presents architectures for the hardware implementation of vector rotation and angle evaluation operations in addition to the FFT architecture. For each components, different implementation alternatives have been discussed.

Chapter 4, which is the first main chapter of the research project presents two robust CFO estimation methods for OFDM systems over frequency selective fading channels. The considered CFO estimators are analysed in depth in terms of complexity, performance in the presence of timing uncertainty and relation to other CFO estimators. Extensive simulation results are presented for various channel and timing ambiguity conditions to compare the performance with other state-of-the-art techniques.

Chapter 5, focuses on the symbol timing synchronization for OFDM systems. This chapter presents a robust blind symbol timing synchronization method for OFDM systems. The chapter also covers the details of different realizations for

implementation of the proposed timing metric. Extensive simulation results are provided to asses the performance of the proposed timing estimator compared with other well-known methods.

In Chapter 6 the proposed synchronization systems presented in Chapter 4 and 5 are extended for MIMO-OFDM systems employing orthogonal space-time coding and the chapter also discusses how to adapt them to MIMO-OFDM systems with spatial streams. The chapter also consider the mutual effect between the timing and frequency synchronization process. The simulation results are then presented to evaluate the performance of the proposed synchronization schemes for STC-MIMO-OFDM systems over various channel conditions.

In Chapter 7 an architectural exploration for the implementation of blind CFO estimator presented in Chapter 4 is discussed. The chapter outlines the design flow used for prototyping on a reconfigurable hardware. The chapter introduces two architectures to implement the considered CFO estimator and discusses different implementation alternatives. The proposed architectures are evaluated in terms of estimation accuracy and resource utilization.

Finally, conclusions are drawn in Chapter 8 and the thesis ends with a possible line of future work.

Chapter 2

Background

This chapter presents the basic principles for wireless communications using OFDM technique. It starts with a general presentation for communication through multipath radio channel. The signal model for OFDM transmission scheme and its main parameters, features and applications are described. Finally, the effect of synchronization imperfections on the received signal and the fundamentals of signal synchronization in OFDM systems are then discussed.

2.1 Multipath Propagation Channels

Multipath propagation occurs because of scattering, reflection, and diffraction of the transmitted signal which arrives at the receiver through multiple paths as shown in Fig. 2.1. The multipath copies might overlap the next bit or symbol and hence causes ISI which has significant impact on the performance of communication systems. This section provides a simplified overview for channel models with their statistical properties.

2.1.1 Baseband Channel Modelling

A radio channel is commonly modelled as wide-sense stationary (WSS) with uncorrelated scattering (US). A linear superposition of uncorrelated echoes is assumed and each path p has a fixed delay τ_p with time-varying gain $h(t, \tau_p)$. The channel can be modelled using tapped delay line (FIR filter) [26] as shown in Fig. 2.2,

$$h(t, \tau) = \sum_{i=0}^{L_h} h(t, \tau_i)\delta(\tau - \tau_i), \tag{2.1}$$

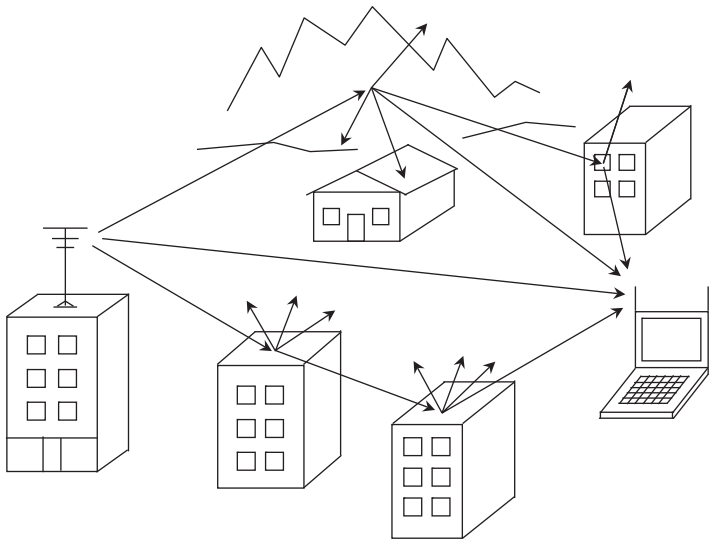

Figure 2.1: Multipath fading channel with multiple copies of the signal arriving at the receiver.

where $(L_h + 1)$ is the number of paths and

$$\tau_p = \sum_{i=0}^{p} \tau_i^{'}. \tag{2.2}$$

Thus, the received signal $y(t)$ can be written as,

$$y(t) = \sum_{i=0}^{L_h} h(t, \tau_i) u(t - \tau_i) + z(t), \tag{2.3}$$

where $u(t)$ is the complex envelope of the transmitted signal and $z(t)$ is the noise signal with variance σ_z^2.

Actually, the number of taps is infinite and the tap coefficients are correlated. However, the WSS with US model implies that the autocorrelation function $\varphi(\tau)$ of the tap gains $h(t)$ depends only on the difference between observation times τ,

$$\varphi(\tau) = E[h(t)h^*(t - \tau)], \tag{2.4}$$

where the notation $E[\,]$ denotes statistical expectation. Therefore, in simulations, a finite filter length (L_h) and statistically independent tap coefficients can be considered [27].

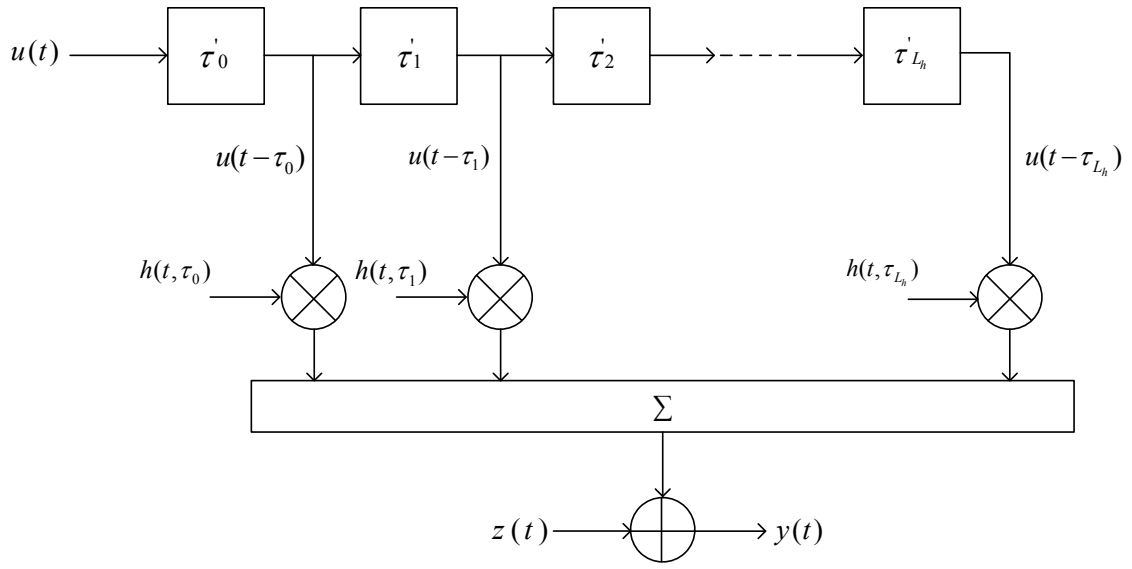

Figure 2.2: Taped delay line (FIR filter) channel model

2.1.2 Multipath Channel Delay Profiles

The power delay profile (PDP) of the channel shows the power versus delay of each multipath echoes. The total delay spread parameter is used to denote the severity of multipath environments and it is defined as the difference between the delay of the first and last arriving multipath component. As discussed previously, the signal transmitted through multipath environments can be affected by ISI. The rms delay spread (τ_{rms}) and coherence bandwidth (B_{coh}) are important channel parameters used to characterize the effect of ISI on the received signal. The delay spread characterizes how the channel correlates the transmitted signal whereas the coherence bandwidth is a measure of the range of frequencies over which the channel components exhibit correlation. The τ_{rms} is defined as the second central moment of the PDP [26],

$$\tau_{rms} = \sqrt{\frac{\sum_{i=0}^{L_h} P_i \tau_i^2}{\sum_{i=0}^{L_h} P_i} - \left(\frac{\sum_{i=0}^{L_h} P_i \tau_i}{\sum_{i=0}^{L_h} P_i} \right)^2}, \tag{2.5}$$

where P_i is the received power of ith multipath component.

The channel is considered as narrowband if the symbol duration (T_s) is much greater than τ_{rms} which implies that all the reflected components arrive within the time frame of a symbol. However, if T_s is much less than the τ_{rms}, then the channel is considered as broadband which introduces significant amount of ISI.

In the frequency domain, the τ_{rms} is inversely proportional to the channel coher-

ence bandwidth,

$$B_{coh} \triangleq \frac{1}{\tau_{rms}}. \tag{2.6}$$

The frequency components of the transmitted signal experience similar attenuation if the bandwidth of the signal (B_{signal}) is much less than the coherence bandwidth of the channel. Therefore, such channels are called frequency flat channels where no ISI is affecting the received signal. However, in frequency selective channels where B_{signal} is much greater than B_{coh}, the frequency components of the transmitted signal exhibit different attenuation. Hence, the received signal is severely affected by ISI and advanced signal processing techniques are required in order to mitigate these effects.

In reality, the channel does not remain constant over time because of the changes in the multipath environment. The delay spread and coherence bandwidth do not offer information on how the channel varies with time. The time variations in the channel translate into spectral broadening. The Doppler spectrum characterizes the fading rate of a multipath component and it depends on the type of propagation [26,27]. The Doppler spread is used as a measure of the spectral expansion caused by motion and is defined as the range of frequencies over which the Doppler spectrum is non-zero. The coherence time of the channel (T_{coh}) is inverse of the Doppler spread (B_d) and it provides a measure of the time duration over which the channel impulse response is mainly invariant with time,

$$T_{coh} \triangleq \frac{1}{B_d}. \tag{2.7}$$

The Doppler spread and coherence time are indicators of the time varying nature of the channel. It means that when two symbols that are passed through the channel with an interval greater than T_{coh}, they will be affected differently by the channel. The channel is called fast or time selective if the symbol duration is larger than the coherence time and the signal will distort significantly since the channel will change during the transmission of the symbol. However, the channel is considered as slow fading if the symbol duration is less than the coherence time where the channel impulse response slowly varying compared to the symbol rate. In this case, the channel can be assumed static over the signalling interval. For rigorous treatment on channel modelling, the reader is referred to [26, 28–30].

2.2 OFDM

In dispersive channels, different echoes of different symbols overlap because of multipath propagation between transmit and receive antennas. In such channels, the system performance is ISI limited especially in high data rate communications when the delay spread of the channel increases larger than multiple of the symbol period. In the literature, several research projects have been conducted in order to overcome the effect of ISI due to the channel dispersion and advanced transmitter and/or receiver techniques have been developed. The channel equalization is one of the efficient techniques that has been widely employed in most high rate wireless systems to combat the ISI. In the following, alternative approach for transmitting over multipath fading channels using OFDM technique is discussed.

2.2.1 Multicarrier Modulation

For ISI immune communication systems, the symbol duration (T_s) should be much larger than the channel delay spread otherwise the error rate becomes intolerable. The multicarrier modulation technique is alternative for single carrier transmission over wideband channels that follows originally from the competing needs of high data rates and ISI free transmission. Instead of trying to mitigate the effects of channel dispersion, the multicarrier modulation employs a set of subcarriers for parallel transmission over the channel. In order to combat the ISI, the high data stream is divided into N substreams each of which has a duration of NT_s which is greater than the channel delay spread. The substreams are transmitted in parallel over N narrow subchannels and the system throughput is the sum of all the subchannels which is the same throughput of single carrier systems. The multicarrier scheme is refereed to as OFDM when the subchannels are orthogonal under the ideal prorogation environments. Denoting the system bandwidth as B, the N orthogonal subcarriers are assumed to be at frequencies $f_n = nB/N$, $n = 0, 1, ..., N-1$ as shown in Fig. 2.3 where [27],

$$\int_{iT}^{(i+1)T} e^{j2\pi f_k t} e^{-j2\pi f_n t} dt = \delta_{nk} \tag{2.8}$$

In OFDM, the spectrum of the subcarriers are overlapped and orthogonal to each other. In order to achieve the subcarriers orthogonality and avoid ICI, the

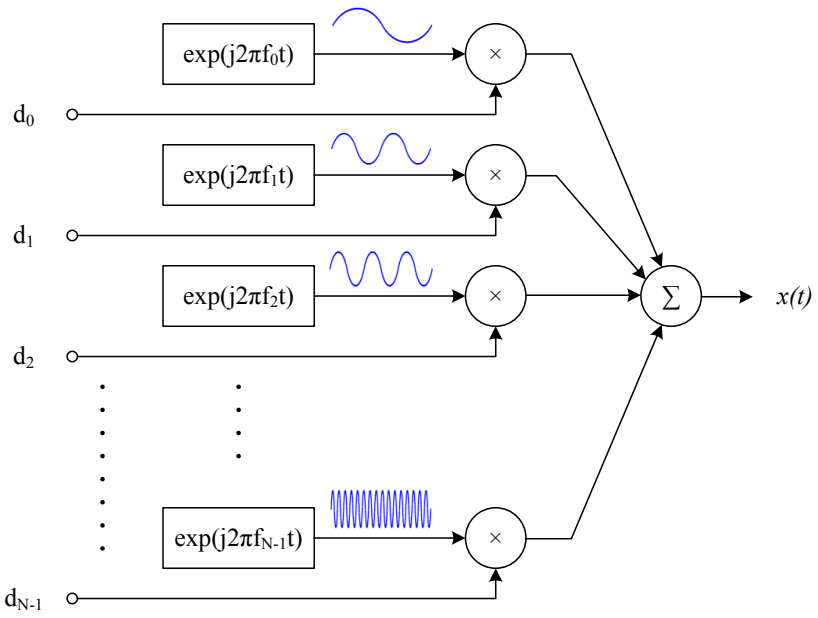

Figure 2.3: The Multicarrier Principle

subcarrier interval (Δf) should be equal to $1/T$, where T is the OFDM symbol duration.

Therefore, in a high efficiency modulation scheme, a robust transmission of high data rates is ensured over frequency selective channels where the subchannels experience relatively flat fading since their bandwidth is selected to be significantly lower than the coherence bandwidth of the channel. In contrast to the single carrier systems which require a complex adaptive time-domain equalizers, the equalization in OFDM systems is quite simple.

2.2.2 System Model

Denoting the symbol of the ith subcarrier at the lth instance as $d_i(l)$, the OFDM modulated signal is given by [27]

$$x(t) = \sum_{l=-\infty}^{l=\infty} \sum_{i=0}^{N-1} d_i(l) g_i(t - lT), \tag{2.9}$$

where $g_i(t)$ is a normalized, frequency-shifted rectangle pulse given as

$$g_i(t) = \begin{cases} \frac{1}{\sqrt{T}} e^{j2\pi f_i t}, & 0 \leq t \leq T \\ 0, & \text{otherwise} \end{cases}. \tag{2.10}$$

In general, at time instant l=0, if the symbol is sampled at nT/N, $n = 0, 1, ...N-1$,

then

$$x_n = \frac{1}{\sqrt{N}} \sum_{i=0}^{N-1} d_i e^{j2\pi in/N}, \quad n = 0, 1, ..., N-1. \tag{2.11}$$

By noting (2.11), this is exactly the IDFT of the transmitted symbol. Therefore, OFDM modulation and demodulation can be efficiently implemented using IDFT and DFT, respectively. Thus, the hardware realization is greatly simplified compared with traditional implementation using multiple oscillators. In addition, the DFT can be efficiently realized using FFT algorithm, especially for large N values, which reduces the number of operations from N^2 to $N \log_2 N$.

The block diagram for the baseband implementation of OFDM systems is illustrated in Fig. 2.4(a). The information bit stream is grouped to form the subsequences $C_i \triangleq [c_{i,1}, ..., c_{i,m}]$, where $m = \log_2 M$ represents the number of bits per symbol and M is the constellation size of the utilized modulation scheme. Subsequently, each C_i is mapped to M-ary phase shift keying (M-PSK) or M-order quadrature amplitude modulation (M-QAM) taking values from the M-ary symbol alphabet $\Omega = \{\alpha_1, ...\alpha_M\}$, where $\alpha_i \in \mathbb{C}$ and $\mathbb{C}$ denotes the set of complex numbers.

Then, the constellation symbols are grouped to form a sequence of independent complex symbols $\mathbf{d}$, to modulate the orthogonal subcarriers during the lth OFDM symbol block,

$$\mathbf{d}(l) = [d_0(l), d_1(l), ..., d_{N-1}(l)]^T, \qquad l = 1, ..., L \tag{2.12}$$

where N is selected as power of two for efficient implementation of the FFT. On each subcarrier, the transmission rate is relatively low which results in flat fading experienced by each subcarrier. The set of data symbols $\mathbf{d}$ is applied to an N-point IDFT process to produce the sequence $\mathbf{x}$ which consists of N time-domain samples that represent the OFDM complex envelope,

$$\mathbf{x}(l) = [x_0(l), x_1(l), ..., x_{N-1}(l)]^T, \tag{2.13}$$

where

$$\mathbf{x}(l) = \mathbf{W}^H \mathbf{d}(l). \tag{2.14}$$

The matrices $\mathbf{W}$ and $\mathbf{W}^H$ represent the normalized $N \times N$ DFT and IDFT matrices,

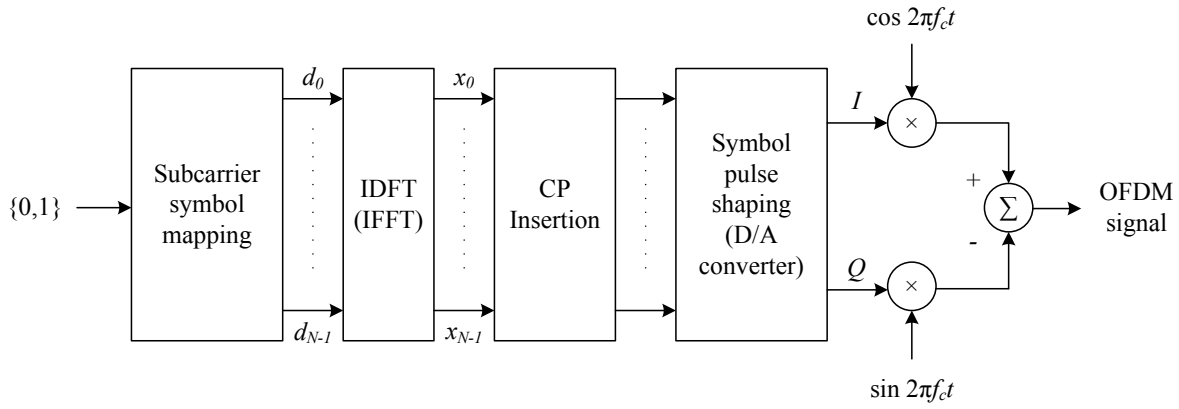

(a) Modulator

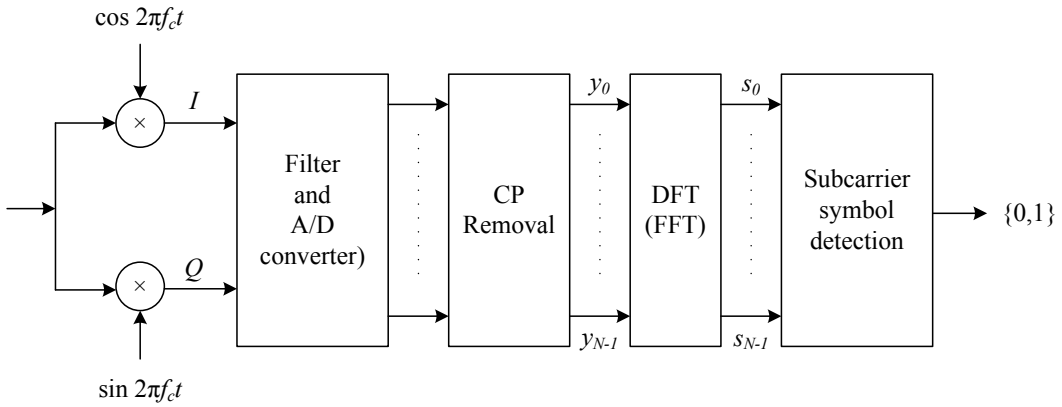

(b) Demodulator

Figure 2.4: The baseband realization of OFDM system

respectively,

$$\mathbf{W}^H = \frac{1}{\sqrt{N}} \begin{bmatrix} 1 & 1 & \cdots & 1 \\ 1 & e^{j\omega} & \cdots & e^{j(N-1)\omega} \\ \vdots & \vdots & \ddots & \vdots \\ 1 & e^{j(N-1)\omega} & \cdots & e^{j(N-1)^2\omega} \end{bmatrix}, \tag{2.15}$$

where $\omega = 2\pi/N$.

Therefore, the nth sample in the sequence $\mathbf{x}(l)$ can be expressed as,

$$x_n(l) = \frac{1}{\sqrt{N}} \sum_{i=0}^{N-1} d_i(l) e^{j\frac{2\pi in}{N}}, \qquad n = 0, 1, ..., N-1. \tag{2.16}$$

Using OFDM modulation, the frequency selective channel is divided into frequency flat channels which considerably reduce the effect of channel frequency selectivity. However, the OFDM symbol is still not immune to ISI which occurs due to the delayed arrival of the multipath components. To combat the ISI in multipath channels and assure ISI free reception, a time domain guard band is inserted between consecutive symbols. The most popular approach, referred to as the cyclic-prefix

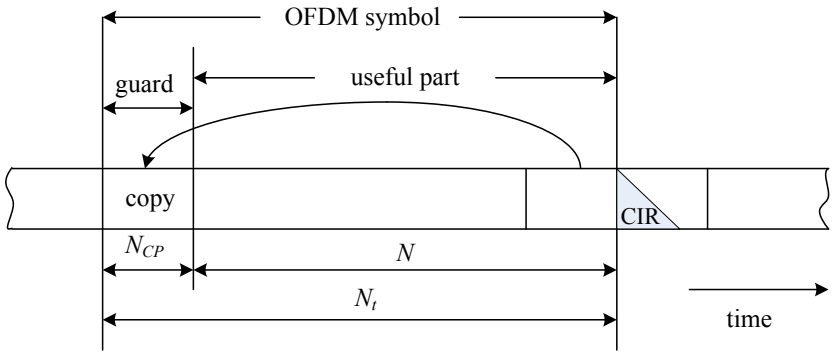

Figure 2.5: Cyclic prefix insertion

(CP), is to copy the last N_{CP} samples of the IDFT output and append them at the beginning of the symbol to be transmitted as shown in Fig. 2.5. The value of N_{CP} should be greater than the channel order (L_h). Therefore, the transmitted OFDM block, denoted as $\bar{\mathbf{x}}$, consists of $N+N_{CP}$ samples with the following frame structure,

$$\bar{\mathbf{x}}(l) = [x_{N-N_{CP}}(l), ..., x_{N-1}(l), x_0(l), ..., x_{N-1}(l)]^T. \tag{2.17}$$

The useful part of the OFDM symbol does not include the N_{CP} prefix samples and has a duration of T seconds. The resulting OFDM block of length $N_t = N + N_{CP}$ samples is up-converted to a radio frequency (RF) centred at f_c and then transmitted through the antenna.

At the receiver front-end, the received signal is down converted into the base-band waveform as shown in Fig. 2.4(b) where I and Q represent the in-phase and quadrature components of the received baseband signal, respectively. The received baseband signal is applied to a matched filter and then sampled at a rate T/N to produce the time domain received samples. The received samples that belong to a single OFDM symbol can be expressed as

$$\bar{\mathbf{y}} = [\mathrm{c}_0,\ \mathrm{c}_1, ..., \mathrm{c}_{N_{CP}-1},\ y_0,\ y_1, ...,\ y_{N-1}], \tag{2.18}$$

where c_i represents the CP samples. The non CP samples $\{y_n\}$ will be referred to as the data samples.

After dropping the first N_{CP} samples, the useful part of the symbol $\mathbf{y}(l) = [y_0(l), y_1(l), ..., y_{N-1}(l)]^T$ can be extracted from the stream of received symbols where,

$$\mathbf{y}(l) = \bar{\mathbf{H}}(l)\mathbf{x}(l) + \mathbf{z}(l), \tag{2.19}$$

The system noise $\mathbf{z}(l) = [z_0(l), z_1(l), ..., z_{N-1}(l)]^T$ is modelled as a white Gaussian process with zero mean and variance $\sigma_z^2 = E[|z_n|^2]$ and $\bar{\mathbf{H}}(l)$ denotes the channel matrix during the lth OFDM block. By dropping the block index l, to simplify the notations, and assuming that the channel remains fixed for one block period, the matrix $\bar{\mathbf{H}}$ can be expressed as

$$\bar{\mathbf{H}} = \begin{bmatrix} h_0 & h_{N-1} & \cdots & h_1 \\ h_1 & h_0 & \ddots & \vdots \\ \vdots & \vdots & \ddots & h_{N-1} \\ h_{N-1} & h_{N-2} & \cdots & h_0 \end{bmatrix}. \tag{2.20}$$

The discrete-time channel impulse response samples $h_p = 0 \ \forall \ p \geq L_h$ where $L_h < N_{CP}$. It can be observed from (2.20) that $\bar{\mathbf{H}}$ is a circulant matrix hence it will be diagonalized by the IDFT/DFT matrices

$$\mathbf{H} = \mathbf{W}\bar{\mathbf{H}}\mathbf{W}^H, \tag{2.21}$$

where $\mathbf{H}$ is $N \times N$ diagonal matrix whose ith diagonal elements can be expressed as [23],

$$H_i(l) = \sum_{p=0}^{L_h} h_p(l) e^{-j\frac{2\pi pi}{N}}. \tag{2.22}$$

Thus, the received signal samples can be written as

$$\mathbf{y}(l) = \mathbf{W}^H\mathbf{H}(l)\mathbf{d}(l) + \mathbf{z}(l). \tag{2.23}$$

and the nth element of $\mathbf{y}$ can be expressed as

$$\mathbf{y}_n(l) = \frac{1}{\sqrt{N}} \sum_{i=0}^{N-1} d_i(l) H_i(l) e^{j\frac{2\pi ni}{N}} + z_n(l). \tag{2.24}$$

The time domain samples $\mathbf{y}(l)$ are processed with DFT to produce the frequency domain samples $\mathbf{s}(l)$, which represent the I-Q values of the received subcarrier symbols,

$$\mathbf{s}(l) = \mathbf{W}\,\mathbf{y}(l), \tag{2.25a}$$

$$= \mathbf{H}(l)\mathbf{d}(l) + \eta(l), \tag{2.25b}$$

where $\eta(l) = \mathbf{W}\,\mathbf{z}(l)$, whose elements are zero mean complex independent Gaussian random variables with variance σ_η^2. The kth element of $\mathbf{s}(l)$ can be expressed as

$$\mathbf{s}_k(l) = \frac{1}{\sqrt{N}} \sum_{n=0}^{N-1} y_n(l) e^{-j\frac{2\pi nk}{N}}. \tag{2.26}$$

However, the channel coefficients in the frequency domain ($\mathbf{H}$) is required to demodulate the frequency domain symbols. At the receiver, the channel can be estimated based on least squares (LS) or linear minimum mean square error (LMMSE) criteria by exploiting pilots or training sequences or using blind approaches. Then, a simple frequency domain equalizer (FEQ) can be employed by scaling the frequency domain symbol using the inversion of channel estimate ($\hat{\mathbf{H}}$) to produce the demodulated data,

$$\hat{\mathbf{d}}(\mathbf{l}) = \frac{\mathbf{s}(l)}{\hat{\mathbf{H}}(l)}. \tag{2.27}$$

The subcarrier symbols are then de-mapped into a parallel bit stream. The parallel-to-serial converter (multiplexer) combines the parallel bit streams into one single serial bit stream at the output.

2.3 Synchronization Imperfection

The stringent synchronization requirement is one of the design challenges for OFDM receivers. For proper demodulation of OFDM signals, two important synchronization tasks, namely symbol timing and frequency synchronization, need to be performed. The timing synchronization determines the optimal timing instants for the symbol while the frequency synchronization align the carrier frequency of the receiver as closely as possible to the carrier frequency of the transmitter node. Compared with single carrier based systems, the signal transmission using multicarriers makes OFDM systems more sensitive to synchronization errors [12]. Demodulation of an OFDM signal in the presence of synchronization errors destroys the orthogonality among the subcarriers and thus introduces ICI and ISI. In addition to the interference introduced due to the frequency jitter and symbol timing errors, the synchronization imperfection may affect the performance of other blocks in the OFDM receiver such as the channel estimation. All of these impairments result into system performance deterioration. Therefore, attaining accurate synchronization is of

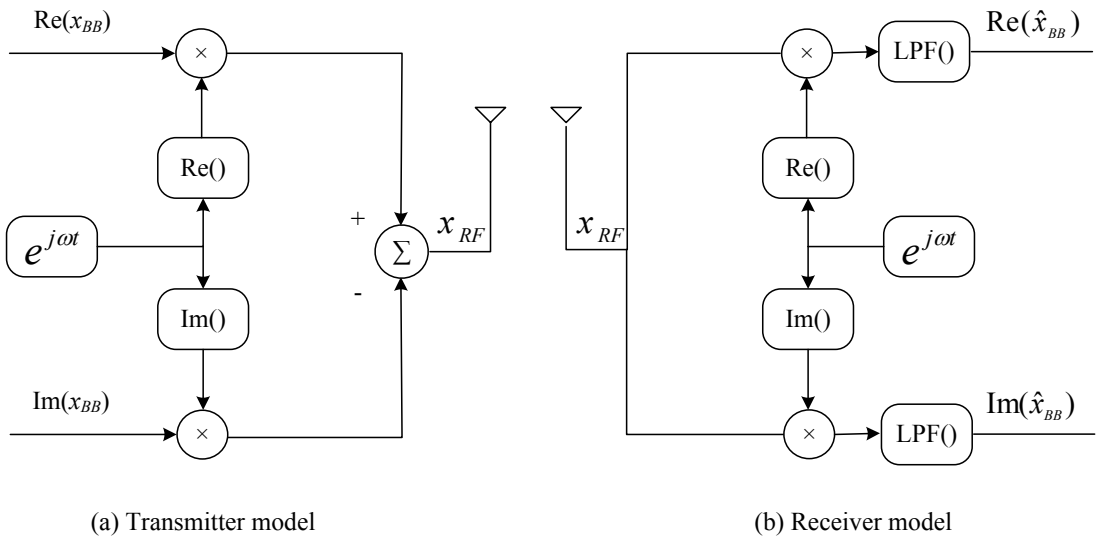

(a) Transmitter model (b) Receiver model

Figure 2.6: The origin of CFO during up/down conversion

critical importance to improve the performance of OFDM systems.

2.3.1 The Effect of Frequency Synchronization Errors

The carrier frequency offset (CFO) is one of the common impairment in wireless communication system that results from the frequency variation of local oscillators used to translate signals between baseband and RF at the transmitter and receiver nodes. A simplified model to generate RF version (x_{RF}) of a complex baseband signal (x_{BB}) with carrier frequency (f_c) is illustrated in Fig. 2.6 where,

$$\begin{aligned} x_{RF} &= \mathrm{Re}\{x_{BB}\}\cos(2\pi f_c t) - \mathrm{Im}\{x_{BB}\}\sin(2\pi f_c t), && \text{(2.28a)} \\ &= \frac{1}{2}(x_{BB}e^{j2\pi f_c t} + x_{BB}^{*}e^{-j2\pi f_c t}). && \text{(2.28b)} \end{aligned}$$

At the receiving node, the received RF signal is down converted and passed through a low-pass filter (LPF) with gain of 2 and passband determined by the bandwidth of the baseband signal. Assuming the carrier frequency of the receiving node is $f_c \pm f_\epsilon$ where f_ϵ represents frequency offset of the carrier, the received baseband signal ($\hat{x}_{BB}$) in terms of the transmitted baseband signal (x_{BB}) can be expressed as

$$\begin{aligned} \hat{x}_{BB} &= \mathrm{LPF}\left(\frac{(x_{BB}e^{j2\pi f_c t} + x_{BB}^{*}e^{-j2\pi f_c t})(e^{j2\pi(f_c \pm f_\epsilon)t})}{2}\right), && \text{(2.29a)} \\ &= x_{BB}e^{\pm j2\pi f_\epsilon t}. && \text{(2.29b)} \end{aligned}$$

It is obvious that the received baseband signal ($\hat{x}_{BB}$) is equal to the transmitted baseband signal (x_{BB}) modulated by a complex sinusoid of frequency ($\pm f_\epsilon$) equal to the difference in carrier frequencies between the transmit and receiver nodes [31].

In OFDM systems, the CFO produces a shift of the received signal in the frequency domain and may result in a loss of mutual orthogonality among subcarriers which substantially affect the performance. To better explain this concept, the DFT output corresponding to the lth OFDM symbol in the presence of CFO is computed [32, 33],

$$\mathbf{s}_k(l) = d_k(l)H_k(l)\frac{\sin(\pi\epsilon)}{N\sin(\pi\epsilon/N)}e^{j2\pi l\frac{(N+N_{CP})}{N}} + \Psi_k(l) + \eta_k(l), \tag{2.30}$$

where ϵ is the normalized frequency error by the subcarrier spacing and $\Psi_k(l)$ denotes the zero-mean ICI term with power $\sigma_\Psi^2 = E[|\Psi_k|^2]$.

From (2.30), it can be observed that the received signal is the sum of three different terms: the additive noise $\eta_k(l)$, the useful term $d_i(l)$ that presents attenuation and phase rotation because of the dispersive channel and frequency synchronization errors and the ICI term due to the loss of orthogonality among the subcarriers at the DFT output. The phase offset is constant across subcarriers in an OFDM symbol and increases with each OFDM symbol. To illustrate the effect of CFO synchronization error, the frequency spectrum of OFDM signal with 5 subcarriers is shown in Fig. 2.7 for $\epsilon = 0$ and 0.2. The dotted lines with the circle markers represent the signal at DFT output. It is obvious from Fig. 2.7(a) that the DFT output only consists of the signal transmitted on the corresponding subcarrier without any interference from the neighbouring subcarriers. However, for $\epsilon = 0.2$ as shown in Fig. 2.7(b), the DFT output consists of both the signal transmitted on the corresponding subcarrier and interference from the transmitted signal on the neighbouring subcarriers. In addition to the reduction in the amplitude of the regarded subcarrier, the presence of CFO provokes the leakage from other subcarriers with interference power is inversely proportional to the frequency spacing.

The ICI reduces the effective SNR (SNR_e) which worsens with the increase of CFO. The SNR loss in the presence of additive noise and ICI induced by frequency synchronization errors is defined as,

$$\rho(\epsilon) = \frac{\text{SNR}}{\text{SNR}_e}. \tag{2.31}$$

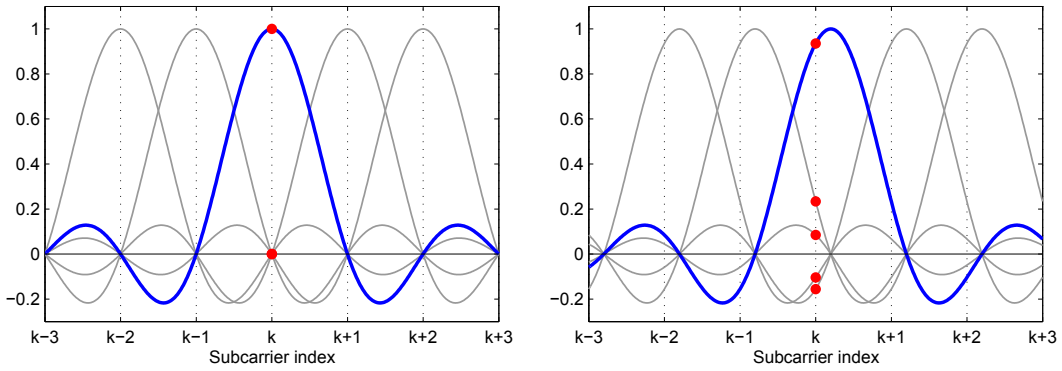

(a) $\epsilon = 0$ (b) $\epsilon = 0.2$

Figure 2.7: The effect of CFO on the subcarriers orthogonality

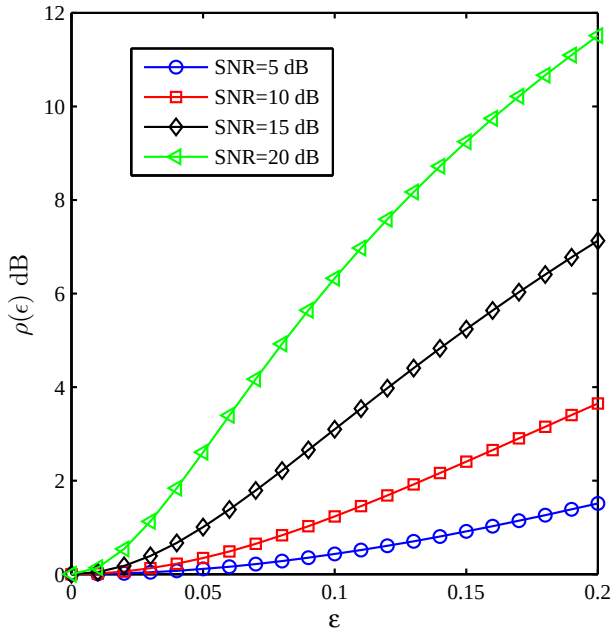

Figure 2.8: SNR loss $\rho(\epsilon)$ due to carrier frequency offset ϵ

The SNR loss $\rho(\epsilon)$ can be approximated for small values of ϵ as [34],

$$\rho(\epsilon) \approx 1 + \frac{1}{3}\frac{\sigma_d^2}{\sigma_\eta^2}(\pi\epsilon)^2. \tag{2.32}$$

The SNR loss in dB as function of the normalized carrier frequency offset ϵ, for different SNR is depicted in Fig. 2.8. From this figure, it is noted that OFDM systems will have significant SNR deterioration as ϵ increases. It is obvious that more degradation is observed as the SNR increases. Therefore, CFO incur non-negligible performance degradation even when the frequency synchronization error is not exceeding 5% of the subcarrier spacing.

2.3.2 The Effect of Timing Synchronization Errors

Initially, the starting point of the OFDM symbol is not well determined. The symbol timing synchronization identifies the set of samples used to calculate the DFT window of the received OFDM symbol. In the ideal situation, the DFT window starts from the first sample of the useful part of OFDM symbol as shown in Fig. 2.9(a). However, due to jitters in the symbol timing estimate, the timing synchronization errors occur and the useful part of the OFDM symbol might not extracted correctly. Denoting the symbol timing offset from the start of the symbol as $\delta \in \{\frac{-N}{2}, \frac{-N}{2}+1, ..., \frac{N}{2}\}$ samples. Hence, the DFT window could start either too early (negative timing error) or too late (positive timing error) as illustrated in Fig. 2.9(b) and (c), respectively. When the DFT window is late (early) after (before) the first sample of the data part of the symbol, i.e. positive (negative) timing errors, the last (first) samples are taken from the next (previous) OFDM symbol. Therefore, ISI will be introduced which consequently deteriorates the performance enormously. For both cases, the post-DFT signal is described as [20]

$$s_k(l) = e^{j\frac{2\pi k\delta}{N}}\alpha(\delta)H_k(l)d_k(l) + I_k(\delta, l) + \eta_k(l), \tag{2.33}$$

where $\alpha(\delta)$ is the attenuation factor of the symbol while the ISI and ICI disturbance are modelled as additional noise $I_k(\delta, l)$ with zero-mean and variance $\sigma_I^2(\delta)$. Both $\alpha(\delta)$ and $I_k(\delta, l)$ depends on the timing error and the channel profile [34].

Because of the channel dispersion, the tail of each received OFDM block extends over the first L_h samples of the successive block as depicted in Fig. 2.9. In order to avoid the ISI, the DFT window should include samples only from one OFDM symbol. In well designed OFDM systems, the length of CP is greater than the CIR duration. Therefore, certain samples of the CP are not affected by the leakage from the previous block. As long as the timing error satisfy the condition

$$L_h - N_{CP} \leq \delta < 0, \tag{2.34}$$

the DFT window starts within the ISI free region of the CP (denoted as safe-region) accommodating samples from only the current symbol as shown in Fig. 2.9(d). In this case, no ISI present at the DFT output and the timing error only results in a cyclic shift of the received OFDM block which can be considered as part of the

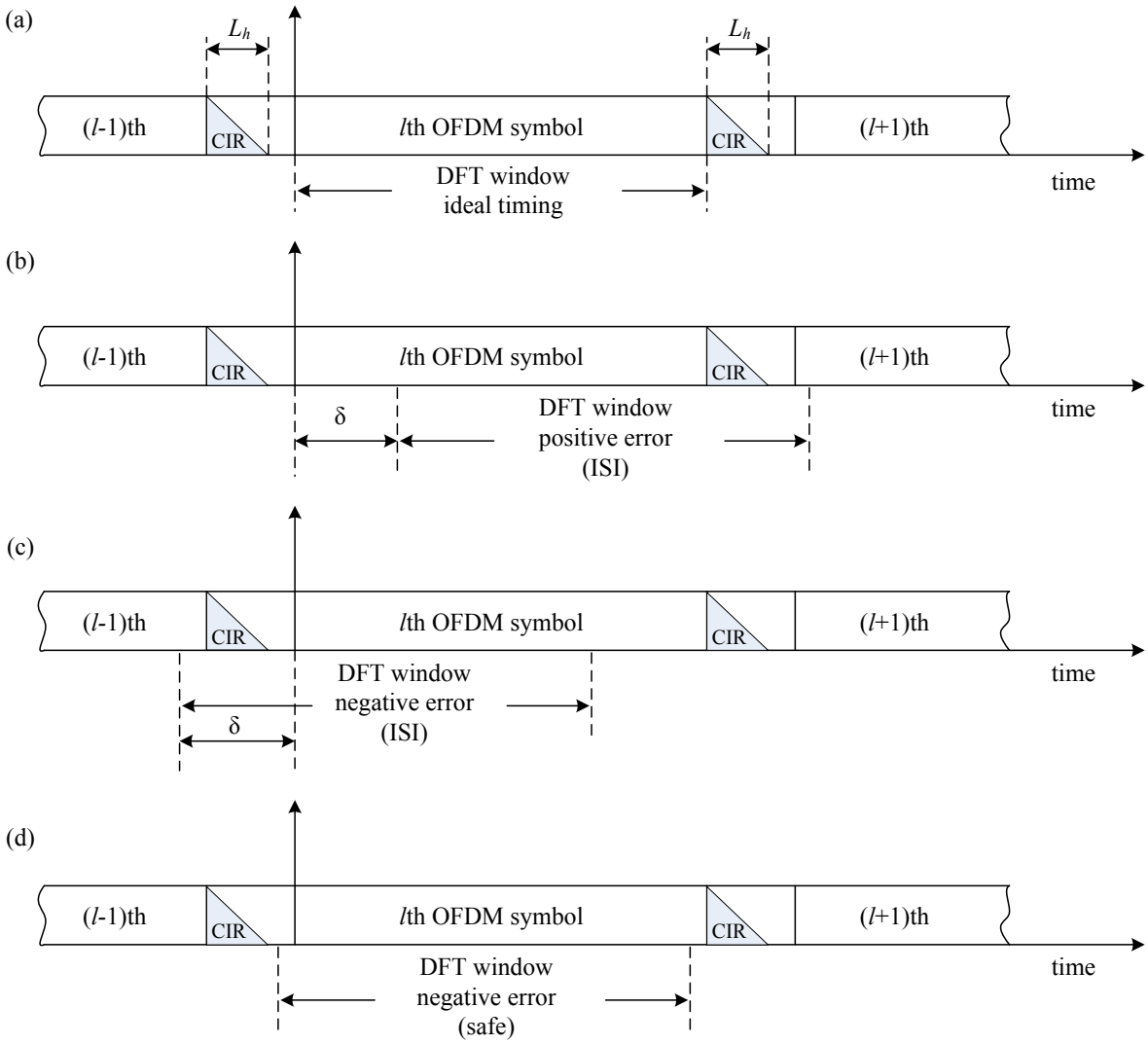

Figure 2.9: The DFT window timing

channel effect.

2.4 Synchronization of OFDM Systems

Generally, synchronization methods for digital receivers fall into one of two categories. In the first category, the synchronization is accomplished by tracking the time and frequency errors by driving some error signal to zero through feedback loop [35]. The main disadvantage of such synchronization methods that possess feedback is their high acquisition time. Therefore, they might not be applicable if the synchronization parameters are quickly varying or when the information is transmitted in burst [36]. The other category of synchronization methods, known as feedforward, perform the estimation using a block of received data. These methods can handle both continuous and burst transmission as the estimates are ob-

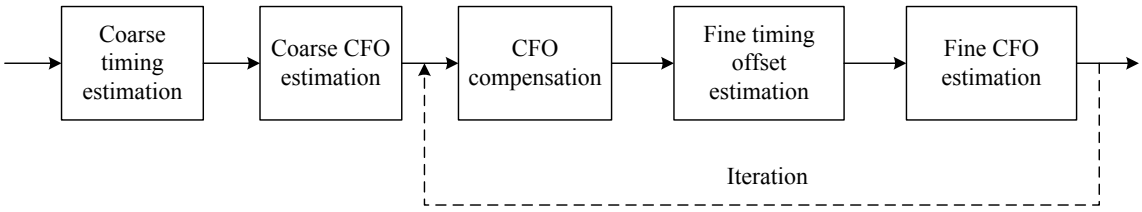

Figure 2.10: Synchronization procedure in OFDM systems

tained by processing the received signal over a short observation window [37]. In addition, depending on the information required to develop the estimation metric, the synchronization strategies whether it is feedback or feedforward are classified as data-aided if some pre-known information such as training sequences or pilots are inserted at the transmitter side to help the receiver to achieve synchronization. Non data-aided methods utilize the intrinsic structure of OFDM symbol such as the cyclic prefix and virtual subcarriers or exploit the signal statistical information to estimate the synchronization parameters [38].

Accurate synchronization is indispensable in OFDM system to tackle the negative impact on the communication performance. However, the synchronization requirements depend on the transmission whether it is continuous or burst. In continuous mode transmission systems, there no stringent requirements on the acquisition time. Therefore, averaging, filtering and feedback from frequency domain can be used to improve the estimation accuracy. However, burst mode systems have somewhat inflexible requirements as the synchronization parameters need to be estimated accurately using short observation time. Hence, averaging over many symbols and pilots might not be appropriate [39].

The synchronization chain in OFDM systems is illustrated in Fig. 2.10. At the beginning, a sync flag which indicates the presence of the signal is estimated. The sync flag can be generated by automatic gain control via power measurement with threshold device or by using some reference symbols which are used for frame detection as well. After detecting the sync flag, the synchronization starts with coarse timing estimation based on a specific timing metric (this operation sometimes referred to as frame detection) where the OFDM symbol boundary is detected for the initial start of the FFT window. After the coarse timing operation, the CFO is estimated and compensation is performed on the received symbol. However, as the performance of the two synchronization process is affected by each other, the initial estimates for the synchronization parameters are not accurate. Therefore,

the coarse synchronization is usually followed by fine tuning stage which consists of CFO compensation, symbol timing offset estimation, CFO estimation in addition to the channel estimation. Hence, after coarse estimation, the receiver needs to run a fine symbol timing offset estimation procedure. The symbol boundary defined by the fine timing estimate is used to estimate the fine frequency offset. It is worth mentioning that the fine synchronization procedure can be repeated to target further improvements in the estimated synchronization parameters [40].

2.4.1 Symbol Timing Synchronization

In the literature, several methods have been developed for symbol timing synchronization in OFDM systems. The basic method for attaining synchronization is to correlate repeated patterns of specially designed training sequence (preamble). In [41], the maximum correlation metric has been utilized to estimate the symbol timing,

$$\hat{\delta} = \arg\max_{\tilde{\delta}} \left\{ \sum_{n=0}^{P_L-1} \bar{y}_{\tilde{\delta}+n}(l) \bar{y}^*_{\tilde{\delta}+n+P_L}(l) \right\}, \tag{2.35}$$

where P_L is the length of the repeated pattern in the training symbol, $\bar{y}$ is the received time-domain signal before removing the CP and $\tilde{\delta}$ is the trial timing offset.

An improved correlation based estimator has been proposed in [13] where the symbol timing is estimated by maximizing the cost function,

$$\hat{\delta} = \arg\max_{\tilde{\delta}} \left\{ \frac{\left| \sum_{n=0}^{P_L-1} \bar{y}_{\tilde{\delta}+n}(l) \bar{y}^*_{\tilde{\delta}+n+P_L}(l) \right|^2}{\left(\sum_{n=0}^{P_L-1} \left| \bar{y}_{\tilde{\delta}+n+P_L}(l) \right|^2 \right)^2} \right\}. \tag{2.36}$$

Utilizing the inherent repeating structure of the CP in the OFDM symbol, a blind timing synchronization can be developed without the overhead of training sequences as reported in [17],

$$\hat{\delta} = \arg\max_{\tilde{\delta}} \left\{ \left| \sum_{n=0}^{N_{CP}-1} \bar{y}_{\tilde{\delta}+n}(l) \bar{y}^*_{\tilde{\delta}+n+N_{CP}}(l) \right| - \frac{\rho}{2} \sum_{n=0}^{N_{CP}-1} \left(\left| \bar{y}_{\tilde{\delta}+n}(l) \right|^2 + \left| \bar{y}_{\tilde{\delta}+n+N_{CP}}(l) \right|^2 \right) \right\}, \tag{2.37}$$

where ρ is defined as

$$\rho = \left| \frac{E\{\bar{y}_{\tilde{\delta}}(l)\bar{y}^*_{\tilde{\delta}+N_{CP}}(l)\}}{\sqrt{E\left\{|\bar{y}_{\tilde{\delta}}(l)|^2\right\} E\left\{\left|\bar{y}_{\tilde{\delta}+N_{CP}}(l)\right|^2\right\}}} \right| = \frac{\text{SNR}}{\text{SNR}+1}. \tag{2.38}$$

Since the timing metric of the above techniques are relaying on the received time-domain signal, their performance is expected to deteriorate severely in frequency selective fading channels. However, performing post-DFT estimation can effectively resolve the multipath problem and deliver better estimates than the time domain techniques in dispersive channels. Therefore, two stage symbol timing synchronization has been widely adopted in the literature where coarse estimation is performed in the acquisition stage using time-domain correlation based methods and this will be then followed by fine synchronization stage to attain sufficient accuracy [41–45]. Most of the fine synchronization techniques are pilot-aided estimators (PAE) based on exploiting the impact of timing error on the channel estimation such that the timing error can be detected. Therefore, such techniques can be considered as cross-block design methods that use channel estimation information to assist the symbol timing synchronization. For instance, in [43] and [44] the CIR is estimated for best placement of DFT window with respect to the estimated CIR where

$$\hat{\delta} = \arg\max_{\tilde{\delta}} \left\{ \left| \hat{h}_{\tilde{\delta}} \right| \right\}. \tag{2.39}$$

However, averaging need to be done over large number of OFDM symbols to achieve reasonable improvement using this approach.

The sensitivity of the pilot-aided channel estimator to timing synchronization errors has been investigated in [20]. Due to the timing synchronization error, it was shown that the effect of rotations in different bases have a major impact on the performance of channel estimator. This property has been exploited to propose an iterative scheme to update the estimated channel coefficients and hence to detect and correct the timing synchronization error as illustrated in [46] where

$$\hat{H}_k^{\tilde{\delta}+1} = \hat{H}_k^{\tilde{\delta}} + (1 - e^{-\frac{j2\pi N_{CP} k}{N}})\hat{h}_{N_{CP}-k} e^{\frac{j2\pi\tilde{\delta}k}{N}}. \tag{2.40}$$

The symbol timing error is detected by minimizing the cost function

$$\hat{\delta} = \arg\min_{\tilde{\delta}} \left\{ \sum_{k=0}^{N-1} \left| (\hat{d}_k l) - \tilde{d}_k(l) \right|^2 \right\}, \tag{2.41}$$

where $\hat{d}_k = \frac{s_k}{\hat{H}_k^{\tilde{\delta}}}$ and $\tilde{d}_k$ =Dec$(\hat{d}_k)$ represent the estimated symbol at the kth subcarrier before and after the decision device, respectively. However, the applicability of this approach is limited to systems that use optimal method for channel estimation. If suboptimal techniques are used, the high sensitivity of the pilot-aided estimator to timing synchronization errors will be violated and the same improvement would not be achieved resulting in a relatively high probability of false detection in the fine synchronization stage [20].

The cost function of the blind symbol timing offset estimator described in [47] is constructed to minimize the inter-block interference (IBI). The differential decoding is utilized to circumvent the need of channel state information (CSI) where

$$\hat{a}_k(l) = \text{dec } \left[s_k(l) s_k^*(l-1) \right], \tag{2.42}$$

and

$$\hat{\tilde{\delta}} = \arg\max_{\tilde{\delta}} \left\{ \sum_{l=1}^{L+1} \sum_{k=0}^{N-1} \left| s_k(l) - \hat{a}_k(l) s_k(l-1) \right|^2 \right\}. \tag{2.43}$$

A similar estimator that is based on the synchronization error interference minimization is proposed in [25, 48] by exploiting the variance of the received signal at the DFT output. The cost function of this estimator is given by,

$$\hat{\tilde{\delta}} = \arg\min_{\tilde{\delta}} \left\{ \frac{1}{N} \sum_{k=0}^{N-1} |s_k(l)|^4 - \left(\frac{1}{N} \sum_{k=0}^{N-1} |s_k(l)|^2 \right)^2 \right\}. \tag{2.44}$$

The estimator reported in [24] takes advantage of the fact that the signal-to-interference-plus-noise ratio (SINR) of the received data drastically drops due to synchronization error. Therefore, the symbol timing offset is intuitively estimated by maximizing the SINR metric where the signal power $S^{'}(l)$ and interference power $I^{'}(l)$ can be given as,

$$S^{'}(l) = \frac{1}{N} \sum_{k=0}^{N-1} \left| s_k(l) s_k^*(l+1) \right|, \tag{2.45}$$

$$I^{'}(l) = \sqrt{\left(\frac{1}{N}\sum_{k=0}^{N-1}|s_k(l)|^2\right)\left(\frac{1}{N}\sum_{k=0}^{N-1}|s_k(l+1)|^2\right) - S'(l)}, \tag{2.46}$$

and the symbol timing offset is estimated using

$$\hat{\delta} = \arg\max_{\tilde{\delta}} \left\{ \sum_{l=1}^{L+1} \frac{S'(l)}{I'(l)} \right\}. \tag{2.47}$$

2.4.2 Carrier Frequency Synchronization

Similar to the symbol timing synchronization, the CFO estimation can be performed with the aid of some known symbols (such as training sequences) or blindly by exploiting the CP redundancy. After performing coarse timing, the correlation based methods can be used to estimate the CFO. Despite their low computational complexity, the estimation accuracy is rigorously affected by multipath distortion and symbol timing uncertainty [13, 17, 41].

A post-DFT maximum likelihood (ML) estimators based on optimal training sequences, such as the orthogonal sequence with constant modulus, have been investigated in [49] and [50]. The estimator reported in [49] assumes perfect knowledge of the channel impulse response and perfect symbol timing synchronization to deduce a null subspace based CFO estimator for OFDM systems by exploiting the training sequence,

$$\hat{\epsilon} = \arg\min_{\tilde{\epsilon}} \left\{ \left\| \bar{\mathbf{W}}_{L_h+1}^H \mathbf{D}^{-1}(l) \mathbf{W} \mathbf{y}(l) \right\|^2 \right\}, \tag{2.48}$$

where $\bar{\mathbf{W}}_{L_h+1}$ is the null subspace of $\mathbf{W}_{L_h+1}$, which contains the last $N - L_h + 1$ columns of $\mathbf{W}$, $\mathbf{D}(l)$ =diag($[d_0(l), d_1(l), ..., d_{N-1}(l)]^T$) and $\tilde{\epsilon} \in (-0.5, 0.5)$ is the trial value of ϵ. The above estimator has been reformulated in [51] to perform joint time and frequency offset estimation. However, the multi-dimensional search over the trial values of ϵ and δ will result into computational burden for this algorithm.

The strict requirement of perfect timing synchronization of the estimator presented in [49] has been solved to some extent in [50] where timing offsets within the SR of the CP are embedded in the channel, so the multi-dimensional search can be avoided,

$$\hat{\epsilon} = \arg\min_{\tilde{\epsilon}} \left\{ \left\| \bar{\mathbf{W}}_{N_{CP}}^H \mathbf{D}^{-1}(l) \mathbf{W} \mathbf{y}(l) \right\|^2 \right\}. \tag{2.49}$$

The estimator reported in [40] utilizes null subcarriers (NSC) applied to the system to perform frequency synchronization. Assuming white Gaussian noise channel, a blind CFO estimator is derived by minimizing the energy at the NSCs (or to maximize the energy at the active carriers),

$$\hat{\epsilon} = \arg\min_{\tilde{\epsilon}} \left\{ \sum_{k \in K_n} |s_k(l)|^2 \right\} = \arg\max_{\tilde{\epsilon}} \left\{ \sum_{k \in K_a} |s_k(l)|^2 \right\}, \tag{2.50}$$

where K_n and K_a denotes the sets of the null and modulated subcarriers in the OFDM symbol, respectively.

A blind post-DFT estimator has been proposed in [22] by minimizing the ICI variance, which is proportional to the CFO. The CFO estimates can be obtained as,

$$\hat{\epsilon} = \arg\min_{\tilde{\epsilon}} \left\{ \sum_{k=0}^{N-1} \mathrm{Var}\left[|s_k(l)|^2 \right] \right\}. \tag{2.51}$$

In [23], a similar estimator is proposed based on the Kurtosis of DFT output. The cost function of this estimator is constructed by exploiting the relation between the Kurtosis, function that measures the non-Gaussianity of the received signal, and the CFO. The CFO estimates are given by,

$$\hat{\epsilon} = \arg\min_{\tilde{\epsilon}} \left\{ \frac{\sum_{k=0}^{N-1} |s_k(l)|^4}{\left(\sum_{k=0}^{N-1} |s_k(l)|^2 \right)^2} \right\}. \tag{2.52}$$

The estimator reported in [52] is based on the assumption that the channel response over two adjacent subcarriers is approximately equal. Thus, a blind CFO estimator is deduced by minimizing the power difference among all adjacent subcarriers where,

$$\hat{\epsilon} = \arg\min_{\tilde{\epsilon}} \left\{ \sum_{k=0}^{N-1} \left[|s_{k+1}(l)|^2 - |s_k(l)|^2 \right]^2 \right\}. \tag{2.53}$$

In contrast to the estimators reported in [40], [49] and [50] which require a linear search over the range of $\tilde{\epsilon}$, the cost function of [23], [22] and [52] can be approximated by a sinusoid which allows for a blind low complexity closed-form estimation using curve fitting that requires only three trial values.

2.5 Chapter Summary

This chapter provided an overview of multipath propagation and channel model used for performance evaluation of communication systems. The mathematical model and design parameters of OFDM systems were presented. This chapter also discussed the synchronization tasks and the effect of timing and frequency synchronization imperfections on system performance. Then, the requirements and categorizes of synchronization in OFDM systems using coarse and fine parameter estimation procedures were highlighted. Furthermore, several state of the art techniques for the implementation of time and frequency synchronization in OFDM systems with their cost function formulation were discussed.

Chapter 3

Synchronization Components Architectures

There are many essential components required to implement the synchronization system in digital communication receivers such as the discrete-time oscillators and computational structures to evaluate some special functions that are common in most synchronization algorithms. The direct digital synthesizer (DDS) generates sines and cosines that play an important role in frequency translation and offset compensation whereas coordinate rotational digital computer (CORDIC) algorithms are mainly adopted for the computation of special functions such as sine, cosine, tangent and arctangent. In addition, the FFT operation is required in some synchronization strategies for parameter estimation in the frequency domain. This chapter is principally focuses on the hardware architectures and different implementation alternatives for the DDS, CORDIC and FFT. These components are the main building blocks that will be used in Chapter 7 to map the proposed frequency synchronization onto reconfigurable platforms.

3.1 Reconfigurable Computing: FPGA

Over the past decades, the advancement in very large scale integration (VLSI) technology and design tools have extensively expanded the application domain of hardware implemented digital signal processing (DSP) systems. The inherent parallelism of most DSP algorithms has made possible for digital circuitry implementation of such arithmetic-intensive functions. Recently, the reconfigurable computing archi-

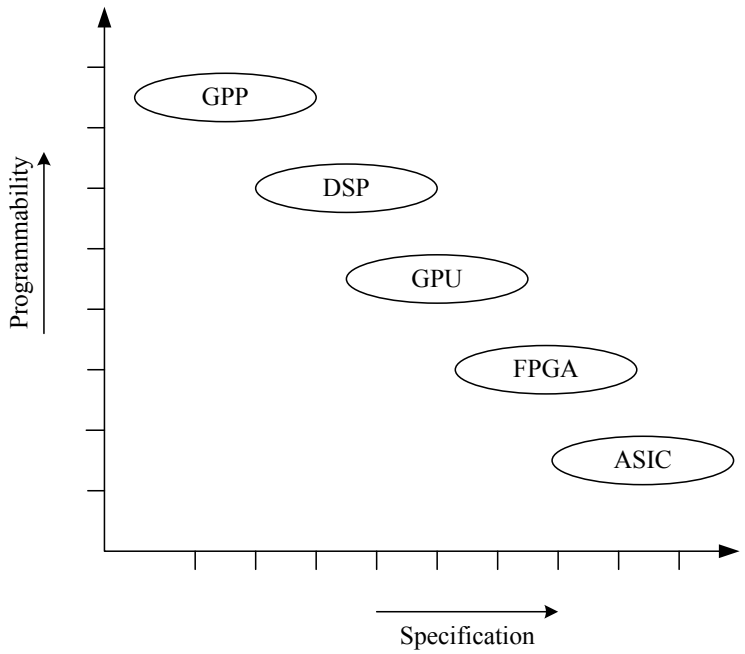

Figure 3.1: Implementation platforms for DSP algorithms

tectures using field programmable gate arrays (FPGAs) have revolutionized the implementation of signal processing algorithms and become potential candidate to replace the traditional way of hardware implementation in multimedia computing and high-speed wired and wireless communications etc [53]. As depicted in Fig. 3.1, the FPGA paradigm suggests a compromise solution between the performance of application specific integrated circuits (ASIC) and flexibility of programmable processors like general purpose processors (GPP), digital signal processors (DSP) and graphic processing units (GPU). Recently, GPUs and FPGAs have gained wide range of interest as software and hardware paradigm, respectively to accelerate compute-intensive applications [54]. Since the introduction of FPGA, there has been a great interest in the deployment of DSP algorithms on reconfigurable hardware due to the benefits that can be gained such as functional specialization, platform reconfigurability, and fine-grained parallelism. The FPGA paradigm offers field customization of the integrated circuit with almost the same attributes as fixed-functionality architecture. In addition, it contains functional resources that can be easily deployed and modified in response to the changing operational conditions and data sets. Moreover, the design of FPGA solution offers fast prototyping capabilities and the low cost requirements [53, 55].

Basically, FPGAs are a pre-fabricated chip that can be configured to function like an integrated circuit with full control over the actual design implementation

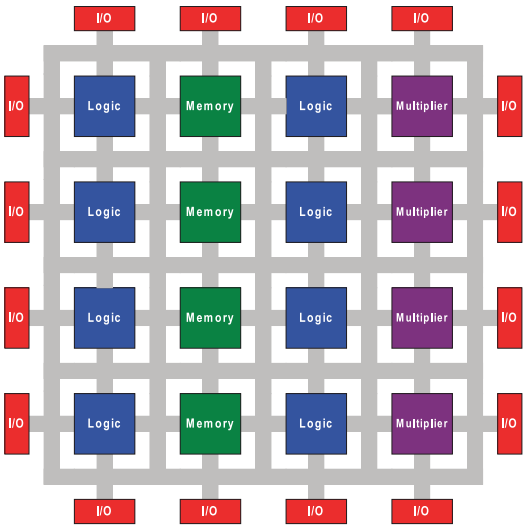

Figure 3.2: Basic FPGA structure [1]

without the need (and delay) for any physical IC fabrication facility. In contrast to the fixed-function of the ASIC technologies such as standard cells, the FPGA can be programmed to change the behaviour of pre-fabricated devices such that the chip is customized to implement certain function after completing the silicon fabrication. In addition, the time and cost consumption to implement a system on FPGA is much less than ASIC fabrication which many take few months to obtain the first prototype. Despite these advantages, the programmable routing fabrics for FPGA platforms compose a significant increase in the area, delay and power consumption. Roughly speaking the area cost of an FPGA is in the order of 20 to 35 times of the standard ASIC cell and consumes 10 times more dynamic power [1]. In terms of speed performance, the ASIC devices are also 3 to 4 times faster than FPGA platforms. However, the FPGA platforms can provide the scalability and performance presented by Moore's law while the modern submicron processes necessitate more expensive and difficult ASIC design [53, 55].

The structure of an FPGA device is illustrated in Fig. 3.2, it offers a two-dimensional array of configurable resources that can implement a wide range of arithmetic and logic functions. In its basic forms, it consists of block of logic cells that include general logic blocks (lookup tables (LUTs), registers, tristate, buffers and multiplexers), memories, dedicated DSP blocks, multipliers and digital clock managers [2]. The FPGA is programmed by compiling the high-level abstraction of the design to produce a bitstream program that configure the static on-chip random-access memory (RAM). The interconnection between the blocks is allowed to be

wired together by the control of bitstream that configures the routing fabric into systems. The chip is connected to the outside word through the input/output (I/O) blocks that can handle a wide range of bandwidth and voltage requirements [1, 56].

3.2 CORDIC Algorithms and Architectures

The CORDIC technique is based on the principle of two-dimensional geometry for iterative evaluation of trigonometric functions. A unified implementation using the generalized CORDIC algorithm has emerged wide range of applications that require vector rotations in circular, hyperbolic and linear coordinate system. This section gives an overview for the concept of CORDIC and discusses some architectural alternatives to trade-off the high performance and low cost implementation requirements.

3.2.1 Basics of CORDIC

The CORDIC algorithm was initially designed to rotate a two-dimensional vector $V_i = [x_i, y_i]$ in a Cartesian coordinate systems through an angle θ, to obtain a new vector $V_o = [x_o, y_0]$ as shown in Fig. 3.3. The rotated vector can be expressed by the following relation [57],

$$x_o = M_i \cos(\beta + \theta) = x_i \cos\theta - y_i \sin\theta, \tag{3.1a}$$

$$y_o = M_i \sin(\beta + \theta) = x_i \sin\theta + y_i \cos\theta, \tag{3.1b}$$

where M_i is the modulus of the input vector and β is the initial angle. This rotation is called perfect rotation because the modulus of the vector is preserved and can be expressed in matrix form as,

$$\begin{bmatrix} x_o \\ y_o \end{bmatrix} = \begin{bmatrix} \cos\theta & -\sin\theta \\ \sin\theta & \cos\theta \end{bmatrix} \begin{bmatrix} x_i \\ y_i \end{bmatrix} = R(\theta) \begin{bmatrix} x_i \\ y_i \end{bmatrix}, \tag{3.2}$$

where $R(\theta)$ is called the rotation matrix.

It is obvious that the direct implementation of the above rotation requires the evaluations of cos θ and sin θ, four multiplications, and two additions. Using the

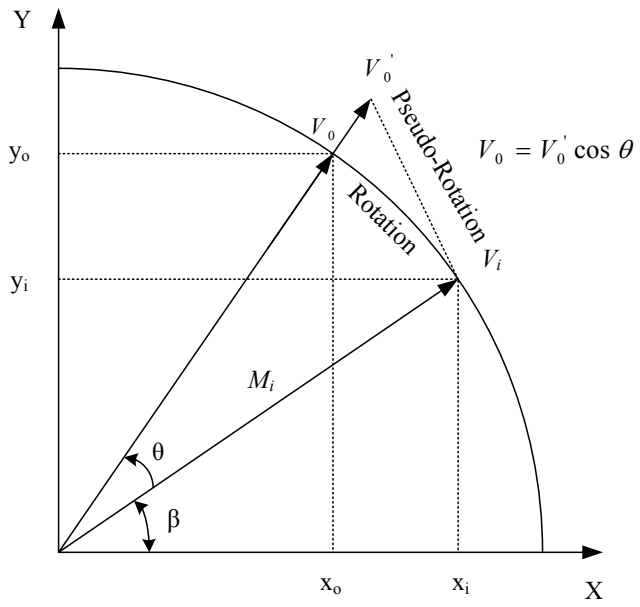

Figure 3.3: Vector rotation

identity of

$$\cos\theta = \frac{1}{\sqrt{1+\tan^2\theta}},$$

and factoring out the cosine, the vector rotation in (3.2) can be rewritten as [58]

$$\begin{bmatrix} x_o \\ y_o \end{bmatrix} = K R_c(\theta) \begin{bmatrix} x_i \\ y_i \end{bmatrix}, \tag{3.3}$$

where

$$K = \left[(1+\tan^2\theta)^{-1/2}\right], \tag{3.4}$$

and

$$R_c = \begin{bmatrix} 1 & -\tan\theta \\ \tan\theta & 1 \end{bmatrix}. \tag{3.5}$$

R_c is called the pseudo-rotation matrix where $V_o^{'}$=$R_c V_i$. As depicted in Fig. 3.3, the magnitude of the pseudo-rotated vector $(V_o^{'})$ is changed by factor of $K = \cos\theta = \left[(1+\tan^2\theta)^{-1/2}\right]$.

3.2.2 Iterative Decomposition and Microrotations

The rotation of the Cartesian point $[x_i, y_i]$ by an angle θ is equivalent to multiplying the complex number $V_i = x_i + jy_i$ by the exponential $e^{j\theta}$. Instead of the direct rotation, the CORDIC algorithm performs the rotation iteratively by approximating θ as the sum of N well-chosen angles and the rotation can accomplished using a series

of rotation by angles α_0, α_1, and so on,

$$\theta \approx \sum_{n=0}^{N-1} \sigma_n \alpha_n, \tag{3.6}$$

where $\sigma_n = \pm 1$ and the desired rotation can be expressed as,

$$R(\theta) = \prod_{n=0}^{N-1} R(\alpha_n). \tag{3.7}$$

Therefore, the fundamental CORDIC recursion for vector rotation is given by [58]

$$\begin{bmatrix} x_o[j+1] \\ y_o[j+1] \end{bmatrix} = \left[(1+\tan^2\alpha_j)^{-1/2}\right] \begin{bmatrix} 1 & -\sigma_j \tan\alpha_j \\ \sigma_j \tan\alpha_j & 1 \end{bmatrix} \begin{bmatrix} x_o[j] \\ y_o[j] \end{bmatrix}. \tag{3.8}$$

In order to avoid multiplication, the elementary angles (α_j) might be chosen carefully so that the tangents are powers of 1/2. Thus, shifting operation can be used in hardware implementation instead of multiplication where,

$$\alpha_j = \tan^{-1}[\sigma_j(2^{-j})] = \sigma_j \tan^{-1}(2^{-j}). \tag{3.9}$$

Therefore, the CORDIC recursion for vector rotation using only add and shift operations can be written as [58–60],

$$\begin{bmatrix} x[j+1] \\ y[j+1] \end{bmatrix} = \left[(1+\sigma_j^2 2^{-2j})^{-1/2}\right] \begin{bmatrix} 1 & -\sigma_j 2^{-j} \\ \sigma_j 2^{-j} & 1 \end{bmatrix} \begin{bmatrix} x[j] \\ y[j] \end{bmatrix}. \tag{3.10}$$

Instead of scaling the output during each recursion, a pseudo-rotation using R_c can be applied and the final magnitude is scaled. For each iteration, the pseudo-rotation scales the magnitude $M[j]$ so that

$$M[j+1] = K[j]M[j] = \frac{1}{\cos\alpha_j} M[j], \tag{3.11a}$$

$$= (1+\sigma_j^2 2^{-2j})^{\frac{1}{2}} M[j]. \tag{3.11b}$$

Noting that $\sigma_j \in \{-1, 1\}$, the scale factor is constant and independent of the angle being rotated where

$$K[j] = \left[(1+2^{-2j})^{-1/2}\right], \tag{3.12}$$

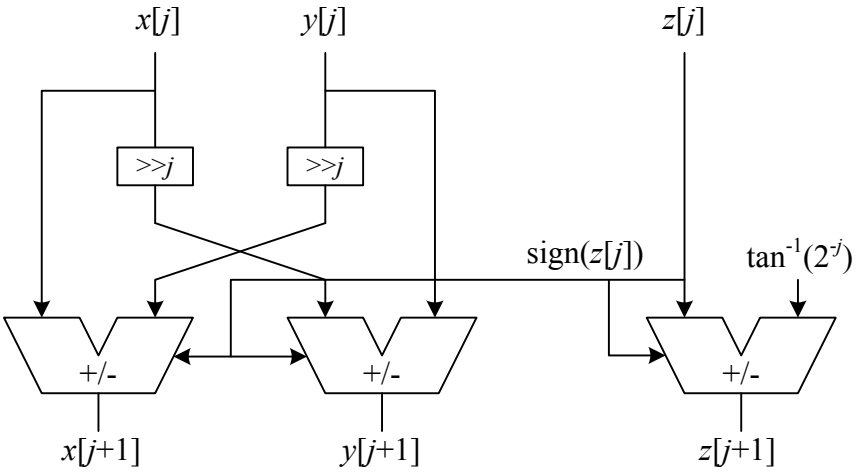

Figure 3.4: Hardware implementation of one iteration of the CORDIC for vector rotation

and the total scale-factor K is equal to

$$K = \prod_{j=0}^{\infty}(1 + 2^{-2j})^{-1/2} \approx 1.6468. \tag{3.13}$$

Since the rotation angle need to be decomposed or accumulated depending on the operation mode (will be discussed in the next section), another recursion needs to be added and the resulting iterations called microrotations [59],

$$x[j+1] = x[j] - \sigma_j 2^{-j} y[j], \tag{3.14a}$$

$$y[j+1] = y[j] + \sigma_j 2^{-j} x[j], \tag{3.14b}$$

$$z[j+1] = z[j] - \sigma_j \tan^{-1}(2^{-j}). \tag{3.14c}$$

The hardware realization for one iteration of the CORDIC algorithm is shown in Fig. 3.4. The iteration core consists of shifters, adders/subtracters and a table to store the elementary rotation angles $\tan^{-1}(2^{-j})$.

3.2.3 Rotation and Vector Mode

The CORDIC algorithm described in the previous section can operate in two different modes: rotation and vectoring mode. In rotation mode, the mircorotations are used to rotate a vector (x_0, y_0) with an angle θ as shown in Fig. 3.5(a) [57]. The recursive CORDIC decomposes the angle into primitive angles and the vector is rotated by these angles. In this mode, the sign of $z[j]$ is used to determine the direction rotation (σ_j) for each mircorotation which is used to produce $x[j+1]$,

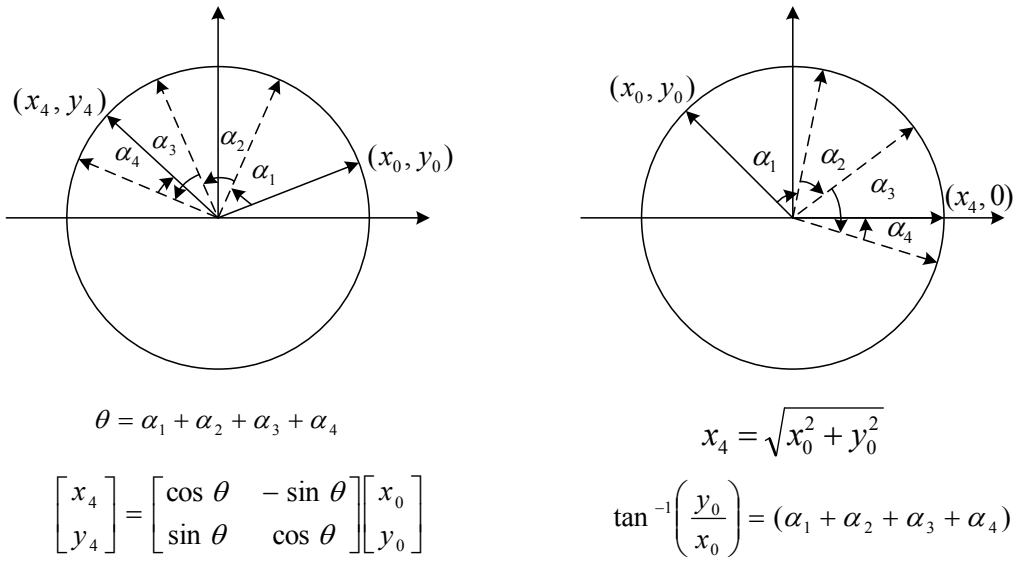

Figure 3.5: The CORDIC in rotation and vectoring mode

$y[j+1]$, and $z[j+1]$. The initial value for z is made equal to θ where

$$z[0] = \theta, x[0] = x_i \text{ and } y[0] = y_i$$

$$\sigma_j = \begin{cases} 1, \text{ if } z[j] \geq 0, \\ -1, \text{ if } z[j] < 0. \end{cases} \tag{3.15}$$

In vectoring mode, series of microrotations are performed by rotating a vector (x_0, y_0) to the x-axis until the y-component is zero as shown in Fig. 3.5(b) [57]. Thus, it can be used for the computation of arctangent and square root. The magnitude of the resulting vector is equal to the magnitude of the initial vector while the sum of angles required to achieve this rotation is equal to the negative of the initial vector. To accomplish this rotation, the sign of $y[j]$ is used to determine the direction of the mircorotations and the z is used to accumulate the rotation angle,

$$z[0] = z_{in}, x[0] = x_i \text{ and } y[0] = y_i$$

$$\sigma_j = \begin{cases} 1, \text{ if } y[j] < 0, \\ -1, \text{ if } y[j] \geq 0. \end{cases} \tag{3.16}$$

3.2.4 CORDIC Architectures

In the sense that CORDIC algorithm performs iterative computation, the programmable processor implementation is commonly suggested. However, the hardware architecture implementation may also be used. In general, the design of CORDIC architecture depends on the intended application where a speed versus area trade-off can be considered. In the following, two possible architectures for the implementation of CORDIC algorithm, the word-serial and pipelined architectures, are discussed in terms of cost and performance trade-off [2, 58, 59].

3.2.4.1 Word-Serial Architecture

The word-serial architecture to implement the CORDIC algorithm is depicted in Fig. 3.6. In this architecture, the microrotations for one iteration given in (3.14) is mapped into hardware and reused to perform CORDIC recursion [59]. The initial values are loaded to the x, y and z register through a multiplexer. Based on the operation mode whether it is rotation or vector, the add/sub selection port is driven by the sign of y and z registers [61]. This architecture is characterized with a multiple-cycle throughput architecture as each iteration corresponds to one clock cycle and the implementation cost mainly depends on the internal computation precision [2]. The microrotations are performed serially and the hardware unit for one iteration is shared N times through feedback from the output registers to the input of the shift-add/sub stage. Each microrotation of the CORDIC requires one shift and add/sub operations that computed during one cycle and the results placed back in the registers. It is worth noting that after each iteration the number of shifts is incremented by a pair of barrel-shifters and the look-up table (LUT) address is incremented on each iteration to present the appropriate elementary angle (α_j) to the add/sub of the z register [58]. Thus, the word-serial architecture has a latency of N cycles and a new output is generated every N cycles. Therefore, this architecture may be relevant for non-critical computation time applications [61].

3.2.4.2 Pipelined Architecture

The iterations in the word-serial CORDIC architecture is performed at N times the data rate. However, if the computation time is critical and fast processing speed is needed, the iteration process can be unrolled so that each iteration uses

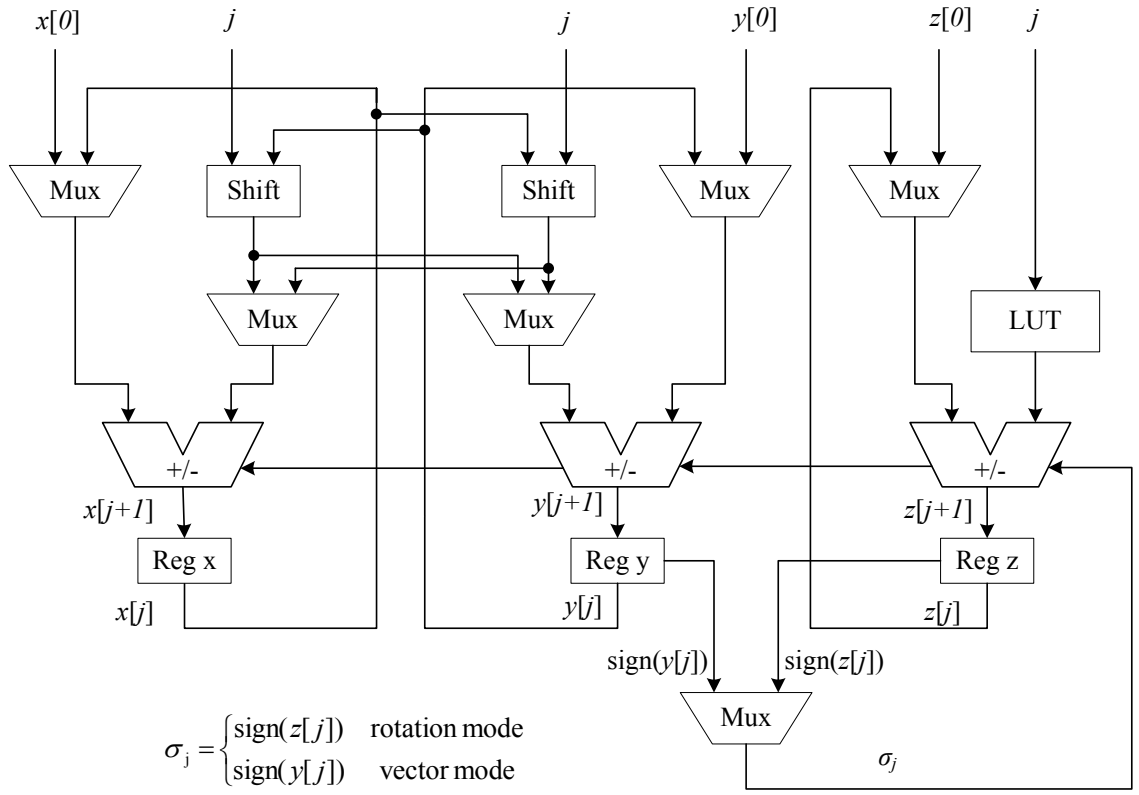

Figure 3.6: CORDIC word-serial architecture

its own hardware to realize a fully pipelined CORDIC architecture as shown in Fig. 3.7. The micro-rotation stages can be implemented in parallel using an array of shift and add/sub stages configured in a pipeline stream [59]. Unlike the serial-word architecture which requires the involvement of barrel-shifter, this architecture uses a fixed shift for each processing element that can be implemented by simple wiring. In addition, unrolling the iterative processes release the LUT storage for the elementary angles since each angle is distributed as constant to the angle add/sub chain as shown in Fig. 3.7. Since the iterations are unrolled, this architecture can be easily pipelined by inserting registers after each processing element resulting in a high throughput [61]. The pipelined CORDIC architecture produce output values after an initial delay of N cycles and after that a new output will be available on every cycle [58]. The implementation size of the pipelined CORDIC architecture is directly proportional to the internal precision times the number of processing elements (iterations). However, the accuracy depends on the number of shift and add/sub stages [2, 61].

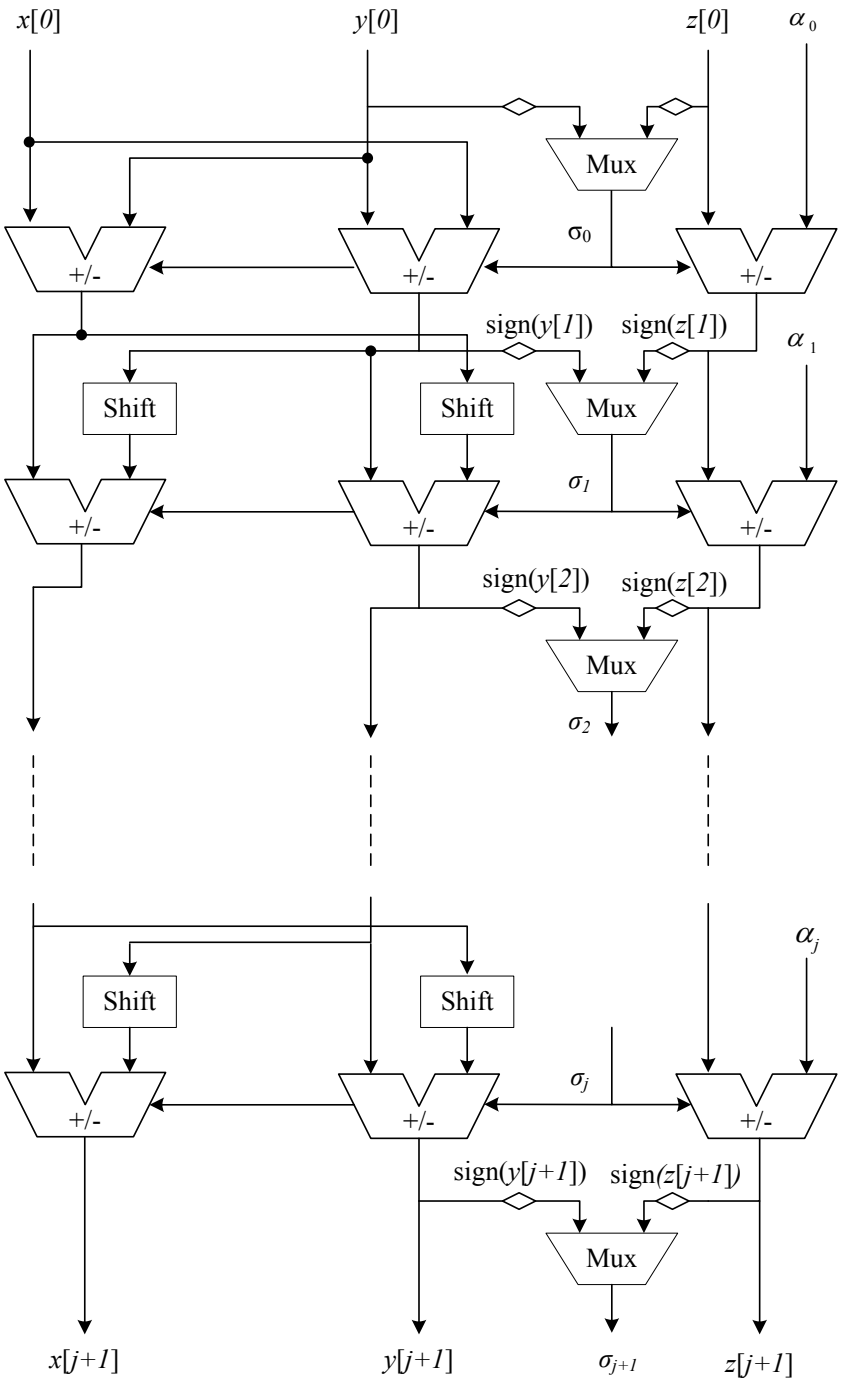

$$\sigma_{j+1} = \begin{cases} \text{sign}(z[j+1]) & \text{rotation mode} \\ \text{sign}(y[j+1]) & \text{vector mode} \end{cases}$$

Figure 3.7: The pipelined CORDIC architecture

3.3 Direct Digital Synthesizer (DDS)

The structure of a typical digital communication receiver is shown in Fig. 3.8. The received signal is first down-converted to baseband (r_n) where I and Q represent the in-phase and quadrature components of the received baseband signal. The mismatch between the crystal oscillators at the transmitter and receiver leaves a frequency offset ($\Delta\omega$) in the down-converted version of the received signal. The receiver needs to compensate for the frequency error before demodulating the received signal. This process is typically made in a frequency correction loop as shown in Fig. 3.8 where the generation of a complex exponential is required [60]

$$r_n e^{-j\Delta\omega n}. \tag{3.17}$$

The samples of the received signal need to be multiplied by samples of sine and cosine functions operating at the desired frequency [62]. A discrete-time oscillator can be constructed by designing a linear-time-invariant (LTI) system whose impulse response is a sinusoid at the desired frequency. Setting the input to an impulse will produce a sinusoidal output. These kinds of discrete time systems have infinite impulse response (IIR) form and the frequency can be adjusted by changing the feedback coefficients. A digital controlled oscillator can also be implemented using counters clocked with a high frequency source and dividing the output frequency by the control word. However, the stability due to the finite arithmetic precision and the poor frequency resolution represents a major problem for such architectures [57]. The above solutions are not a preferred implementation for the controlled oscillators which have a great influence on the performance of the synchronization loop.

The other attractive architecture is known as the direct digital synthesizer (DDS) which is preferred solution for producing a sinusoid with precise frequency resolution and fast clocking speed. The DDS plays an important role in high performance communication systems for waveform synthesis in digital phase locked loops. Hence, it is commonly used in many applications such as digital modems and software defined radio (SDR) [2, 62]. A detailed description for the DDS architecture is presented in the next sections.

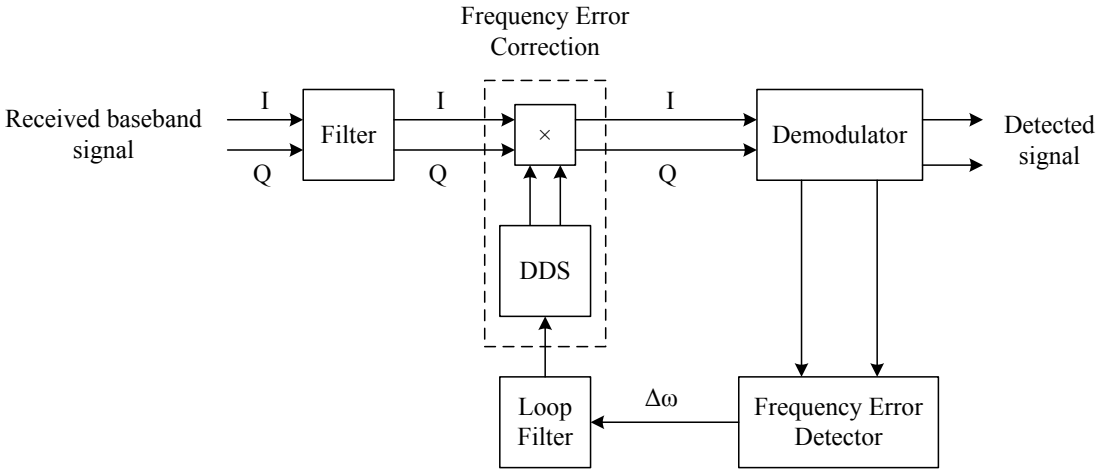

Figure 3.8: The role of DDS in a digital communication receiver

3.3.1 DDS Architecture

The DDS can be described as a frequency-controlled synthesizer of sinusoidal waveforms. The basic idea of DDS is to employ an addressing scheme with appropriate LUT that stores the values of a single cycle of prototype sinusoidal waveform of length $N = 2^{B_{\Theta(n)}}$ that correspond to specific values of the sinusoid's argument $\Theta(n) = n\frac{2\pi}{N}$ where n is the time series sample index [2]. To obtain an analogue output, the DDS output samples are applied to a digital-to-analogue converter (DAC) and a low-pass filter or the output samples can be utilized directly in the digital domain [60].

The block diagram of the DDS is shown in Fig. 3.9. A digital integrator which consists of an adder and register is used to produce the phase argument which is mapped using the LUT to generate the output waveform [62]. The phase increment which represents the digital word determines the output frequency. In order to reduce the size of the LUT, the high precision output of the accommodated phase is reduced to a lower precision representation by removing B insignificant bits to match the width of the LUT which represents the address port to perform the mapping process [2]. However, this approach introduces phase quantization error to the recalled samples of a sinusoid from the LUT which consequently leads to the presence of spurious lines in the spectrum of the output waveform. Another useful approach is to exploit the inherent symmetry of the sinusoidal waveform to achieve more resource efficient implementation in terms of the memory requirements [57]. This implementation is shown in Fig. 3.10 which utilizes LUTs with shorter depth compared with the conventional implementation shown in Fig. 3.9 where the two

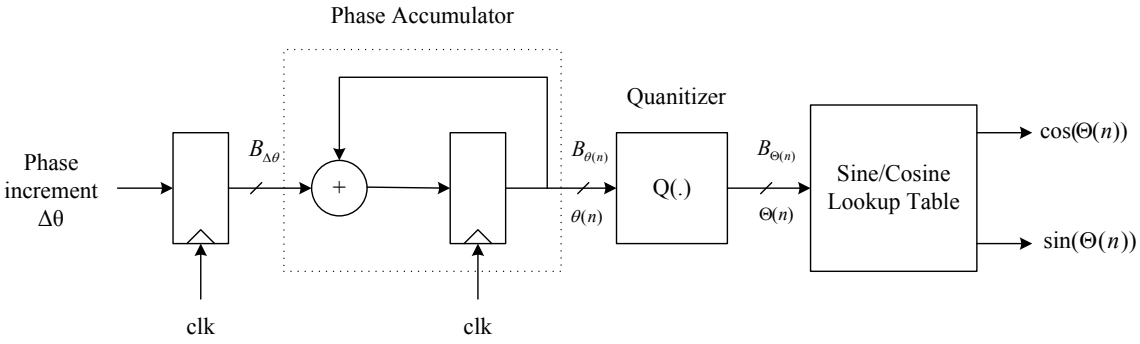

Figure 3.9: The basic architecture for DDS

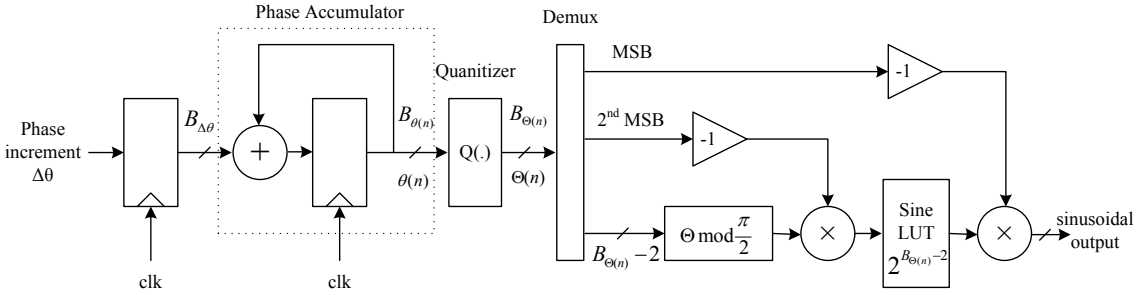

Figure 3.10: Design of a DDS architecture with reduced memory size

most significant bits of the quantized phase angle are used to perform quadrant mapping. The two approach can be used together or separately depending on the architecture design requirements [57, 62].

3.3.2 Spectral Purity Considerations: Enhanced DDS Architectures

The sinusoidal samples generated using the DDS architecture in Fig. 3.9 are affected by the phase and amplitude quantization because of the limited width and depth of the lookup table. The phase quantization, discarding the least significant part of the high-precision phase accumulator, results in undesirable spectral modulation proportional to the quantization error [57],

$$e^{j\theta(n)} = e^{j\Theta(n)}e^{j\delta\theta(n)} = e^{j\Theta(n)}\left[\cos\left(\delta\theta(n)\right) + j\sin(\delta\theta(n))\right] \approx e^{j\Theta(n)}[1 + j\delta\theta(n)], \quad (3.18)$$

where

$$\delta\theta(n) = \theta(n) - \Theta(n). \quad (3.19)$$

When the phase increment is constant, the phase quantization error $\delta\theta(n)$ due to the discarded least significant part of the LUT address is periodic. Therefore, the

spectrum of the phase error is discrete and it is the source of spurious spectral lines, a harmonic rich low-level phase modulation. The spurious free dynamic range (SFDR), a measure used to characterize the DDS sinusoid spectral purity, is defined as the ratio (in dB) of the amplitude of the desired frequency to the highest frequency component of the undesired frequency (the largest spurious spectral lines) [2, 57].

Several techniques have been investigated in the literature to reduce the peak amplitude of the spectrum spurlines due to the phase accumulator quantization as depicted in Fig. 3.11. The desired complex sinusoidal output can be expressed as

$$e^{j\theta(n)} = \cos\left[\Theta(n)\right] - \delta\theta(n)\sin\left[\Theta(n)\right] + j\left\{\sin\left[\Theta(n)\right] + \delta\theta(n)\cos\left[\Theta(n)\right]\right\}. \quad (3.20)$$

Since the the phase quantization error is known, a compensation for the sinusoidal output of the LUT based on (3.20) can be applied as shown in Fig. 3.11(a). This method is known as Error-Forward compensation and has significant performance in increasing the spur dynamic range. However, the only noticeable disadvantage is the increased resource requirements where two additional multiplications and additions are required. The other approach to combat the effect of phase truncation in DDS without the necessity of multipliers is called Error-Feedback. In this technique, the phase quantization error is treated as additive noise process and the compensation is applied before the quantization block. However, the phase quantization error $\delta\theta(n)$ is only known after the quantization. Therefore, this approach employs a linear predictor $F(z)$ to estimate the $\delta\theta(n)$ from previous values as illustrated in Fig. 3.11(b). The spur dynamic range performance of the Error-Feedback technique is not good as Error-Forward and mainly depends on the design of FIR prediction filter. A practically common and simple approach to mitigate the phase noise effect in DDS is known as phase dithering as shown in Fig. 3.11(c). In this structure, the periodicity of the phase noise is broken up by adding an additive random sequence to the high-precision accumulator output before the quantization process. This random sequence is known as dither signal with approximate variance equal to the least significant integer bit of the phase accumulator. The phase dithering technique offers a noticeable increase in the SFDR performance with no significant additional logic resources [2, 57, 62].

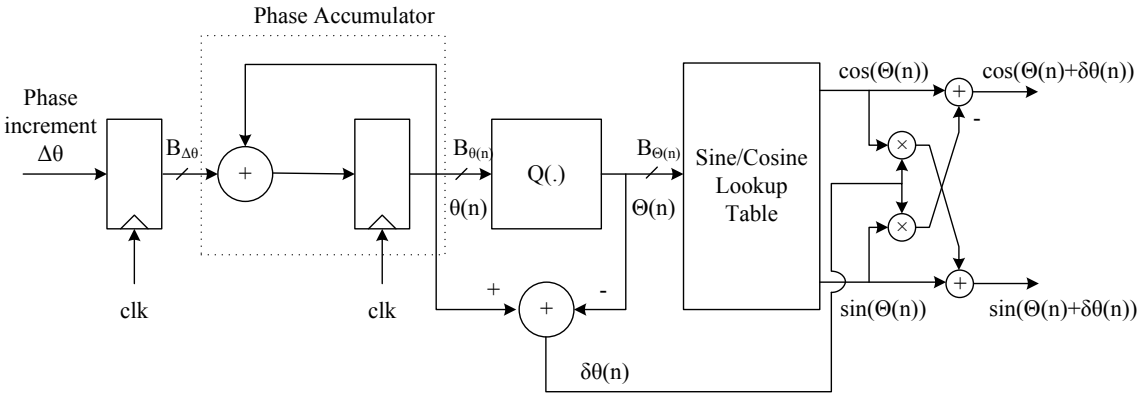

(a) Error-Forward

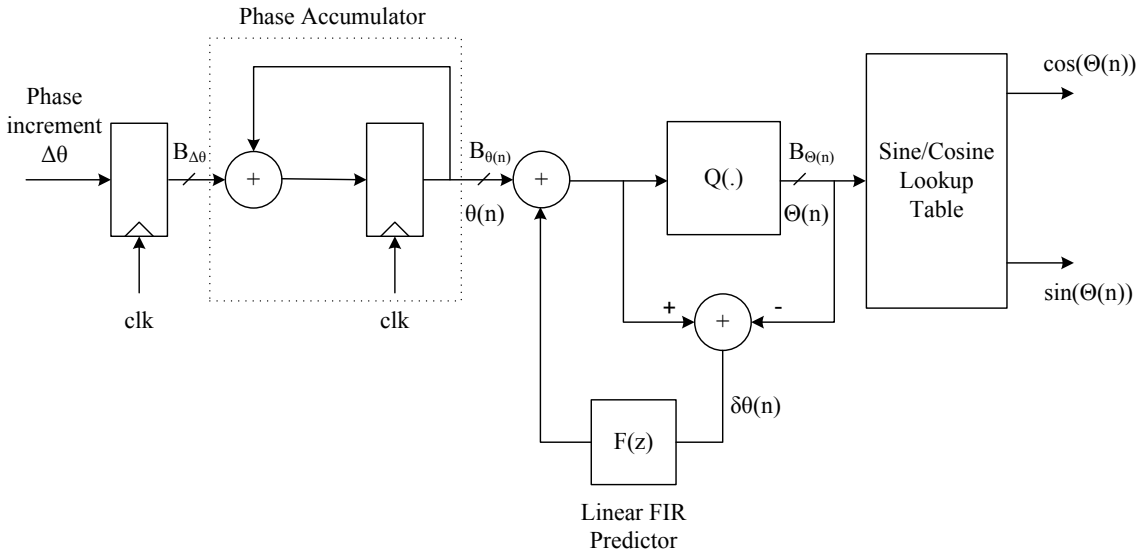

(b) Error-Feedback

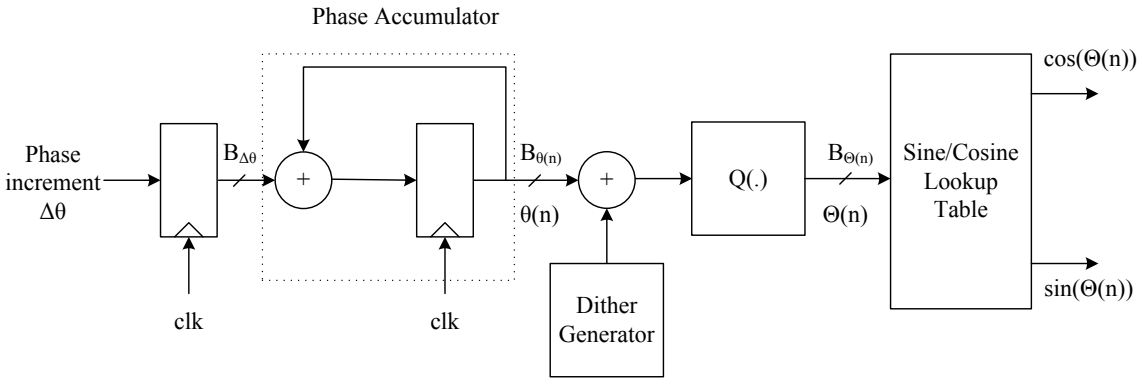

(c) Phase-Dithered

Figure 3.11: DDS architectures with reduced spurs characteristics

3.4 FFT Architecture

The DFT is one of the most important transforms in the field of digital signal processing. The DFT $X(k)$ for a discrete sequence $x(n)$ of length N is defined as

$$X(k) = \sum_{n=0}^{N-1} x(n) W_N^{nk}, \qquad k = 0, 1, ...N-1. \tag{3.21}$$

where N is the transform size and W_N is a complex coefficients called the twiddle factor

$$W_N = e^{-j2\pi/N}. \tag{3.22}$$

The IDFT is given by

$$x(n) = \frac{1}{N} \sum_{n=0}^{N-1} X(k) W_N^{-nk}, \qquad n = 0, 1, ...N-1. \tag{3.23}$$

Over the past years, several FFT algorithms have been reported in the literature for the computation of DFT on a general purpose processors. Therefore, the FFT had a great impact in a wide-range of current applications and systems. The most popular FFT algorithm is the Cooley-Tukey originally proposed in 1965 [60]. The FFT butterflies are the main building block used to compute the DFT in addition to the twiddle-factor multiplier. The butterfly processing elements computes the DFT of size m where m is the radix. The radix size determines the number of twiddle-factor multiplications. Increasing the radix of the FFT will requires fewer twiddle-factor multiplications. However, this is at the expense of available transform size. For example, the radix-2 butterfly can be used to construct FFT for a sequence of power-of-two while the radix-4 butterfly is the construction unit for FFT operating on sequences of size power-of-four [63, 64].

The efficient hardware implementation of the FFT processing reflects into either lower resource requirements or higher throughput compared with software based implementation on programmable processors such as GPPs and GPUs. Generally, there are two common architectures for the implementation of the FFT on custom hardware platform (for instance VLSI technology or FPGA platforms), the bursty and streaming I/O architectures [2]. This section presents briefly the main characteristics of these architectures. The details are out of the scope of this thesis and the reader is referred to [60] for advanced architectural treatment.

3.4.1 Burst I/O Architecture

The latency of the burst architectures is longer than the length of the input sequence. In these architectures, the input frame is first loaded, the FFT is computed and then the output data is unloaded [2]. During the FFT computation of the current frame, a delay must be inserted before loading the next subsequent frame [63]. Thus, burst architectures are mainly characterized by their low resources requirements for a given parametrization of the FFT algorithm at the expense of the achieved performance throughput. The implementation diagram of the radix-2 burst FFT architectures is illustrated in Fig. 3.12. It is obvious that one physical butterfly has been employed and reused over multiple time periods for all the processing stages of the FFT data-path. A pre-computed twiddle factors is sorted in a memory. In addition, the butterfly reads and writes the input and output data sequences to two random access memories as depicted in Fig. 3.12. The writing of the intermediate outputs to the memories is handled with switch module unit. The butterfly PE reads the data sequences from the two memories for processing, performs the ith stage calculation and the intermediate computed data results are written back to the same locations in each of the random access memory through the switching unit [2, 64].

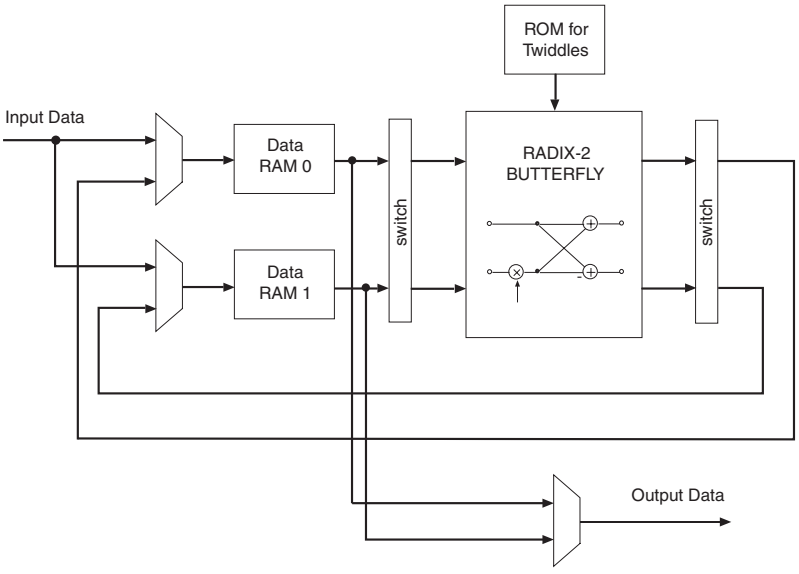

Figure 3.12: Radix-2 burst I/O FFT architectures [2]

3.4.2 Streaming I/O Architecture

In the streaming architectures, several butterfly processing elements (PEs) are cascaded to form the FFT data-path in a pipelined fashion for continuous data processing. The data moves through the pipeline which distinguish it from the burst architecture that requires continuous read and written from the same memory location as described in the previous section. Therefore, the streaming architecture enables to stream the I/O operations by processing the data at the clock speed of the design. However, this implementation taxonomy can also be used for burst I/O situations by incorporating handshake signals [2, 64].

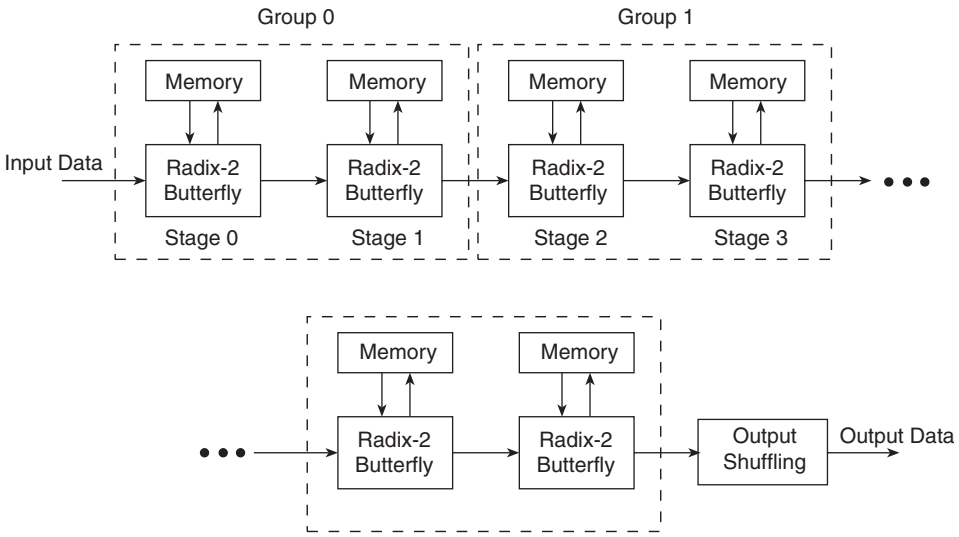

Figure 3.13: The pipelined streaming I/O architecture [2]

The streaming architecture is presented in Fig. 3.13 for the implementation of radix-2 FFT processor where each pair of adjacent PEs is considered as a group. Each PE includes a twiddle-factor multiplier and memory in addition to the memory used to store the input and intermediate data. Compared with the burst architecture, the streaming architecture has a simple timing control logic and consumes more resources of the chip fabric than the burst counterpart [2]. However, the streaming architectures require reordering the input data sequence such that the butterflies stages process the appropriate input data. Based on the data buffering and reordering strategies, the FFT data-paths of the pipelined architectures are mainly divided into delay-feedback and delay-commutator streaming architectures [63, 64]. In the delay-feedback architecture, a feedback register is employed to store the input data during the processing stage. The input data is first acquired and redirected through the delay register to appear again in appropriate order with other inputs of the but-

terfly. This architecture can be used to efficiently map the data-path of several FFT algorithms such as radix-2 and radix-4. However, the number of pipelined stages is the constraint for such architectures and the pipelining benefits can be limited due to the delay registers. In contrast, the delay-commutator architecture utilizes different strategy to reorder the moving sequences through data-path of the pipeline. Instead of redirecting the data through feedback register, the input data is delayed and commutated using switch unit to present at the butterfly input in correct order for processing. Obviously, the data-paths of delay-commutator architectures are more complex than delay-feedback architectures and the constraint for pipelining operation is only the hardware granularity. Therefore, it is more preferable choice for very high-frequency applications as the data-path of the FFT processor can be heavily pipelined for maximum throughput performance [60, 63, 64].

3.5 Chapter Summary

This chapter presented an overview for most essential synchronization components in digital communication receivers. It highlights the important role of DDS, CORDIC and FFT in different steps of the synchronization process such as the frequency error estimation and correction. The chapter started by discussing the state-of-the-art platforms for the implementation of signal processing systems. The main advantages for the implementation of computation intensive signal processing tasks using reconfigurable hardware architectures such as FPGAs are highlighted. Different implementation architectures for the CORDIC, DDS and FFT algorithms were presented. The area versus performance trade-offs for the examined architectures to satisfy the design requirements is discussed. The pipelined parallel architectures of CORDIC and FFT processors have been presented for the implementation of high performance signal processing systems. In addition, compact architectures for the implementation of DDS with enhanced spectral purity are also discussed.

Chapter 4

Blind CFO Estimation Methods for OFDM Systems over Frequency Selective Fading Channels

As mentioned earlier in Chapter 2, the symbol timing and frequency synchronization are essential tasks in the wireless digital receiver to ensure reliable data transmission. This chapter focuses on robust non data-aided (blind) carrier frequency synchronization methods for OFDM systems over frequency selective fading channels. The chapter begins with an introduction to discuss the related work in the literature. The OFDM system model in the presence of frequency synchronization error and timing ambiguity is then presented. In this chapter, two robust CFO estimators for OFDM systems based on the power and phase difference measurement approaches are described. The CFO estimators are designed to be totally blind and produce reliable estimates using short length of observation window. A comprehensive performance evaluation for the CFO estimators in terms of mean squared error (MSE) and bit error rate (BER) over different channel conditions is then presented. Furthermore, the performance is also examined in various timing uncertainty scenarios, and the MSE degradation is compared to other timing error robust CFO estimators.

4.1 Introduction

Although OFDM is highly robust against various transmission impairments, it is very sensitive to synchronization errors, particularly CFO and symbol timing offsets (STO). OFDM signal synchronization consists of two major components, symbol timing (ST) recovery and CFO estimation. The STO results from the unknown delay between the transmitter and receiver. Doppler shifts and the noncoherent up and down frequency conversion performed at the transmitter and receiver are the main causes for the CFOs. Based on the CP length and channel parameters, OFDM systems can usually tolerate certain amount of STO errors. However, the requirements for frequency synchronization is tighter and CFOs must be estimated and compensated accurately prior the DFT process. Accurate CFO estimation is critical for OFDM systems to maintain the orthogonality amongst all subcarriers to avoid ICI. OFDM systems can not tolerate offsets that are larger than a small fraction of the subcarrier spacing without a large degradation of the system SNR. For example, a signal-to-interference ratio (SIR) of 20 dB is achieved for frequency offsets less than 4% of the subcarrier spacing [65]. Concurrently, the CFO estimation for OFDM systems has received considerable attention and has been addressed in various publications to develop efficient frequency synchronization schemes [34, 38, 39]. However, the problem remains open due to the difficulty of resolving the conflicting design requirements such as accuracy, low complexity, robustness and efficiency.

Over the past years, numerous data-aided techniques for CFO estimation have been developed [13–15]. However, they suffer from low power and bandwidth efficiencies. More recently, non data-aided (blind) schemes have given more attention due to their high power and bandwidth efficiency. In addition to their high computational complexity compared to data-aided estimators, the main drawback of most blind CFO estimation methods is that the estimation accuracy is severely deteriorates in frequency selective fading channels, hence, inconsistent estimates might be produced. Therefore, deducing a blind CFO estimator that necessitates short observation with reasonable computational complexity and high accuracy is very challenging because of the conflicting nature of these specifications.

4.1.1 Related Work

In the literature, several blind schemes have been proposed for CFO synchronization in OFDM systems. Some of these techniques operate in time domain, perform the estimation prior the DFT, such as the well referred-to CP based estimator (CPE) that utilizes the CP extension of the OFDM symbols in time domain as reported in [17]. This estimator is attractive because of its low complexity, however the MSE performance in fading channels suffers from a severe deterioration [23,32]. The CPE is widely used in the literature as a reference for performance comparison [18,23,52]. Alternatively, frequency domain techniques, which perform the estimation post the DFT, are considered to be more robust however it requires more computational power. Frequency domain techniques exploit the DFT output to construct CFO estimators and some of these techniques have provided a good compromise between efficiency, complexity, and accuracy such as [22], [23], [52] and [32].

A blind Kurtosis based CFO estimator (KBE) with reasonable complexity has been proposed in [23]. The Kurtosis metric is a function that measures the non-Gaussianity of the received signal. The cost function of this estimator is constructed by exploiting the relation between the Kurtosis and the CFO. The resulting cost function was approximated by a sinusoid which allowed for a blind low complexity closed-form estimator. The closed-form estimation was implemented using curve fitting that requires only three trial values. However, the performance of this estimator has suffered from a severe degradation in frequency selective fading channels. Moreover, the low complexity implementation has added a new constraint because the subcarriers must be modulated using a constant modulus constellation. In [22], a blind CFO estimator has been proposed by minimizing the variance of the ICI which is proportional to the CFO. As will be shown later in this chapter, the minimum variance estimator (MVE) and KBE are linearly related, where the cost function of [22] is an affine transformation for the cost function of [23]. Hence, their performance is identical and they have the same modest performance in frequency selective fading channels.

Minimizing the power difference between all adjacent subcarriers in the frequency domain was used in [52] to deduce an efficient CFO estimator, hence it is denoted as the power difference estimator-frequency (PDE-F). The PDE-F is more robust than the KBE, MVE and CPE in frequency selective fading channels [52]. However, its

performance highly depends on the channel fading conditions where the performance degrades drastically in highly frequency selective fading channels and it has the same constant modulus limitation which constraints the selection of the modulation scheme to MPSK. Surprisingly, the cost function of the PDE-F is sinusoidal as well which leads to closed-form estimator with low complexity implementation using the three points curve fitting approach described in [23].

The power spectrum analysis of the received signal for CFO estimation has been reported in [66] and [19]. The estimator in [66] is based on smoothing the power spectrum of the received signal and the cost function is a scaled version of the PDE-F. The estimator of [19] exploits the fact that some frequencies in the power spectrum of the received signal are missing when the CFO is perfectly compensated. However, the missing frequencies are a function of the channel order. Therefore, this estimator requires the knowledge of the channel order to set the interval over which the cost function to be minimized. It can be shown that the cost functions of [66] and [19] are equivalent to the cost functions of [52] and [67], respectively. Thus, both estimators will suffer MSE deterioration in frequency selective channels [19].

The reason for the degraded performance of the previously mentioned frequency-domain techniques at medium and high SNRs is the fact that the channel fades selectively with respect to the overall OFDM signal spectrum. Hence, the assumption that adjacent subcarriers have equal frequency responses is more accurate in fading channels with small delay spreads. This actually becomes apparent at high SNRs where the difference between the subchannels frequency response causes the MSE to saturate and creates an error floor [23, 52]. Moreover, the MVE and KBE estimators involve all subcarriers in the estimation process which makes them more sensitive to the frequency selectivity of the channel compared to the PDE-F which just uses the difference between adjacent subcarriers.

The CFO estimation using phase rotation measurements is widely used for frequency synchronization in single carrier systems [68–70]. Some of these techniques are usually designed as data-aided estimators where the data symbols are assumed to be known at the receiving side [70]. Blind CFO estimators based on phase rotation measurements have been proposed as well, such as the Viterbi-and-Viterbi (VAV) phase estimation algorithm which was generalized for CFO estimation of burst MPSK modulations [37]. The generalized VAV estimator exhibits several desirable features such as low complexity and accurate estimation at high SNR. The

main limitation of this technique is the poor performance that can be achieved at moderate and low SNRs unless averaging over a very large number of symbols is employed which limits its applicability to packet-switched wireless networks. The estimator proposed in [32] is based on the generalized VAV algorithm and adapted to OFDM systems where the CFO is estimated directly as the phase difference between subcarriers in two consecutive symbols. The main drawback of this estimator is the limited estimation range that is inversely proportional to the modulation order and the SNR degradation caused by ICI. Hence, the frequency synchronization system in [32] has been introduced to estimate the residual CFO (RCFO) in the tracking mode of the synchronization process.

4.1.2 CFO Estimation in the Presence of Timing Uncertainty

Unfortunately, the majority of the CFO estimation methods reported in the literature including the previously discussed assume perfect timing synchronization. In practice, such an assumption is too restrictive in noisy and frequency selective channels where most of the existed timing metrics exhibit a plateau in the CP region and can not achieve precise symbol timing. In general, most of the research conducted for OFDM systems assume that a wide range of timing errors can be tolerated due to the use of CP. However, the tolerable range for the symbol timing errors might be valid for bit error rate (BER) analysis, it might not be the case for other processes such as CFO estimation.

Consequently, the problem of CFO estimation in the presence of timing uncertainty has been addressed by some researchers. For instance, the maximum-likelihood CFO estimator in [49] denoted as ZMLE, which exploits the null-subspace inherent in OFDM due to the limited length of the channel, has shown a sensitive performance to timing errors even for small STOs. To combat the performance degradation due to the symbol timing uncertainty, an explicit estimation for STO and CFO has been proposed in [51]. The estimator of [51] has a robust performance in the presence of timing errors, however, it requires two dimensional search over the trial CFO and STO intervals which results in a high computational burden. On the other hand, the estimator proposed in [50] implicitly embeds the STO in the channel impulse response to deduce timing error robust (TER-MLE) CFO estima-

tor. Hence, the computational complexity has significantly decreased by employing one dimensional search with little performance degradation compared with the joint MLE (JMLE) reported in [51].

In this chapter, two robust blind (without the aid of training sequences or preambles) CFO estimators for OFDM systems over frequency selective fading channels are presented. The first estimator is based on the power difference measurements among constant-modulus modulated subcarriers. The cost function of this estimator is formulated to minimize the power differences between the subcarriers in consecutive OFDM symbols based on the assumption that the channel changes slowly in the time domain, hence, it will be denoted as PDE-T [71]. This estimator tackles the performance degradation observed in [52] in severe frequency selective conditions by reformulating the cost function in the time direction rather than the frequency direction. The other estimator is designed by measuring the phase differences between the subcarriers over two consecutive OFDM symbols. This estimator is based on the highly efficient generalized VAV algorithm [33]. An iterative structure is proposed to combat the ICI and the estimation range problems observed in [32], hence, it will be denoted as iterative GVAV (IGVAV). The IGVAV estimator exploits the unique features inherent to OFDM systems which substantially enhanced the performance of the VAV algorithm and added several advantages such as accuracy, robustness, and fast estimation.

Both PDE-T and IGVAV estimators are totally blind and do not require any prior knowledge of the channel state information or the SNR. Consequently, the receiver design is simplified due to the decoupling of the CFO and channel estimation processes. Additionally, both estimators have low computational complexity due to the closed-form estimation and require short observation window to perform the estimation.

Furthermore, for all the techniques discussed in the previous paragraphs, timing synchronization is always assumed to be perfect including the PDE-T and IGVAV estimators proposed in [71] and [33], respectively. Therefore, it will be important to assess the performance of various CFO estimators in more realistic scenarios where timing estimation is not perfect. Hence, this chapter is also dedicated for performance investigation of the considered CFO estimators over fading channels with different frequency selectivity and timing uncertainty conditions compared with other blind and DA CFO estimators for OFDM systems [72].

In the next section, the mathematical model for OFDM systems in the presence of frequency synchronization error with timing uncertainty is presented. Then, the PDE-T and IGVAV CFO estimators are formulated. A comprehensive comparison with other frequency synchronization systems in terms of MSE, BER performance and computational complexity is discussed. The frequency synchronization algorithms that are in scope of this chapter and will appear in the numerical simulation section are the CPE [17], KBE [23] and PDE-F [52] schemes. These methods have similar cost functions, where the CFO is estimated blindly by exploiting the received OFDM symbol without the aid of training, and comparable complexities to the PDE-T and IGVAV. In addition the TER-MLE estimator [50] is also considered for comparison due to its robustness in timing uncertainty conditions. The full details of the cost functions formulation for all the algorithms that are in scope of this chapter were presented in Chapter 2 (Section 2.4.2).

4.2 System Model

In OFDM, a sequence $\mathbf{d}(l) = [d_0(l), d_1(l), .., d_{N-1}(l)]^T$ of independent complex symbols is used to modulate N orthogonal subcarriers during the lth OFDM symbol block. The elements of the data sequence $\mathbf{d}$ are usually drawn uniformly from QAM or MPSK constellations. The channel $\mathbf{H}(l)$ =diag$([H_0(l), H_1(l), ..., H_{N-1}(l)]^T)$ is assumed to be constant over the symbol duration. Defining $\epsilon \in (-0.5, 0.5)$ as the normalized frequency mismatch between the transmit and receive local oscillators over the subcarrier interval. The frequency offset is assumed to be fixed but unknown during each estimation process. The time domain samples of the received signal after discarding the CP samples, $\mathbf{y}(l) = [y_0(l), y_1(l), ..., y_{N-1}(l)]^T$, can be written as

$$\mathbf{y}(l) = e^{j\frac{2\pi\epsilon l}{N}(N+N_{CP})}\mathbf{C}(\epsilon)\mathbf{W}^H\mathbf{H}(l)\mathbf{d}(l) + \mathbf{z}(l), \tag{4.1}$$

where the matrix $\mathbf{C}(\epsilon)$ represents the effect of the accumulated phase shift caused by the CFO on the time domain samples,

$$\mathbf{C}(\epsilon)\text{=diag}\left(\left[e^{\frac{j2\pi\epsilon}{N}\times 0}, e^{\frac{j2\pi\epsilon}{N}\times 1}, ..., e^{\frac{j2\pi\epsilon}{N}\times(N-1)}\right]^T\right). \tag{4.2}$$

The nth element of $\mathbf{y}$ can be expressed as

$$y_n(l) = \frac{1}{\sqrt{N}} e^{j\frac{2\pi\epsilon l}{N}(N+N_{CP})} \sum_{i=0}^{N-1} d_i(l) H_i(l) e^{j\frac{2\pi n}{N}(i+\epsilon)} + z_n(l). \tag{4.3}$$

The vector $\mathbf{y}(l)$ is fed to the DFT to produce the frequency domain symbols,

$$\begin{aligned} \mathbf{s}(l) &= \mathbf{W}\,\mathbf{C}^*(\hat{\epsilon})\mathbf{y}(l), \\ &= \mathbf{W}\,\mathbf{C}(\tilde{\epsilon})\mathbf{W}^H\mathbf{H}(l)\mathbf{d}(l) + \eta(l), \end{aligned} \tag{4.4}$$

where $\hat{\epsilon}$ is the estimate of ϵ, $\tilde{\epsilon} = \epsilon - \hat{\epsilon}$ is the CFO estimation error, and $\eta(l) = \mathbf{W}\,\mathbf{C}^*(\hat{\epsilon})\mathbf{z}(l)$. The kth element of $\mathbf{s}(l)$ can be expressed as

$$s_k(l) = \frac{1}{\sqrt{N}} \sum_{n=0}^{N-1} y_n(l) e^{-j\frac{2\pi n}{N}(k+\hat{\epsilon})}. \tag{4.5}$$

In the above system model, perfect symbol timing has been assumed. However, due to the symbol timing uncertainty, the sequence $\mathbf{y}$ might not be extracted correctly from the stream of received samples. Assuming that the timing uncertainty is within the safe region (SR) given in (2.34), by reversing the positions of $\mathbf{H}$ and $\mathbf{d}$ and denoting

$$\mathbf{D} = \mathrm{diag}([d_0, d_1, ..., d_{N-1}]^T), \tag{4.6}$$

and

$$\mathbf{h} = [h_0, h_1, ..., h_{L_h}]^T, \tag{4.7}$$

the received signal model in (4.1) can be rewritten to include the timing ambiguity in the SR explicitly [51],

$$\mathbf{y} = \mathbf{C}(\epsilon)\mathbf{T}(\delta)\mathbf{W}^H\mathbf{D}\mathbf{W}_{L_h+1}\mathbf{h} + \mathbf{z}, \tag{4.8}$$

where $\mathbf{W}_{L_h+1}$ is $N \times (L_h + 1)$ matrix containing the first $L_h + 1$ columns of $\mathbf{W}$ and

$$\mathbf{T}(\delta) \triangleq [e_{\delta+1}, ..., e_N, e_1, ..., e_\delta], \tag{4.9}$$

with $e_i = \mathbf{I}_{N\times N}(:, i)$ represents the distortion caused by timing offset where δ is assumed to be uniformly distributed over the SR interval. In order to mitigate the effect of timing uncertainty, the above model suggests joint STO and CFO data-

aided estimation as reported in [51]. However, a two-dimensional search over the trial offsets is required.

Another signal model can be deduced by embedding the timing ambiguity implicitly in the channel impulse response [50, 51],

$$\mathbf{y} = \mathbf{C}(\epsilon)\mathbf{W}^H\mathbf{D}\mathbf{W}_{N_{CP}}\bar{\mathbf{h}} + \mathbf{z}, \tag{4.10}$$

where

$$\bar{\mathbf{h}} \triangleq [\mathbf{0}^T_{\delta\times 1} \qquad \mathbf{h}^T \qquad \mathbf{0}^T_{(N_{CP}-\delta-L_h+1)\times 1}]. \tag{4.11}$$

The above signal model can be utilized to construct timing error robust CFO estimator as reported in [50]. The TER-MLE will be used to benchmark the performance of the considered blind CFO estimators in different timing uncertainty scenarios.

4.3 Blind CFO Estimator Based on Power Difference Measurements

This section presents a robust CFO estimator for OFDM systems using the power difference measurements technique. Based on the signal model described in the previous section, if the CFO is estimated and compensated perfectly, i.e. $\hat{\epsilon} = \epsilon$ then $\mathbf{C}(\epsilon)\mathbf{C}^*(\hat{\epsilon}) = \mathbf{I}$ which is the $N \times N$ identity matrix. Thus, the DFT output for the noise-free and perfect symbol timing i.e. $\delta = 0$, case be expressed as

$$\mathbf{s}(l)|_{\hat{\epsilon}=\epsilon} = \mathbf{H}(l)\mathbf{d}(l). \tag{4.12}$$

In this case, the power of the kth DFT output can be expressed as

$$|s_k(l)|_{\hat{\epsilon}=\epsilon}|^2 = |H_k(l)|^2 |d_k(l)|^2 . \tag{4.13}$$

Moreover, if the data symbols d_k are selected from a constant modulus (CM) constellation and all subcarriers have equal power, then (4.13) is reduced to,

$$|s_k(l)|_{\hat{\epsilon}=\epsilon}|^2 = |H_k(l)|^2 . \tag{4.14}$$

This is because the power of normalized CM signals is equal to one. Under the assumption that the channel frequency response parameters $H_k(l)$ change slowly in

the time domain with respect to T,

$$|s_k(l)|_{\hat{\epsilon}=\epsilon}|^2 \approx |s_k(l+1)|_{\hat{\epsilon}=\epsilon}|^2, \tag{4.15}$$

When $\hat{\epsilon} \neq \epsilon$, ICI will be introduced at the DFT output [52], and the approximation described in (4.15) is no longer valid.

The channel correlation over two consecutive OFDM symbols can be exploited by noting that (4.15) is valid for all subcarriers, the value of ϵ can be estimated by minimizing the following cost function,

$$J_{PDE-T}(\mu) = \sum_{l=1}^{L} \sum_{k=0}^{N-1} \left(|s_k(l)|^2 - |s_k(l+1)|^2 \right)^2, \tag{4.16}$$

where μ is the trial value of ϵ and L represents the number of times that the cost function is averaged over the symbols in each estimation process. Therefore, the estimates of ϵ, denoted as $\hat{\epsilon}$, can be obtained by minimizing the cost function given in (4.16),

$$\hat{\epsilon} = \arg \min_{\mu \in (-0.5, 0.5)} J_{PDE-T}(\mu). \tag{4.17}$$

That is to say, without the knowledge of the channel information, the CFO can be estimated blindly by minimizing the interference due to the frequency synchronization error. The considered interference minimization metric exploits the power difference between the subcarriers in consecutive OFDM symbols. It is obvious that the trial value μ which minimizes the cost function in (4.16) will bring back the correlation between the subcarriers. The cost function of the PDE-T estimator is formulated in the time direction utilizing the power difference between the same subcarrier in consecutive OFDM symbols rather than the frequency direction between the adjacent subcarriers in the OFDM symbol as reported in [52]. The PDE-T scheme exploits the property that for low and medium mobility speeds, the channel response changes more slowly in the time direction compared with the frequency direction. Thus, it is expected that the PDE-T estimator will provide a robust performance over fading channels with different selectivity conditions.

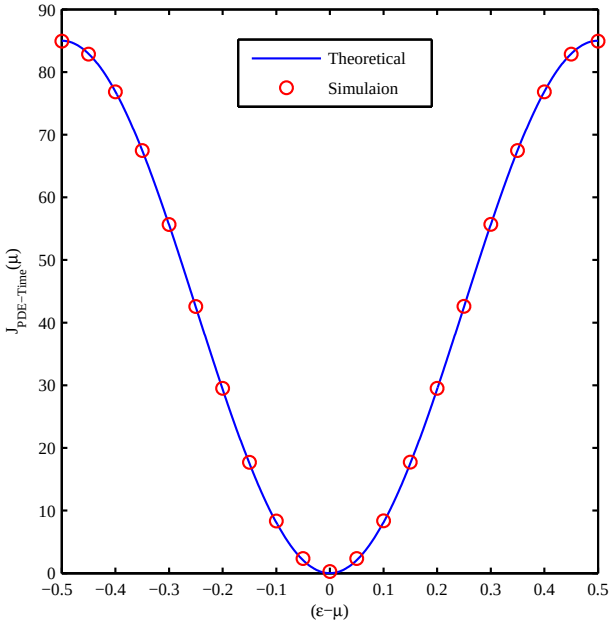

Figure 4.1: The cost function of the PDE-T over AWGN channel, $L = 10^4$, $N = 64$, $N_{CP} = 16$, SNR=30 dB and QPSK modulation

4.3.1 Low Complexity Implementation

An exhaustive line search or adaptive search methods can be used to minimize the cost function of the PDE-T estimator given in (4.16). However, the computational complexity and estimation accuracy are mainly depends on the CFO trial grid over which the search operation is performed. Even for adaptive minimization techniques, the complexity is still not affordable and the parameters setting such as the step size and initial point needs to pay some special attention in order to avoid the algorithm divergence.

Fortunately, following the same procedure used in [23] and [52], the cost function described in (4.16) can be approximated by a simple sinusoid. The mathematical derivation for the cost function approximation is shown in Appendix A where,

$$J_{PDE-T}(\mu) \approx A\cos[2\pi(\epsilon - \mu)] + C, \tag{4.18}$$

where A and C are constants independent of μ with $A < 0$.

The cost function given by (4.16) is depicted in Fig. 4.1 for an OFDM system with $N = 64$ and $N_{CP} = 16$. The channel is assumed to be additive white Gaussian noise (AWGN) with SNR=30 dB and normalized CFO $\epsilon = 0.2$. As can be noted from this figure, the cost function has a minimum value when $(\epsilon - \mu) = 0$ which

means that the interference due to the CFO is minimal. Moreover, it can be noticed that the cost function is well approximated to a sinusoid which can help to minimize the computational complexity significantly as described below.

Since the cost function is sinusoidal, the minimization process, which is usually performed using methods such as the line search or the gradient descent, can be replaced by a simple parameter estimation process to simplify the minimization process. This approach leads to closed-form estimation of ϵ by evaluating (4.16) at three special trial points, namely $(-1/4,\ 0,\ 1/4)$. The CFO estimate $\hat{\epsilon}$ can be obtained as follows (see Appendix B for the derivation)

$$\hat{\epsilon} = \begin{cases} \frac{1}{2\pi}\tan^{-1}(b/a) & a \geq 0 \\ \frac{1}{2\pi}\tan^{-1}(b/a) + \frac{1}{2} & a < 0 \text{ and } b \geq 0 \\ \frac{1}{2\pi}\tan^{-1}(b/a) - \frac{1}{2} & a < 0 \text{ and } b \leq 0 \end{cases} \tag{4.19}$$

where

$$a = \frac{1}{2}[J_{PDE-T}(1/4) + J_{PDE-T}(-1/4)] - J_{PDE-T}(0), \tag{4.20}$$

and

$$b = \frac{1}{2}[J_{PDE-T}(1/4) - J_{PDE-T}(-1/4)]. \tag{4.21}$$

4.3.2 Relations to MVE and KBE Methods

The MVE [22] and KBE [23] methods presented in Section (2.4.2) have similar cost functions and similar performance. To show the similarity of the cost functions, note that, for $L \gg 1$, the cost function of KBE $J_{KBE}(\mu)$ can be expressed as

$$J_{KBE}(\mu) \approx \frac{\sum_{k=0}^{N-1} E[|s_k(l)|^4]}{\left(\sum_{k=0}^{N-1} E[|s_k(l)|^2]\right)^2}. \tag{4.22}$$

In this case, the denominator of (4.22), denoted as K, represents the total energy of the signal which is a constant independent of μ [23] where

$$K \triangleq \left(\sum_{k=0}^{N-1} E[|s_k(l)|^2]\right)^2 = \left(\sigma_d^2 \sum_{k=0}^{N-1} E[|H_k(l)|^2] + N\sigma_\eta^2\right)^2. \tag{4.23}$$

Similarly, for $L \gg 1$, the cost function of the MVE estimator $J_{MVE}(\mu)$ can be expressed as,

$$J_{MVE}(\mu) = \mathrm{Var}\left[|s_k(l)|^2\right] = \frac{1}{N}\sum_{k=0}^{N-1} E[|s_k(l)|^4] - \left(\frac{1}{N}\sum_{k=0}^{N-1} E[|s_k(l)|^2]\right)^2. \quad (4.24)$$

Therefore, the two cost functions have the relation,

$$J_{MVE}(\mu) \approx \frac{K}{N} J_{KBE}(\mu) - \frac{K}{N^2}. \quad (4.25)$$

From (4.25), it can be noted that $J_{MVE}(\mu)$ is an affine transform of $J_{KBE}(\mu)$. Moreover, since the two cost functions have a sinusoidal shape and the estimation is performed using the curve fitting approach given in (4.19), we conclude that the performance of both algorithms is the same.

Due to the equivalence between the MVE and the KBE, in the following, the relationship between the PDE-T estimator and the KBE is discussed. The cost function of the PDE-T estimator can be written as,

$$J_{PDE-T}(\mu) = \sum_{k=0}^{N-1} |s_k(l)|^4 + \sum_{k=0}^{N-1} s_k(l+1)|^4 - 2\sum_{k=0}^{N-1} |s_k(l)|^2 |s_k(l+1)|^2. \quad (4.26)$$

By observing the cost function of the PDE-T estimator given in (4.26), it is obvious that the PDE-T includes two additional terms compared with the cost function of the KBE in (4.22). The third term of (4.26) represents the correlation of the subcarriers in consecutive OFDM symbols. The reason for performance deterioration of the KBE method [23] is that as the frequency selectivity of the channel increases, the distribution of the received signal tend to be Gaussian even if the CFO is perfectly compensated. Thus, the kurtosis function can not produce a reliable metric to measure the CFO. On the other hand, for the PDE-T, it is expected that an extra gain can be accomplished as will be demonstrated in the numerical results section. This is due to the additional terms in (4.26) which will weaken the correlation among the subcarriers and reduce the degradation in frequency selective fading channels significantly.

4.4 Blind CFO Estimator Based on Phase Difference Measurements

This section presents an efficient CFO estimator based on phase difference measurements approach. In the following, the proposed iterative scheme for the Viterbi-and-Viterbi algorithm is only presented and analysed in the presence of various timing uncertainty conditions. However, for more detailed analysis and investigations about this technique, the reader is referred to [32, 33].

Assuming an observation period of $2(N + N_{CP})$ samples which comprises two OFDM symbols, the kth element of frequency domain sequence $\mathbf{s}(l)$ can be expressed as

$$s_k(l) = e^{j\frac{2\pi\epsilon l}{N}(N+N_{CP})} \sum_{i=0}^{N-1} \frac{\sin(\pi\epsilon)}{N\sin[\pi(i+\epsilon-k)/N]} d_i(l) H_i(l) e^{j\pi\breve{N}(i+\epsilon-k)} + \eta_k(l), \quad (4.27)$$

where $\breve{N} = (N-1)/N$. Separating the kth subcarrier gives,

$$s_k(l) = d_k(l) H_k(l) \frac{\sin(\pi\epsilon)}{N\sin(\pi\epsilon/N)} e^{j\pi\epsilon[\frac{2l}{N}(N+N_{CP})+\breve{N}]} + \Psi_k(l) + \eta_k(l), \quad (4.28)$$

where $\Psi_k(l)$ denotes the ICI leak to the kth subcarrier due to the loss of orthogonality among the subcarriers,

$$\Psi_k(l) = e^{j\frac{2\pi\epsilon l}{N}(N+N_{CP})} \sum_{i=0,\ i\neq k}^{N-1} \frac{\sin(\pi\epsilon)}{N\sin[\pi(i+\epsilon-k)/N]} d_i(l) H_i(l) e^{j\pi\breve{N}(i+\epsilon-k)}. \quad (4.29)$$

Assuming that the modulating symbols have zero mean and are uncorrelated, the ICI can be considered as a Gaussian random variable because N is large [65]. Consequently, the signal model in (4.28) can be written as

$$s_k(l) = \frac{\sin(\pi\epsilon)}{N\sin(\pi\epsilon/N)} d_k(l) H_k(l) e^{j\pi\epsilon[\frac{2l}{N}(N+N_{CP})+\breve{N}]} + D_k(l), \quad (4.30)$$

where $D_k(l) = \Psi_k(l) + \eta_k(l)$ represents the disturbance term.

In polar form, $s_k(l)$ can be expressed as [73]

$$s_k(l) = |A_k(l)|\, e^{j\left\{\pi\epsilon\left[\frac{2l}{N}(N+N_{CP})+\breve{N}\right]+\theta_k(l)+\phi_k(l)+\varsigma_k(l)\right\}}, \quad (4.31)$$

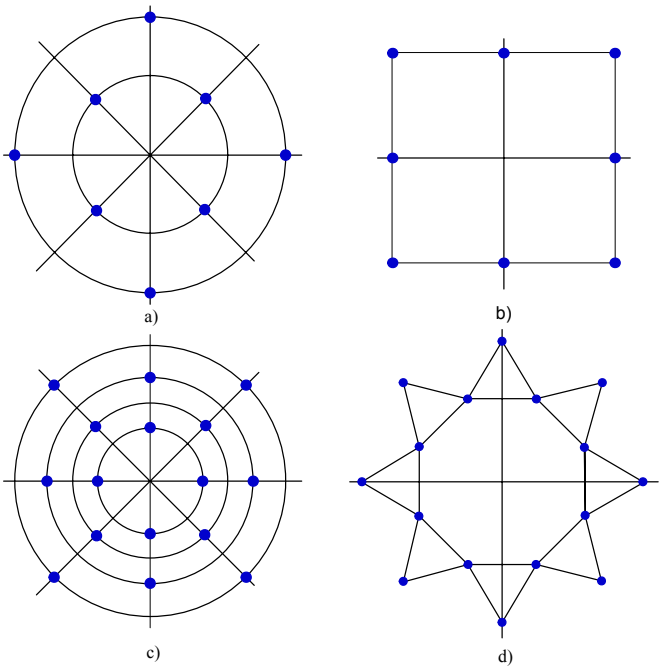

Figure 4.2: Examples for 8 and 16-QAM constellation with rotational symmetric phases. a) $M = 8$, $K = 8$. b) $M = 8$, $K = 8$, c) $M = 16$, $K = 8$, d) $M = 16$, $K = 16$.

where

$$A_k(l) = \frac{\sin(\pi\epsilon)}{N\sin(\pi\epsilon/N)} d_k(l) H_k(l) \rho_k(l) \tag{4.32}$$

the data symbol phase is denoted as $\theta_k(l)$, $\phi_k(l)$ represents the phase offset introduced by the fading channel, $\rho_k(l)$and $\varsigma_k(l)$ represent the effect of the complex noise and ICI on the received signal amplitude and phase, respectively. By comparing the signal model given in (4.31) with single carrier signal model [74] and noting that ϵ is independent of the subcarrier index k, the N subcarriers cab be utilized to obtain estimates by applying single carrier synchronization algorithms as in [16, 36].

The VAV algorithm is based on the property that certain QAM and MPSK constellations obey a rotational symmetry angle of $2\pi/K$ as shown in Fig. 4.2, where K is an integer that represents the number of possible phase angles in the constellation and M is the modulation order [37]. The VAV estimator for single carrier signals is given by [37],

$$\hat{\epsilon} = \frac{1}{2\pi K} \arg\left\{ \sum_{l=1}^{L} b_l F(|s(l-1)|) F(|s(l)|) e^{j\Delta(l)} \right\}, \tag{4.33}$$

where $\Delta(l) \triangleq K[\arg\{s(l)\} - \arg\{s(l-1)\}]$, b_l is an arbitrary filter function and $F(\cdot)$ is an arbitrary real nonlinearity. The VAV can be applied to OFDM by computing

$\Delta_k(l)$ for the kth subcarrier given in (4.31),

$$\Delta_k(l) = \frac{2\pi\epsilon K(N+N_{CP})}{N} + K[\theta_k(l) - \theta_k(l-1)] + K[\phi_k(l) - \phi_k(l-1)] + K[\varsigma_k(l) - \varsigma_k(l-1)]. \tag{4.34}$$

where the first term in $\Delta_k(l)$ contains the desired CFO information and the second term is an integer multiple of 2π that can be eliminated by taking the exponent of Δ_k. Based on the assumption that the channel remains unchanged over the observation window, the third term which represents the phase difference due to the fading channel can be neglected. The last term represents the effect of the AWGN and ICI.

The exponentiation of (4.34) gives,

$$e^{j\Delta_k(l)} = e^{j\frac{2\pi\epsilon K}{N}(N+N_{CP}) + j\varphi_k(l)}, \tag{4.35}$$

where

$$\varphi_k(l) = K[\varsigma_k(l) - \varsigma_k(l-1)]. \tag{4.36}$$

Therefore, the CFO estimate using the VAV algorithm as applied to OFDM can be expressed as [32]

$$\hat{\epsilon} = \frac{N}{2\pi K(N+N_{CP})} \arg\left\{ \sum_{l=1}^{L} b_l \sum_{k=0}^{N-1} F(|s_k(l-1)|) F(|s_k(l)|) e^{jK[\arg\{s_k(l)\} - \arg\{s_k(l-1)\}]} \right\}. \tag{4.37}$$

By assuming that $F(|s_k(.)|) = |s_k(.)|^K$, the CFO estimates can be expressed as [33]

$$\hat{\epsilon} = \frac{N}{2\pi K(N+N_{CP})} \arg\left\{\Phi(k,l)\right\}. \tag{4.38}$$

where

$$\Phi(k,l) = \sum_{l=1}^{L} b_l \sum_{k=0}^{N-1} \left[s_k(l) s_k^*(l-1)\right]^K. \tag{4.39}$$

Using the VAV algorithm, accurate CFO estimates can be obtained blindly using an observation window of two OFDM symbols. The maximum CFO that can be estimated without ambiguity using VAV is given by,

$$|\epsilon_{\max}| = \frac{N}{2\pi K(N+N_{CP})}. \tag{4.40}$$

For $K \leq 4$, the estimation range is reasonable because CFOs and Doppler shifts

$\hat{\epsilon} = 0$

for $i = 1$ to I_t (I_t : number of iterations)

$\mathbf{s}(l-1) = \mathbf{W}\mathbf{C}^*(\hat{\epsilon})\mathbf{y}(l-1)$

$\mathbf{s}(l) = \mathbf{W}\mathbf{C}^*(\hat{\epsilon})\mathbf{y}(l)$

$\hat{\epsilon}_{temp} = \frac{N}{2\pi K(N+N_{CP})} \arg\{\Phi(k,l)\}$

$\hat{\epsilon} = \hat{\epsilon} + \hat{\epsilon}_{temp}$

end

Figure 4.3: The iterative scheme of the VAV algorithm

are generally a small fraction of the subcarrier spacing in the tracking mode. For large K values, the value of $\epsilon_{\max}$ is noticeably small. In the next subsections, the proposed iterative algorithm is presented as a solution for such cases.

4.4.1 The Iterative VAV

The ICI introduced by the CFO has a major impact on the quality of the frequency domain symbols at the DFT output as demonstrated in in (4.28). The quality of such symbols which are contaminated by noise and ICI is usually assessed using the effective SNR (SNR_e),

$$\text{SNR}_e = \frac{E[|d_k|^2]}{E[|\eta_k|^2] + E[|\Psi_k|^2]}. \tag{4.41}$$

For example, given that SNR=20 dB and $\epsilon = 1/8$, then $\text{SNR}_e \approx 10$ dB [17]. Consequently, the performance of the VAV estimator will be significantly influenced by the value of ϵ which indicates that a severe performance deterioration might be obtained since the value of ϵ is uniformly distributed over (-$\epsilon_{\max}$, $\epsilon_{\max}$). An efficient remedy for such problem is to use the VAV algorithm iteratively as depicted in Fig. 4.3.

Using this iterative approach, the inaccurate estimate obtained in the first iteration is used to reduce the ICI before performing the second iteration. As a consequence, the second estimate will be performed under higher SNR_e which leads to a better estimate. Repeating this process for a few times gives $\hat{\epsilon}_{temp} \approx 0$, $\text{SNR}_e \approx \text{SNR}$ and $\hat{\epsilon} \approx \epsilon$. Simulation results have shown that using three iterations is sufficient to produce a performance that is approximately equal to the $\epsilon = 0$ case.

4.4.2 Estimation Range

In addition to its role in improving the estimates' MSE, the iterative configuration has an other advantage which is the estimation range extension. As it can be observed from (4.40), the value of ϵ_{max} is inversely proportional to K, for large values of K, ϵ_{max} becomes much smaller than 1/2. On the other hand, using lower order modulations decreases the system capacity. Fortunately, the iterative structure can be used to loosen the bond between the estimation range and the system capacity. To explain how this goal can be achieved, assume that the N subcarriers are divided into two groups that consists of N_1 and N_2 subcarriers, $N_1 \ll N_2$. Moreover, we assume that each group of subcarriers is modulated using two different modulation schemes with parameters K_1 and K_2 where $K_1 \ll K_2$. In such a case, the N_1 subcarriers can be used in the first iteration given that $\epsilon < \epsilon_{max,K_1}$. In the subsequent iterations, the CFO seen by the estimator is $\hat{\epsilon}_{temp}$ which should be smaller than ϵ_{max,K_2}. Therefore, all the subcarriers can now be involved to produce accurate estimates in the remaining iterations. As an example, consider an OFDM system where $N = 256$ and $N_{CP} = 16$, given that N_1 subcarriers are BPSK modulated, then $K_1 = 2$ and $\left|\epsilon_{\max}^{(1)}\right| \approx 0.23$. The remaining $N_2 = N - N_1$ subcarriers are modulated using the 16-QAM then $K_2 = 8$ and $\left|\epsilon_{\max}^{(2)}\right| \approx 0.058$. Therefore, the maximum CFO that can be estimated is determined by K_1. However, the value of N_1 should be large enough to provide estimates that are smaller than $\left|\epsilon_{\max}^{(2)}\right|$. In practice, this technique does not have a noticeable effect on the system capacity because all practical OFDM systems have a number of subcarriers with lower order modulations such as BPSK [7]. Obviously, relying solely on these subcarriers for CFO estimates would not produce accurate estimates as in the case where all subcarriers are invoked in the estimation process. Another major advantage of this approach is the substantial complexity reduction achieved by considering only $N_1 < N$ subcarriers in the first $I_t - 1$ iterations and using the N subcarriers only in the final iteration. Furthermore, since most of the current standards [7] include a small number of unmodulated subcarriers, i.e. pilots, a semi-blind estimator can be constructed by using those pilots in the first $I_t - 1$ iterations, followed by all subcarriers to produce the final CFO estimate.

Table 4.1: The computational complexity of the considered CFO estimators

	Additions	**Multiplications**	**DFT**
CPE	$(N_{CP}+3)(N+N_{CP})L$	$4L(N+N_{CP})$	0
KBE	$12NL$	$15NL$	$3L$
PDE-F	$12NL$	$21NL$	$3L$
PDE-T	$N(12L+6)$	$N(21L+18)$	$3(L+1)$
IGVAV	$\sim 4NL$	$\sim 18NL$	$3(L+1)$

4.5 Computational Complexity

This section is dedicated to the computational complexity evaluation of the presented CFO estimation schemes. The computational complexity of the considered estimators is assessed in terms of real arithmetic operations, namely additions/subtractions and multiplications, in addition to the number of DFT operations. As it can be noted from (4.16), the computational complexity for the PDE-T is dominated by the number of magnitude-squared, DFT and addition/subtraction operations. The N-point radix-2 FFT roughly requires $(N/2)\log_2 N$ complex multiplications and each is equivalent to four real multiplications and two real additions. Therefore, the PDE-T estimator requires $3(L+1)$ DFT operations, $N(21L+18)$ multiplications and $N(12L+6)$ additions.

The computational complexity of the IGVAV can be deduced from (4.38). The major computations performed for each estimate are $\sum_i^{I_t} N_i L(\log_2(K_i)+1)$ complex multiplications, $\sum_i^{I_t}(N_i-1)L$ complex additions and I_t DFT operations where N_i and K_i denote the number of subcarriers and the modulation removal factor used in the ith iteration, respectively. For the IGVAV estimator, it is assumed that all subcarriers are modulated using quadrature phase shift keying (QPSK) thus $K=4$, the number of iterations is equal to 3.

Although there are some divisions and non-linear operations such as the $\tan^{-1}$ computation, the number of times these operations are performed is very little and all estimators use almost the same number of operations. Consequently, the divisions and non-linear operations are ignored for all estimators. Table 4.1 presents a summary of the computational power required for the considered CFO estimators. As can be noted from this table, the IGVAV estimator requires the smallest number of addition and multiplication operations as only small number of subcarriers are involved in the first two iterations. In general, the computational complexity of the considered CFO estimators is comparable to the MVE, KBE and PDE-F systems

as the total amount of computation is dominated by the DFT operations.

For example, assuming that the CFO is estimated continuously for system parameters of L=1, N=64 and N_{CP}=16, the PDE-T and IGVAV require 2496 and 1152 real multiplications, respectively. On the other hand, the KBE and PDE-F require 960 and 1344 real multiplications, respectively however, the KBE and PDE-F methods need higher averaging factor to attain the required accuracy in fading channels. Hence, the computational load will increase considerably, for L=5, 4800 and 6720 multiplications are required for the KBE and PDE-F, respectively to obtain an estimate. However, the PDE-T and IGVAV produce reliable estimate using L=1 even for severe conditions and there is no need for further averaging.

4.6 Numerical Results

Monte Carlo simulations are used to assess the performance of the CFO estimators over AWGN and frequency selective multipath fading channels. In each simulation run, 10^6 OFDM symbols are used. The performance is evaluated by means of normalized MSE, where the MSE of the CFO estimates is normalized with respect to the subcarriers' frequency spacing. The considered OFDM system has the following parameters: $N = 64$, $N_{CP} = 16$, subcarriers data rate is 4.17 kb/s, the data symbols are drawn from QPSK constellation and perfect symbol timing is assumed unless otherwise specified. In all simulations, the CFO ϵ is uniformly selected such that $|\epsilon| \leq 0.9\epsilon_{\max}$ where $\epsilon_{\max}$ is the maximum CFO that can be estimated.

To demonstrate the efficiency of the PDE-T and IGVAV estimators, three different frequency selective fading channel models are used as depicted in Table 4.2. Each of the three channels has different selectivity level that is determined by the number of multipath components, the maximum delay and the gains of each component [28]. Obviously, Channel-I has the least severe fading while Channel-III has the most severe fading conditions. The path gains are generated as complex independent stochastic variables and fading with Jakes' Doppler spectrum [29]. The PDE-T and IGVAV estimators are compared with KBE [23], MVE [22], CPE [17] and PDE-F [52] estimators because they have comparable computational complexity where the cost functions can be approximated by a sinusoid and the CFO estimates are obtained by employing parameter estimation. Furthermore, the considered estimators are assessed in the presence of symbol timing uncertainty and the performance

Table 4.2: The channels' parameters

	Path Gains	Path Delays	Delay Spread
Channel-I	$0.35, 0.25, 0.18, 0.13, 0.09$	$0, 1, 2, 3, 4$	1.74
Channel-II	$0.34, 0.28, 0.23, 0.11, 0.04$	$0, 1, 2, 6, 11$	6.37
Channel-III	$0.25, 0.25, 0.25, 0.25$	$0, 4, 8, 12$	20

is compared with other timing error robust estimator to examine the effect of timing errors on the CFO estimation.

To observe the behaviour of the IGVAV estimator for different values of ϵ and K, the IGVAV system is simulated and the values of $\hat{\epsilon}$ is plotted versus ϵ as depicted in Fig. 4.4. It can be noted from this figure that $\hat{\epsilon}$ follows ϵ linearly almost for the entire range where $|\epsilon| \leq \epsilon_{\max}$. When $|\epsilon|$ approaches $\epsilon_{\max}$, the resulted CFO estimation might have opposite signs. Therefore, in the following simulations we used $|\epsilon| \leq 0.9\epsilon_{\max}$.

The MSE of the IGVAV estimator versus the SNR as a function of the number of iterations for AWGN channels is depicted in Fig. 4.5. As noted from this figure, the MSE which results after performing two iterations is very close to the $\epsilon = 0$ case for a wide range of SNRs. The degradation observed at low SNRs cannot be removed by performing more iterations because the estimate accuracy is dominated by the AWGN. At high SNRs, the small error floor can be eliminated by performing a third iteration and thus the MSE performance becomes almost identical to the $\epsilon = 0$ case. Consequently, performing three iterations should be sufficient to completely eliminate the effect of the ICI at moderate and high SNRs. The MSE performance of the iterative estimator using the proposed estimation range extension approach is also presented where N_1 BPSK modulated subcarriers are used in the first and second iterations. In this case, the modulation removal factors K_i and the maximum estimation ranges $\left|\epsilon_{\max}^{(i)}\right|$ during the ith iteration are $K_1 = K_2 = \frac{1}{2}K_3 = 2$ and $\left|\epsilon_{\max}^{(1)}\right| = \left|\epsilon_{\max}^{(2)}\right| = 2\left|\epsilon_{\max}^{(3)}\right| = \frac{N}{4(N+N_{CP})} = 0.2$, respectively. All other subcarriers $N_2 = N$ -N_1 are modulated using QPSK and only involved in the third iteration. Extensive simulations have shown that using $N_1 = 14$ is sufficient for the system to acquire the CFO in the first two iterations and to produce MSE equivalent to the $\epsilon = 0$ case as shown in Fig. 4.5. This process is crucial when the subcarriers have higher order modulation where $K > 4$ to extend the estimation range of the IGVAV.

Fig. 4.6 depicts the MSE performance of the considered estimators over AWGN

channels. It can be seen that the MSE decreases, approximately, linearly for SNR $\gtrsim$ 8 dB for all estimators except the IGVAV where the MSE starts to decrease linearly for SNR $\gtrsim$ 15 dB. Also, it is obvious that PDE-F exhibits a slight flatness at high SNRs. While the MVE/KBE and PDE-T estimators have demonstrated equivalent MSE over the whole range of SNR, the CPE and IGVAV estimators outperform all other estimators by about 4 dB and 15 dB respectively at moderate and high SNRs. In addition, it is clearly demonstrated that the performance of the PDE-T using the search approach coincides exactly with the parameter estimation method which confirms the validity of the sinusoidal approximation for the cost function.

To evaluate the MSE in mild and moderate frequency selective fading channels, we use channel-I and II as shown in Fig. 4.7 and Fig. 4.8, respectively. As demonstrated in these figures, PDE-T and IGVAV outperform all other systems for the entire range of SNRs over both channels. The MSE difference becomes substantial at high SNRs where the MSE of all other considered estimators saturates and becomes flat. The robustness of both IGVAV and PDE-T against frequency selectivity can be observed from the negligible MSE difference over both channels. The MSE of PDE-F significantly deteriorates when the channel delay spread increases. Similar MSE deterioration has been observed for all the considered systems except the IGVAV and PDE-T. The MVE/KBE estimators are the most vulnerable to large delay spreads at moderate and high SNRs.

The MSE performance of the considered estimators with different averaging factor over highly frequency selective fading channels is depicted in Fig. 4.9 where Channel-III is used. This figure clearly shows the high immunity of PDE-T and IGVAV estimators against severe multipath fading conditions. While the MSE of all the considered estimators starts to saturate at SNR $\gtrsim$ 20 dB, the MSE of IGVAV and PDE-T continues to decrease by increasing the SNR approximately in a linear manner. Moreover, the MSE of the IGVAV and PDE-T using $L = 1$ is much smaller than the MSE of PDE-F at high SNRs even for the $L = 5$ case. Therefore, no averaging is needed for the PDE-T and IGVAV estimators even under sever frequency selective fading conditions.

To evaluate the MSE performance of the PDE-T and IGVAV systems over time varying frequency selective fading channels with various mobility conditions, we consider two different maximum Doppler shifts for Channel-III model, namely 50 and 200 Hz, which corresponds to vehicle speeds of approximately 24.5 and 98 km/hour,

respectively. As depicted in Fig. 4.10, the IGVAV and PDE-T still outperform all the other considered estimators. The MSE of the IGVAV, PDE-T and PDE-F start to converge for vehicle speeds $\gtrsim$ 100 km/hour, which is an evidence that the PDE-T and IGVAV estimators maintains its efficiency even in time varying channels. Fig. 4.10 also shows that the MSE of MVE/KBE does not change drastically as a function of f_d.

The OFDM system performance in terms of BER over Channel-II with the employment of the considered CFO estimators is presented in Fig. 4.11 for QPSK and 16-PSK signalling. The perfect knowledge of the channel at the receiver has been assumed in order to highlight the effect of synchronization error. However, at the receiver, the channel need to be estimated and the performance of channel estimator is also affected by the synchronization error. In Fig. 4.11 (a), the Channel-II model is used and the BER is evaluated for MVE/KBE, PDE-F, PDE-T and IGVAV CFO estimators. As can be noted from this figure, the BER degradation due to the frequency synchronization error over Channel-II is negligible for the PDE-T and IGVAV where almost equivalent performance to the perfect frequency synchronization condition can be achieved at moderate and high SNRs. However, a slight deterioration can be noted at low SNRs. On the other hand, the other estimators produce significant BER degradation in particular the MVE/KBE estimators while a little deterioration can be observed in the PDE-F case at high SNRs over this channel. To observe the effect of large delay spread, the BER results presented in Fig. 4.11 (b) are generated using a severe case of Channel-II where the delay spread spans the entire CP region. This channel has the same tap gains as Channel-II however the taps' delays are [0 4 8 12 16]. It is obvious that the BER deterioration is significant when the MVE/KBE and PDE-F estimators are employed while the robustness of the PDE-T and IGVAV estimators can be noticed over this channel as the achieved BER is the same as perfect frequency synchronization condition.

The BER performance of the OFDM system over Channel-III is presented in Fig. 4.12 for QPSK and 16-PSK signalling. Again, the PDE-T and IGVAV estimators have demonstrated a robust BER performance compared to the other CFO estimation methods where significant BER degradation can noticed in particular for the MVE/KBE. Moreover, it is clear that the BER degradation due to the frequency synchronization error increases as the modulation order increases where a significant degradation can be noted for M=16 case.

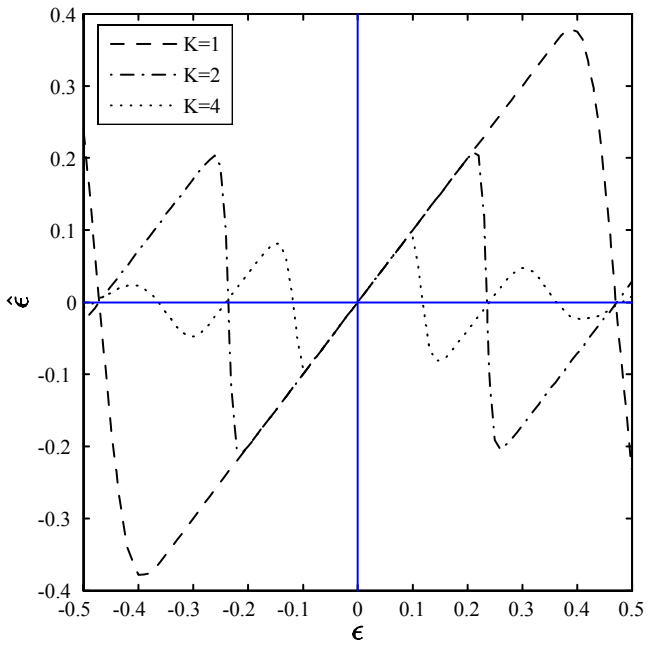

Figure 4.4: The CFO estimate $\hat{\epsilon}$ versus ϵ for different values of K, SNR= 40 dB.

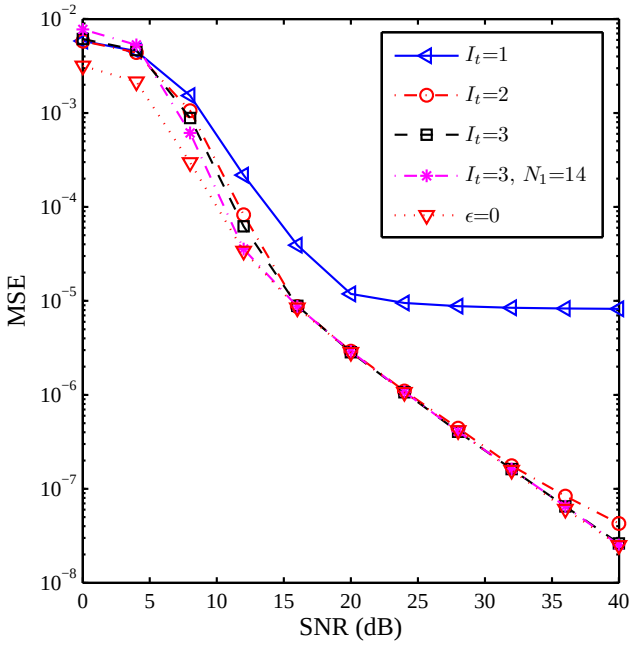

Figure 4.5: The MSE of the IGVAV estimator for different number of iterations I_t over AWGN channels, $L = 1$.

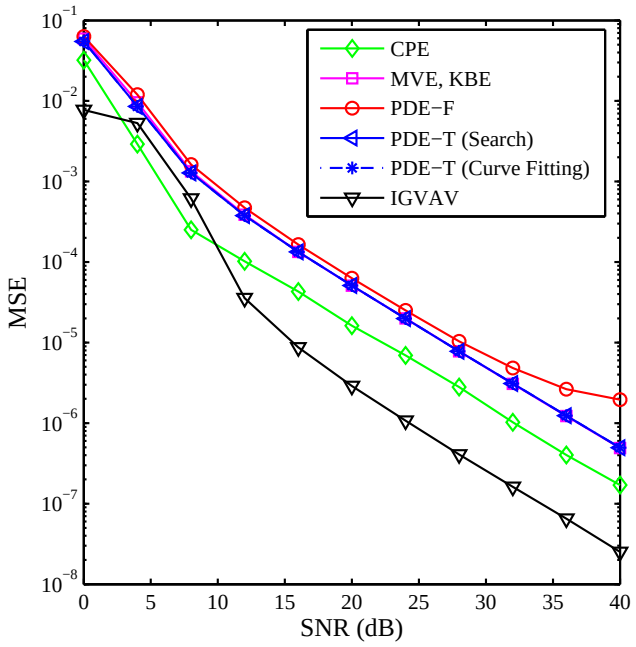

Figure 4.6: MSE versus SNR over AWGN channels, $L = 1$.

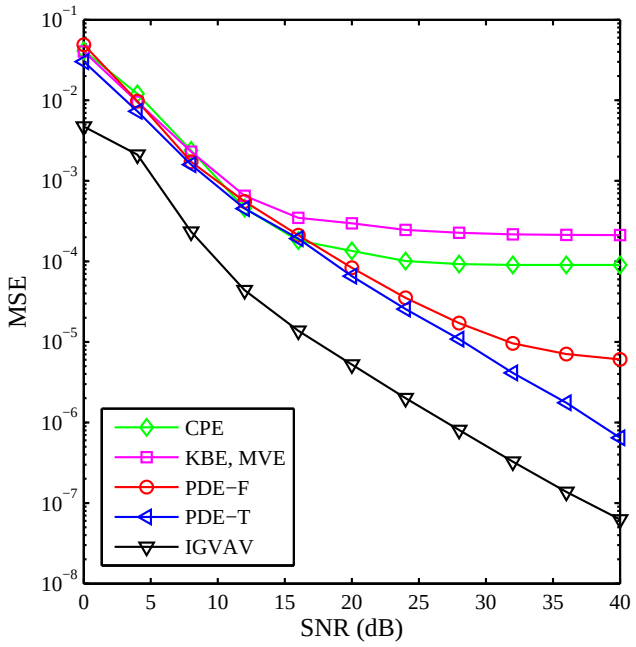

Figure 4.7: MSE versus SNR over Channel-I, $L = 1$

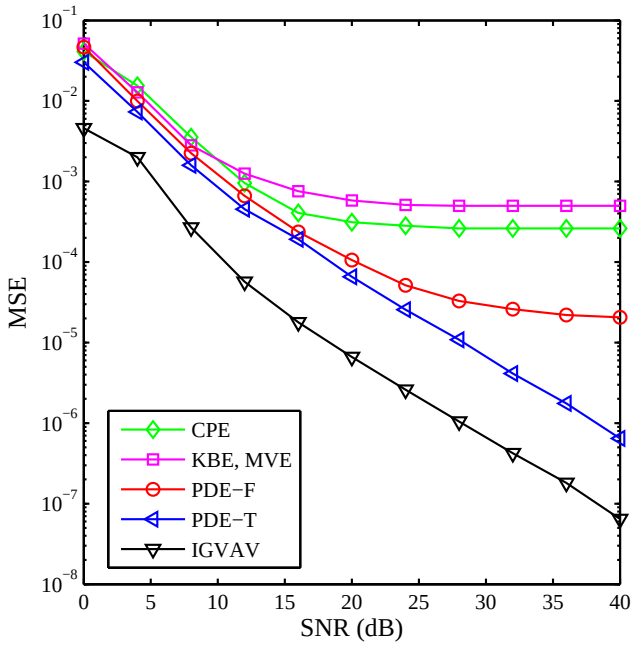

Figure 4.8: MSE versus SNR over Channel-II, $L = 1$

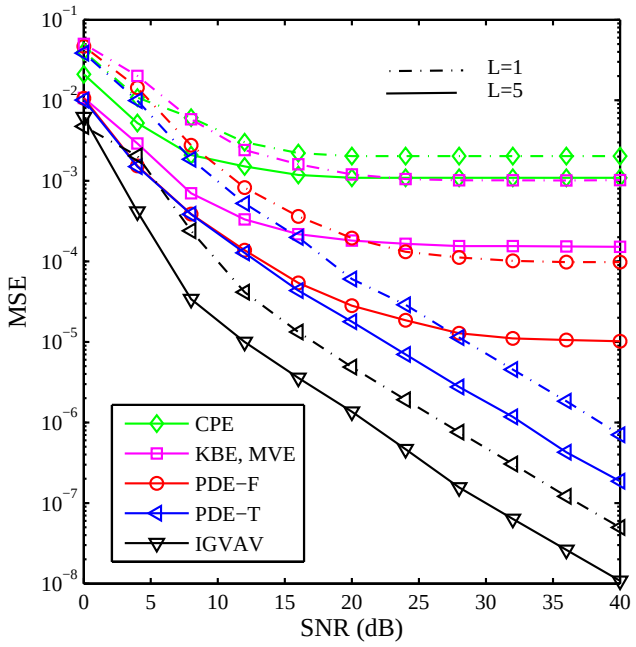

Figure 4.9: MSE versus SNR over Channel-III, $L = 1, 5$

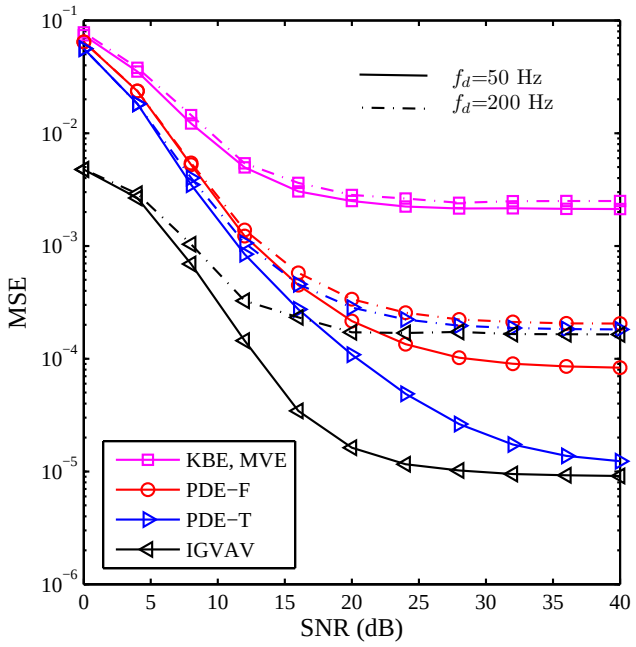

Figure 4.10: MSE versus SNR over Channel-III with different Doppler shift values, $L = 1$, $f_d = 50$ and 200 Hz.

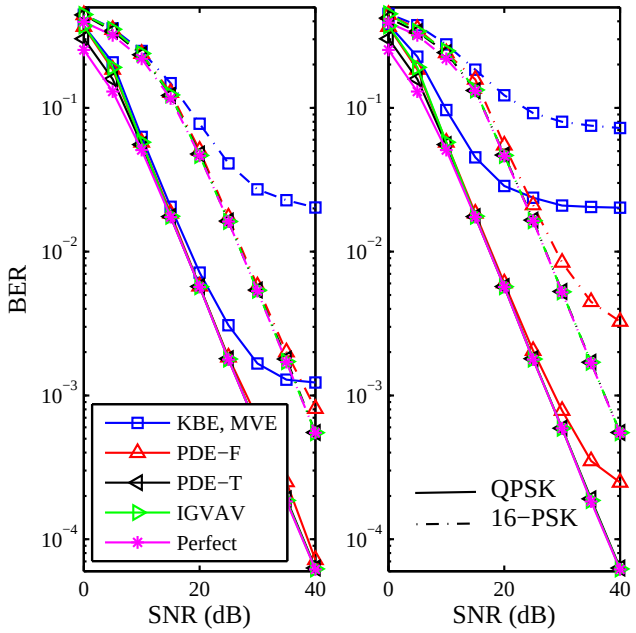

Figure 4.11: BER versus SNR for OFDM system with QPSK and 16-PSK, (a) Channel-II (b) The severe case of Channel-II

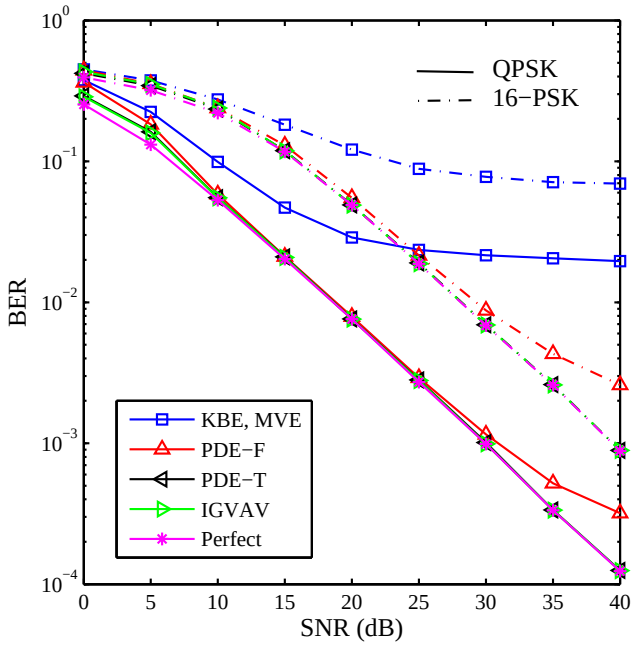

Figure 4.12: BER versus SNR over Channel-III for OFDM system with QPSK and 16-PSK

In the following, the simulation results are presented to demonstrate the effect of timing errors on the performance of the considered CFO estimators which have different estimation strategies including time domain, frequency domain, DA and blind schemes. In all simulations, the introduced timing errors are modelled as random integers uniformly distributed in a given range of interest. In addition to the CFO estimators discussed in the previous section, the simulation results presented in this section consider another two CFO estimators that are based on maximum-likelihood approach, ZMLE [49] and TER-MLE [50]. The TER-MLE estimator has a robust performance in the presence of timing uncertainty, hence it will be used for comparison to assess the sensitivity of the PDE-T and IGVAV CFO estimators to timing errors.

Fig. 4.13 presents the MSE of the CPE, ZMLE and TER-MLE estimators over Channel-II. The timing error is uniformly distributed in the range $[-(N_{CP}-L_h), 0]$, which corresponds to the SR of the timing estimates where $-N_{CP}+L_h \leq \delta \leq 0$. As can be noted from this figure, the considered estimators are highly sensitive to timing errors even if they fall in the SR. In the case of CPE, the degradation is demonstrated as an increase in the error floor level by a factor of ~ 10. The same behaviour is expected in similar correlation based CFO estimators. On the other hand, the TER-MLE estimator has demonstrated some robustness to the timing

errors. However, the MSE degradation can be noted which is equivalent to 5 dB SNR reduction. Unlike the previous two estimators, the ZMLE estimator suffered from a severe degradation in the MSE performance demonstrated by a high level error floor.

The results in Fig. 4.14 are obtained under the conditions and assumption used in Fig. 4.13 for the MVE/KBE, PDE-F, PDE-T and IGVAV estimators. By contrast to the estimators considered in Fig. 4.13, the estimators considered in Fig. 4.14, which have similar estimation strategy, demonstrated high robustness against timing errors with a performance that is equivalent to the perfect timing case. Moreover, the performance degradation due to the channel conditions is clearly depicted in this figure.

Fig. 4.15 depicts the MSE degradation in the presence of timing uncertainty. The function $M\tilde{S}E$ is defined as,

$$M\tilde{S}E = \frac{MSE|_{\delta\neq 0}}{MSE|_{\delta=0}}, \tag{4.42}$$

and the timing error is modelled as random integer uniformly distributed over $[0, \delta_{\max}]$ or $[\delta_{\min}, 0]$. As it can be noted from this figure, the ZMLE, TER-MLE and IGVAV estimators seem to be very sensitive to positive timing errors while the CPE, MVE/KBE, PDE-F and PDE-T estimators have demonstrated more robustness to positive timing errors. However, the ZMLE, TER-MLE and IGVAV estimators were remarkably sensitive as $M\tilde{S}E > 10^4$ was recorded for a timing uncertainty of only one sample. With the exception of ZMLE, all the considered estimators demonstrated less sensitivity to timing errors in the SR. However, the observed degradation is still significant for the CPE and ZMLE estimators. In contrary to the positive errors case, the estimator of CPE reported higher sensitivity when the errors are in the SR. The MVE/KBE, PDE-F, PDE-T and IGVAV estimators offer negligible degradation when the timing offset is within the SR.

Finally, for the case of negative timing errors, the timing error range is extended outside the SR to include the entire CP region as shown in Fig. 4.16. As depicted in this figure, the PDE-T and IGVAV estimators in addition to the MVE/KBE and PDE-F still can tolerate the timing errors in this region and the MSE degradation is less than ~ 10 at the end of the CP region. While the other considered estimators suffer from a severe degradation, particularly at the end of the CP region.

The simulation results clearly illustrate the superior performance of the IGVAV and PDE-T. Both estimators have demonstrated superb robustness against ambiguity of the timing estimates and frequency selectivity of the channel which are added to their distinct feature as blind estimation method. The main features and limitations of the considered estimators in this chapter, compared with other frequency synchronization methods, are summarized in Table 4.3. The details of the complexity analysis for the closed-form CFO estimators have been presented in Table 4.1. The computational complexity of the ZMLE and TER-MLE estimators is mainly depends on the search resolution and the required estimation accuracy. Because the cost function formulation for both ZMLE and TER-MLE require to forth from time to frequency domain for each trial CFO, the computational load will increase considerably due to the FFT operations compared with the other closed-form CFO estimators (i.e. KBE, PDE-F, PDE-T and IGVAV) especially when the ZMLE and TER-MLE are considered for CFO estimation in the acquisition stage where $\epsilon \in (-0.5, 0.5)$.

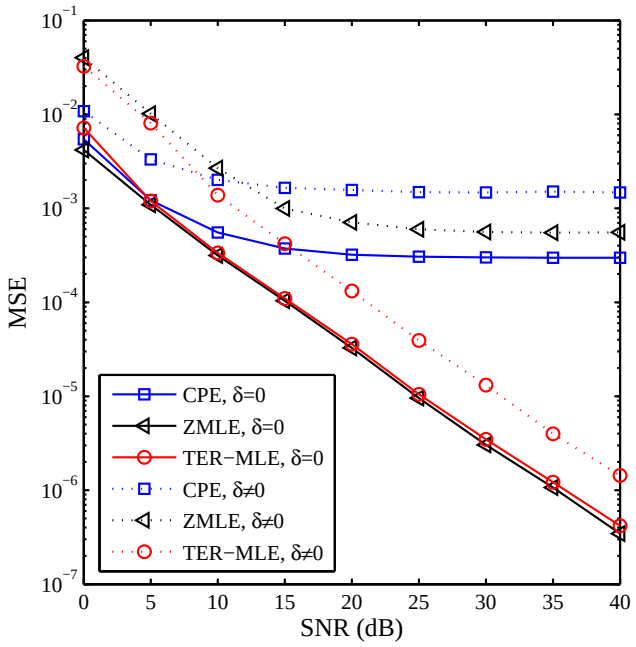

Figure 4.13: MSE versus SNR over Channel-II for a group of CFO estimators with high sensitivity to timing errors.

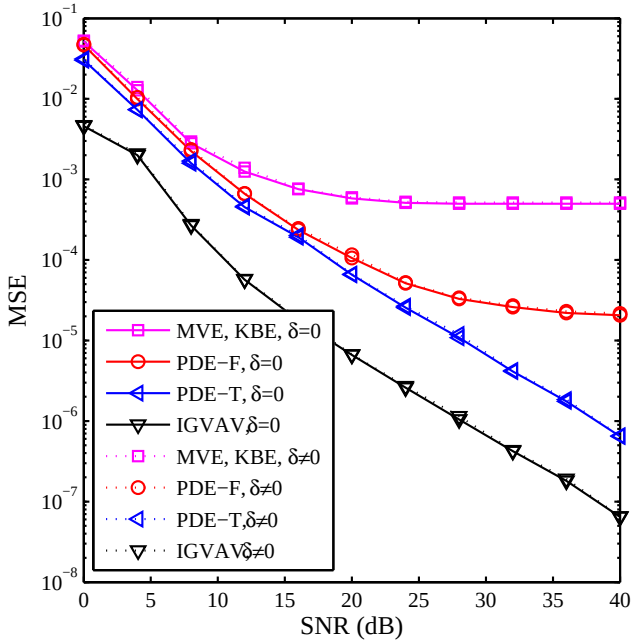

Figure 4.14: MSE versus SNR over Channel-II for a group of CFO estimators with high tolerance to timing errors.

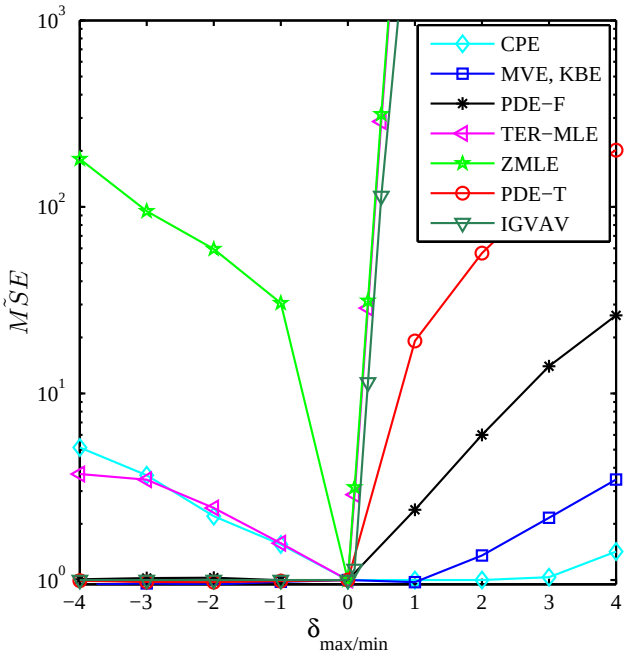

Figure 4.15: MSE versus the timing error uncertainty within the SR, Channel-II, SNR=30 dB.

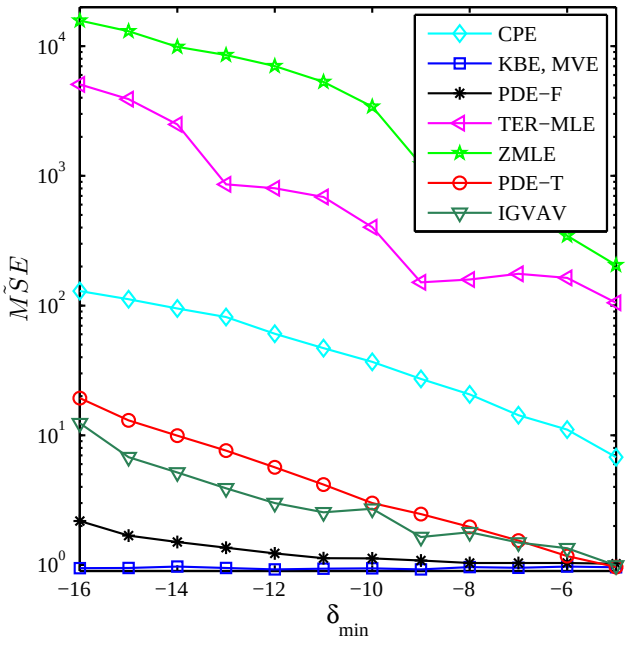

Figure 4.16: MSE versus the timing error uncertainty out of the SR but within the CP region, Channel-II, SNR=30 dB.

Table 4.3: Comparative chart of CFO estimators for OFDM systems (*: Low, **:Medium, ***:High)

Methods	Complexity	Accuracy	Bandwidth Efficiency	Convergence Speed	Estimation Range	Timing Error Robustness
CPE [17]	*	*	***	*	**	*
MVE [22], **KBE** [23]	**	*	***	*	**	***
PDE-F [52]	**	**	***	**	**	***
ZMLE [49]	***	***	*	***	**	*
TER-MLE [51]	***	***	*	***	**	***
PDE-T [71]	**	***	***	***	**	***
IGVAV [33]	**	***	***	***	*	***

4.7 Chapter Summary

In this chapter, two robust blind CFO estimators for OFDM systems over frequency selective fading channels have been presented. The PDE-T estimator is based on the power difference measurements between constant-modulus modulated subcarrirs in consecutive symbols. The PDE-T achieves a significant performance improvement by formulating the cost function in the time direction to mitigate the degradation due to the frequency selectivity of the channel. The IGVAV estimator utilizes the Viterbi and Viterbi algorithm to perform CFO estimation by measuring the phase difference among the subcarriers in consecutive symbols. The proposed iterative process of the IGVAV is very efficient because it improves the accuracy by eliminating the ICI and it helps to extend the unambiguous estimation range of the estimator. The MSE is used to assess the performance of the proposed systems using Monte Carlo simulations and the results were compared to the MSE of other well established estimators. The numerical results obtained for various channel conditions have confirmed the robustness and the superiority of PDE-T and IGVAV estimators to produce accurate estimation over short observation window in severe channel conditions. Additionally, the considered frequency synchronization algorithms have demonstrated robust performance in the presence of timing uncertainty within and outside the safe-region of the CP which adds another distinctive advantage to the PDE-T and IGVAV CFO estimators compared with other synchronization techniques. Moreover, it is worth mentioning that the PDE-T is more suitable for coarse estimation compared to the IGVAV which can be used in the fine synchronization stage due to its limited acquisition range.

Chapter 5

Symbol Timing Synchronization Schemes for OFDM Systems based on Power Difference Measurements

The focus of this chapter is to present an efficient blind symbol timing synchronization technique for OFDM systems with constant modulus constellation based on the power difference measurements approach. At the beginning, the problem of symbol timing synchronization is introduced and then the related works in the literature for blind symbol timing synchronization are discussed. A generic OFDM system model in the presence of symbol timing offsets is described. Then, the proposed symbol timing estimator based on the power difference measurements is presented. Furthermore, some implementation aspects for efficient realization of the proposed timing estimator are discussed. A low complexity and self-noise free realization for the feedforward and feedback configurations are highlighted. Simulation results are then presented for the performance evaluation of the proposed configurations for OFDM system in different channel conditions and the results are compared with other timing synchronization techniques.

5.1 Introduction

Despite the major advantages, OFDM systems are very sensitive to symbol timing synchronization errors. The reason is that STO have to be accurately estimated and compensated before the DFT process, otherwise ISI and ICI will be introduced [75,76]. Also, symbol timing jitter due to inaccurate STO estimation and correction will lead to considerable degradation in the performance of the channel estimation performed via interpolation in coherent OFDM systems [41, 77]. Symbol timing synchronization refers to the correct detection of the start of an OFDM symbol to avoid ISI and hence increase the SNR of the system. Although, OFDM systems are more tolerant to STO due to the use of CP, the tolerance range depends on the delay spread of the channel and the length of the CP [77]. Therefore, the tolerance range to STOs might be very narrow in frequency selective channels with large delay spreads. Consequently, STO estimation for OFDM systems has attracted noticeable attention by researchers [17, 18, 20, 24, 25, 40, 42–44, 47, 48, 78].

Based on the information required for synchronization at the receiver side, STO estimators are categorized as either data-aided or non data-aided [37]. Similar to the CFO estimation, various data-aided methods for STO estimation, by inserting training sequences, pilots or other types of pre-known data at the transmitter to assist timing synchronization at the receiver side, have been introduced in the literature [13, 78, 79]. Non data-aided or blind STO estimators are becoming more attractive due to their bandwidth efficiency as neither training sequences nor pilot signals are required, however channel state information might be required to assist timing synchronization [80]. As an example, the widely cited cyclic prefix estimator (CPE) [17] and the estimator proposed in [18] do not require prior knowledge of the transmitted data, however the knowledge of the channel delay spread is required. Some estimators are totally blind in the sense that they are non data-aided and do not require any channel state information [25, 47]. The accuracy, computational complexity, efficiency and estimation time are the main metrics used to assess the performance of synchronization techniques. The following section discusses several state-of-the-art methods for symbol timing synchronization in OFDM systems.

5.2 Related Work

In the literature, several blind STO estimators are developed by exploiting the correspondence between STO and interference, which results due to timing offsets. In such estimators, a cost function is constructed based on a particular interference metric and STO estimates are obtained by minimizing or maximizing the cost function. As an example, the estimator proposed in [25] minimizes the interference by minimizing the variance of the frequency-domain subcarriers after the DFT which is a monotonic function of the STO, hence it is denoted as the minimum variance estimator (MVE). The MVE approach can also be used to jointly estimate the STO and the CFO in OFDM systems as reported in [48]. Although this estimator is accurate in AWGN channels, it suffers from serious performance degradation in frequency selective channels. Similarly, another estimator has been proposed in [47] where the cost function is constructed by measuring the inter-block interference (IBI) of differentially encoded data. The IBI estimator outperforms the MVE in terms of accuracy, however it requires a large number of data blocks to deliver reliable estimates. A joint CFO and STO estimator has been proposed in [24] that minimizes the interference by maximizing the signal-to-interference-and-noise ratio (SINR) post the DFT, which outperforms the MVE and IBI estimators. However, this estimator also suffers from high error floors in frequency selective channels. Moreover, the early-late gate (ELG) configuration of the MVE [25] and the SINR [24] estimators suffers from large self-noise values demonstrated as error floors at high SNRs.

It is worth noting that most STO estimation algorithms based on minimizing the ICI/ISI such as the MVE, IBI and SINR perform well in AWGN and flat fading channels. However, such algorithms suffer from a severe performance deterioration in frequency selective channels. One of the main reasons for the degraded performance in such channels can be explained by noting that in frequency selective channels, individual subcarriers experience flat fading while the composite OFDM signal experiences frequency selective fading. Therefore, using subcarriers that are far from each other, in the frequency domain, to produce a timing synchronization metrics causes a degraded performance if the channel is changing rapidly in the frequency domain. Based on this observation and inspired by the superior performance of the CFO estimation scheme presented in the previous chapter, this chapter discusses a novel technique for symbol timing synchronization in OFDM systems based on the

power difference measurements approach.

The newly proposed timing synchronization scheme minimizes the interference (ICI and ISI) that results due STOs using two different approaches, in the first approach the power difference is minimized between adjacent subcarriers within the same OFDM symbol based on the assumption that the channel response on those subcarriers is approximately equal. In this sense, this estimator utilizes the subcarriers only in the frequency domain hence it is denoted as the power difference estimator (PDE) in the frequency domain (PDE-Frequency). The second estimator is designed by measuring the power difference between subcarriers with equal index values in two consecutive OFDM symbols. This estimator is derived based on the assumption that the channel is changing slowly in the time domain with respect to two OFDM symbols and it is denoted as the PDE-Time [81, 82].

In addition, the proposed PDE-F/T estimators are suitable for both feedforward and ELG realizations and they are totally blind because the pre-knowledge of the transmitted data or the channel state information (CSI) are not required. Unlike the estimators of [25] and [24], the proposed ELG synchronizer does not suffer from the self-noise problem. For complexity reduction and performance enhancements purposes, the low cost CPE is exploited to provide coarse initial estimates for the proposed PDE-F/T timing estimator [17]. However, the CPE is implemented as a totally blind estimator where the SNR is fixed and the channel delay spread is unknown. Moreover, a new performance metric denoted as the deviation from the safe region (DSR) is proposed to provide more informative performance assessment metric for STO estimators. The performance of the proposed PDE-F/T configurations is evaluated for various channel conditions and compared to the performance of other timing estimators.

In the next section, a generic mathematical model for OFDM systems in the presence of symbol timing offset is derived. Then, the proposed timing synchronization method for OFDM systems with constant modulus constellations using the power difference measurements approach is discussed. A comprehensive comparison with other timing synchronization schemes using different performance evaluation metrics such as MSE, BER, $P_{lock-in}$ and DSR is presented. The following blind symbol timing offset estimators are in the scope of this chapter, MVE [25,83], SINR [24] and IBI [47], where their performance is compared with the feedforward and feedback versions of the proposed PDE-F/T timing synchronizer because of their similar es-

timation strategy and comparable complexity. The full details of the cost functions formulation for all the algorithms that considered in this chapter were presented in Chapter 2 (Section 2.4.1).

5.3 System Model

Consider an OFDM system with N subcarriers modulated by a sequence of complex data symbols $\mathbf{d} = [d_0, d_1, ..., d_{N-1}]^T$. The data symbols are selected uniformly from a constellation with constant modulus such as MPSK. The modulation and demodulation processes can be implemented efficiently using an N-point IFFT and FFT, respectively as illustrated in Fig. 5.1 where P/S and S/P denote parallel to serial and serial to parallel conversion, respectively. The complex baseband OFDM symbol after the CP insertion during the lth signalling period of duration T_t second can be expressed as

$$\bar{\mathbf{x}} = [x_{N-CP},\, x_{N-CP+1},\, ...,\, x_{N-1},\; x_0,\, x_1,\, ...,\, x_{N-1}]^T. \tag{5.1}$$

The sequence $\bar{\mathbf{x}}$ of length $N_t = N + N_{CP}$ samples is upsampled, filtered and up-converted to a radio frequency centred at f_c before transmission through the antenna. The channel is composed of $L_h + 1$ independent multipath components each of which has a gain h_m and delay $m \times T_s$, where $m \in \{0,\, 1, ..., L_h\}$. The channel taps are assumed to be constant over one OFDM symbol and change slowly over two consecutive symbols, which corresponds to a quasi static multipath channel [20]. The received sequence $\bar{\mathbf{y}}$ consists of N_t samples that belong to a single OFDM symbol has the following frame structure

$$\bar{\mathbf{y}} = [c_0,\; c_1,\; ..., c_{N_{CP}-1},\; y_0,\, y_1,\, ...,\, y_{N-1}]. \tag{5.2}$$

where c_i represents the CP samples. The non CP samples $\{y_n\}$ will be referred to as the data samples.

The received sequence $\bar{\mathbf{y}}$ can be expressed as

$$\bar{\mathbf{y}} = \check{\mathbf{H}}\bar{\mathbf{x}} + \bar{\mathbf{z}}, \tag{5.3}$$

where the channel matrix $\check{\mathbf{H}}$ is an $N_t \times N_t$ Toeplitz matrix, and the noise vector $\bar{\mathbf{z}}$

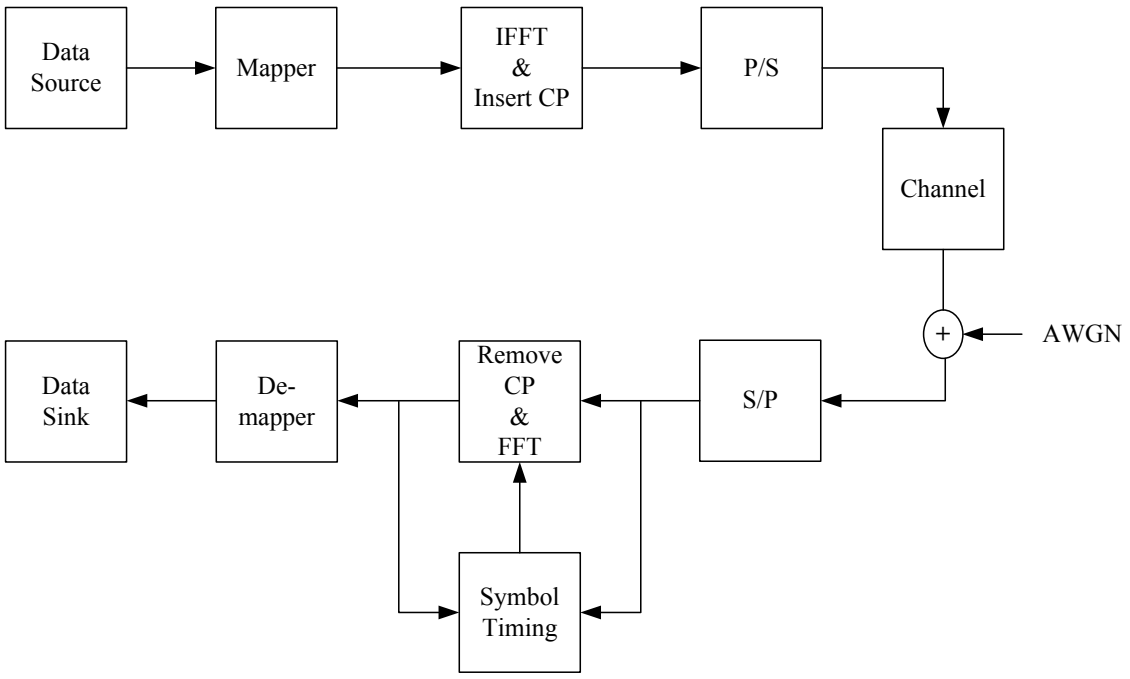

Figure 5.1: System block diagram showing the role of timing synchronization block.

is modelled as a white Gaussian noise process with zero mean and variance $\sigma_{\bar{z}}^2$.

After removing the CP samples, a sequence $\mathbf{y} = [y_0,\ y_1,\ ....,y_{N-1}]$ of length N samples is fed to the DFT to produce the frequency domain symbols,

$$\begin{aligned} \mathbf{s} &= \mathbf{W}\,\mathbf{y}, \\ &= \mathbf{H}\mathbf{d} + \eta, \end{aligned} \tag{5.4}$$

where $\eta = \mathbf{W}\,\mathbf{z}$ and $\mathbf{H}$ is the channel frequency response as described in Chapter 2.

However, the position of y_0 with respect to the received stream of samples is initially unknown, hence the sequence $\mathbf{y}$ can not be extracted from $\bar{\mathbf{y}}$ correctly. Consequently, the DFT window will have an offset $\delta \in \left\{\frac{-N}{2},\ \frac{-N}{2}+1,\ ..,\ \frac{N}{2}\right\}$. The role of the timing synchronization block shown in Fig. 5.1 is to estimate the timing offset such that the DFT window is adjusted to include samples from one OFDM symbol. Therefore, the DFT output depends on δ, which can be one of the two cases as described in the following subsections.

5.3.1 Positive Timing Error ($\delta > 0$)

In this case, the first δ data samples will be missing from the DFT window and there will be δ samples from the next OFDM symbol. Based on the value of δ, the DFT window will contain N samples that belong to the data samples of the

lth OFDM symbol, the CP and data samples from the next OFDM symbol. If we denote the sequence of samples within the DFT window as $\mathbf{v}$, the nth sample in $\mathbf{v}$ can be expressed as,

$$v_n = \begin{cases} y_{n+\delta}, & 0 \leq n \leq \kappa \\ \overrightarrow{c}_{n-N+\delta}, & \kappa < n \leq \kappa + N_{CP} \\ \overrightarrow{y}_{n-N+\delta-N_{CP}}, & \kappa + N_{CP} < n \leq N-1,\ \delta > N_{CP} - L_h \end{cases} \tag{5.5}$$

where $\kappa \triangleq N - \delta - 1$, $\overrightarrow{c}$ and $\overrightarrow{y}$ denote the CP and data samples from the next OFDM symbol, respectively.

Due to the linearity of the DFT, the sequence $\mathbf{v}$ can be decomposed into three subsequences, as depicted in Fig. 2.9 for the case of positive timing error, where each of which has $(N-\delta)$, $\min(\delta,\, N_{CP}-L_h)$ and $\max(\delta - N_{CP} + L_h,\, 0)$ non-zero samples, respectively. The three subsequences are zero-padded from the right, left or both sides to have a total of N samples, which is applied to the DFT. As an example, it can be noted from (5.5) that the first subsequence, denoted as $\mathbf{v}_1$, consists of $N-\delta$ non-zero samples aligned to the left of the DFT window, thus it should be zero-padded with δ zeros to the right [77]. Hence,

$$\mathbf{v}_1 = [v_0 = y_\delta,\ v_1 = y_{\delta+1},\ .....,\ v_\kappa = y_{N-1},\ v_{N-\delta} = 0,\ .....,\ v_{N-1} = 0]. \tag{5.6}$$

Therefore, the kth subcarrier at the DFT output due to this sequence can be expressed as

$$s_k|\mathbf{v}_1 = \frac{1}{N} \sum_{n=0}^{\kappa} \sum_{m=0}^{L_h} \sum_{i=0}^{N-1} h_m d_i e^{\frac{j2\pi i(n+\delta-m)}{N}} e^{\frac{-j2\pi nk}{N}}. \tag{5.7}$$

The last summation in (5.7) can be simplified as

$$\sum_{n=0}^{\kappa} e^{\frac{j2\pi i(n+\delta-m)}{N}} e^{\frac{-j2\pi nk}{N}} = \frac{e^{\frac{j2\pi(k-im+k\delta)}{N}} - e^{\frac{j2\pi(k+i\delta-im)}{N}}}{e^{\frac{j2\pi i}{N}} - e^{\frac{j2\pi k}{N}}}. \tag{5.8}$$

Substituting (5.8) in (5.7) and separating the variable m yields,

$$s_k|\mathbf{v}_1 = \frac{1}{N} \sum_{i=0}^{N-1} d_i e^{\frac{j2\pi k}{N}} \frac{e^{\frac{j2\pi k\delta}{N}} - e^{\frac{j2\pi i\delta}{N}}}{e^{\frac{j2\pi i}{N}} - e^{\frac{j2\pi k}{N}}} \sum_{m=0}^{L_h} h_m e^{\frac{-j2\pi im}{N}}. \tag{5.9}$$

Obviously, the last summation in (5.9) is just the channel frequency response at the ith subcarrier, i.e. H_i. Therefore, replacing the last summation by H_i and collecting

the common factors gives

$$s_k|\mathbf{v}_1 = \frac{1}{N}\sum_{i=0}^{N-1} H_i d_i \frac{1-e^{\frac{j2\pi\delta(i-k)}{N}}}{1-e^{\frac{-j2\pi(i-k)}{N}}} e^{\frac{j2\pi k\delta}{N}} e^{\frac{j2\pi(k-i)}{N}}. \tag{5.10}$$

Finally, separating the useful part of s_k from the interference terms gives,

$$s_k|\mathbf{v}_1 = \alpha_\delta \breve{H}_k d_k + \frac{1}{N}\sum_{\substack{i=0 \\ i\neq k}}^{N-1} \breve{H} d_i \frac{1-e^{\frac{j2\pi\delta(i-k)}{N}}}{1-e^{\frac{-j2\pi(i-k)}{N}}} e^{\frac{j2\pi(k-i)}{N}}, \tag{5.11}$$

where $\breve{H}_i = H_i e^{\frac{j2\pi\delta k}{N}}$ denotes the channel frequency response combined with the phase rotation introduced by the timing error, $\alpha_\delta = \frac{N-\delta}{N}$ is the attenuation due to the missing data samples, and the second term in (5.11) represents the ICI resulted from the loss of orthogonality among the subcarriers.

Similarly, the DFT output due to $\mathbf{v}_2$ can be expressed as

$$s_k|\mathbf{v}_2 = \sum_{m=0}^{L_h} \vec{h}_m \sum_{i=0}^{N-1} \left[d_i e^{\frac{j2\pi i(\delta-m)}{N}} \sum_{n=N-\delta}^{\kappa+m} e^{\frac{j2\pi n(i-k)}{N}} + \vec{d}_i e^{\frac{j2\pi i(N_{CP}+\delta-m)}{N}} \sum_{n=\kappa+m+1}^{N-1} e^{\frac{j2\pi n(i-k)}{N}} \right]. \tag{5.12}$$

The third most-right term sequence $\mathbf{v}_3$ is zero-padded only from the left side thus,

$$s_k|\mathbf{v}_3 = \frac{1}{\sqrt{N}} \sum_{n=N-\delta+N_{CP}}^{N-1} v_n e^{\frac{-j2\pi nk}{N}}, \qquad \delta > N_{CP} \tag{5.13}$$

By substituting the values of v_n with the third term in (5.5) we obtain

$$s_k|\mathbf{v}_3 = \frac{e^{\frac{-j2\pi kN_{CP}}{N}}}{N} \sum_{i=0}^{N-1} \overset{\rightarrow}{\breve{H}}_i \vec{d}_i \frac{1-e^{\frac{j2\pi(i-k)(\delta-N_{CP})}{N}}}{1-e^{\frac{j2\pi(i-k)}{N}}} \tag{5.14}$$

By defining the desired signal component as $\beta_k \triangleq \alpha_k \breve{H}_k d_k$, s_k be expressed as

$$s_k = \beta_k + \bar{s}_k|\mathbf{v}_1 + s_k|\mathbf{v}_2 + s_k|\mathbf{v}_3 + \eta_k \tag{5.15}$$

where $\bar{s}_k|\mathbf{v}_1 = s_k|\mathbf{v}_1 - \beta_k$.

As can be noted from (5.15), the timing offset attenuates the amplitude, rotates the phase of the desired data symbol and introduces both ICI and ISI. The term $\bar{s}_k|\mathbf{v}_1$ is composed of a mixture of all data symbols, except the kth data symbol of the current OFDM symbol. Therefore, this term can be considered as ICI, which is independent of β_k. The term $s_k|\mathbf{v}_2$ is composed of a mixture from all data symbols

from the current and next data symbols. Hence, this term has an ICI and ISI components. Moreover, $s_k|\mathbf{v}_2$ and β_k are correlated due to the overlap between the current and next OFDM symbols as a results of the delay spread of the multipath channel. The term $s_k|\mathbf{v}_3$ is independent of β_k but correlated with $s_k|\mathbf{v}_2$.

5.3.2 Negative Timing Error ($\delta < 0$)

The $\delta < 0$ case is different from the $\delta > 0$ case due to the CP samples located at the first N_{CP} positions before y_0. For $L_h - N_{CP} \leq \delta < 0$, δ is located in the CP region that does not contain ISI. Although y_0 will not be the first sample in the DFT window, the samples included in the DFT window belong to the ISI-free region. Thus,

$$\mathbf{v} = [v_0 = y_{N+\delta}, v_1 = y_{N+\delta+1}, ..., v_{N_{CP}+\delta} = y_0, ..., v_{N-1} = y_{N+\delta-1}]^T. \quad (5.16)$$

Due to the linearity of the DFT process, it is straightforward to show that

$$\mathbf{s} = \mathbf{H}\phi\mathbf{d} + \eta, \quad (5.17)$$

where ϕ =diag($[\phi_0, \phi_1, ..., \phi_{N-1}]$), $\phi_k = e^{\frac{-j2\pi\delta k}{N}}$. It can be noticed from (5.17) that the timing error within this region causes only a fixed phase rotation proportional to k, which can be combined with the phase rotation caused by the multipath fading channel. Consequently, the kth element of s can be expressed as

$$s_k = \breve{H}_k d_k + \eta_k, \qquad 0 \leq k \leq N-1 \quad (5.18)$$

Therefore, timing errors within this region do not introduce ISI nor ICI hence, this region is denoted as the safe region (SR) where

$$L_h - N_{CP} \leq \delta \leq 0. \quad (5.19)$$

For $\delta < L_h - N_{CP}$, the DFT output can be obtained as described for the $\delta > 0$ case however, $s_k|\mathbf{v}_1$ has $\min(N, N - |\delta| + N_{CP} - L_h)$, $s_k|\mathbf{v}_2$ has $\min(N_{CP} - L_h, |\delta| - N_{CP} + L_h)$ and $s_k|\mathbf{v}_3$ has $\max(|\delta| - N_{CP}, 0)$ non-zeros samples. While the samples of $\mathbf{v}_2$ are a mixture of samples from the current and previous OFDM symbols, the non-zero samples of $\mathbf{v}_3$ belong to the previous OFDM symbol solely. The nth sample

of $\mathbf{v}$ given that $\delta \leq N_{CP}$ can be expressed as

$$v_n = \begin{cases} \overleftarrow{y}_{n+N+\delta+N_{CP}}, & 0 \leq n \leq \max(|\delta| - N_{CP},\ 0) \\ c_{n-N+\delta}, & \max(|\delta| - N_{CP},\ 0) \leq n < \max(|\delta| - N_{CP},\ 0) + N_{CP}, \\ y_{n+\delta}, & \max(|\delta| - N_{CP},\ 0) + N_{CP} \leq n \leq N-1 \end{cases} \tag{5.20}$$

where $\overleftarrow{y}$ denotes the samples from the previous OFDM symbol.

5.4 Proposed Timing Synchronization Scheme

This section describes the proposed STO estimator for OFDM systems over frequency selective fading channels. The proposed method can be realized using two schemes depending on the assumption made on the channel conditions. Based on the signal model described in the previous section, if the first sample fed to the DFT window v_0 belongs to the samples of the SR described in (5.19) then the DFT output of the kth subcarrier during the current OFDM symbol with negligible AWGN can be expressed as

$$s_k = \breve{H}_k d_k. \tag{5.21}$$

Computing the power of the DFT output and noting that $|H_k|^2 = |\breve{H}_k|^2$ gives

$$|s_k|^2 = |H_k|^2 |d_k|^2 . \tag{5.22}$$

For CM constellations $|d_k|^2 = |d_i|^2 \triangleq S \ \forall\ i,k$ which is assumed to be normalized to one,

$$|s_k|^2 = |H_k|^2 . \tag{5.23}$$

However, if the condition for δ in (5.19) is not satisfied, ICI and ISI will be introduced. Hence, (5.21) can be expressed as

$$s_k = \beta_k + I_k, \tag{5.24}$$

where the total interference $I_k = \bar{s}_k|\mathbf{v}_1 + s_k|\mathbf{v}_2 + s_k|\mathbf{v}_3$.

It is worth noting that the variance of the interference I_k is proportional to δ [41, 77], consequently, the variance of s_k is proportional to δ as well [25]. In this chapter, a novel timing synchronization metric is deduced to estimate the STO by

minimizing the interference term I_k as described in [25], [47] and [24]. The proposed timing metric is based on the power difference measurements approach. The cost function of the proposed symbol timing estimator can be formulated by evaluating the power difference among the subcarriers in the frequency direction or the time direction as described below:

5.4.1 PDE-Frequency

If the condition for δ in (5.19) is satisfied and by assuming that the channel changes slowly in the frequency domain, then the channel frequency response over any two adjacent subcarriers is approximately equal. Thus,

$$|s_k(l)|^2 \approx |s_{k+1}(l)|^2 . \tag{5.25}$$

However, if the condition for δ in (5.19) is not satisfied, then ICI and ISI will be introduced at the DFT output due to symbol timing imperfection as given in (5.24) and the approximation given in (5.25) is no longer valid. In fact, the correlation between the power of adjacent subcarriers will be diminished because of the timing offset. Based on this observation, symbol timing estimator can be deduced by minimizing the interference term I_k via minimizing the power difference between adjacent subcarriers in the same OFDM symbol. This estimator is denoted as the power difference estimator (PDE-Frequency) and for short PDE-F. The basic idea of the PDE-F STO estimator is to select $\hat{\delta}$ such that the correlation between neighbouring subcarriers will be restored. Therefore, the cost function of the PDE-F can be constructed by accumulating the power differences between the adjacent subcarriers in the OFDM symbol. Moreover, the cost function can be smoothed by averaging the power difference measurements over L OFDM symbols. Thus, the PDE-F cost function can be expressed as

$$J_{PDE-F}(\delta, L) = \sum_{l=1}^{L} \sum_{k=0}^{N-1} \left[|s_k(l)|^2 - |s_{k+1}(l)|^2 \right]^2 . \tag{5.26}$$

The symbol timing estimates can be obtained by minimizing (5.26) with respect to δ,

$$\hat{\delta} = \arg \min_{\gamma} J_{PDE-F}(\gamma), \tag{5.27}$$

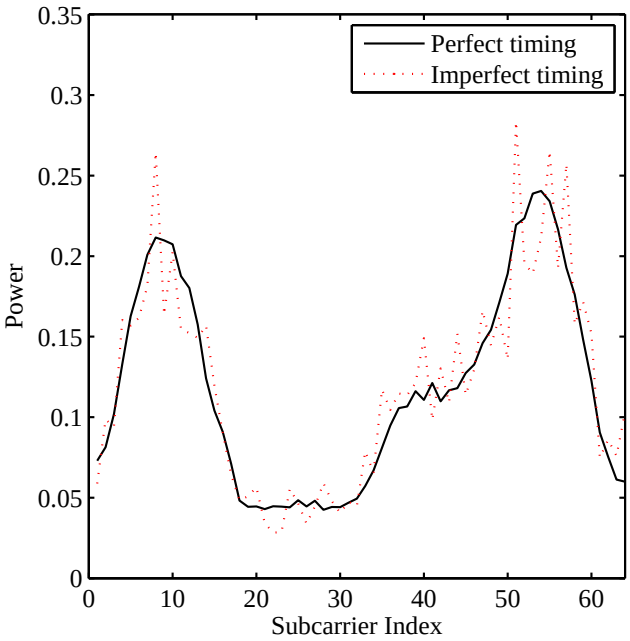

Figure 5.2: The received signal power at the output of FFT for perfect and imperfect timing information, N=64, QPSK modulation, SNR=20 dB, L=1.

where γ denotes the trial values of δ, $\gamma \in \left\{\frac{-N}{2}, \frac{-N}{2}+1, ..., \frac{N}{2}\right\}$. It is worth mentioning that the cost function of the proposed timing estimator is similar to the CFO estimator expect that the search interval is the trial timing offset.

The received signal power at the output of the DFT of OFDM system with $N = 64$ for perfect and imperfect symbol timing is shown in Fig. 5.2 (please note that the plot here is continuous just for illustration purposes). It can be clearly seen that the adjacent subcarriers are correlated in case of perfect timing ($\delta = 0$) and the assumption of having approximately the same channel response over neighbouring subcarriers is valid. However, for imperfect symbol timing ($\delta = 10$) it can be noticed that the correlation between neighbouring subcarriers no longer exists due to the ICI and ISI.

5.4.2 PDE-Time

This scheme is based on the assumption that the channel changes slowly in the time domain. Consequently, the channel frequency response at subcarrier k over two consecutive OFDM symbols is approximately constant. Therefore, the following approximation can be deduced if the condition for δ in (5.19) is satisfied,

$$|s_k(l)|^2 \approx |s_k(l+1)|^2 . \tag{5.28}$$

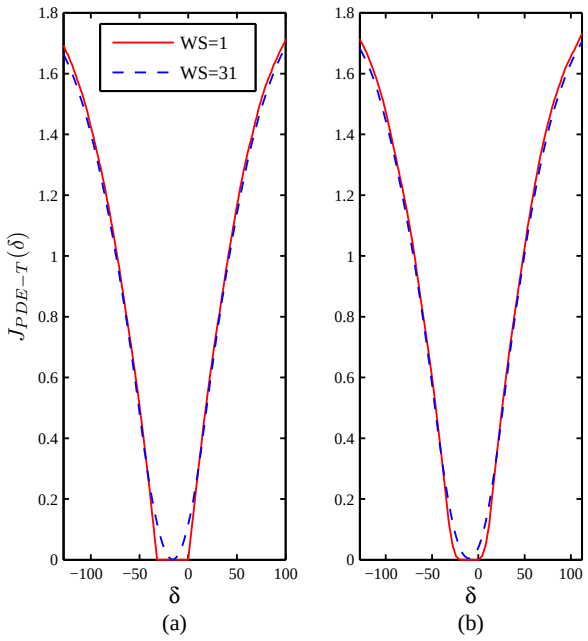

Figure 5.3: The cost function $J_{PDE-T}(\delta)$, $L = 10^4$, $N_{CP} = 32$, $N = 256$, $\sigma_z^2 = 0$ and QPSK modulation, (a) AWGN (b) Channel-II.

If the condition for δ (5.19) is not satisfied then ICI and ISI will be introduced at the DFT output due to symbol timing imperfection and the approximation in (5.28) is no longer valid. Similar to the PDE-F STO estimator, the cost function of the PDE-T can be constructed by measuring the power difference between all subcarriers with same index value over two consecutive OFDM symbols. Moreover, the cost function can be smoothed by averaging the power difference measurements over $L+1$ OFDM symbols. Therefore, the PDE-T cost function can be expressed as,

$$J_{PDE-T}(\delta, L) = \sum_{l=1}^{L+1} \sum_{k=0}^{N-1} \left[|s_k(l)|^2 - |s_k(l+1)|^2 \right]^2 . \tag{5.29}$$

The symbol timing estimates can be obtained by minimizing (5.29) with respect to δ,

$$\hat{\delta} = \arg \min_{\gamma} J_{PDE-T}(\gamma), \tag{5.30}$$

The cost function for the PDE-T timing metric is depicted in Fig. 5.3 for an OFDM system with $N = 256$ and $N_{CP} = 32$. As can be noted from this figure, in an AWGN channel, the interference is zero for $-32 \leq \delta \leq 0$, which is the SR. In frequency selective fading channels, the SR is reduced to $L_h - N_{CP} \leq \delta \leq 0$. The SR provides OFDM systems with some tolerance to timing errors since any point in the SR can be considered as the correct timing point [41].

5.5 Realization of the Proposed PDE-F/T Timing Estimator

This section presents two possible structures, feedforward and feedback, to realize the proposed timing synchronization metrics reported in the previous section. Strategies to enhance the performance and reduce the complexity of the proposed configurations are discussed.

5.5.1 Feedforward Configuration

The block diagram of the feedforward realization of the proposed symbol timing estimator is depicted in Fig. 5.4. For the PDE-F version of the proposed timing estimator, the delay D is set to 1 while D is set to N for the PDE-T case. In addition, the feedforward realization of the proposed PDE-F/T estimator can be designed by noting that:

5.5.1.1 Sliding Window Adder

The cost function for the proposed PDE-F/T estimator has a flat region which corresponds to the SR as depicted in Fig. 5.3. The values of the cost function for timing offsets in the neighbourhood of the SR are very small. Consequently, it is highly likely that one of those points will have the minimum value if the cost function is directly minimized, which leads to an estimation error. To minimize the probability of selecting such points, a sliding window adder with a particular window size (WS) can be used to eliminate this region. The window size of the sliding adder needs to be selected carefully to guarantee optimum performance for the proposed PDE-F/T estimators. The main task of the sliding adder is to select a unique minimum point in the cost function profiles in addition to the smoothing of the cost function, which is beneficial at low SNRs. In the following we discuss two proposed settings for window size of the sliding adder:

Adaptive Window Size As the length of the flat region of the PDE-F/T cost function depends on the delay spread of the channel, an adaptive setting for the window size of the sliding adder based on the knowledge of the channel order can be used to assure optimum performance for the proposed timing estimator. This

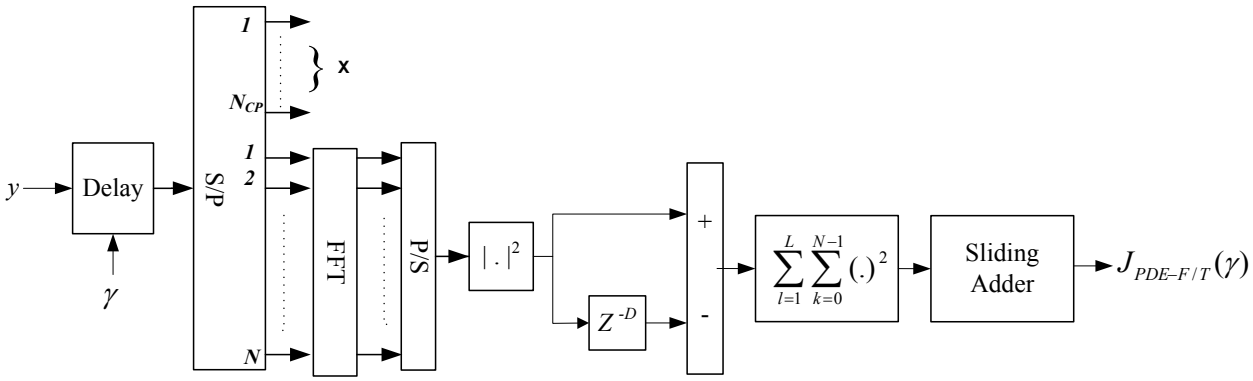

Figure 5.4: The feedforward realization for the proposed PDE-F/T timing estimators, PDE-F: D=1, PDE-T: D=N.

assumption has been made in [17] and [18] as well where the knowledge of the channel delay spread is required. Ideally, for the proposed PDE-F/T synchronization metric if the channel order is known, the WS will be set to $N_{CP} - L_h + 1$ as shown in Fig. 5.5. In practice, channel order is not known a priori and has to be estimated at the receiver. In the literature, several techniques have been proposed for channel order determination like in [84, 85]. In the numerical results section, the effect of the channel order estimation errors on the performance of the proposed estimators will be evaluated.

Fixed Window Size The optimum WS that can be used without noticeable performance degradation depends on L_h and the SNR as well. However, to make the system totally blind, a fixed WS should be used. Extensive simulation results have demonstrated that using WS=$N_{CP} - 1$ samples is a reasonable selection for various L_h and SNR values as shown in Fig. 5.5. The cost function using the sliding window adder is presented in Fig. 5.3. It is obvious that cost function after the sliding adder has a unique minimum which represents the middle sample of the SR.

5.5.1.2 Low-Complexity Implementation

Relying on exhaustive search to find $\hat{\delta}$ requires the computation of the cost function at N samples. Such approach requires significant computational power, particularly for large values of N. On the other hand, using efficient minimum search techniques might deteriorate the system performance since the cost function is not monotonic for small values of L. Therefore, the PDE-F/T will be preceded by a low complexity estimator to provide coarse estimation and the PDE-F/T will provide the final

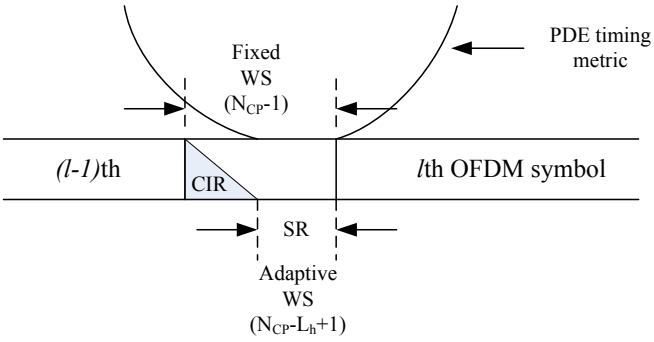

Figure 5.5: Illustration for the adaptive and fixed sliding widow adder

estimate in a similar way to the system proposed in [20]. As suggested in [20], using CPE [17] is attractive due to its low complexity. The implemented CPE considers a fixed SNR and unknown L_h and the estimation error produced by the CPE is mostly in the range [0, N_{CP}] [20]. Consequently, it should be sufficient to restrict the search space for the feedforward PDE-F/T to $|\gamma| \leq N_{CP}$.

Therefore, the PDE-F/T can be constructed as a feedforward estimator by setting an initial trial value γ, computing the power difference of the DFT output either between adjacent subcarriers in one OFDM symbol or the subcarriers in consecutive OFDM symbols, and adding the power differences for all subcarriers to form the cost function. This process is repeated for $2N_{CP} + 1$ trial values, the $2N_{CP} + 1$ values are filtered using a sliding window adder, then the trial value that corresponds to the minimum power difference value is selected as the timing offset estimate $\hat{\delta}$.

5.5.2 Early-Late Gate PDE-F/T Configuration

In the last section, the feedforward configuration of the proposed timing synchronizer is presented where the power difference measurements between the subcarriers are used as a metric to tune the synchronization parameters. In the proposed scheme the cost function need to be evaluated over all the possible synchronization points resulting into high computational complexity. Another attractive realization of the proposed timing metric is to use early-late gate feedback configuration which is a very common technique in single carrier transmission systems as shown in Fig. 5.6. Instead of evaluating the proposed metric over the whole range of possible synchronization points and searching for the minimum point, the ELG synchronizer computes the cost function early at $(\delta - \tau_\delta)$ and late at $(\delta + \tau_\delta)$ where τ_δ is the time shift relative to the timing offset δ [24, 25, 37]. Once the early and late gates'

outputs are equal, the point in the middle will be considered as the minimum point in the cost function. The difference between the two outputs forms the error signal,

$$e_{\delta}(l+1) = J_{PDE-F/T}(\hat{\delta} - \tau_{\delta}, l) - J_{PDE-F/T}(\hat{\delta} + \tau_{\delta}, l), \tag{5.31}$$

where $J_{PDE-F/T}(\delta)$ is the cost function given in (5.26) or (5.29) with $L = 1$.

Initially, the actual value of δ is unknown, hence the outputs of the early and late gates give large error values. The error signal is used to sweep the numerical control oscillator (NCO) until the error signal is ideally zero. Therefore, the timing offset estimate $\hat{\delta}$ is the middle point between $-\tau_{\delta}$ and τ_{δ}. Similar to conventional feedback synchronizers, the error signal is fed back to the NCO through a filter to update the estimated symbol timing. In the case of perfect symbol timing, the average value of the error signal is approximately zero because the early and late branches produce equal output values. Otherwise, a non-zero error signal will be produced to drive the system towards the equilibrium point. The parameter τ_{δ} can be selected based on the S-curve of the feedback synchronizer, which depends on the channel conditions [37, 86]. As an example, Fig. 5.7 presents the S-curve of the ELG-PDE-T using the same system and channel models used to generate Fig. 5.3 for τ_{δ}=8, 16 and 24.

In general, the selection of τ_{δ} has a substantial effect on the performance of the ELG-PDE-F/T. As an example, choosing $\tau_{\delta} < N_{CP}/2$ affects the system stability due to the flat region in the cost function as depicted in Fig. 5.3. Setting $\tau_{\delta} > N_{CP}/2$ increases the acquisition range of the system, however it also increases the loop self-noise because the early and late gate outputs have high variance due to the computation of $J_{PDE-F/T}(\delta \pm \tau_{\delta})$ where $\delta \pm \tau_{\delta} \notin SR$. As a consequence, the loop jitter will dominate the performance of the synchronizer. For instance, the time shift (τ_{δ}) is set to $N/4$ in [24, 25] as a compromise between the linear behaviour of the loop and the acquisition range.

A highly accurate timing synchronization loop based on the proposed synchronization metric can be realized by using the border case of $\tau_{\delta} = N_{CP}/2$ which is the most suitable choice since the acquisition range is equal to N_{CP}, and the loop self-noise is minimal in the steady state operation such that the linear behaviour of the loop is preserved. In this case, its obvious from (5.31) that the time shift between the two branches will be equal to the CP length and the FFT operation in

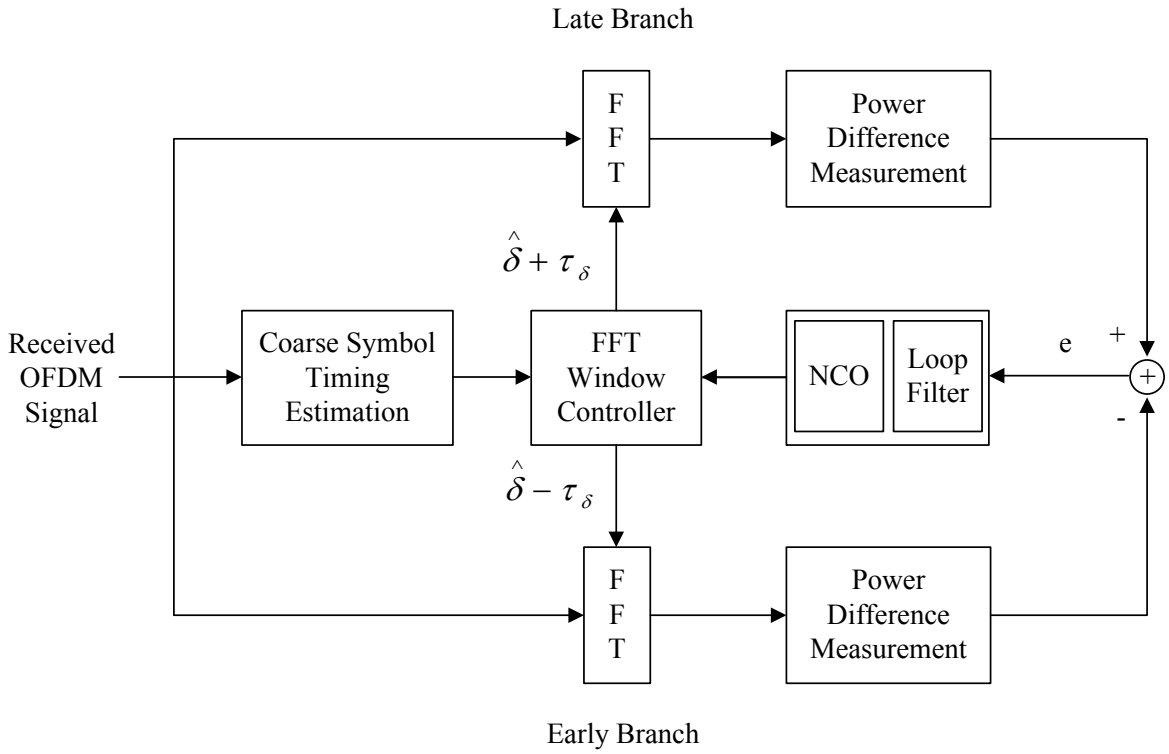

Figure 5.6: Block diagram of the proposed ELG synchronization loop based on PDE-F/T.

each branch is performed on samples belonging to the same symbol. Accordingly, a very accurate recovery for the symbol timing can be achieved based on the tolerable region in the CP. To accommodate for the limited acquisition range and to avoid the long acquisition time, the proposed synchronization loop utilizes a coarse timing synchronizer to provide the initial estimate to the synchronization loop. The acquisition range is defined as the positive slope region of the S-curve. Therefore, similar to the feedforward case, the CPE estimator of [17] can be used to provide coarse timing estimation for the ELG-PDE-F/T, which allows to design self-noise free ELG system.

The approximated linearized discrete-time model of the proposed ELG-PDE-F/T is shown in Fig. 5.8. The symbol timing is tracked by a NCO, implemented in the model as an integrator with gain k_v. The timing detector is approximated by a linear gain k_p obtained from the S-curve of the timing discriminator. The considered loop filter is the well-known proportional plus integral structure with gains k_1 and k_2 as shown in Fig. 5.6. The loop transfer function in the z-domain is given by [86],

$$L(z) = \frac{k(1 - z^{-1} - k_2 z^{-2})}{(1 - z^{-1})^2 + k(1 - z^{-1} - k_2 z^{-2})}, \tag{5.32}$$

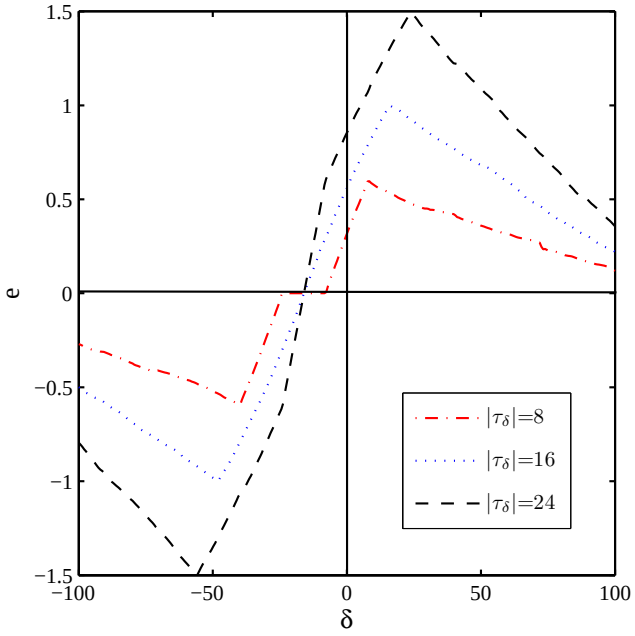

Figure 5.7: The S-curve of the proposed early-late gate estimator based on PDE-T, e and δ represent the loop and timing errors, respectively.

where $k = k_1 \times k_p \times k_v$. The discrete model of the loop can be approximated by a 2^{nd} order continous-time model,

$$L(s) = \frac{N(s)}{s^2 + 2\varsigma\omega_n s + \omega_n^2}, \tag{5.33}$$

where ς and ω_n are the damping factor and natural frequency, respectively.

$$\omega_n = \frac{1}{T_s}\sqrt{kk_2}. \tag{5.34}$$

and

$$\varsigma = \frac{1}{2}\sqrt{\frac{k}{k_2}}. \tag{5.35}$$

The loop bandwidth (B_L) is an important design parameter and for type-II loops it can be expressed in terms of natural frequency (ω_n) and damping factor (ς),

$$B_L = \frac{\omega_n}{2}(\varsigma + \frac{1}{4\varsigma}). \tag{5.36}$$

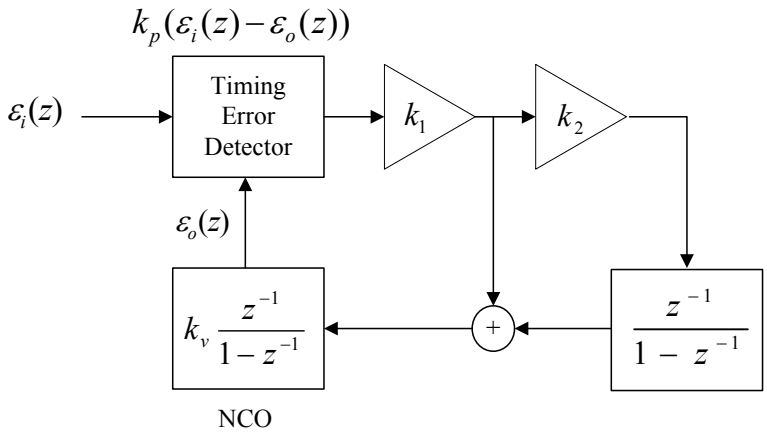

Figure 5.8: The linear discrete-time model of the early-late gate PDE-F/T synchronizer.

5.6 Computational Complexity

The complexity of the proposed timing synchronization scheme is assessed in terms of real multiplications, real additions/subtractions and the number of DFT operations. The computational complexity can be obtained by considering the cost functions given in (5.26) and (5.29) for the PDE-F and PDE-T, respectively where $|\gamma| \leq |N_{CP}|$. For the feedforward timing configuration, the PDE-F scheme requires $(2N_{CP}+1)L$ DFT operations, $3NL(2N_{CP}+1)$ real multiplications and $3NL(2N_{CP}+1)$ additions/subtractions. However, the computation required for PDE-T are $(2N_{CP}+1)(L+1)$ DFT, $N(3L+2)(2N_{CP}+1)$ real multiplications and $N(3L+1)(2N_{CP}+1)$ additions/subtractions operations.

For the ELG-PDE-F/T, the main computations required at each time step are 2 DFT operations, $6N$ real multiplications, and $6N$ additions/subtractions. Therefore, the total number of multiplications required is $4N(\log_2 N+1.5)$. Note that the complexities of the MVE [25], IBI [47] and SINR [24] are roughly $4N(\log_2 N+1.5)$, $4N(\log_2 N+3)$ and $4N(\log_2 N+4)$, respectively [24]. Therefore, the proposed PDE complexity is equivalent to the MVE and less than the IBI and SINR estimators. As a numerical example for system parameters of N=64 and N_{CP}=16, in addition to the FFT of each branch, the PDE-F/T requires 384 real multiplications for each step which is equivalent to the MVE approach. On the other hand, the IBI and SINR schemes require 768 and 1024 real multiplications, respectively. A summary of the computational complexity of the PDE-F/T timing estimator is depicted in Table (5.1).

Overall, it can be noted that the proposed system has reasonable computational

Table 5.1: The computational complexity of the PDE-F/T timing estimator

	Additions	**Multiplications**	**DFT**
FF-MVE	$3NL(2N_{CP}+1)$	$3NL(2N_{CP}+1)$	$(2N_{CP}+1)L$
FF-IBI	$4NL(2N_{CP}+1)$	$6NL(2N_{CP}+1)$	$(2N_{CP}+1)(L+1)$
FF-PDE-F	$3NL(2N_{CP}+1)$	$3NL(2N_{CP}+1)$	$(2N_{CP}+1)L$
FF-PDE-T	$N(3L+1)(2N_{CP}+1)$	$N(3L+2)(2N_{CP}+1)$	$(2N_{CP}+1)(L+1)$
ELG-MVE	$6N$	$6N$	2
ELG-IBI	$8N$	$12N$	2
ELG-SINR	$14N$	$16N$	2
ELG-PDE-F/T	$6N$	$6N$	2

complexity when it is compared to other feedforward and feedback synchronizers such as the ones proposed in [25], [83] and [47]. The complexity of the proposed feedforward PDE-F/T and the feedforward version of the estimator proposed in [47] is mainly determined by the averaging factor L. However, the PDE-F/T has the advantage that using $L = 1$ is sufficient to provide reliable estimates even for severe channel conditions.

Obviously, the complexity of the feedforward configuration for most state-of-the-art blind timing synchronizer discussed previously is dominated by the large number of FFT trials as the cost function of the timing metric requires to forth from time to frequency domain [24]. One possible strategy to reduce the complexity is to use the feedback configuration [24, 25] or provide some coarse estimation that allows to restrict the search space for the timing offsets within few samples as discussed in the previous section. Although this would reduce the number of FFT trials for the feedforward version however, the computational complexity of the feedforward frequency domain timing synchronizers is still high. Therefore, using adaptive search techniques instead of the line search procedure with the exploitation of highly efficient run-time configurable FFT architectures might be beneficial to reduce the complexity of the feedforward version and that would need more investigation in the future.

5.7 Numerical Results

Monte Carlo simulations are used to evaluate the performance of the proposed PDE timing estimators over frequency selective multipath fading channels. The performance of the proposed estimators is compared to the performance of the CPE [17], MVE [25] and IBI [47] estimators. The OFDM system considered in this chapter has

$N = 256$ and $N_{CP} = 32$. All data symbols are QPSK modulated with symbol rate of 4.17 kb/s. The multipath fading channel models described in the previous chapter are used. The channels are assumed to be slowly time varying unless it is otherwise specified. In each simulation run, 10^6 independent OFDM symbols are transmitted, and the timing error δ is uniformly distributed over the range $[-\frac{1}{2}N, \frac{1}{2}N]$.

The following results demonstrate the performance of feedforward timing estimator with sliding adder of adaptive size. Therefore, the channel order is assumed to be known where $\hat{L}_h = L_h$ and the window size of the sliding adder is adaptively selected. This setting allows the timing synchronizer to estimate the start of the data samples of the symbol. The MSE is used as a metric to compare the accuracy of the proposed schemes with other timing estimators where

$$MSE = E[(\hat{\delta} - \delta)^2]. \tag{5.37}$$

The MSE performance of the proposed PDE-F/T timing estimators compared with CPE and MVE over AWGN channels is presented in Fig. 5.9. As depicted in the figure, all the considered timing estimators perform well over AWGN channels and the MSE decreases, approximately, linearly with the increase of SNR in dB except for the CPE where MSE degradation is observed at low SNRs. Also, it can be noted that the PDE-F and MVE have almost equivalent performance over the entire range of SNR. However, the PDE-T outperforms the other considered methods at moderate and high SNRs.

To evaluate the performance over frequency selective multipath fading channels, the Channel-I model is used and the MSE performance of the considered timing estimators is presented in Fig. 5.10. It can be noted that the proposed estimators (PDE-F and PDE-T) substantially outperform the MVE and CPE for the entire range of SNRs which emphasizes the efficiency of the proposed technique over such channels. Both MVE and CPE suffered from severe performance deterioration which appears as an error floor at high SNRs. It is clear that the CPE has demonstrated more sensitive performance in frequency selective fading channels compared with the other considered estimators.

The MSE performance of the proposed timing estimators is investigated in time varying mobile channel scenarios. We consider Channel-I and Channel-III model with various maximum Doppler shift (f_d) values. The MSE is evaluated versus the

maximum Doppler shift (f_d) for SNR= 30 dB over both channels and the results are presented in Fig. 5.11. Although some degradation in the MSE performance can be observed at high Doppler values, the proposed timing estimators still perform remarkably better than the MVE and the CPE for the entire Doppler's range considered. In addition, it is clear that PDE-F outperforms PDE-T for high Doppler shift values.

The effect of error in the channel order estimate on the performance of the timing estimator is presented in Fig. 5.12. As an example, the MSE performance of the PDE-T timing estimator is simulated in the case of Channel-I with no Doppler shifts. As can be noted from this figure, the proposed estimator managed to deliver reliable estimates even for channel order estimation errors of 15%. Practically, channel order estimation can be accomplished with error percentages much smaller than 15% [84, 85].

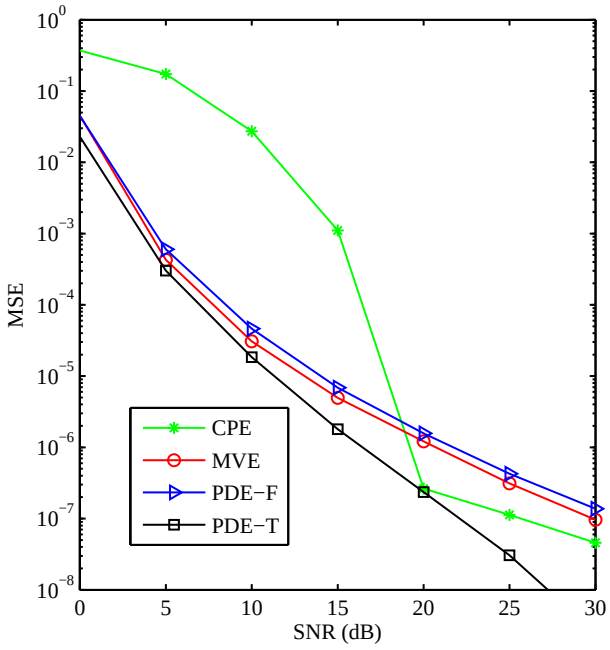

Figure 5.9: The MSE performace of the CPE, MVE, PDE-F and PDE-T timing estimators over AWGN channels.

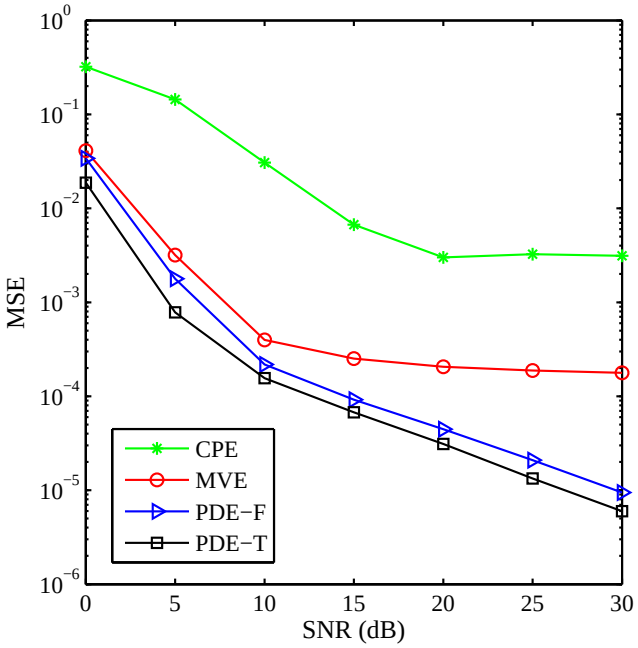

Figure 5.10: MSE performance of the symbol timing estimators over frequency selective fading channel, Channel-I.

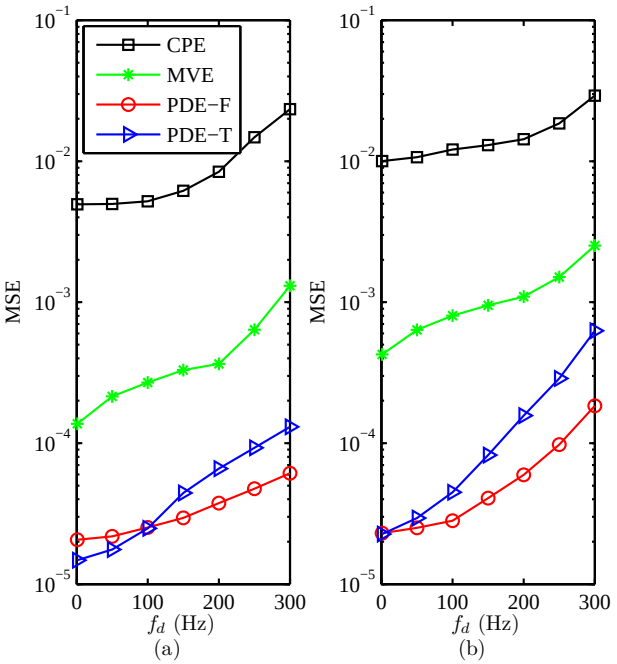

Figure 5.11: MSE of the symbol timing estimate over mobile fading channel: (a) Channel-I, (b) Channel-III, SNR=30 dB.

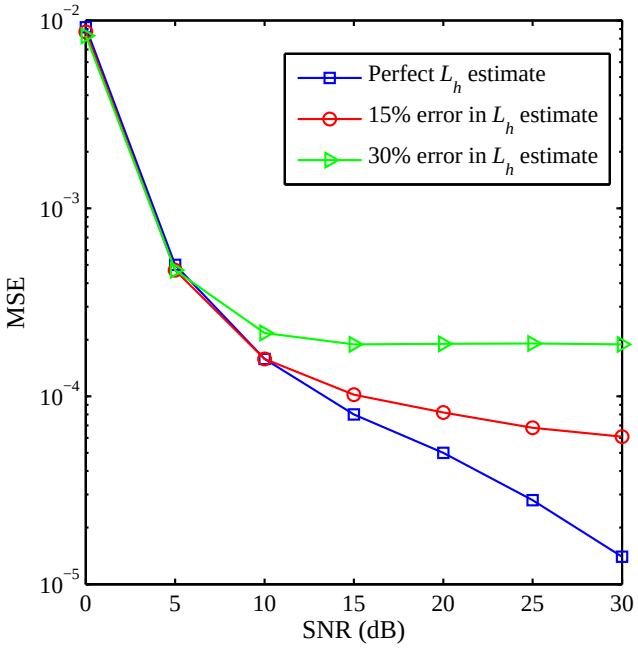

Figure 5.12: The effect of errors in the channel order estimate, L_h, on the MSE performance of PDE-T timing estimator.

The performance of feedforward PDE-F/T timing estimators with sliding adder of fixed window size is demonstrated in the following results. The channel order is assumed to be unknown and the sliding adder window size is fixed at $N_{CP} - 1$ samples. This allows to realize a totally blind timing estimator based on PDE-F/T synchronization metric. The estimates of the proposed PDE-F/T timing estimators are adapted to identify the tolerable region rather than the start of the symbol in a similar way to the IBI estimator reported in [47]. In this case, the performance of the considered synchronizers is evaluated in terms of the widely-used the lock-in probability ($P_{lock-in}$) [18], which is the probability that the timing error is within the SR (lock-in region). Moreover, a new metric is proposed as an alternative for the conventional MSE because the MSE does not take into account the presence of the SR. The new metric measures the deviation of the estimation error from the SR, hence it is denoted as the deviation from the safe region (DSR),

$$DSR = \frac{1}{K}\sum_{k=1}^{K} e_{\delta}^{2}(k) \tag{5.38}$$

where K is the number of OFDM symbols considered in the simulation experiment,

k is the estimate index, and

$$e_\delta = \begin{cases} \hat{\delta} - \delta, & \hat{\delta} - \delta > 0 \\ 0, & -N_{CP} + L_h \leq \hat{\delta} - \delta \leq 0 \\ \hat{\delta} + N_{CP} - L_h, & -N_{CP} + L_h > \hat{\delta} - \delta \end{cases} . \tag{5.39}$$

As it can be noted from (5.39), the DSR is equal to the MSE for $e_\delta \geq 0$, however the MSE is very pessimistic for negative timing errors.

The difference between the MSE and DSR metrics is presented in Fig. 5.13 for the CPE estimator with and without the knowledge of $\hat{L}_h = L_h$ and $\hat{L}_h = 0$, respectively. As it can be noted from this figure, the MSE for the $\hat{L}_h = L_h$ case is very pessimistic for both $L = 1$ and 2 cases. Obviously, the CPE performs very poorly for $\hat{L}_h = 0$ regardless the metric or the value of L.

The $P_{lock-in}$ performance of the proposed PDE-F/T timing estimators compared with MVE and IBI estimators is presented in Fig. 5.14 for $L = 1$ and 2 over Channel-II. As it can be noted from this figure, both PDE-F and PDE-T significantly outperform the other considered estimators where $P_{lock-in} \sim 1$ for SNR=4 dB and SNR=8 dB, respectively. Thus, using $L = 1$ is sufficient for the proposed PDE-F/T timing estimators. The MVE outperforms the IBI however it suffers from an error floor at high SNRs. All systems have demonstrated noticeable improvement by using an averaging factor $L = 2$, however the IBI improvement was the highest.

The DSR performance of the PDE-F/T, MVE and IBI timing estimators is presented in Fig. 5.15 for $L = 1$ and 2 over Channel-II. It can be noted from this figure that the MVE is very sensitive to the frequency selectivity of the channel, which is demonstrated by high error floors at SNR$\geq$ 16 dB. The IBI demonstrated some DSR improvement by increasing the SNR, however the improvement is marginal. Unlike the MVE and IBI, the PDE-F/T estimators demonstrated significant DSR reduction by increasing the SNR. The improvement gained by incorporating an averaging factor $L = 2$ was insignificant for the MVE, while it was significant for the PDE-F/T and IBI.

To assess the robustness of the proposed timing estimators in severe conditions, we consider the performance of PDE-T over Channel-III model with various maximum Doppler shift values. Fig. 5.16 shows the DSR performance as a function of the Doppler shift (f_d) for SNR = 10, 15 and 20 dB, the averaging factor $L = 1$

and 2. This figure clearly confirms the robustness of the proposed estimator as it managed to perform fairly well at low SNRs with high Doppler shifts, even without incorporating any averaging. As an example, at SNR = 15 dB, the DSR of the timing estimation is about two samples at $f_d = 200$ Hz using $L = 1$, and less than one sample using $L = 2$. For the 20 dB case, the proposed system provides reliable DSR values for the entire range of f_d even without averaging.

The performance of the proposed PDE-F/T estimators in the presence of CFO is evaluated over Channel-III. The DSR versus the normalized CFO (ϵ) for SNR=10 dB is presented in Fig. 5.17. This figure clearly depicts the robustness of the proposed timing estimators in the presence of CFO particularly the PDE-T. For CFO ~ 0.5 and without averaging, the DSR value is less than 3 and 1 samples for the PDE-F and PDE-T at SNR=10 dB, respectively.

To assess the effect of initial timing errors on the performance of CFO estimation, the MSE performance of the CFO estimators considered in Chapter 4 is evaluated versus DSR over Channel-II and Channel-III for SNR=30 dB as illustrated in Fig. 5.18. The timing error is uniformly distributed in the range $[\delta_{\min}, \delta_{\max}]$ and measured in terms of DSR. This figure demonstrates the superior robustness of the PDE based CFO estimators to the timing errors. In particular, the PDE-T CFO estimator tolerates wide range of timing errors where the MSE is in the order of 10^{-4} for DSR $\leq 10^1$ samples. In contrast, the ZMLE and TER-MLE estimators have demonstrated sensitive performance to the timing errors even for low DSR values. In addition, as the CPE has been used before the proposed PDE timing estimator, the coarse estimation will help to reduce the CFO. Therefore, it is expected that the coupling effect between the two synchronization process will have insignificant effect on their performance as revealed in Fig. 5.17 and Fig. 5.18.

The blind PDE synchronization schemes that require constant modulus constellations can be applied to OFDM systems with QAM modulation by averaging the cost function over multiple symbols. The $P_{lock-in}$ and DSR versus the averaging factor (L) for the PDE-T with 16-QAM signalling over Channel-II is shown in Fig. 5.19 for SNR=10 and 20 dB. As revealed from this figure, averaging over the symbols can be used as remedy to apply the PDE-T for such systems. In fact, there are some other approaches that can be exploited to extend the PDE to QAM systems. For example, the PDE can be implemented as a "decision directed estimator" or by partitioning the QAM constellation into subset of constant modulus constellations.

However, such techniques require "relatively" high SNRs, and their computational complexity is higher. Nevertheless, the constant modulus condition is not an obstacle for applying the proposed PDE for OFDM systems with QAM signalling as discussed below.

In what follows, we demonstrate how the proposed PDE-T timing estimator can be applied to wireless OFDM systems based on QAM modulation and discuss the advantages of incorporating the PDE-T in future standards. The proposed timing estimators presented in the pervious sections are derived to be totally blind and the STOs are estimated from only the data symbols. However, the proposed methods can efficiently exploit the preambles or pilots available in most of the current OFDM standards. The pilots and reference symbols are usually have constant modulus constellations [7, 9]. For example, the downlink of IEEE 802.16 Wireless MAN standard that is commercially known as WiMAX has constant modulus reference symbols. However, these symbols are arranged as two consecutive OFDM symbols each of which consists of 256 subcarriers. The second symbol has a CP of 64 samples [[9], Fig. 207]. The first OFDM symbol has only 64 subcarriers modulated by the reference symbols and the remaining subcarriers are modulated by zeros. The second OFDM symbol is similar to the first one except that a 128 subcarriers are modulated by the reference symbols. Another major difference between the two symbols is that the subcarriers of the first OFDM symbols have 3 dB power boost. Consequently, the populated 128 subcarriers can not be utilized to implement the PDE-T. Alternatively, the 128 null subcarriers can be used to implement the PDE-T because the PDE-T requires that $|d_k(l)|^2 = |d_k(l+1)|^2$, which is satisfied for the null subcarriers.

To evaluate the performance of the PDE-T for WiMAX systems, the data subcarriers are modulated using QAM with modulation order M= 16, 64. The CP length is set to $N/4$, which corresponds to 64 samples. The system performance is assessed in terms of the bit error rate (BER) under Channel-II conditions. Moreover, a special channel model with delay spread that spans the entire CP region is considered as well. This channel has the same tap gains as Channel-II however the taps' delays are [0 16 31 46 64]. This channel corresponds to severe case scenario where the SR has only one sample. The BER of the WiMAX system using the above mentioned channels with 16 and 64-QAM is depicted in Fig. 5.20 (a) and (b), respectively. As it can be observed from the figure, the BER degradation due to

the timing errors introduced by the PDE-T is negligible for Channel-II, and a slight BER degradation was observed at SNR>30 dB for the severe channel case.

Furthermore, the Stanford University Interim (SUI) channel models [87] have been selected as WiMAX operating environments. The set of six typical channels were used to simulate the IEEE 802.16 channel models. Each model has three taps and is characterized by a relative delay, relative power, and maximum Doppler shift. Each SUI channel corresponds to a particular terrain category; A, B, and C. Type A include SUI-5, 6 (hilly, heavy tree density). Type B include SUI-3, 4 (moderate tree density) and type C include SUI-1, 2 (flat, light tree density). All SUI channel models have maximum Doppler shift below 0.5 Hz, except the SUI-5 which has 2.5 Hz. Therefore, in this case the radio channel can be considered as slowly time varying.

The BER of the WiMAX system using SUI-5 and SUI-6 channels with 16 and 64-QAM is depicted in Fig. 5.21 (a) and (b), respectively. The maximum delay spread of the SUI-5 channel is less than the CP length and spans 70% of the CP. While the delay spread of SUI-6 exceeds the CP length thus the system will operate in the presence of ISI. As can be observed from the figure, the BER degradation due to the timing errors introduced by the PDE-T is negligible for SUI-5, and a slight BER degradation was observed at high SNR for the case of SUI-6 channel.

As it can be noted in the above discussed case, we exploited some of the constant modulus pilot/reference subcarriers to implement the PDE-T. However, since the PDE-T does not require any pilots, future and updated versions of OFDM standards can replace the pilot and reference symbols with data symbols, given that other blind techniques are used for frequency offset and channel estimation. Consequently, the capacity of such systems will increase significantly.

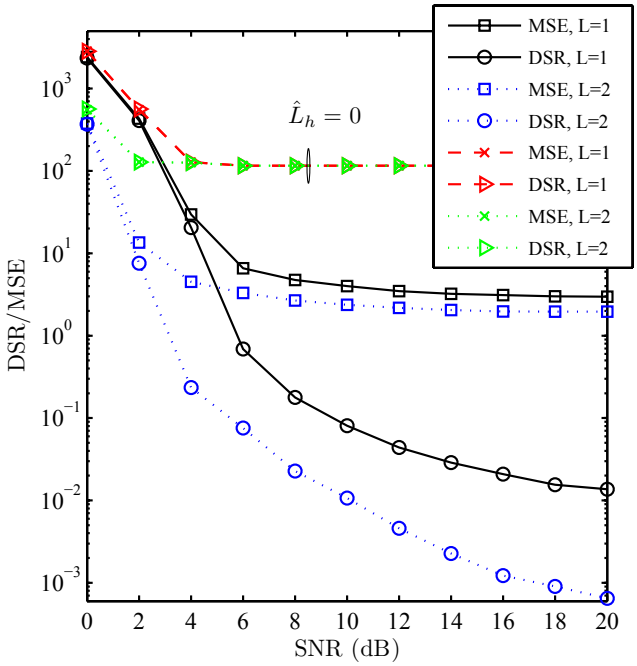

Figure 5.13: The DSR and MSE of the CPE over Channel-II, $\hat{L}_h = L_h$ and $\hat{L}_h = 0$.

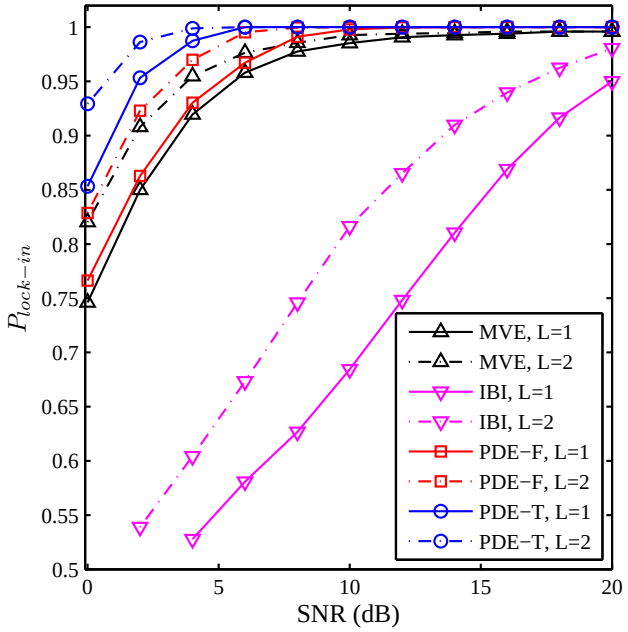

Figure 5.14: $P_{lock-in}$ of the feedforward PDE-F/T, MVE and IBI versus SNR over Channel-II, L = 1, 2.

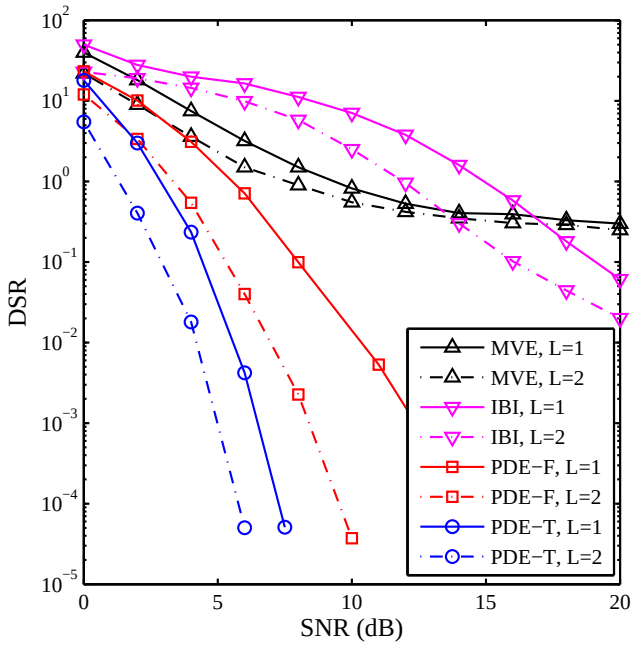

Figure 5.15: DSR of the feedforward PDE-F/T, MVE and IBI estimators versus SNR over Channel-II, L = 1, 2.

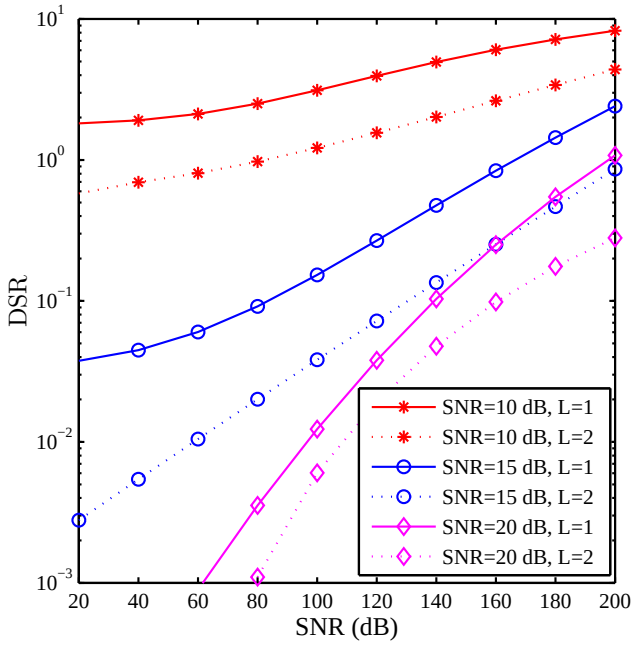

Figure 5.16: DSR of the feedforward PDE-T versus f_d for various SNRs over Channel-III, $|\tilde{\delta}| \leq N_{CP}$, L = 1, 2.

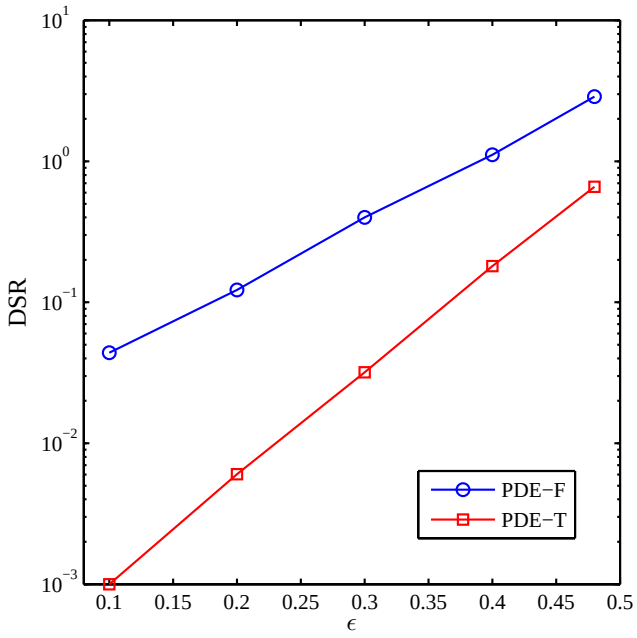

Figure 5.17: DSR of the feedforward PDE-F and PDE-T versus CFO for over Channel-II, L = 1, SNR=10 dB.

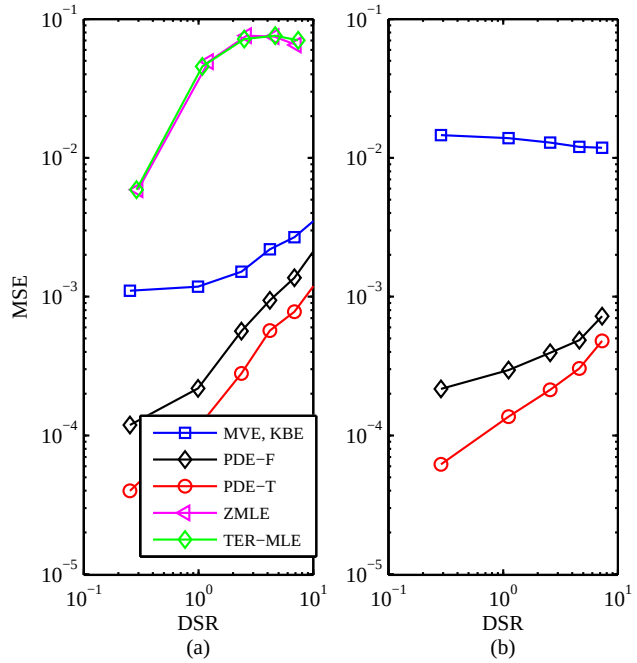

Figure 5.18: MSE versus DSR for different CFO estimators, L=1 and SNR=30 dB (a) Channel-II (b) Channel-III.

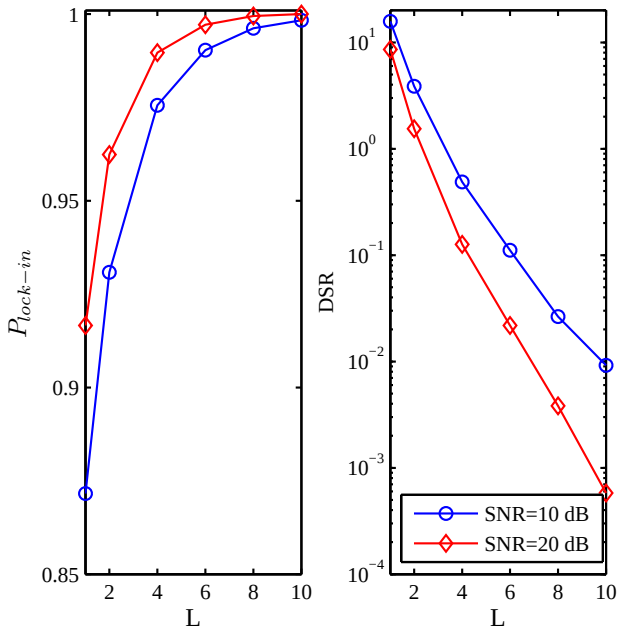

Figure 5.19: DSR versus averaging factor for the PDE-T feedforward over Channel-II with 16-QAM.

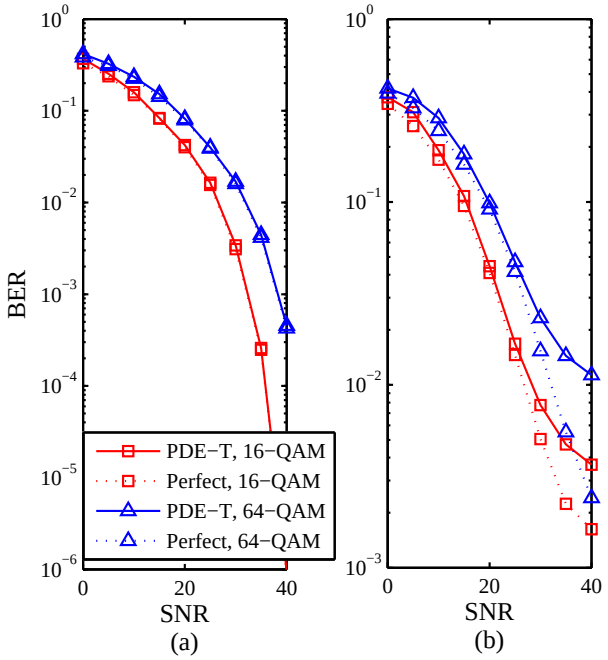

Figure 5.20: The BER performance of the PDE-T for 16-QAM and 64-QAM, (a) Channel-II, (b) The severe case of Channel-II.

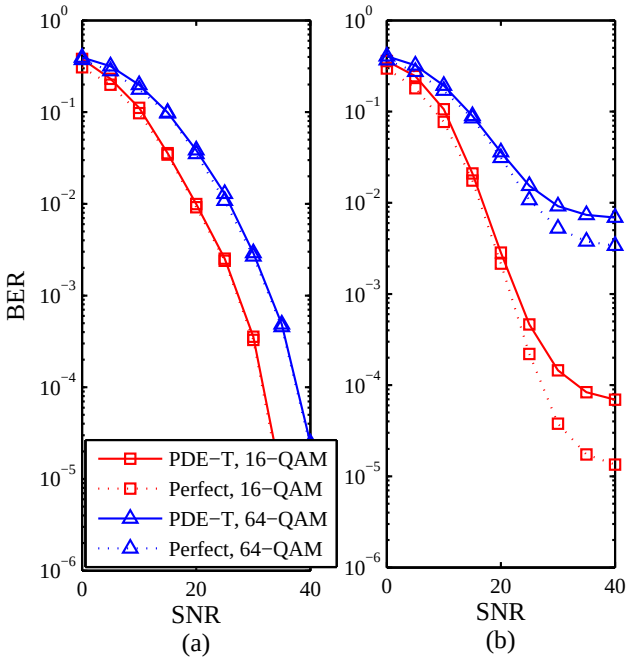

Figure 5.21: The BER performance of the PDE-T for 16-QAM and 64-QAM, (a) SUI-5, (b) SUI-6.

To demonstrate the efficiency of the proposed self-noise free configuration for the ELG version of the PDE timing estimator, we simulated both the conventional and proposed configuration for PDE-T over Channel-II with SNR=30 dB. The conventional configuration for the ELG synchronizer uses $\tau_\delta = N/4$ as suggested in [25] and [24]. The average probability of making a timing error of δ sampling periods, $P_e(\delta)$, is measured for both configurations as depicted in Fig. 5.22 for various B_L values. It is obvious that the conventional configuration has considerable timing errors outside the SR due to the symbol timing jitter which dominates the system performance. Decreasing the B_L will reduce the probability of timing synchronization errors as depicted in this figure, however, even for $B_L = 1/100$ the conventional configuration still has timing errors outside the tolerable region. Thus, the feedback synchronizers of [25] and [24] suggest to use loop bandwidth of $B_L < 1/100$. Using the proposed self-noise free configuration, the symbol timing jitter is significantly reduced and the PDE timing synchronization loop offers accurate symbol timing compared with the conventional configuration. The estimates are mainly within the SR which allows for timing offsets to the left (i.e. within the guard interval) to occur without any loss of performance. It is clear that the proposed scheme has considerable lower probability of synchronization error which allows to use higher B_L values.

Using the proposed self-noise free configuration for the ELG version of the PDE-F/T, both the $P_{lock-in}$ and DSR are expected to demonstrate quite well even at low SNRs. Consequently, the performance of the ELG PDE is investigated over Channel-III model. For fair comparison, the MVE system implemented in this work used the same τ_δ values and was preceded by a CPE estimator. Therefore, the performance difference between the MVE and PDE timing estimators is solely due the different metrics used. It is worth noting that the acquisition time for such loops is in the order of $1/B_L$ symbols [37]. In Fig. 5.23, the $P_{lock-in}$ of the MVE, PDE-F and PDE-T is presented versus SNR for $B_L = 1/10$ and $1/16$. It can be noted from this figure that $P_{lock-in}$ of the PDE-F/T takes values above of 0.8 for $B_L = 1/16$ even at SNR = 0 dB. For $B_L = 1/10$, the PDE-F/T experienced minor performance deterioration for SNR$\leq$4 dB, while $P_{lock-in}$ of the PDE-F and PDE-T was almost 1 for SNR$>$ 8 and 4 dB, respectively. It is obvious that the MVE suffers from an error floor for $B_L = 1/10$ and the $P_{lock-in} < 1$ even for high SNRs.

The DSR performance of the proposed ELG PDE-F/T and MVE is presented in Fig. 5.24. As can be noted from this figure, the DSR of the ELG-PDE is considerably less than MVE. Moreover, using $B_L = 1/16$ offers DSR values of about 9 and 3 samples at SNR = 0 dB for the PDE-F and PDE-T, respectively. The above results for the feedback synchronization loop based on the self-noise free configuration of the ELG have clearly demonstrated the significance of this approach in terms of performance and reduction of the acquisition time.

Finally, the proposed timing synchronization loop is coupled with CFO estimator in order to investigate the mutual coupling effect between the synchronization processes. The PDE-T synchronization metric has been used for the timing and CFO estimators. The MSE performance of CFO estimator is depicted in Fig. 5.25 for different CFOs. It is obvious that timing errors of the synchronization loop have trivial effect on the performance of the CFO estimator for CFOs ≤ 0.2. For higher CFOs, the performance of the PDE-T deteriorates with an error floor at high SNRs. However, as mentioned before, using the CPE as a coarse estimator will reduce the effect of CFO on the proposed synchronization loop.

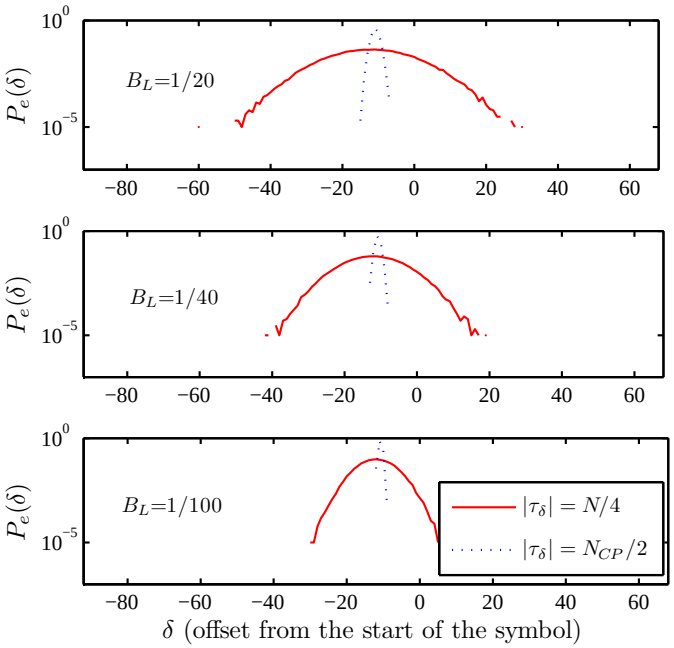

Figure 5.22: $P_e(\delta)$ of the conventional and proposed ELG configurations for the PDE-T over Channel-II, SNR=30 dB.

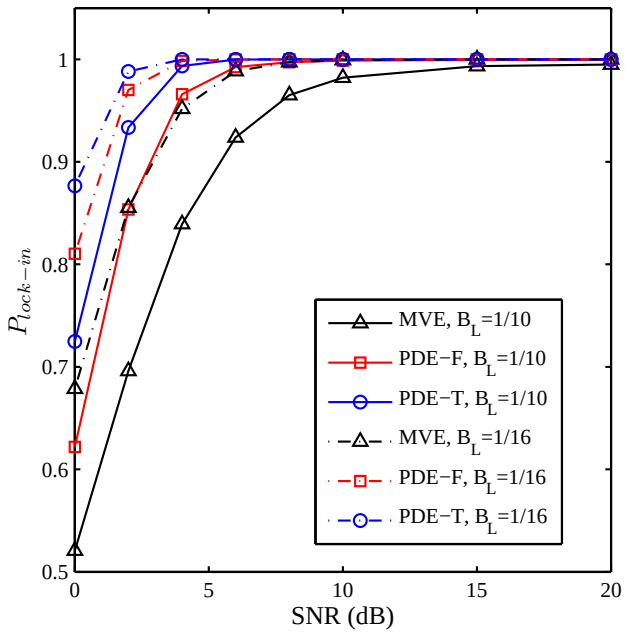

Figure 5.23: $P_{lock-in}$ of the ELG MVE and PDE-F/T using different B_L values over Channel-III.

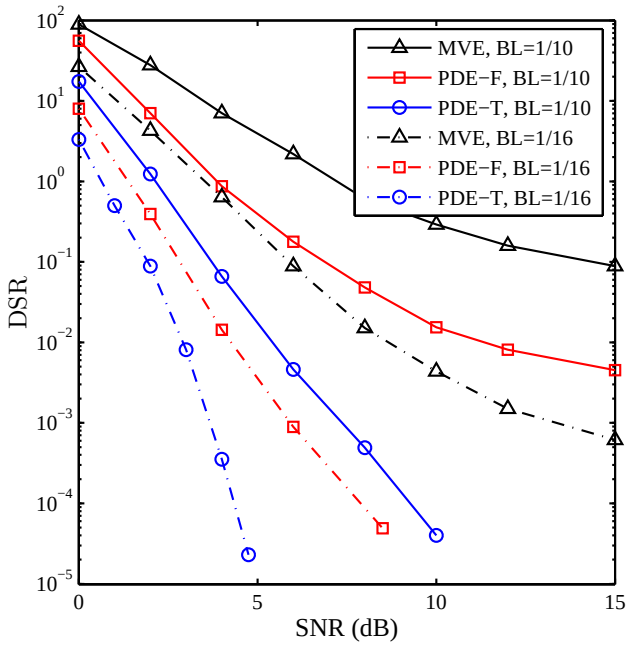

Figure 5.24: The DSR of the ELG MVE and PDE-F/T using different B_L values over Channel-III.

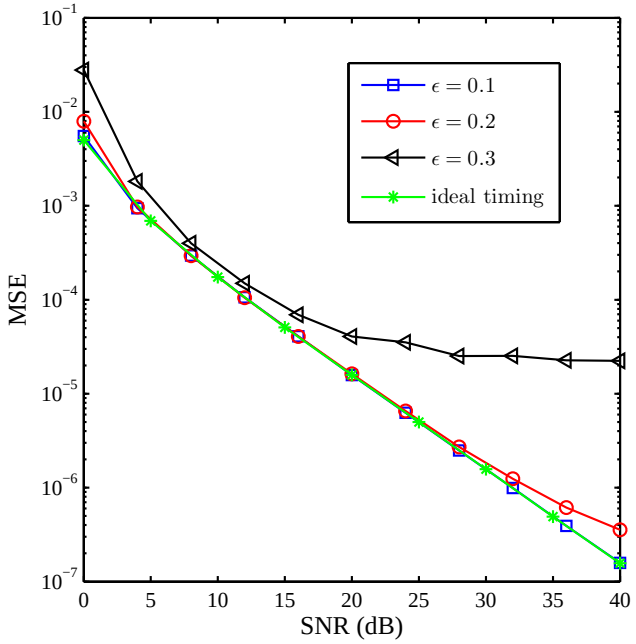

Figure 5.25: MSE versus SNR for the PDE-T CFO estimator coupled with ELG PDE-T timing synchronizer.

5.8 Chapter Summary

In this chapter, a novel blind symbol timing synchronization method for OFDM systems with constant-modulus signalling based on the power difference measurements approach was presented and evaluated. The proposed scheme requires no training overhead making it suitable for bandwidth-limited wireless systems. A totally blind feedforward configuration for the proposed timing estimator has been discussed. In addition, the proposed technique was formulated as synchronization loop based on early-late fashion to achieve efficient implementation. The performance of the proposed synchronizers was evaluated via Monte Carlo simulations over different types of channel models and compared with other well-established synchronization methods. The results have confirmed that the proposed methods substantially outperform the other considered synchronizers over frequency selective fading channels for the entire range of SNRs. Furthermore, the self-noise free realization has added considerable improvement to the performance of the proposed synchronization loop in terms of accuracy and acquisition time.

Chapter 6

Efficient Symbol Timing Recovery and Frequency Synchronization Schemes for MIMO-OFDM Systems

This chapter presents an efficient symbol timing recovery and frequency synchronization methods for MIMO-OFDM systems with constant-modulus constellation using the power difference measurements approach developed in the previous two chapters. The chapter begins with an introduction and then discusses the key methods for symbol timing synchronization and CFO estimation in MIMO-OFDM systems. Then, the signal model for MIMO-OFDM transmission system is presented and the effect of synchronization errors is highlighted. Subsequently, the PDE approach for symbol timing recovery and CFO estimation in MIMO-OFDM systems over frequency selective fading channels is introduced. Finally, Monte Carlo simulation results are presented for the performance assessment of the PDE schemes for MIMO-OFDM systems. To demonstrate the robustness and efficiency of the proposed synchronization techniques, different channel conditions and PDE configurations are considered and compared with other state of the art techniques.

6.1 Introduction

It is well known that multiple transmit and receive antennas formed as MIMO configuration is a key technology for future high data rate wireless communication systems that can increase the capacity of wireless systems in addition to providing reliable high data rate transmission [88]. In MIMO systems, independent data streams share the same frequency bands and time slots, therefore the spectral efficiency is improved significantly [89].

The early research on the MIMO configuration were based on the assumption of flat fading channels. OFDM is a multicarrier modulation technique that employs orthogonal subcarriers. Besides its bandwidth efficiency, it can efficiently deal with multipath problems. For wideband transmission, the combination of MIMO configuration with OFDM is vital to overcome the frequency selectivity and time dispersion introduced by multipath propagation channels. MIMO-OFDM transforms a frequency selective MIMO channels into a number of flat fading MIMO channels on each subcarrier [89]. Consequently, MIMO-OFDM is currently considered as the state of the art physical layer technology for several next generation high data rate wireless networks, e.g. broadband wireless access WiMAX IEEE 802.16e standard [9], high-throughput wireless LAN IEEE 802.11n [8] and 3GPP long term evolution (3GPP-LTE) [90].

Similar to single-input single-output (SISO) OFDM systems, synchronization errors are still a major impairment for MIMO-OFDM systems [11, 91]. The synchronization errors destroy the orthogonality between different subcarriers and cause ICI and ISI which consequently introduce severe degradation to the system performance if the STO and CFO not properly compensated [92]. Therefore, precise synchronization is indispensable for reliable transmission using MIMO-OFDM scheme. Hence, the time and frequency synchronization problem for MIMO-OFDM based systems has been widely investigated in the literature. The following section surveys some well-established methods to achieve time and frequency synchronization in MIMO-OFDM systems and highlights their features and limitations.

6.2 Related Work

In the literature, most of the existing methods for MIMO-OFDM systems are mainly based on the cyclic property of the transmitted signals, which may be induced by the transmission of training sequences with repetition structures. The majority of these techniques are based on extending SISO techniques which usually require major modifications and special design of the training sequences in order to adapt them to MIMO-OFDM systems. As an example, extensions of Schmidl's technique in [13] are discussed in [93] and [94] where orthogonal polyphase and time-orthogonal training sequences are used, respectively. In these methods, the symbol timing and CFO estimation are carried out using the autocorrelation for the repeated patterns of the received preamble [95]. Although the performance of the symbol timing and CFO estimators is improved compared with the SISO case because of the spatial diversity, these approaches still have limited accuracy in frequency selective fading channels which makes them suitable only for frame detection and coarse CFO estimation [94].

Consequently, more sophisticated algorithms are required to achieve precise symbol timing and fine CFO estimation in MIMO-OFDM systems. A fine synchronization stage that utilizes the cross correlation between the received signal and a local generated training sequence is proposed in [96]. A four step approach using several repeated parts in addition to the CP was reported in [97] for synchronization and channel estimation. Although, the preamble proposed in [97] is quite efficient, the fine synchronization is not very accurate in frequency selective channels and no method was presented to set up the threshold of the timing metric. Despite their moderate computational complexity and capability to incorporate both time and frequency synchronization, the main drawbacks of the above mentioned techniques are the deterioration of power/bandwidth efficiency and the requirement of careful design for the preambles.

Blind techniques exploit the intrinsic information contained in the OFDM symbol such as cyclic prefix, virtual subcarriers (VS) or the cyclostationarity (CS) of OFDM transmissions to estimate the synchronization parameters. The blind schemes are becoming more attractive because of their high power and bandwidth efficiency. A blind CFO estimator for MIMO-OFDM is reported in [98] where the virtual subcarriers are exploited to formulate the cost function. A hybrid technique that uses pilots and the null subcarriers to estimate the CFO in MIMO-OFDM systems is

proposed in [99]. A semi-blind joint estimation for the CFO and the channel is also reported in the literature [100, 101]. Although the above aforementioned methods have a large acquisition range, their main drawback is the high computational complexity due to the exhaustive line search used to minimize the cost function.

Relying on a kurtosis-type criterion, the non-Gaussian property of the received signal can be utilized to deduce a blind CFO estimator for MIMO-OFDM systems as reported in [23]. This estimator is equivalent to the ICI minimization estimator reported in [22] as explained earlier in Chapter 4. A robust and low complexity CFO estimator was recently reported in [52] for MIMO-OFDM systems. This estimator is based on the assumption that the channel frequency response over two adjacent subcarriers is almost the same. Hence, the cost function was developed by minimizing the power difference between adjacent subcarriers. Although this estimator outperforms the estimators of [23] and [22], it suffers from a significant performance degradation under severe fading conditions which is translated into an error floor at moderate and high SNRs. Therefore, this estimator is mainly suitable for channels with short delay spreads.

A blind CFO estimator for MIMO-OFDM systems is derived in [102] by minimizing the components of the signal power spectrum (MCSPS). Although this scheme outperforms the estimator described in [23], it requires a large number of OFDM symbols to obtain reliable CFO estimates. Moreover, the channel length is assumed to be known. Thus, it can not be considered as a totally blind estimator. One of the main advantage for the estimators presented in [23], [52] and [102] is their low computational complexity since a closed-form estimation is given by using parameter estimation.

For the symbol timing estimation in MIMO-OFDM system, several techniques are developed by exploiting the knowledge of the channel response to tune the symbol timing. In [93,94], the symbol timing is estimated by searching for the dominant path of the CIR for best placement of the DFT window. Maximum-likelihood estimation is presented in [103] to jointly optimize the symbol timing and channel estimation.

A more advanced scheme is proposed in [104] where the SIR of the received signal is estimated based on the knowledge of CIR and used as a timing metric to optimize the DFT placement. In such methods, in addition to the requirement of estimating the CIR before starting the symbol timing synchronization which requires more computational overhead, the error in the CIR estimate decreases the probability of

achieving correct timing due to the correlation noise and spectral leakage problems in addition to the ambiguity in the estimate when the initial timing does not satisfy the allowable timing offset range. Thus, the main drawback of the above discussed methods is the joint effect of the two estimation blocks where CIR estimates are affected by STO errors, and STO estimates are affected by CIR estimation errors. Decoupling the STO and CIR requires substantial computational power as described in [105] for MISO-OFDM systems.

In this chapter, efficient timing recovery and CFO estimation methods are proposed to mitigate the degraded performance of most synchronization schemes in highly frequency selective fading channels. The proposed synchronization metric is based on the power difference measurements method developed in the preceding chapters and applied to MIMO-OFDM systems that employ space-time coding (STC) schemes with a fixed common CFO among all transmit-receive antenna pairs [106, 107]. This assumption is justifiable because the controlled antennas in MIMO systems usually share a single RF oscillator. Moreover, the differences in Doppler shift between all transmit-receive antenna pairs are small [23]. By assuming that the channel response remains approximately constant over the STC blocks, a robust synchronization metric is derived by minimizing the power difference among the subcarriers.

The two realizations for the PDE timing estimator discussed in Chapter 5 are investigated and can be applied to MIMO-OFDM systems with any orthogonal space-time coding (OSTBC) scheme. In addition, the chapter also discusses how to adapt the proposed synchronization technique to MIMO-OFDM systems with spatially multiplexed streams. Decoupling the synchronization and channel estimation processes in addition to the blind feature are the main advantage of the proposed method over other synchronization schemes. The proposed synchronization scheme can be applied to either STBC or spatial multiplexed MIMO-OFDM systems, however, it requires an orthogonal preambles at the start of the frame. Additionally, the proposed CFO estimator has low computational complexity since a closed-form estimation can be achieved using a three-point parameter estimation as described in [102]. Furthermore, low complexity feedforward and self-noise free ELG feedback configurations are used for efficient realization of the proposed timing synchronization scheme [108].

6.3 System Model

Consider a MIMO-OFDM communication link with M_T transmit and M_R receive antennas. A sequence of N complex data symbols which are drawn uniformly from QAM or MPSK constellations are used to modulate N orthogonal subcarriers during the lth OFDM symbol block using the mth transmit antenna,

$$\mathbf{d}_m(l) = [d_m^0(l), d_m^1(l), ..., d_m^{N-1}(l)]^T, \quad m = 1, 2, ..., M_T. \tag{6.1}$$

The data symbols modulate the N orthogonal subcarriers using N-points IDFT to produce the time-domain sequence $\mathbf{x}_m(l) = [x_m^0(l), x_m^1(l), ..., x_m^{N-1}(l)]^T$ where

$$\mathbf{x}_m(l) = \mathbf{W}^H \mathbf{d}_m(l). \tag{6.2}$$

A time domain guard band is appended and the resulting OFDM block of length $N_t = N + N_{CP}$ samples is converted to the analogue domain, up-converted to a radio frequency centred at f_c and then transmitted through the mth transmit antenna.

At each receiving antenna, a superposition of signals from all transmit antennas is received and then down converted to baseband. In the centralized clock generation topology, all the transmit antennas are driven by a centralized local oscillator (LO) and so are all the receive antennas which reduces the power consumption compared with distributed topology. As a result, the CFO difference among all transmit-receive antenna pairs is practically negligible, we assume that all transmit and receive antenna pairs experience a common and fixed CFO [98, 99, 102]. For perfect symbol timing, and after discarding the first N_{CP} samples, the received sequence can be written as,

$$\mathbf{y}(l) = e^{j\frac{2\pi\epsilon l N_t}{N}} \mathbf{D}^{(M_R)}(\mathbf{C}(\epsilon)) \bar{\mathbf{H}} \mathbf{D}^{(\mathbf{M_T})}(\mathbf{W}^H) \mathbf{d}(l) + \mathbf{z}(l), \tag{6.3}$$

where $\mathbf{D}^{(M)}(\mathbf{A})$ is a block diagonal matrix with M diagonal blocks, each of which is the matrix $\mathbf{A}$ and

$$\mathbf{y}(l) = [y_1^0(l), y_1^1(l), ..., y_1^{N-1}(l)....y_{M_R}^0(l), y_{M_R}^1(l), ..., y_{M_R}^{N-1}(l)]^T, \tag{6.4}$$

$$\mathbf{d}(l) = [d_1^0(l), d_1^1(l), ..., d_1^{N-1}(l)....d_{M_T}^0(l), d_{M_T}^1(l), ..., d_{M_T}^{N-1}(l)]^T, \tag{6.5}$$

and

$$\mathbf{z}(l) = [z_1^0(l), z_1^1(l), ..., z_1^{N-1}(l)....z_{M_R}^0(l), z_{M_R}^1(l), ..., z_{M_R}^{N-1}(l)]^T. \tag{6.6}$$

The channel $\bar{\mathbf{H}}$ consists of $M_R \times M_T$ subblocks

$$\bar{\mathbf{H}} = \begin{bmatrix} \bar{\mathbf{H}}_{1,1} & \cdots & \bar{\mathbf{H}}_{1,M_T} \\ \vdots & \ddots & \vdots \\ \bar{\mathbf{H}}_{M_R,1} & \cdots & \bar{\mathbf{H}}_{M_R,M_T} \end{bmatrix} \tag{6.7}$$

and each subblock is an circulant matrix representing the channel impulse response between the nth transmit and the mth receive antenna where

$$\left[\bar{\mathbf{H}}_{m,n}\right]_{i,j} = h_{m,n}^{(i-j) \bmod N}. \tag{6.8}$$

Denoting

$$\mathbf{y}_n(l) = [y_n^0(l), y_n^1(l), ..., y_n^{N-1}(l)]^T. \tag{6.9}$$

$$\mathbf{d}_n(l) = [d_n^0(l), d_n^1(l), ..., d_n^{N-1}(l)]^T. \tag{6.10}$$

$$\mathbf{z}_n(l) = [z_n^0(l), z_n^1(l), ..., z_n^{N-1}(l)]^T. \tag{6.11}$$

the received sequence at the nth antenna output can be expressed as [102],

$$\mathbf{y}_n(l) = e^{j\frac{2\pi\epsilon l N_t}{N}} \mathbf{C}(\epsilon) \sum_{m=1}^{M_T} \bar{\mathbf{H}}_{mn}(l) \mathbf{W}^H \mathbf{d}_m(l) + \mathbf{z}_n(l), \tag{6.12}$$

The set $\mathbf{y}(l)$ is fed to the DFT to produce the frequency domain symbols. Using the property of circulant matrices,

$$\begin{aligned} \mathbf{s}(l) &= \mathbf{D}^{(M_R)}(\mathbf{W}\,\mathbf{C}^*(\hat{\epsilon}))\mathbf{y}(l), \\ &= e^{j\frac{2\pi\epsilon l N_t}{N}} \mathbf{D}^{(M_R)}(\mathbf{W}\,\mathbf{C}(\tilde{\epsilon})\mathbf{W}^H)\mathbf{H}(l)\mathbf{d}(l) + \mathbf{D}^{(M_R)}(\mathbf{W})\mathbf{z}(l), \end{aligned} \tag{6.13}$$

where

$$\mathbf{H} = \begin{bmatrix} \mathbf{H}_{1,1} & \cdots & \mathbf{H}_{1,M_T} \\ \vdots & \ddots & \vdots \\ \mathbf{H}_{M_R,1} & \cdots & \mathbf{H}_{M_R,M_T} \end{bmatrix} \tag{6.14}$$

The subblocks of $\mathbf{H}$ are diagonal matrix $\mathbf{H}_{mn}(l)$ that represents the channel frequency response of the (m,n)th antenna pairs during the lth OFDM symbol du-

ration. The (k,k)th element of $\mathbf{H}_{mn}(l)$ is $H^k_{mn}(l) = \sum_{i=0}^{L_h} h^i_{mn}(l)e^{-j2\pi ik/N}$ where $h^i_{mn}(l)$ is the channel impulse response of the (m,n)th antenna pairs. The received sequence $\mathbf{s}_n(l)$ at the DFT output of the nth antenna can be expressed as,

$$\begin{aligned}\mathbf{s}_n(l) &= \mathbf{W}\,\mathbf{C}^*(\hat{\epsilon})\mathbf{y}_n(l), \\ &= e^{j\frac{2\pi\epsilon l N_t}{N}}\mathbf{W}\,\mathbf{C}(\tilde{\epsilon})\mathbf{W}^H\sum_{m=1}^{M_T}\mathbf{H}_{mn}(l)\mathbf{d}_m(l) + \mathbf{v}_n(l), \end{aligned} \tag{6.15}$$

where $\hat{\epsilon}$ is the estimate of ϵ, $\tilde{\epsilon} = \epsilon - \hat{\epsilon}$ is the CFO estimation error, and $\mathbf{v}_n(l) = \mathbf{W}\,\mathbf{C}^*(\hat{\epsilon})\mathbf{z}_n(l)$. The matrix $\mathbf{W}\,\mathbf{C}(\tilde{\epsilon})\mathbf{W}^H$ is not diagonal, unless $\tilde{\epsilon} = 0$. Hence, the orthogonality among the demodulated subcarriers will be destroyed due to the introduced ICI and it can be verified that for $\epsilon \in [-0.5, 0.5]$, the ICI disappears only if $\tilde{\epsilon} = 0$.

In the above signal model, perfect symbol timing is assumed. By analogy to the SISO case presented in the previous chapter, the MIMO-OFDM systems can also tolerate a certain amount of timing errors (δ) depending on the channel delay spreads. However, to prevent ISI and ICI due to the timing error, the DFT window should include samples that belong to a single OFDM symbol, hence δ should be bounded by the safe-region (SR) borders given in (5.19) [105].

However, when the symbol timing does not satisfy the SR condition (i.e. for both positive timing error $\delta > 0$ or negative timing error $\delta < L_h - N_{CP}$), the DFT window will start out of the SR as described in (5.19), thus ICI and ISI will be introduced due to the loss of subcarriers' orthogonality. The demodulated signal will consist of the desired signal and other unwanted disturbances composed of ICI, ISI and the additive noise [105],

$$s^k_n(l) = \sum_{m=1}^{M_T}\left[\beta^k_{mn} + I^k_{mn}\right], \tag{6.16}$$

where β is the desired signal component and I models the additive disturbance composed by the ISI and ICI introduced due to the timing errors and CFO in addition to the noise.

6.4 Proposed Timing Recovery and CFO Estimation Schemes

In this section, we present the proposed PDE for MIMO-OFDM system employing an OSTBC with T symbol duration in each block as shown in Fig. 6.1. Without loss of generality, a 2×2 MIMO-OFDM system employing Alamouti code is considered. To achieve space-time diversity, the Alamouti code [109] can be applied to each subcarrier independently. During the first symbol period, let the two OFDM symbols transmitted simultaneously from antenna 1 and 2 to be $\mathbf{d}_1(l)$ and $\mathbf{d}_2(l)$ where:

$$\mathbf{d}_1(l) = [d_1^0(l), d_1^1(l), ..., d_1^{N-1}(l)], \tag{6.17}$$

and

$$\mathbf{d}_2(l) = [d_2^0(l), d_2^1(l), ..., d_2^{N-1}(l)]. \tag{6.18}$$

According to Alamouti coding, the next symbol period $-\mathbf{d}_2(l)^*$ is transmitted from antenna 1, and $\mathbf{d}_1(l)^*$ is transmitted from antenna 2, where $(.)^*$ denotes the complex conjugate operation. Based on the assumption that the channel varies slowly in time with respect to the rate of the STC blocks, we assume that the channel remains constant over at least two consecutive STC blocks.

The channel frequency response on the kth subcarrier from the mth transmit antenna to the nth receive antenna is denoted $H_{mn}^k(l)$. In the case of perfect synchronization (STOs and CFOs are perfectly estimated and compensated i.e. $\hat{\epsilon} = \epsilon$ and $\hat{\delta} = \delta$), the DFT output on the kth subcarrier of the nth receive antenna at the lth and $(l+1)$th symbol duration can be expressed as:

$$s_n^k(l)|_{\hat{\epsilon}=\epsilon,\ \hat{\delta}=\delta} = H_{1n}^k(l)d_1^k(l) + H_{2n}^k(l)d_2^k(l), \tag{6.19}$$

and

$$s_n^k(l+1)|_{\hat{\epsilon}=\epsilon,\ \hat{\delta}=\delta} = -H_{1n}^k(l)d_2^k(l)^* + H_{2n}^k(l)d_1^k(l)^*. \tag{6.20}$$

The power of the kth DFT output for the two symbols can be expressed as:

$$\begin{aligned}|s_n^k(l)|_{\hat{\epsilon}=\epsilon,\ \hat{\delta}=\delta}|^2 = {} & |H_{1n}^k(l)|^2|d_1^k(l)|^2 + |H_{2n}^k(l)|^2|d_2^k(l)|^2 \\ & + d_1^k(l)d_2^k(l)^*H_{1n}^k(l)H_{2n}^k(l)^* + d_1^k(l)^*d_2^k(l)H_{1n}^k(l)^*H_{2n}^k(l),\end{aligned}$$

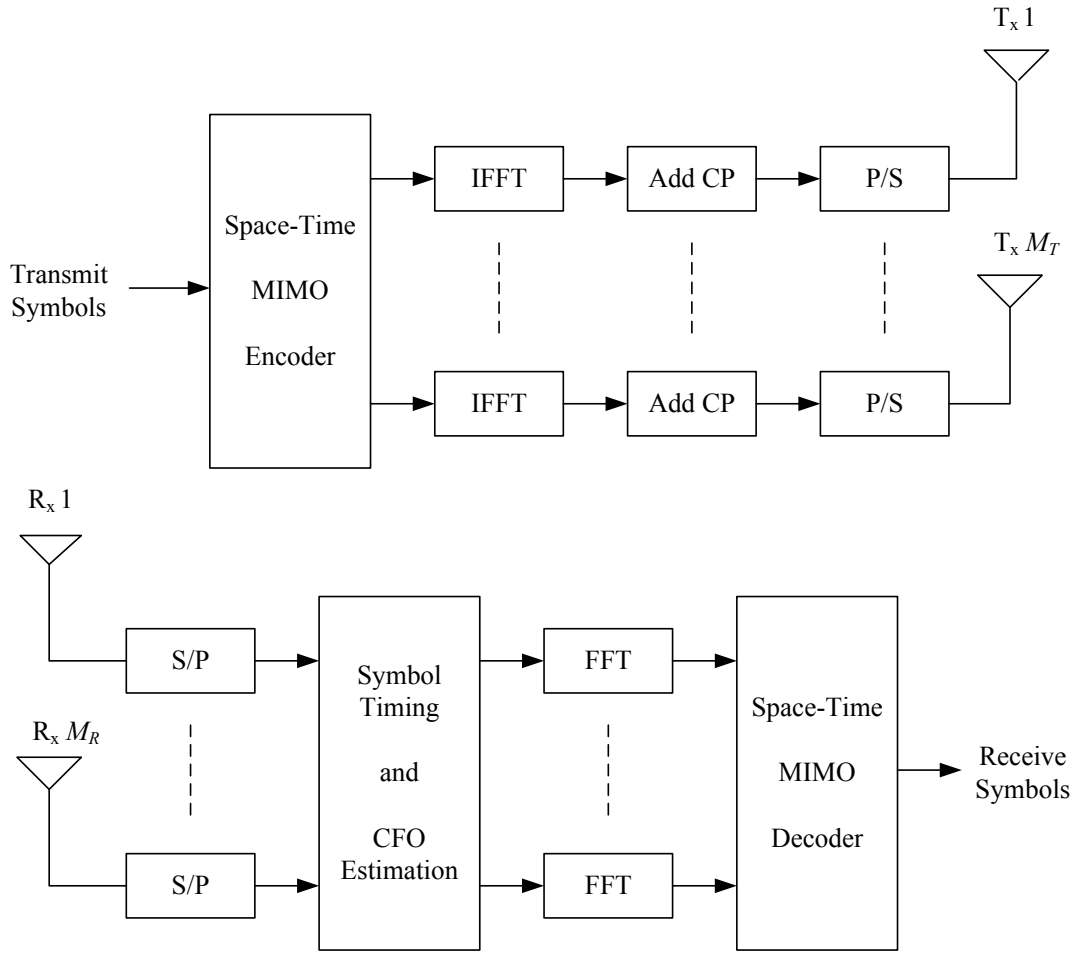

Figure 6.1: Block diagram for MIMO-OFDM system employing space-time coding.

and

$$\left|s_n^k(l+1)|_{\hat{\epsilon}=\epsilon,\ \hat{\delta}=\delta}\right|^2 = |H_{1n}^k(l)|^2|d_2^k(l)|^2 + |H_{2n}^k(l)|^2|d_1^k(l)|^2 - d_1^k(l)d_2^k(l)^* H_{1n}^k(l)H_{2n}^k(l)^* - d_1^k(l)^* d_2^k(l)H_{1n}^k(l)^* H_{2n}^k(l).$$

Let p_n^k denote the total power of kth subcarrier on the nth receive antenna over a block with T symbol duration. In the case of Alamouti coding, the total power of the jth block is given by

$$p_n^k(j)|_{\hat{\epsilon}=\epsilon,\ \hat{\delta}=\delta} = |s_n^k(l)|^2 + |s_n^k(l+1)|^2. \tag{6.21}$$

Given that the data symbols are selected from a constant modulus (CM) constellation with a unity normalized power, the total power of the jth block can be written as [52],

$$p_n^k(j)|_{\hat{\epsilon}=\epsilon,\ \hat{\delta}=\delta} = 2\left[|H_{1n}^k(l)|^2 + |H_{2n}^k(l)|^2\right]. \tag{6.22}$$

By observing the DFT output of a perfectly and non-perfectly synchronized MIMO-OFDM systems which are given in (6.19) and (6.16), respectively. It can be noted that the DFT output in the presence of synchronization imperfection given in (6.16) contains an additional term which is the interference due to synchronization error. The interference is a function of both δ and ϵ as shown in the previous chapters where the cost function constructed from the power difference measurements for the interference is two-dimensional versus δ and ϵ. Because of the CP, the PDE cost function, as a function of δ, will have N_{CP} minimum points for flat fading channels where $\{\delta\} \in [-N/2, N/2]$. On the other hand, the PDE exhibits only one unique minimum at $\epsilon = 0$ where $\{\epsilon\} \in [-0.5, 0.5]$. Therefore, the power difference measurements of the interference based on the channel correlation over adjacent subcarriers or the same subcarrier in conseutive STC blocks can be exploited to estimate the values of δ and ϵ.

For narrowband fading channels, the channel frequency response changes slowly in frequency domain. Hence, the frequency response over two adjacent subcarriers is approximately equal. Therefore,

$$p_n^k(j) \approx p_n^{k+1}(j). \tag{6.23}$$

To combat the channel frequency selectivity due to wideband fading, the power difference measurements can be performed across the time domain given that the CIR changes slowly over the period of two STC blocks,

$$p_n^k(j) \approx p_n^k(j+1). \tag{6.24}$$

However, the above approximations given in (6.23) and (6.24) are only valid when the CFO is estimated and compensated perfectly and the symbol timing satisfy the SR condition. The PDE approach first eliminates the effect of the modulation symbols, this operation is called the modulation removal. As the data symbols belong to constant modulus constellations, the modulation removal process can be done by computing the power of the DFT outputs, $|s_n^k(l)|^2 = s_n^k(l)s_n^k(l)^*$. Then, the power difference among the subcarriers can be used to estimate δ and ϵ simultaneously. If the data symbols have non-constant modulus constellations, some reference symbols can be exploited to construct the cost function as explained in the previous chapter.

Alternatively, the decomposition of the constellation into constant modulus sub-constellations or decision-directed approaches can be used. However, in addition to the added complexity, the performance deterioration for the PDE scheme is observed at low SNR values.

Consequently, the cost function of the proposed (PDE-F) synchronization scheme can be constructed by minimizing the power difference measurements among all adjacent subcarriers in one STC block as follows,

$$J_{PDE-F}(\epsilon,\delta)=\sum_{n=1}^{M_R}\sum_{j=1}^{L}\sum_{k=0}^{N-1}\left[p_n^k(j)-p_n^{k+1}(j)\right]^2. \tag{6.25}$$

While the cost function of PDE-T synchronization metric is formulated based on the power difference measurements between all subcarriers over two consecutive STC blocks,

$$J_{PDE-T}(\epsilon,\delta)=\sum_{n=1}^{M_R}\sum_{j=1}^{L}\sum_{k=0}^{N-1}\left[p_n^k(j)-p_n^{k}(j+1)\right]^2, \tag{6.26}$$

where L represents the number of STC blocks used in the estimation process to improve the accuracy of the cost function. The value of L determines the observation period, i.e., the number of STC blocks required to produce the parameters' estimates. For $L=1$, the observation window is equal to one STC block duration for the PDE-F and two STC block duration for the PDE-T. In addition, the cost function accuracy can be further improved by exploiting the spatial diversity of the M_R receive elements.

The synchronization parameters' estimates can be obtained by minimizing the cost functions given in (6.25) or (6.26),

$$\left\{\hat{\epsilon},\hat{\delta}\right\}=\arg\min_{\substack{\mu\in(-0.5,0.5)\\ \gamma\in(-N/2,N/2)}} J_{PDE-F/T}(\mu,\gamma), \tag{6.27}$$

where γ and μ are the trial values of δ and ϵ, respectively. It is worth mentioning that the minimization process given in (6.27) is a mixed discrete/continuous search operation where $\gamma\in\left\{\frac{-N}{2},\frac{-N}{2}+1,.....,\frac{N}{2}\right\}$ and $\mu\in(-0.5,0.5)$. Thus, γ has discrete step size of 1 sample while the step size for μ is determined based on the required search resolution that specify the accuracy of the parameter estimates.

As observed from (6.27), the two-dimensional search process is complex and time

consuming. In addition, the accuracy of $\hat{\epsilon}$ is limited by the search resolution. Therefore, the two dimensional search is decomposed into two separate one dimensional frequency and timing estimation processes using the results obtained in Chapter 4 and 5, respectively. By observing the signal model in the presence of CFO, the ICI can be considered as disturbance in addition of the AWGN. Therefore, if the STO estimation is performed in the presence of CFO, the DFT output $s_n^k(l)|_{\hat{\epsilon}\neq\epsilon}$ and $s_n^k(l)|_{\hat{\epsilon}=\epsilon}$ will be similar but with different SNRs, i.e.

$$s_n^k(l)|_{\delta=0} = s_n^k(l)|_{\hat{\epsilon}=\epsilon} + \Psi_n^k, \tag{6.28}$$

where Ψ_n^k is the ICI induced additional noise. Thus, the presence of CFO is not an obstacle to perform the timing estimation as demonstrated in [24, 25, 47].

Accordingly, the synchronization process starts with the symbol timing estimation by minimizing the PDE-F/T cost function described in (6.25) and (6.26) respectively,

$$\hat{\delta} = \arg \min_{\gamma\in(-N/2,N/2)} J_{PDE-F/T}(\gamma). \tag{6.29}$$

It can be noted the estimator accuracy is not bounded by the search step size if a feedforward configuration is used. In addition, the feedback realization using the ELG approach described in Chapter 5 (Section 5.5.2) can also be invoked. An example for the normalized cost function and S-curve of the proposed ELG-PDE-F estimator for 2×1 MIMO-OFDM system employing STC over a flat fading channel is presented in Fig. 6.2 (a) and (b), respectively. It is clear that the cost function exhibits an inverted plateau shape where the low area corresponds to the SR, hence the DFT window can start in any point in the SR without introducing performance deterioration. The S-curve of the proposed timing estimator is generated by setting the early and late branch at the CP border (i.e. $\tau_\delta = N_{CP}/2$) to minimize the self-noise in the steady state as discussed in the Chapter 5.

When the symbol timing synchronization is accomplished, the CFO estimation can be started where the cost function is given by

$$\hat{\epsilon} = \arg \min_{\mu\in(-0.5,0.5)} J_{PDE-F/T}(\mu). \tag{6.30}$$

The value of $\hat{\epsilon}$ should be compensated prior to the next timing estimation. Obviously, the initial STO estimate may not be sufficiently accurate because of the

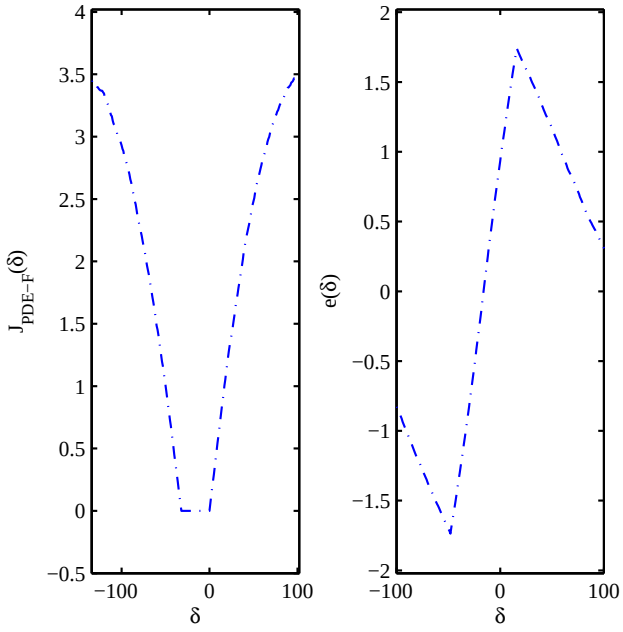

Figure 6.2: STC MIMO-OFDM system over flat fading channel, $M_T = 2$, $M_R = 1$ and $L = 10^4$ (a) The cost function $J_{PDE-F}(\delta)$ (b) The S-curve of the proposed PDE-F estimator.

SNR degradation due to the CFO which is very common in most synchronization techniques during the acquisition mode. However, a low cost pre-synchronizer can be used to provide the initial estimate to the timing synchronization loop and to reduce the CFO effect. In the acquisition mode, it is not necessary for the estimated parameters to be accurate as the proposed timing synchronization loop can tolerate a certain amount of CFO without severe deterioration in the performance as will be illustrated in the numerical results section. In addition, the initial timing error will have a marginal effect on the performance of the proposed CFO estimator because of the superior robustness to timing uncertainty as discussed in Chapter 4. In the tracking mode, the coupling effect where the accuracy of one estimate is affected by the estimation error of the other is usually neglected as the proposed synchronization scheme can easily tolerate it [24, 37, 110].

The minimization process of $J_{PDE-F/T}(\mu)$ is more complicated compared with $J_{PDE-F/T}(\gamma)$ because $\mu \in (-0.5, 0.5)$ which is an infinite interval. Adaptive search methods and feedback configurations can be used for the cost function minimization however, at the expense of some performance deterioration [22, 52]. Fortunately, it is straightforward to use the results of Chapter 4 to show that the cost function

described in (6.30) can be approximated by the following simple sinusoid,

$$J_{PDE-F/T}(\mu) \approx A\cos[2\pi(\epsilon - \mu)] + C, \tag{6.31}$$

where the A and B are constants with respect to μ with $A < 0$.

Therefore, the minimization process can be replaced by the parameter estimation approach described in Chapter 4 where the estimation of $\hat{\epsilon}$ can be performed by evaluating $J_{PDE-F/T}$ at three trial offsets $\mu = -1/4,\ 0,\ 1/4$. Consequently, $\hat{\epsilon}$ can be estimated using the following

$$\hat{\epsilon} = \begin{cases} \frac{1}{2\pi}\tan^{-1}(b/a) & a \geq 0 \\ \frac{1}{2\pi}\tan^{-1}(b/a) + \frac{1}{2} & a < 0 \text{ and } b \geq 0 \\ \frac{1}{2\pi}\tan^{-1}(b/a) - \frac{1}{2} & a < 0 \text{ and } b \leq 0 \end{cases} \tag{6.32}$$

where a and b are given in (4.20) and (4.21), respectively.

6.5 Application of PDE to MIMO-OFDM Systems with Spatially Multiplexed Streams

The previous section presents the application of the PDE approach to MIMO-OFDM systems that employ OSTBC. In what follows, we discuss how the proposed PDE synchronization method can be incorporated to MIMO-OFDM systems with spatially multiplexed streams. Considering MIMO-OFDM system that employ preamble which is a piece of known data prefixed to the data part of the transmitted packet. For the preambles, it is important that the subchannels from different transmit to every receive antenna is uniquely identified and the transmitted preambles on different transmit antenna have to be orthogonal and shift orthogonal to each other to facilitate the synchronization and channel estimation processes.

Different preamble structures for MIMO-OFDM systems that meet the above prerequisite is shown in Fig. 6.3. The structure shown in Fig. 6.3(a) known as time multiplexed (TM) where each preamble sequentially transmitted from the different antennas. While the time orthogonal (TO) shown in Fig. 6.3(b) achieves the orthogonality by using the Walsh-Hadamard or the Fourier matrix, which both are given by [1, 1;1, -1] for 2 transmitter case. The TM and TO preamble structures increase

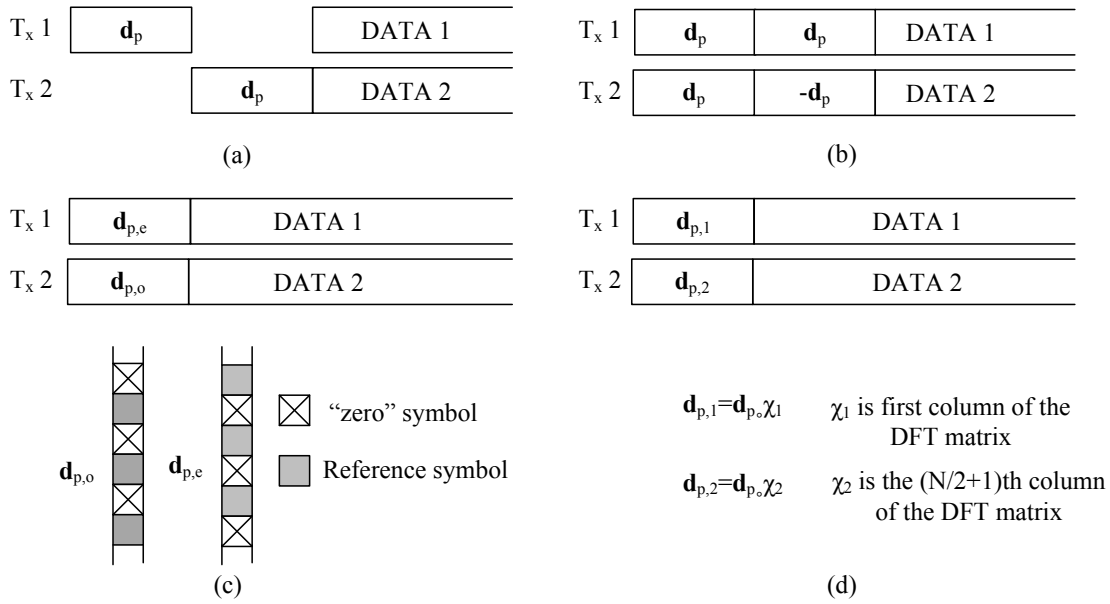

Figure 6.3: Different Preamble Structures for MIMO-OFDM Systems, (a) Time multiplexed (b) Time orthogonal (c) Subcarrier multiplexed (d) Subcarrier orthogonal.

the overhead of the transmitted reference symbols especially in high dimensional MIMO-OFDM systems. On the other hand, the preamble structures shown in Fig. 6.3(c) and (d), known as subcarrier multiplexed (SM) and subcarrier orthogonal (SO), respectively, simultaneously transmit the preamble symbols on all transmit antennas where the orthogonality is achieved in the frequency domain. Thus, there is no overhead in the transmitted preamble compared with a SISO system. In the SM scheme, the antennas transmit the training sequences simultaneously over certain subcarriers in order to avoid the interferences and achieve orthogonality. For example in Fig. 6.3(c), Tx 1 transmit on the even subcarriers while Tx 2 transmit on the odd subcarriers. In SO structure, the orthogonality is achieved in the frequency domain by multiplying the transmitted symbols with orthogonal vectors such as the Fourier sequences. Thus, the transmitted symbol is given by

$$\mathbf{d} = (\mathbf{d}_p \circ \chi_1) \otimes \mathbf{e}_1 + (\mathbf{d}_p \circ \chi_2) \otimes \mathbf{e}_2 + ... + (\mathbf{d}_p \circ \chi_{M_T}) \otimes \mathbf{e}_{M_T}, \tag{6.33}$$

where $\circ$ denotes element-wise multiplication, χ_{m_t} equals the $(1+(m_t-1)\lfloor N/M_T \rfloor)$th column of the DFT matrix ($\mathbf{W}$), $\mathbf{e}_m$ denotes $M_T \times 1$ vector $\mathbf{e}_m = [\mathbf{0}_{m-1}, 1, \mathbf{0}_{M_T-1}]^T$ of which all elements are zero except the mth, which is 1 and $\otimes$ denotes the Kronecher or direct matrix product.

The SO preamble structure does not increase the transmission overhead and it

can be exploited to adapt the proposed PDE-T synchronization scheme to MIMO-OFDM systems. As discussed previously in the literature, the most common approach to achieve synchronization in MIMO-OFDM systems is to transmit repeated version of the preambles and the received sequences are correlated to estimate the synchronization parameters. Alternatively, the PDE-T can be adapted for such systems by exploiting the received consecutive symbols where the reference symbols are usually have constant modulus constellations. In this case, the repetition is not required and two different reference symbols need to be transmitted or even replaced with data symbols given that the other estimation blocks are implemented blindly as well.

6.6 Numerical Results

This section presents the performance evaluation results of the proposed synchronization techniques for MIMO-OFDM systems. Monte Carlo simulations are used to assess the system performance over flat and frequency selective multipath fading channels. The performance of the considered CFO estimators are compared in terms of MSE of the CFO estimates' while $P_{lock-in}$ and DSR measures are used to assess the performance of timing estimators. In each simulation run at least 10^4 independent OFDM symbols are used. A MIMO-OFDM system employing OSTBC is used and the subcarriers modulated using QPSK, the subcarriers' data rate is 4.17 kb/s, and the carrier frequency is equal to 2.2 GHz. The total transmission power P was maintained fixed regardless the value of M_T, hence the power for each transmit antenna is equal to P/M_T. To demonstrate the efficiency of the proposed PDE synchronization techniques for MIMO-OFDM systems, the same channel models described in the previous chapters are used.

In the following, the simulation results of the proposed PDE-T CFO estimator are presented and compared to the KBE [23], MVE [22] and PDE-F [52] CFO estimators adapted to the considered MIMO-OFDM system with $N = 64$ and $N_{CP} = 16$. The MSE performance of the considered CFO estimators over flat fading channel as a function of SNR is given in Fig. 6.4 using M_T=M_R=2. It can be seen from this figure that KBE, MVE and the PDE-T estimators have equivalent performance over the entire range of SNR except for the PDE-F which exhibits a slight flatness at high SNRs.

The performance of the CFO estimators over frequency selective channels is depicted in Fig. 6.5 using Channel-I and Channel-II. As demonstrated by Fig. 6.5, the PDE-T outperforms all other estimators for the entire range of SNRs over both channel models. Moreover, using Fig. 6.5 we observe that KBE and MVE estimators are very sensitive to frequency selective fading even when the fading is so mild. The PDE-F estimator has demonstrated some robustness for the case of Channel-I, however, the MSE has severely deteriorated when Channel-II is used. Unlike the other considered estimators, the PDE-T has demonstrated high robustness over both channel models with a MSE that remained almost unchanged in both cases.

The performance of the proposed CFO estimator for MIMO-OFDM systems with different transmit-receive antennas over Channel-I is depicted in Fig. 6.6. The results show that the MSE for PDE-T and PDE-F decreases as the number of transmit and receive antennas increases since the spatial diversity provided by multiple transmit-receive antennas reduces the estimation error. The Kurtosis based estimator exhibits an error floor as the number of transmit-receive antennas increases due to the coupling effect which brings the symbol distribution closer to Gaussian [23]. For all the considered M_T and M_R combinations, the PDE-T has offered a continuously decreasing MSE, no error floor, and significantly outperformed the other considered estimators.

The MSE performance over severe frequency selective channels, Channel-III, is given in Fig. 6.7, which demonstrates the invulnerability of the proposed PDE-T against severe fading conditions. While the MSE of the PDE-T decreases linearly as the SNR increases, the MSE of the other estimators saturates at low SNRs with high MSE error floor levels. In addition, although the averaging over multiple symbols has improved the MSE for all the estimators as revealed in Fig. 6.7, it did not eliminate the error floor problem. Nevertheless, the MSE of PDE-T for L=1 is much less than the MSE of the estimators of [23] and [22] for L=5 over the entire SNR range and at high SNRs for the case of PDE-F. This implies that the PDE-T can render accurate estimates within the duration of one estimation block and no averaging is required even under severe frequency selective fading conditions. Avoiding averaging remarkably reduces the computational complexity requirements for the PDE-T when compared to other methods where averaging is essential.

To evaluate the performance of the proposed estimator over a time varying frequency selective fading channel, a mobile frequency selective fading channel is for-

Table 6.1: MSE values of the considered estimators for different SUI channels at SNR=40 dB

	SUI-2	**SUI-4**	**SUI-5**	**SUI-6**
MVE, KBE	2.13×10^{-5}	1.0×10^{-4}	5.0×10^{-4}	1.1×10^{-1}
PDE-F	2.5×10^{-7}	4.0×10^{-7}	1.0×10^{-5}	7.9×10^{-3}
PDE-T	2.0×10^{-7}	2.0×10^{-7}	2.2×10^{-7}	2.6×10^{-5}

mulated using Channel-III model, with two different maximum Doppler shifts f_d=50 and 200 Hz. The MSE performance presented in Fig. 6.8 confirms the robustness of the PDE over other well established estimators. As expected and confirmed by Fig. 6.8, the MSE of the Kurtosis and minimum variance estimators deteriorate severely under such severe fading conditions regardless the Doppler shift values. Moreover, we observe that the PDE-T still outperforms the estimator of PDE-F at low-to-medium Doppler shifts. However, the MSE of both estimators starts to converge at high Doppler shifts. Consequently, the PDE-T can be considered to be efficient in time varying channels as well.

The robustness of the proposed estimator is investigated over the considered channels with various level of frequency selectivity and wide range of Doppler shifts (f_d). The MSE performance of the PDE-F and PDE-T versus f_d is depicted in Fig. 6.9 for SNR=40 dB. For the case of moderate and severe frequency selective channels, Channel-II and III, it can be noted that the proposed PDE-T estimator outperforms PDE-F for the entire range of f_d and the performance difference is substantial for the low and moderate values of f_d. As demonstrated in Fig. 6.9, the performance difference between the considered estimators is decreases as f_d increases and they converge at very high values of f_d. For the case of a mild frequency selective channel, Channel-I, it can be noted that the PDE-T outperforms PDE-F at low values of f_d. At moderate and high values of f_d, the MSE for PDE-T is slightly larger than PDE-F.

Generally speaking, there is a significant gain in the performance by formulating the cost function of the proposed estimator along the time direction rather than the frequency direction, and more significantly in moderate and severe frequency selective fading channels. The proposed estimator assumes slow time varying conditions, making it ideally suited to applications such as fixed, nomadic or limited mobility type WiMAX systems that can provide very high data rates. However, it can also work well for fast fading scenarios as the results reveal in Fig. 6.8 and Fig. 6.9,

where the performance of the other considered estimators is severely affected by the frequency selectivity degree of the mobile channel.

To validate the performance of the proposed estimator for a practical broadband wireless communication system, WiMAX with STC MIMO configuration is considered as an example. The simulation parameters are readjusted according to fixed WiMAX IEEE 802.16 standard [9] where N=256, N_{CP}=64, and Δf=15.625 KHz. The performance of the estimator is investigated in different SUI channel conditions. The SUI radio channels can be considered as slow time varying frequency selective fading channels. Moreover, according to the considered OFDM system parameters, the channel models SUI-1 to SUI-5 maximum delay spread is less than the CP duration, hence no ISI is introduced. Channel model SUI-6 delay spread is larger than the CP, consequently the system is operating in the presence of ISI.

Fig. 6.10 presents the results for the SUI-4, SUI-5 ans SUI-6 channel models which are typical examples for channels with moderate and long delay spreads. It can be noted from this figure the PDE-T slightly outperforms the PDE-F for the SUI-4 channel and both estimators have no error floors even at high SNRs. Unlike SUI-4 case, the MSE of the PDE-F over SUI-5 starts to saturate at SNR $\gtrsim$ 20 dB while the MSE of the PDE-T did not have any noticeable degradation. The MVE and KBE have exhibited a degraded performance over both channel models; however, the MSE can be considered satisfactory since the error floor level is not very high. In SUI-6 environments, the MVE, KBE and PDE-F fail to provide reliable estimates even at high SNRs. The impact of the ISI in SUI-6 environments was severe on the PDE-T as well, which demonstrated by error floor that starts to appear at SNR $\gtrsim$ 20 dB. However, unlike the other estimators, the PDE-T is still capable of providing reliable estimates at moderate and high SNRs. More numerical results for the considered estimators associated with different SUI channel models are presented in Table (6.1).

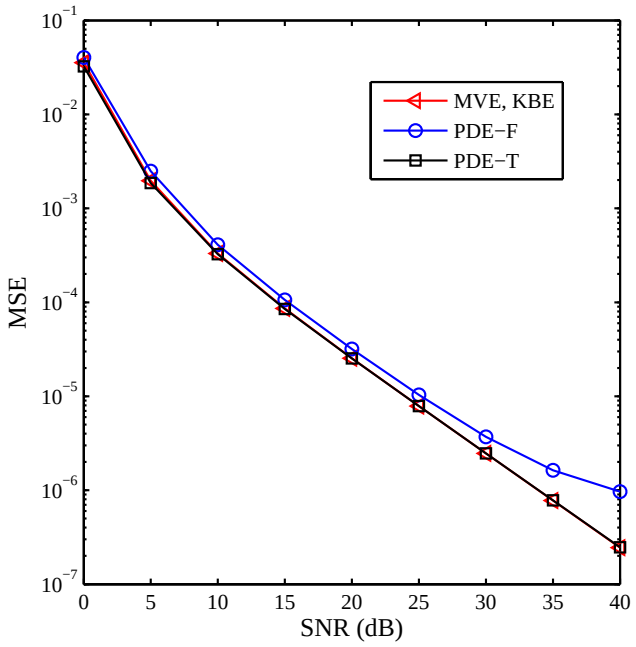

Figure 6.4: MSE versus SNR over flat fading channel, $N = 64$, $N_{CP} = 16$, L=1, $M_T = M_R = 2$.

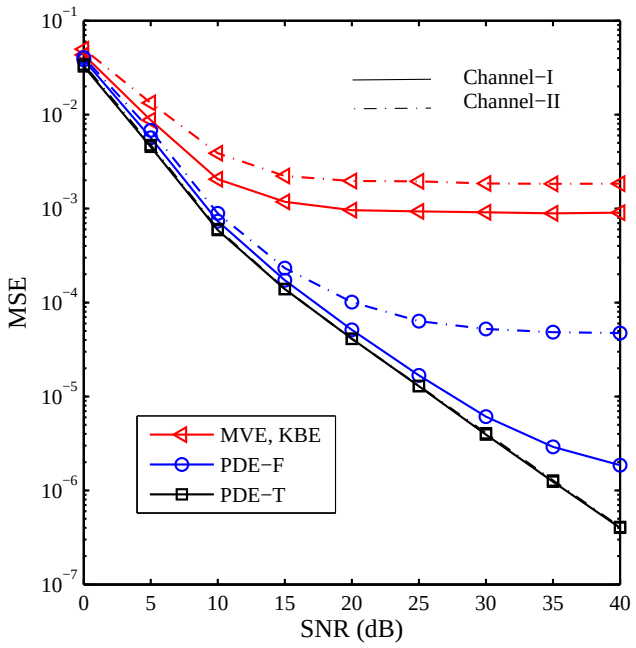

Figure 6.5: MSE versus SNR for frequency selective channels with different delay spreads $\sigma^2(\tau)$, $N = 64$, $N_{CP} = 16$, $L = 1, M_T = M_R = 2, f_d$ =0.

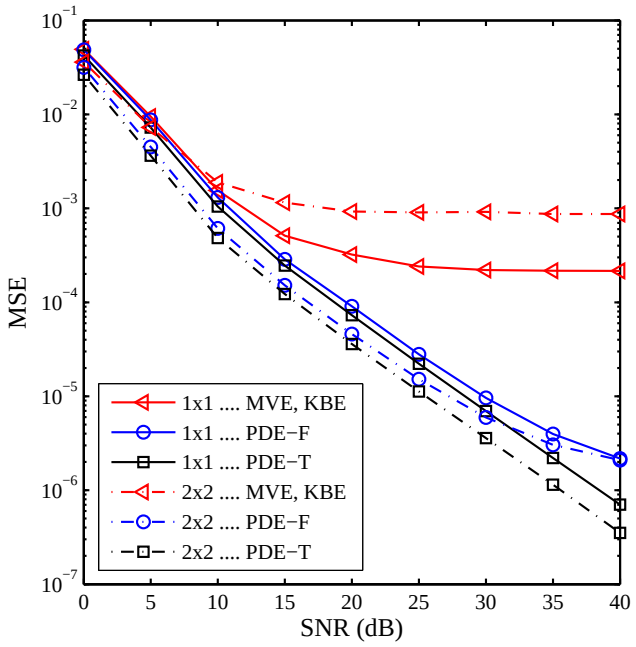

Figure 6.6: MSE versus SNR for frequency selective channels with MIMO configuration, $N = 64$, $N_{CP} = 16$, L=1, $\sigma^2(\tau)$=1.74, f_d=0.

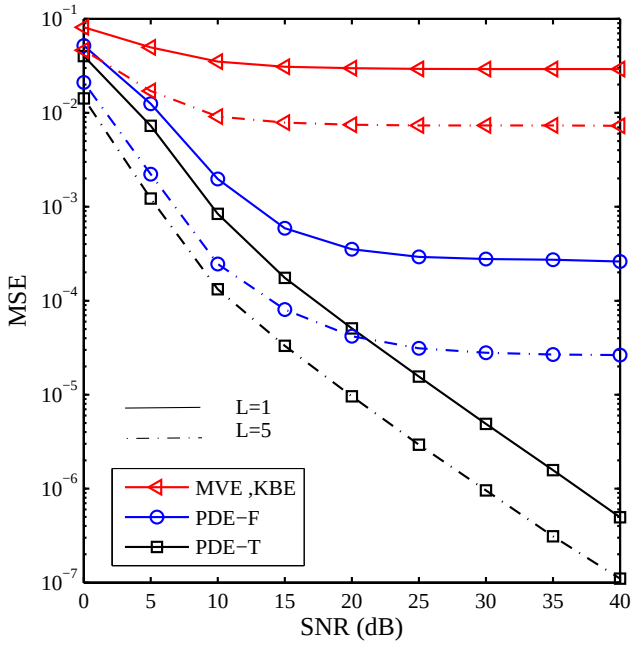

Figure 6.7: MSE versus SNR for different Doppler shift, $N = 64$, $N_{CP} = 16$, L=1, $M_T = M_R$=2, Channel-III, f_d=50 and 200 Hz.

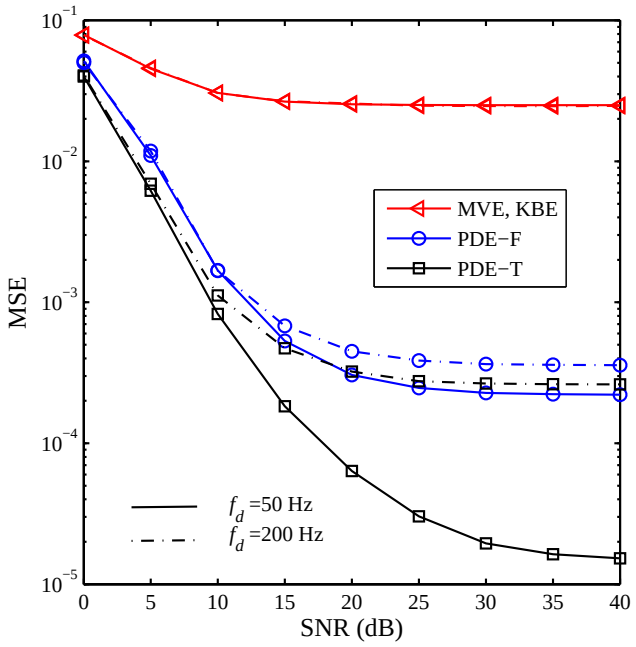

Figure 6.8: MSE versus SNR for different Doppler shift, $N = 64$, $N_{CP} = 16$, L=1, $M_T = M_R$=2, $\sigma^2(\tau)$=20, f_d=50 and 200 Hz.

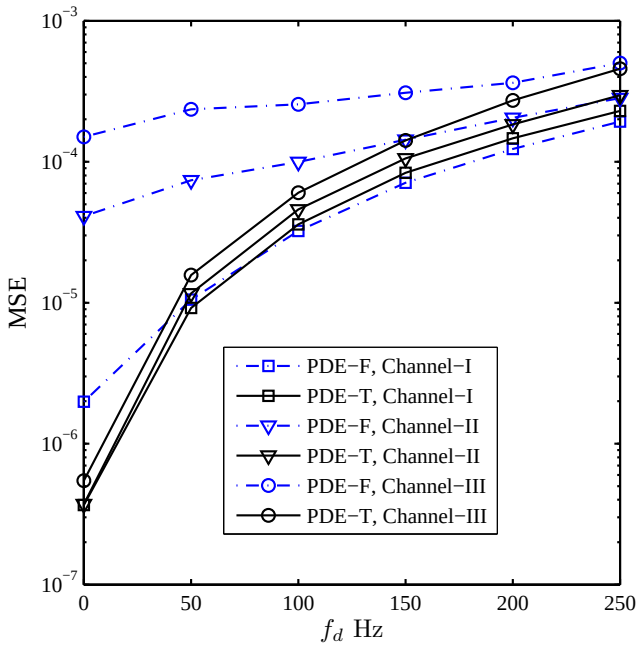

Figure 6.9: MSE versus different Doppler shifts over channels with different frequency selectivity conditions, $N = 64$, $N_{CP} = 16$, L=1, $M_T = M_R$=2.

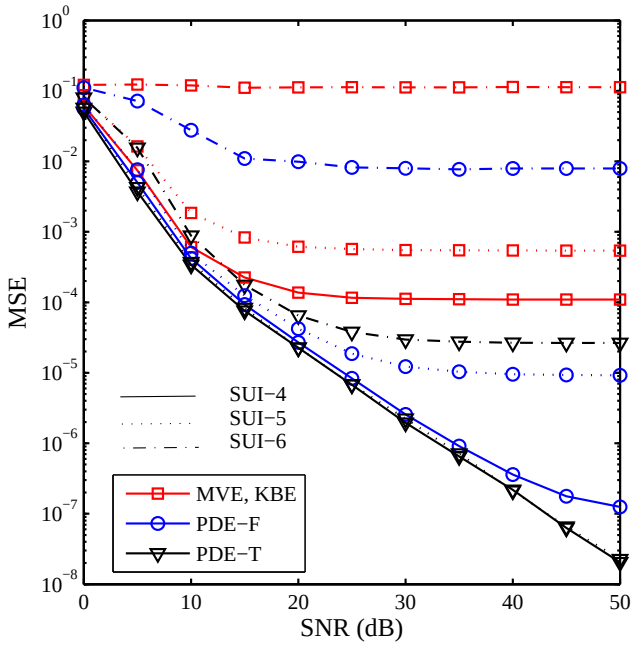

Figure 6.10: MSE versus SNRs over SUI-4, SUI-5 and SUI-6 channels, N=256, N_{CP}=64, L=1, $M_T = M_R$=2.

In the following, the performance evaluation results of the proposed timing estimators are presented. The ELG configuration has been invoked to implement the proposed synchronization technique and the following parameters have been considered unless otherwise specified, $N = 256$, $N_{CP} = 32$ and $B_L = 1/10$. The performance of the MVE [83], PDE-F and PDE-T timing estimators in terms of $P_{lock-in}$ and DSR are depicted in Fig. 6.11 and 6.12, respectively, over flat and frequency selective fading channel (Channel-II). In flat fading channel, it can be noted that both MVE and PDE-T have equivalent performance over the entire range of SNR, while the PDE-F suffered little performance degradation at low SNRs. For the case of moderate frequency selective channel (Channel-II), the proposed PDE timing estimators (PDE-F/T) have robust performance with accurate timing estimates, $P_{lock-in} \sim 1$ and DSR $\lesssim 10^{-3}$ at SNR $\gtrsim 5$ dB. The proposed timing estimators exhibit little degradation compared to flat fading channel. However, the MVE demonstrated more sensitive performance to the frequency selectivity of the channel achieving $P_{lock-in} \sim 1$ and DSR $\lesssim 10^{-3}$ at SNR $\gtrsim 15$ dB.

The performance of the MVE, PDE-F and PDE-T timing estimators for different transmit and receive antenna configurations over severe frequency selective channel (Channel-III) in terms of $P_{lock-in}$ and DSR are shown in Fig. 6.13 and Fig. 6.14, respectively. For both figures, the sensitivity of the MVE and PDE-F can be

obviously noted for 1×1 case. The reason of the performance deterioration is that the difference between the channel response over adjacent subcarriers causes the DSR of the PDE-F to saturate at SNR $\gtrsim 15$ and creates an error floor in the order of 10^{-2} in terms of DSR. The MVE involves all the subcarriers in the estimation process, which makes it more sensitive to the frequency selectivity of the channel. For the 2×2 configuration, it is clear that both PDE-F and PDE-T benefit from the diversity, which is demonstrated by a noticeable improvement in the performance compared with 1×1 case. On the contrary, the performance of the MVE is worsen for the 2×2 configuration with high level error floor even at moderate and high SNRs.

The results of Fig. 6.15 and Fig. 6.16 depict the $P_{lock-in}$ and DSR performance respectively for different loop bandwidth (B_L). MIMO-OFDM system with $N = 64$, $N_{CP} = 16$ and the severe frequency selective channel (Channel-III) has been considered. In this case, the channel dispersion spans about 75% of the CP and the SR comprises only 4 samples. It can be observed from the results that the proposed timing estimators (PDE-F/T) still perform well and achieve $P_{lock-in} \sim 1$ and DSR $\lesssim 10^{-2}$ at SNR $\gtrsim 15$ dB . The effect of channel selectivity is obvious on the performance of PDE-F compared with PDE-T. In addition, decreasing the B_L reduces the loop jitter which significantly improves the performance of both schemes at the expense of convergence time.

The convergence performance of the timing estimator is evaluated in the presence of CFOs. The simulation results shown in Fig. 6.17 and 6.18 present the system performance in terms of $P_{lock-in}$ and DSR for different values of CFOs. It shows that the proposed synchronization loop can produce reliable symbol timing estimates for $\epsilon \lesssim 0.2$ for both PDE-F and PDE-T using $B_L = 1/10$. However, it is obvious that the PDE-T outperforms the PDE-F for different CFOs. For larger CFOs, more reliable estimates can be obtained by decreasing the B_L. However, the proposed PDE timing synchronizer is preceded with low-cost coarse estimator and the estimation error $|\epsilon - \hat{\epsilon}| \ll 0.2$. Consequently, the PDE scheme can be used to provide the final estimate. In addition to its advantage to allow self-noise free recovery loop implementation as discussed in Chapter 5, the coarse estimator will help to reduce the CFO to the tolerable range of the timing estimator without decreasing the loop bandwidth.

The performance of the proposed timing estimator is evaluated in time varying

frequency selective fading channel as shown in Fig. 6.19. The Channel-III model with maximum Doppler shift of f_d=50, 200 Hz is considered. It is clear that the proposed system is still performing well in time varying channels. A comparable performance for both schemes (PDE-F and PDE-T) is observed for f_d=50 Hz. However, it clear that the PDE-F outperforms the PDE-T for f_d=200 Hz.

Finally, the performance of the proposed PDE-T synchronization technique exploiting the preambles in MIMO-OFDM system with spatial streams is evaluated. The feedforward version of the PDE-T timing estimator has been considered for MIMO-OFDM system with $N = 64$ and $N_{CP} = 16$ that employ subcarrier orthogonal (SO) preamble. The Fourier sequences have been used to achieve the orthogonality between different transmit antennas. The performance of the PDE-T timing estimator over Channel-II in terms of $P_{lock-in}$ and DSR is presented in Fig. 6.20 and Fig. 6.21 respectively for different antenna configurations. It is obvious that the performance of the timing estimator is improved when the diversity is increased achieving $P_{lock-in} \approx 1$ and DSR $\leq 10^{-2}$ at SNR $\geq$ 12 dB for 4×4 MIMO-OFDM systems. The MSE performance of the PDE-T CFO estimator is presented in Fig. 6.22 for different antenna configurations. Again, the superior performance of the proposed CFO estimation can be observed where the MSE is approximately decreases as the SNR increases without an error floor.

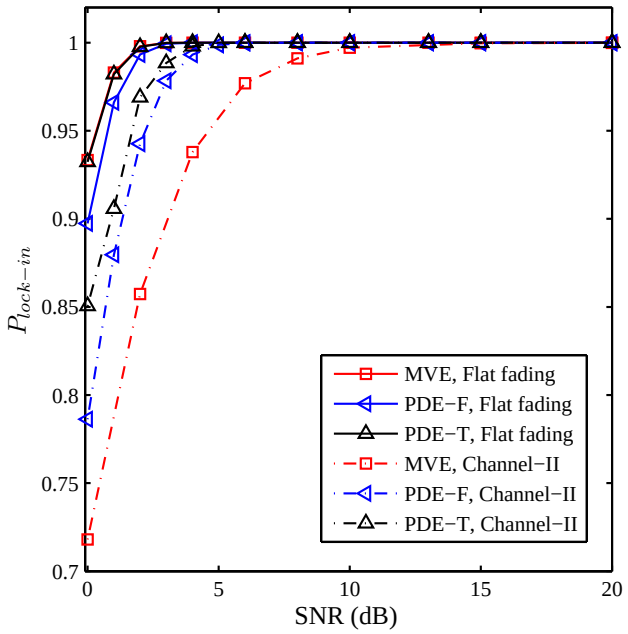

Figure 6.11: $P_{lock-in}$ versus SNR for 2×2 MIMO-OFDM system over flat and frequency selective fading (Channel-II), $N = 256$, $N_{CP} = 32$ and $B_L = 1/10$.

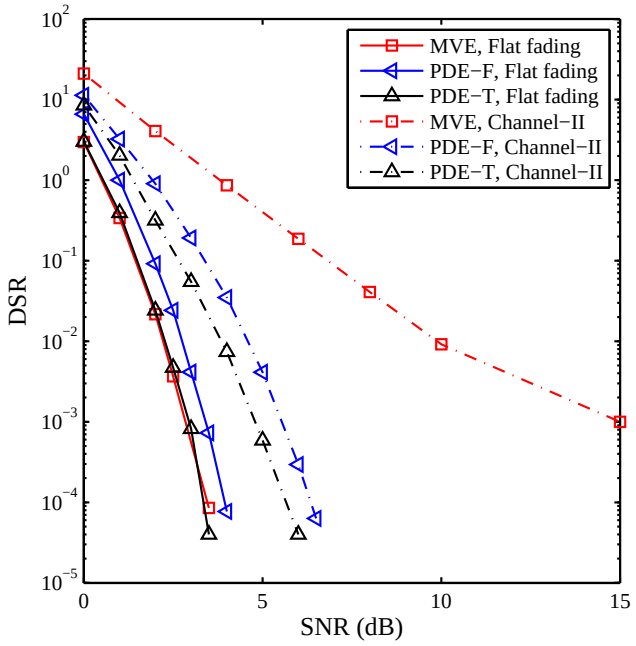

Figure 6.12: DSR versus SNR for 2×2 MIMO-OFDM system over flat and frequency selective fading channel (Channel-II), $N = 256$, $N_{CP} = 32$ and $B_L = 1/10$.

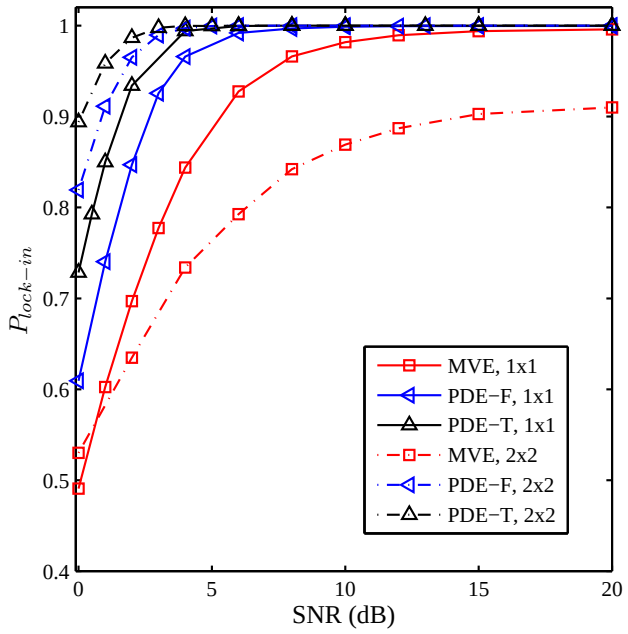

Figure 6.13: $P_{lock-in}$ versus SNR for 1×1 and 2×2 systems over severe frequency selective channel (Channel-III), $N = 256$, $N_{CP} = 32$ and $B_L = 1/10$.

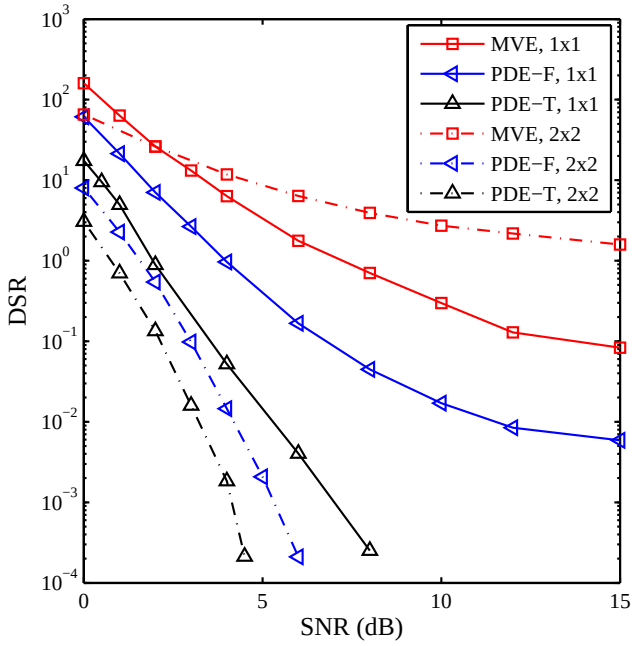

Figure 6.14: DSR versus SNR for 1×1 and 2×2 MIMO-OFDM system over severe frequency selective channel (Channel-III), $N = 256$, $N_{CP} = 32$ and $B_L = 1/10$.

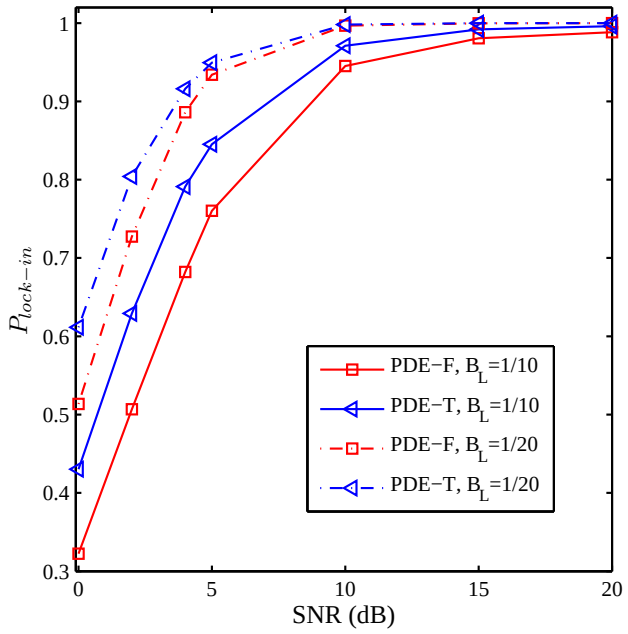

Figure 6.15: $P_{lock-in}$ versus SNR for 2×2 MIMO-OFDM system over severe frequency selective channel (Channel-III), $N = 64$, $N_{CP} = 16$ and $B_L = 1/10, 1/20$.

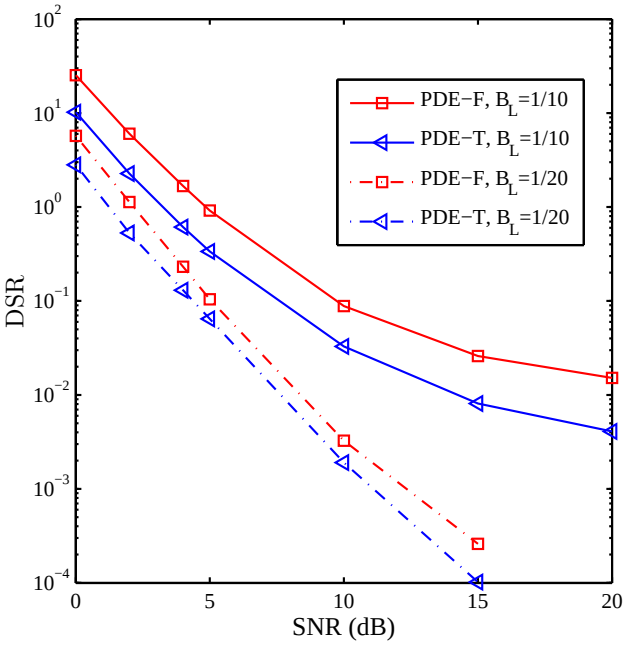

Figure 6.16: DSR versus SNR for 2×2 MIMO-OFDM system over severe frequency selective channel (Channel-III), $N = 64$, $N_{CP} = 16$ and $B_L = 1/10, 1/20$.

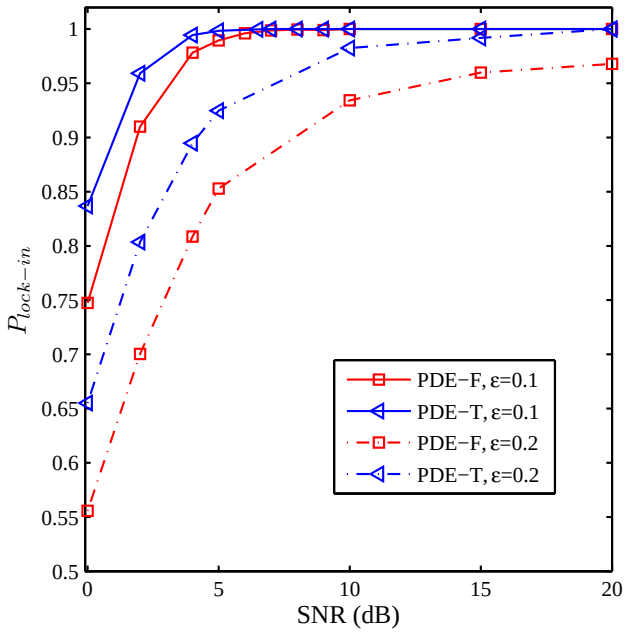

Figure 6.17: $P_{lock-in}$ versus SNR for 2×2 MIMO-OFDM system over Channel-III with different values of CFO, $N = 256$, $N_{CP} = 32$ and $B_L = 1/10$.

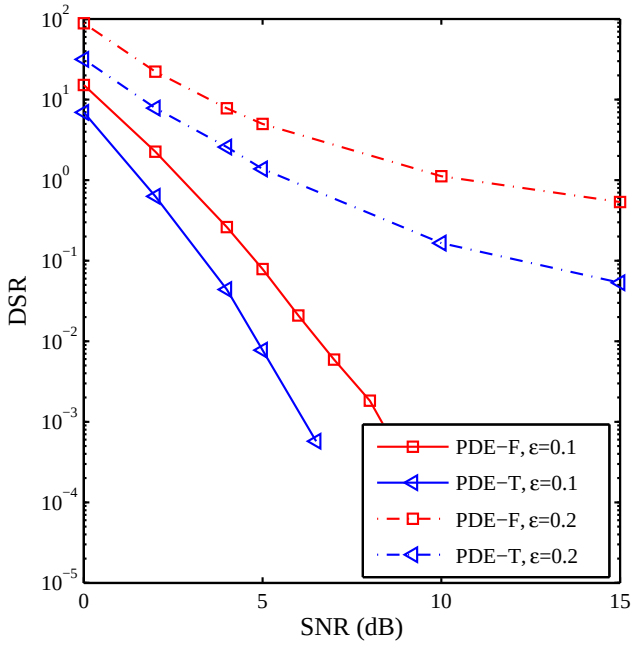

Figure 6.18: DSR versus SNR for 2×2 MIMO-OFDM system over Channel-III with different values of CFO, $N = 256$, $N_{CP} = 32$ and $B_L = 1/10$.

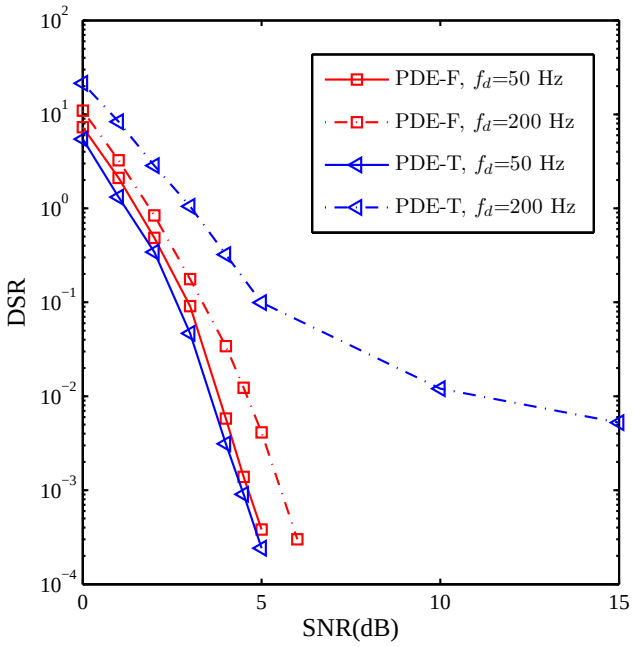

Figure 6.19: DSR versus SNR over time varying frequency selective channel (Channel-III), $N = 256$, $N_{CP} = 32$ and $B_L = 1/20$.

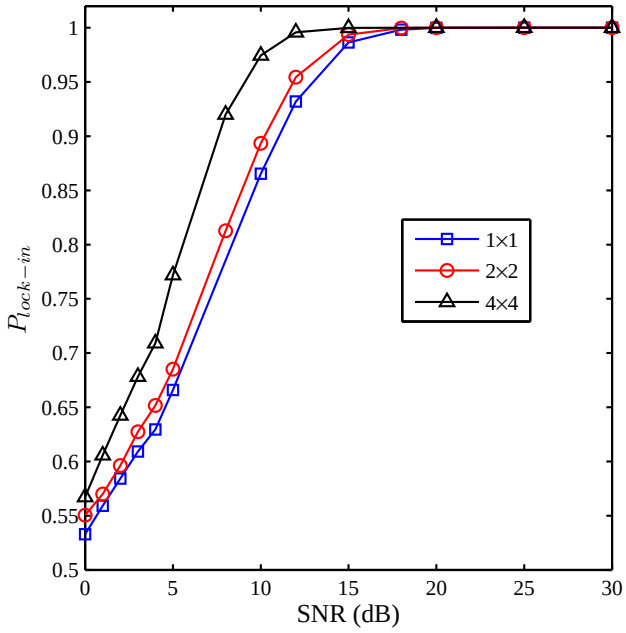

Figure 6.20: $P_{lock-in}$ versus SNR for feedforward PDE-T for MIMO-OFDM system over Channel-II, $N = 64$, $N_{CP} = 16$.

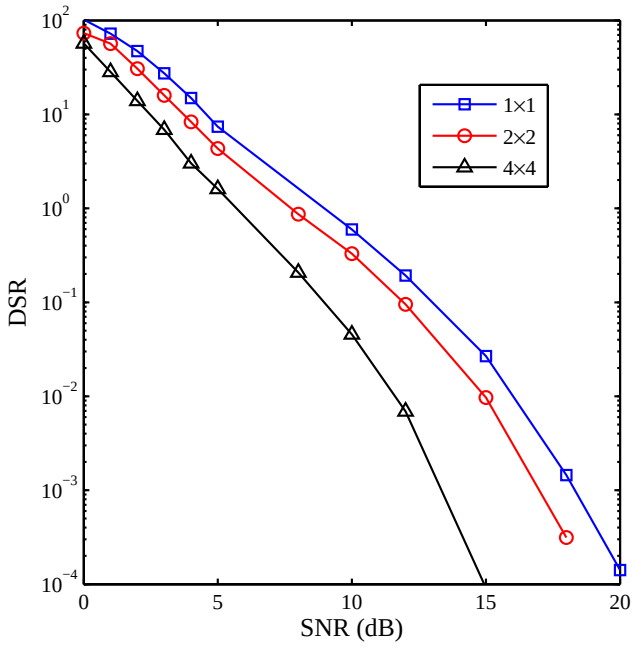

Figure 6.21: DSR versus SNR for feedforward PDE-T for MIMO-OFDM system over Channel-II, $N = 64$, $N_{CP} = 16$.

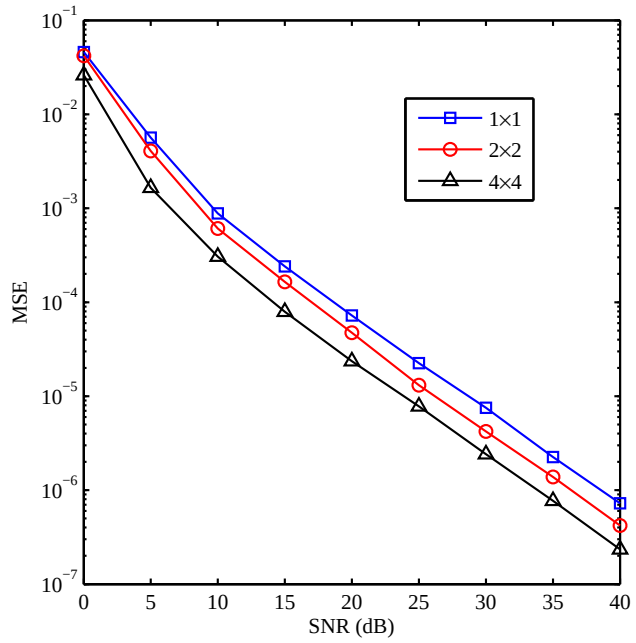

Figure 6.22: MSE versus SNR for PDE-T CFO estimator for MIMO-OFDM system over Channel-II, $N = 64$, $N_{CP} = 16$.

6.7 Chapter Summary

In this chapter, a new technique for blind symbol timing recovery and carrier frequency offset estimation in MIMO-OFDM systems employing OSTC with constant-modulus signalling is presented. The proposed symbol timing and frequency synchronization schemes are based on exploiting the interference introduced at the DFT output due to synchronization imperfection. The synchronization parameters were selected such that the interference is minimized by minimizing the power difference among the subcarriers based on the assumption of approximate channel response either over adjacent subcarrier in one STC block or over the same subcarrier in consecutive STC blocks. Therefore, the synchronization process does not require the knowledge of the channel response and the transmitted data.

Using Monte Carlo simulations, it was confirmed that the proposed PDE-F/T synchronization scheme is efficient and robust in both flat and multipath fading channels even at low SNRs. The results demonstrated the robustness of PDE-T scheme in severe frequency selective channels, while both configurations (PDE-F and PDE-T) demonstrated comparable performance in time varying wideband channels. A little performance improvement could be observed using PDE-F compared with PDE-T in fast fading conditions. Hence, for an optimum performance an adaptive configuration could be suggested. However, using fixed configuration based on either scheme should be sufficient to deliver reliable estimate under various channel conditions. In terms of computational complexity, the proposed synchronization techniques (both STO and CFO estimators) are very efficient because the CFO estimates' were obtained using parameter estimation method while the symbol timing estimator is realized with feedback configuration using ELG approach.

Chapter 7

Architectural Exploration of Blind CFO Estimation in OFDM Systems for Prototyping on Reconfigurable Platform

This chapter discusses the architectural aspects of prototyping the proposed CFO estimator, in particular the PDE approach discussed in Chapter 4, on reconfigurable hardware device. Exploring the design space, two architectures for mapping the considered CFO estimation technique on field programmable gate array (FPGA) have been presented. The proposed architectures with different implementation alternatives have been simulated and verified for FPGA implementation using the Xilinx's DSP design flow.

7.1 Introduction

Advanced carrier synchronization techniques perform sophisticated signal processing tasks. To meet the requirements of system performance, the hardware implementation of the synchronization unit in OFDM receivers has been investigated in literature [111–124]. However, most of the reported hardware architectures are based on the conventional delay-correlation method, where synchronization parameters are estimated by correlating different segments of training sequences or the CP portions of the OFDM symbols [111, 114–116]. For example, hardware efficient

implementations for the correlator have been proposed by replacing the conventional correlator with a first order low pass filter or sign-bit quantization of the correlator output [112, 120]. However, the sign-bit quantization introduces more deterioration in the estimation performance. Assuming that the synchronization during the acquisition mode does not need to be very accurate, the sign-bit architecture for the CPE reported in [121] has been introduced in [113] to acquire the synchronization parameters of multi-standard systems. Instead of using a unified correlator for coarse and fine synchronization, the decoupled architecture has been proposed in [118] to produce more compact synchronization hardware. In contrast to the correlation based architectures, one architecture for blind CFO estimation has been reported in [119], where the maximum signal to interference-plus-noise ratio (SINR) metric is used to estimate the unknown CFO. As the estimation accuracy mainly depends on the search resolution, the proposed architecture adopts an iterative search-based scheme to avoid the exhausted search for the global minimum. However, such a feedback structure requires a large number of symbols for convergence which limits its application to continuous-mode transmission.

The rapid increase in the processing requirements of modern wireless devices has exceeded the speed of current digital signal processors (DSPs), which are incapable of fulfilling the system throughput requirements. In parallel, the computational capability of reconfigurable computing platforms, such as FPGAs, which are far more cost efficient than application specific integrated circuits (ASIC), has increased significantly in the last decade. The highly parallel architecture and embedded DSP modules allow for the implementation of complex signal processing. In addition, FPGA solutions have the advantage of both flexibility and reprogrammability with fast and easy design flow that enables different ways to trade-off the implementation results [125, 126]. As an example, the mapping of a single carrier synchronization algorithm on FPGA hardware architecture using Xilinx's design tool was discussed in [123] where the intellectual property (IP) cores are exploited to assemble a configurable block for carrier frequency synchronization. It has been shown that rapid development can be achieved while still offering the designer the full range of optimization possibilities and design space exploration for a specific architecture [124].

This chapter explores the architectural design aspects of mapping the PDE algorithm for CFO estimation on a reconfigurable platform. Two architectures are presented, the parallel stream architecture (PSA) exploits the FPGA parallelism

while the multiplexed stream architecture (MSA) employs multiplexing for more efficient hardware implementation [127]. The proposed architectures can be configured in a dual-mode of operation to implement the PDE either in the frequency or time direction for optimum performance depending on channel conditions. The high-level design flow using Xilinx system generator (XSG) is used to implement the proposed architectures by mapping the algorithmic steps into XSG IP components. The proposed architectures are evaluated in terms of estimation accuracy and the hardware cost for different implementation alternatives.

7.2 XSG for Rapid Architecture Exploration

Although most FPGA designs are implemented using hardware description languages (HDL), the use of higher level model based tools such as XSG are becoming increasingly popular whereby the abstractions can be mapped on device primitives efficiently. The XSG design tool provides a library of bit-true and cycle-accurate behavioural models for FPGA IPs to design and refine the hardware implementation of DSP systems. The XSG IP cores are helpful for design exploration and prototyping by which flexible high level abstraction environment can be used to model key portions of the design without much hardware implementation details. The model based design methodology using XSG can provide a rough estimate for the hardware cost as well as the implementation performance. Moreover, the XSG IP cores can be simulated much faster than conventional HDL simulators and their capabilities can be extended transparently and automatically to fit kindly into a system level framework. In addition to the IP cores library, the XSG allows the data flow and HDL models to be composed into the design environment. Therefore, using the XSG as the main design tool allows a simple and intuitive hardware design and verification for DSP algorithms. It is apparent that the XSG is bridging the gap between simulation and implementation by rapid prototyping Matlab co-simulated algorithms into FPGA-running blocks, providing a balance between hardware abstraction level and real-time system implementation [56, 125].

The design flow using XSG is shown in Fig. 7.1, which often starts by describing the algorithm in mathematical terms and then floating point simulation with no hardware details to examine the algorithm in the design environment. After clearly identifying the functionality and dataflow issues, the hardware implementation de-

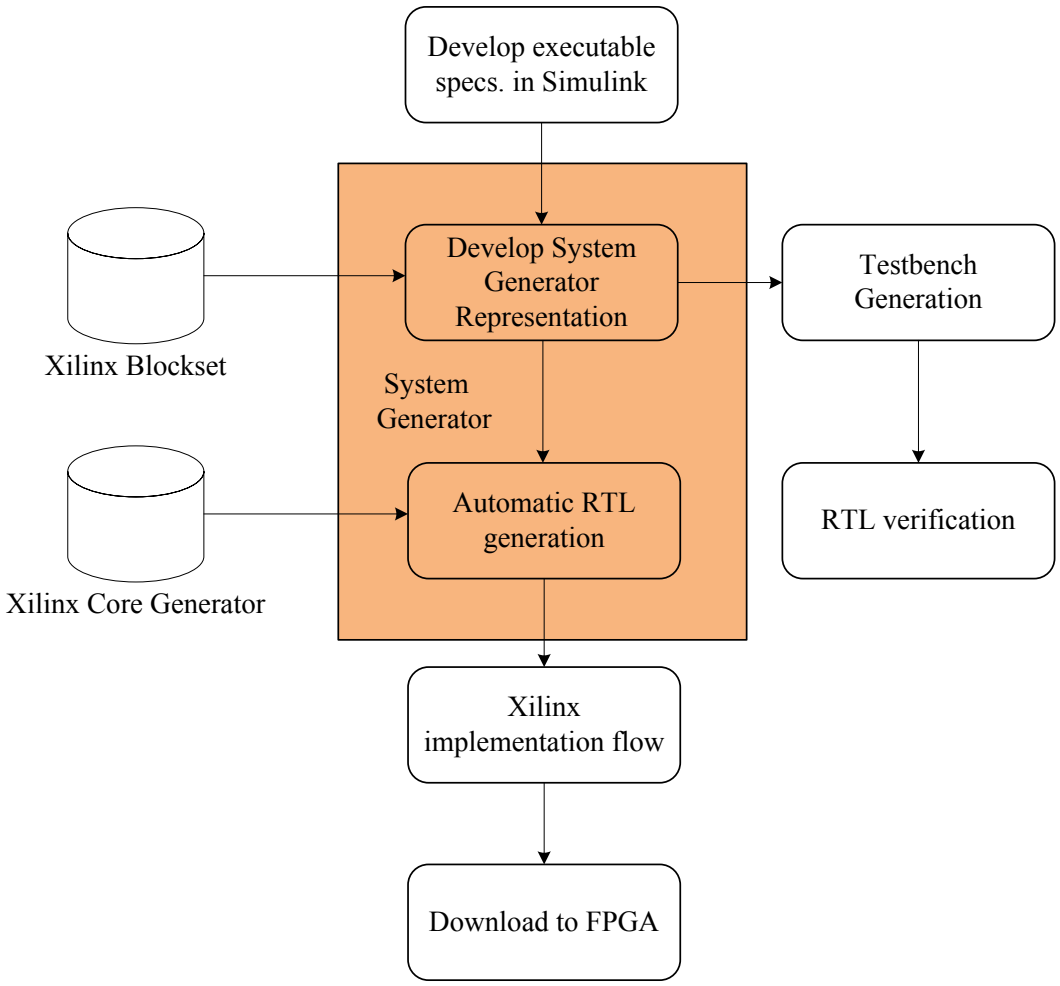

Figure 7.1: Design flow using XSG [3]

tails for the implementation platform can be inserted using XSG. The Xilinx core generator can be invoked afterwards to generate vastly optimized netlists by mapping the configured design parameters into entities and architectures and defining the ports, signals and attributes for hardware implementation. Then, the FPGA device can be programmed by executing the downstream implementation tools to generate the bit stream file in addition to command and timing constraint files for HDL simulation and FPGA synthesis, all in graphical user-friendly environments. In addition, test vectors can be extracted from Simulink model for use with ISE simulators to generate an optional functional verification testbench [3]. Due to its advantage of fast design time and architectural exploration capability, where different IP cores can be analysed for trade-off options, this chapter utilizes the XSG design tool to investigate the architectural aspects for mapping the PDE for CFO estimation on reconfigurable hardware device [125, 128].

7.3 Architecture Design

This section presents two architectures to implement a dual-mode PDE CFO estimator on reconfigurable hardware platform. The proposed architectures can be configured to implement either the PDE in the frequency direction or time direction. For the purpose of rapid prototyping, the Xilinx DSP design flow shown in Fig. 7.1 has been used to behaviourally model the designed architectures and rapidly explore different implementation alternatives to trade-off the design.

7.3.1 Parallel-Stream Architecture

The PDE scheme for CFO estimation requires the computing of cost function either in the frequency or time direction. These cost functions need to be evaluated for three trial CFOs so that the curve fitting method given in (4.19) can be applied for minimization. The highly parallel structure of the FPGA device allows simultaneous computation for the cost function of each trial CFO. Thus, the direct mapping of the PDE estimation method on a reconfigurable platform will result in three processing streams with parallel FFT modules to evaluate the cost function for each trial offset. The configurable parallel-stream architecture (PSA) for the PDE algorithm is shown in Fig. 7.2. The proposed architecture has four main hardware modules in addition to the control logic. The control logic unit accommodates the latency and allows data streaming between the modules.

7.3.1.1 Trial CFO Compensation Module

The CFO compensation module receives the OFDM input samples and produce three output streams each compensated with a trial CFO. In this work, two implementation alternatives for the CFO compensation module have been investigated. The first one is direct digital synthesizer (DDS) with a multiplier as described in Chapter 3 while the other option is to replace the LUT based implementation of DDS and the multiplier with the generalized coordinate rotational digital computer (CORDIC) algorithm configured in rotation mode.

DDS : To compensate for the frequency error, the received samples need to be multiplied by a complex sinusoid of an arbitrary frequency. The DDS is a circuit that accepts a digital tuning word at its input and the output is a sinusoidal waveform

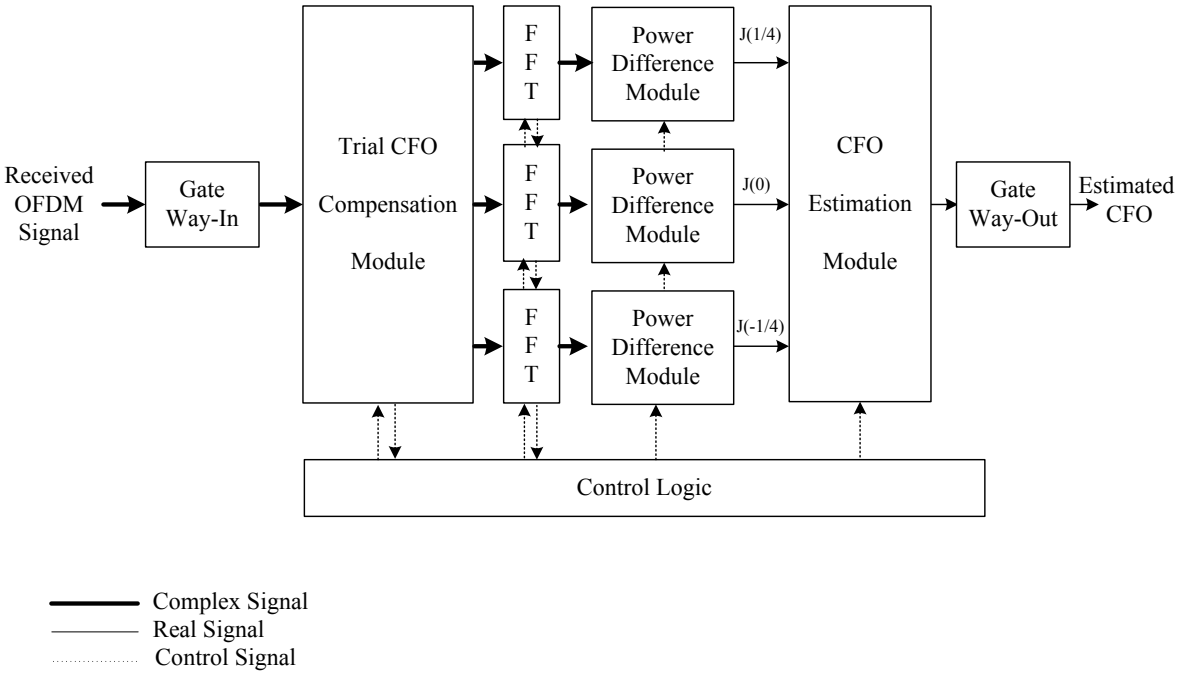

Figure 7.2: Parallel-stream architecture of the PDE CFO estimator for OFDM systems

whose frequency corresponds to that tuning word [62]. In its simplest form, the DDS is a combination of a phase generator circuit and a look-up table loaded with pre-computed values for one period of sinusoidal functions as described in Chapter 3. The phase generator is basically an integrator computing a phase slope to be mapped to a sinusoid using the look-up table [2]. For the architectures investigated in this work, the Xilinx's DDS IP core is utilized to provide the ability to make implementation trade-offs in order to achieve the most efficient solution for a given system. The DDS core has been configured with phase-dithered approach for noise shaping as presented in Fig. 3.11(c).

CORDIC : The other possible alternative for implementing the CFO compensation module is the CORDIC technique [117]. The CORDIC can be used to rotate the input vector by the input rotation angle, where a vector rotation is performed using a series of iterative microrotations of $\tan^{-1}(2^{-i})$ for each iteration . The most beneficial point about CORDIC is that its implementation in hardware requires only a shift and add/subtract operation for each microrotation. However, the CORDIC algorithm introduces a scale factor to the amplitude of the result which requires an extra circuitry and processing time for compensation [58, 117]. For the architectures developed in this chapter, the Xilinx's CORDIC IP core has been utilized. The CORDIC IP is configured in rotation mode of operation in circular coordinates with

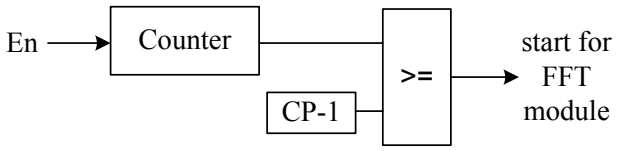

Figure 7.3: Control logic to start the FFT processing

parallel word pipelining architecture described in Fig. 3.7 in order to achieve the throughput requirements and increase the system performance. In addition, a coarse rotation stage is integrated to rotate the input sample from the full circle into the first quadrant since the CORDIC algorithm is only valid over the first quadrant.

7.3.1.2 FFT Module

The Xilinx's FFT IP core has been used to transform the time domain samples into frequency domain. The FFT IP core can be configured to implement one of the architectures, radix-4 burst input/output, radix-2 burst input/output, radix-2 light burst input/output and pipelined steaming input/output [2]. These architectures have different throughput, latency and resource usage which allows for a compromise of the overall architecture in terms of design specification and application requirements. In the developed architectures, the FFT block has been configured to run radix-2 pipelined streamed input/output architecture shown in Fig. 3.13 as it takes the least time for FFT transform among all other architectures. For the streaming mode, the current inputs arrive at the FFT block at the moment the previous inputs go through processing as described in Chapter 3 [2]. Therefore, input stalling is not needed and the architecture data path can be heavily pipelined in order to increase the throughput. To recover the transmitted subcarrier, the CP should be removed before performing the FFT operation, in other words, the FFT should process only the samples belonging to the data part of the symbol. For the streamed input/output FFT architecture, this has been accomplished by controlling the start port of the FFT block so that the processing is performed on the data part of the symbol. A simple way to realize such control logic is to use a counter accompanied by a comparator as shown in Fig. 7.3, where the counter is set to count the number of samples of the OFDM symbol and the output is compared with the CP length to produce the start input of the FFT block.

7.3.1.3 Power Difference Module

The power difference module is used to sequentially accumulate the power differences between the subcarriers. The power function is implemented using dedicated multipliers and the pipelining is configured by using the internal pipeline stages of the dedicated multipliers. The architecture for the power difference module is shown in Fig.7.4-a which can be configured to compute the power difference either between adjacent subcarriers (one sample delay, PDE-F) or the same subcarrier in consecutive OFDM symbols (one symbol delay, PDE-T) of the FFT output stream. An efficient way to implement the delay blocks is to use shift register look-up tables (SRLs), which are part of the FPGA fabric [56]. However, for the PDE-T, the power difference is calculated between two consecutive OFDM symbols, which requires a delay equal to the number of samples in the OFDM symbol. In order to save the fabric, such long delays especially when it is coupled with large bit width would be preferable to implement using block RAM (BRAM) and some associated address counters as shown in Fig. 7.4-b where the dual-port feature of the BRAM is exploited to generate the required delay. The computed power differences are accumulated in a register, which is cleared at the end of the FFT processing. Another capture register has been used for the purpose of streaming since the accumulator reloads its content with an incoming sample after computing the last power difference value for an output sample.

7.3.1.4 CFO Estimation Module

The CFO estimation module is shown in Fig. 7.5. It processes the evaluated cost functions $J(-1/4)$, $J(0)$ and $J(1/4)$ to produce a CFO estimate. The CORDIC IP core has been utilized for arctangent function evaluation where the input vector (a, b) is rotated until the b component approaches zero to generate an output angle $\tan^{-1}(b/a)$. Due to the limited convergence range, the CORDIC algorithm for arctangent evaluation generally starts with coarse rotation [2]. Then, the resulting vector is successively rotated by fine angles of $\pm\tan^{-1}(1/2^i)$ for the ith iteration until the b component goes to zero. Finally, if the reflection is applied, a correction to the resulting angle is required by subtracting it from $\pm\pi$ as illustrated in (4.19). Since the magnitude is not an output parameter, the CORDIC IP core is relaxed from scale factor compensation when it is used for arctangent evaluation [117].

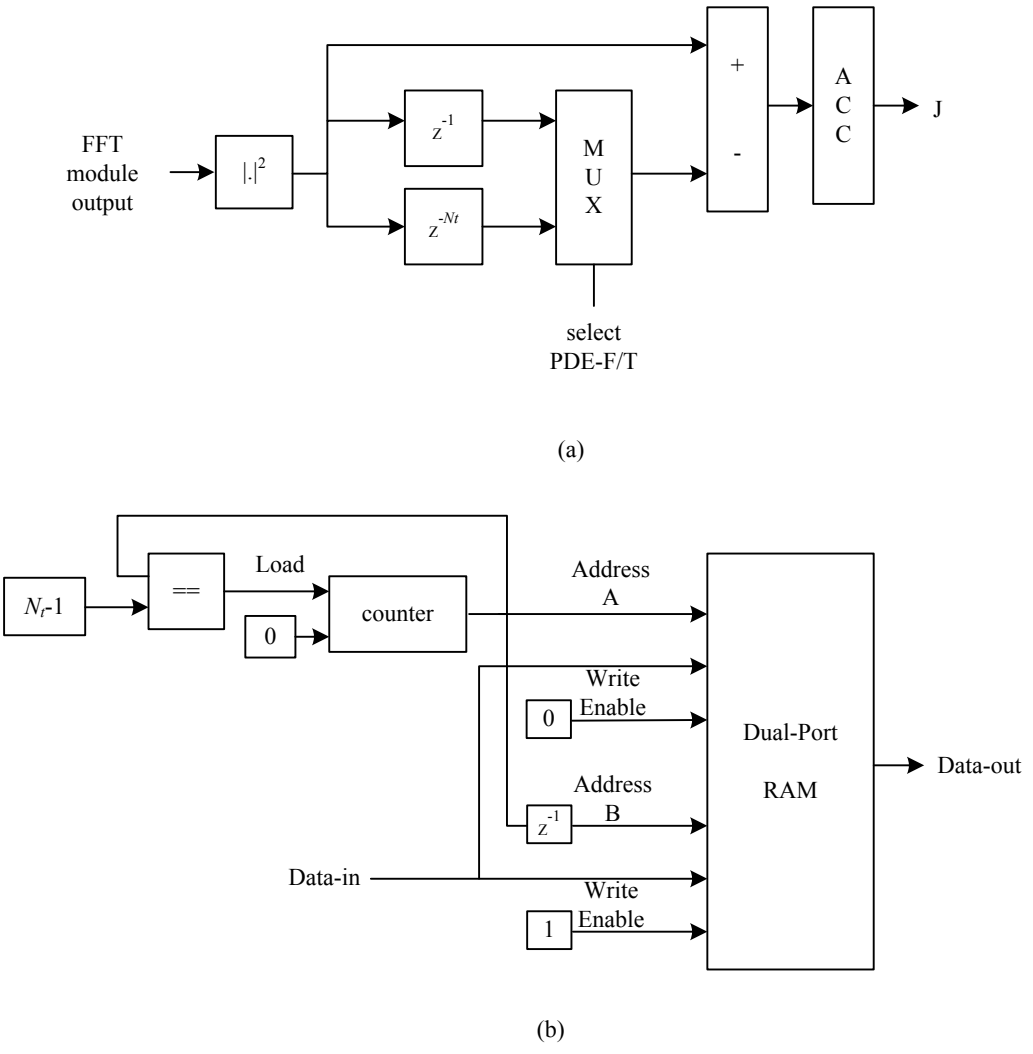

Figure 7.4: Power difference module: (a) configurable PDE-T/F implementation, (b) Delay implementation using RAM

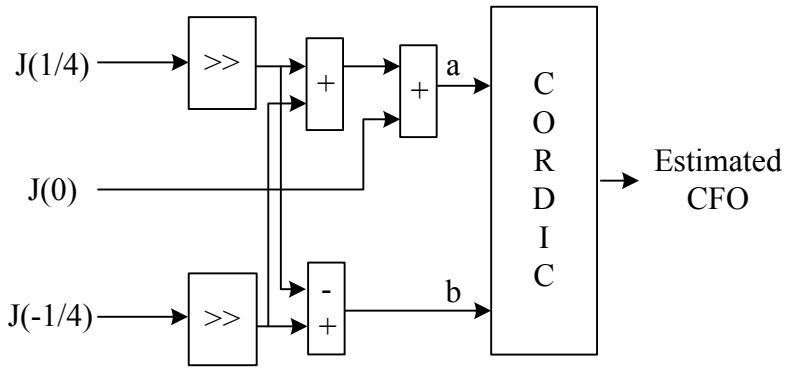

Figure 7.5: The CFO Estimation module

7.3.2 Multiplexed-Stream Architecture (MSA)

This section presents an alternative architecture for mapping the PDE CFO estimation algorithm on a reconfigurable platform. The block diagram of the proposed multiplexed-stream architecture is shown in Fig. 7.6, where three parallel streams are multiplexed into one stream. A single FFT and power difference modules have been used to evaluate the PDE cost function for the multiplexed streams. The proposed MSA adopts the dual-port RAM feature where independent read and write operations can occur simultaneously. As depicted in Fig. 7.6, BRAMs have been used to store the output streams of the trial CFO compensation module. The dual-port BRAMs have been configured so that port A is designated as the write port and port B as the read port, thus, enabling the memory space for the BRAM to be accessed simultaneously at different speeds with multiple data widths. Hence, separate address counters have been used for the read and write operations where the address port for the read operation (port B) runs three times faster than the address port for the write operation (port A), to enable multiplexing of the BRAMs output data into a single stream for FFT processing. This would require that the clock frequency for the FFT core in the multiplexed-stream design runs three times faster than its counterpart in the parallel-architecture design. A single FFT/power difference module has been used to evaluate the PDE cost function for the multiplexed-streams. A capture register is also used to stream the operation and the evaluated cost functions are then demultiplexed and processed to estimate the CFO in a similar manner like the PSA. Although the advantage of MSA is that a single FFT/power difference module has been used resulting in resource efficient implementation, it should be noted that the multiplexing operation would greatly increase the global routing of the design. Additionally, the FFT module would have to run at a much higher clock frequency to meet the timing requirements.

The concepts of regularity and modularity are important aspects for efficient implementation using VLSI technology that helps to simplify the design in different level of abstraction. The regularity attribute means that the design can be decomposed into simple and similar sub-modules while the modularity reflects on the aspect that functionality of each block can be tested separately and interfaced with other blocks of the design without ambiguity to compose the whole system. The FFT and CORDIC processors are the main building blocks in the proposed

architectures presented in this chapter. The calculations involved in both FFT and CORDIC algorithms offer high regularity, modularity and pipelineability where the basic processor cell is comprised of FFT butterfly and basic CORDIC iteration, respectively. Therefore, the hardware orientation of the proposed architectures inherits its regularity from the FFT and CORDIC algorithm that can help to construct efficient architectures for a variety size of input sequences and different CORDIC resolutions by exploiting the algorithm parallelism and the pipelining concept to increase the data throughput and reduce the memory requirements however, this would requires more control and timing logic circuits.

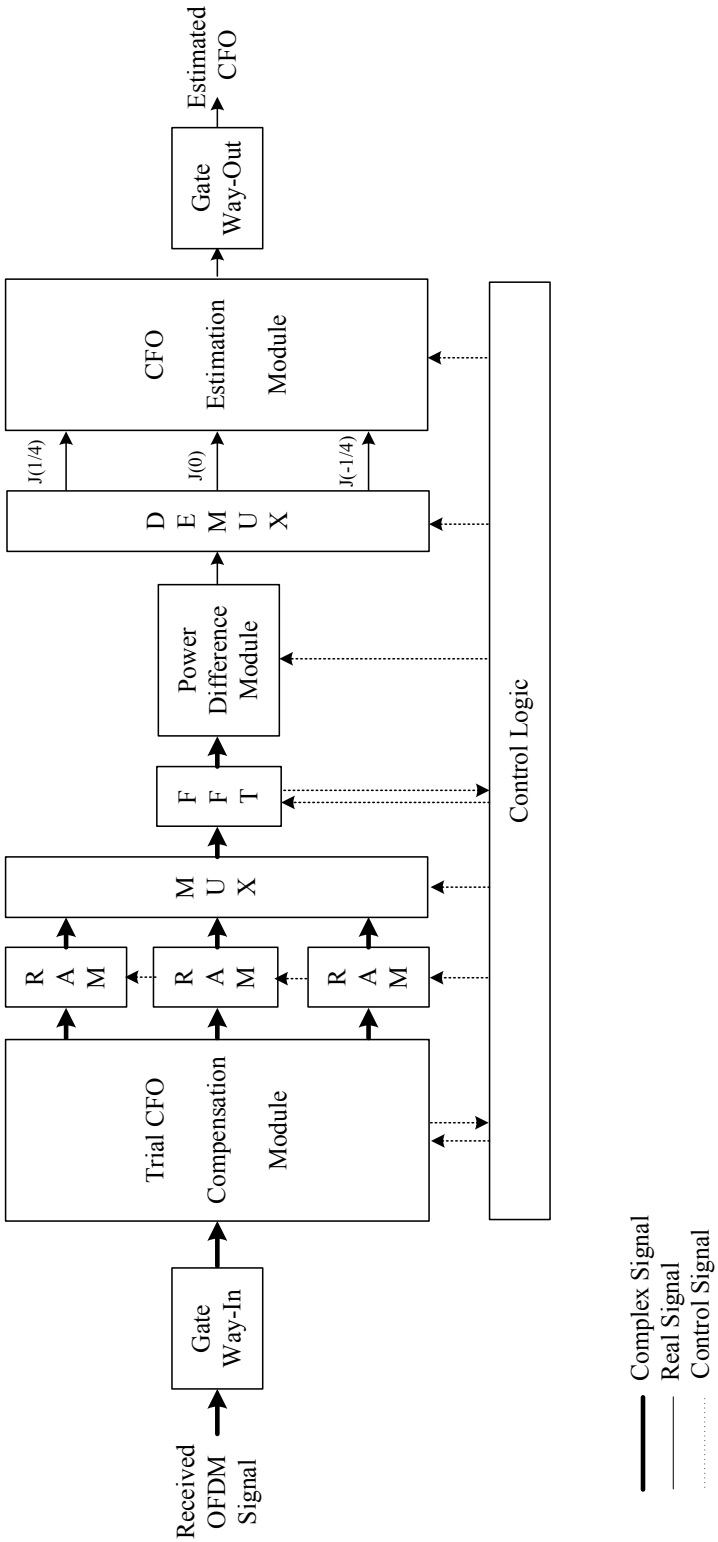

Figure 7.6: A resource efficient multiplexed-stream architecture of the PDE CFO estimator for OFDM systems

7.4 Simulation Results

This section presents the hardware evaluation results of the proposed architectures for the considered PDE CFO estimation algorithm. For hardware design, it is important to adjust the design parameters so that the resulting architecture will have minimum resource utilization with negligible degradation in the performance due to finite hardware precision. For the proposed PDE-F/T architecture, the impact of the word length, the DDS phase width and the number of CORDIC iterations on the estimation accuracy and hardware utilization have been investigated. The design has been implemented using XSG design flow, where the HDL code is generated to behaviourally simulate and verify the functionality of the design. The design is synthesized using Xilinx ISE design tools and then placed and routed on the FPGA platform (xc6vsx315t) with the package (3ff1156) to obtain the results of hardware resource utilization.

7.4.1 Testbench OFDM System

To verify the proposed CFO estimation hardware architecture, an OFDM system of 64 subcarriers with 16 samples of CP has been simulated. The subcarriers utilize quaternary phase shift keying (QPSK) modulation and the channel is assumed to be additive white Gaussian noise (AWGN) with normalized CFO of 0.2. The received OFDM signal is passed to the CFO estimation hardware module through a gate way-in interface block. In each simulation run, the mean square error (MSE) is evaluated over 10^4 received OFDM symbols and used to assess the estimation accuracy of the proposed architectures.

7.4.2 Estimation Accuracy

This section discusses the effect of finite precision for the hardware modules on the CFO estimation accuracy. This would help to tune the configurable design parameters so that the architecture has a compact area with an insignificant effect on the CFO estimation accuracy. In the preceding section, two implementation alternatives for the trial CFO compensation module have been discussed. For the DDS based implementation, the phase/output width sets the width of the internal phase calculations that control the frequency resolution and output precision for the

generated sinusoids. The DDS compiler IP has been configured with phase width of 12 and 14 bit and the MSE performance of the proposed PDE-F/T hardware module is depicted in Fig. 7.7 and compared with floating point precision. It is obvious that when the proposed hardware architecture has been configured to implement the PDE-F, the MSE performance for the DDS phase widths of 12 and 14 bit is approximately equivalent to the floating point precision. However, when it has been configured to implement the PDE-T, a slight degradation in the MSE performance can be noted at high SNR for DDS phase width of 12 bit. Therefore, to assure nearly approximate performance to the floating point precision for both PDE-F/T, the DDS compiler IP core has been configured with phase/output width of 14-bit so that the performance degradation due to the finite hardware precision can be diminished as depicted in Fig. 7.7.

The other alternative is the CORDIC based implementation for which the number of internal add/sub iterations control the accuracy of the CORDIC algorithm. The internal precision of the add/sub iterations is set based on the required accuracy of the output and the number of internal iterations where increasing the number of iterations will consumes more hardware resources. The proposed hardware module has been configured to implement the PDE-T and the MSE performance versus the SNR is shown in Fig. 7.8 for different CORDIC iterations. It is apparent that the number of CORDIC iterations has a significant impact on the estimation accuracy of the implemented CFO estimation architecture. For the CORDIC used in the trial CFO compensation module, the MSE performance for the proposed hardware module deteriorates if the number of iterations was less than 8 as shown in Fig. 7.8. Therefore, to alleviate the impact of finite precision and achieve approximately equivalent performance to the floating point precision, at least 8 iterations should be used. The MSE performance of the proposed PDE-T hardware architecture with different iterations for the CORDIC used in the CFO estimation module is shown in Fig. 7.9. This figure reveals that at least 10 iterations should be used in order to get comparable performance to the floating point precision. Otherwise, the proposed system will suffer from an MSE floor at high SNR.

Finally, it is important to decide the tunable range of the word length for the proposed architecture since it has a significant impact on the estimation accuracy and the area consumption. The MSE performance of the configurable PDE-F/T hardware module for 8 and 12-bit word length is shown in Fig. 7.10. It is obvi-

Table 7.1: Summary for the hardware module configurable parameters

Module	Iteration	Output/Phase Width (bit)
DDS	-	14
FFT	-	24*
CORDIC/CFO Estimation	10	12
CORDIC/CFO Compensation	8	12

* phase factor bit width

ous that the word length contributes considerably to the accurate estimation of the proposed system. For 8-bit word length, the MSE performance for both PDE-F/T schemes deteriorate resulting in MSE flooring at high SNR. Furthermore, increasing the word length to 12-bit will improve the MSE performance and ensure marginal degradation in the estimation accuracy in comparison with the floating point precision for both schemes. However, increasing the word length will consume more hardware resources as will be illustrated in the next section. Table 7.1 summarizes the parameters setting of the configurable IP cores used in the proposed CFO estimation architecture.

7.4.3 Resource Utilization

The hardware resource utilization for the proposed architecture with different implementation alternatives and word length are illustrated in Tables 7.2 and 7.3. The Xilinx resource estimator has been used to estimate the resource utilization in terms of the number of slice LUT (look-up table) and other slice logics. The resource utilization of DDS based PSA and MSA for 8 and 16-bit word lengths are listed in Table 7.2. It is noticeable that the MSA can achieve a significant reduction in the required fabric resources with comparable throughput compared to the PSA. However, it is clear that the MSA requires more BRAM units to store the outputs of the CFO compensation module whereas the PSA works with an input streaming fashion where no BRAMs are required. Also, it is obvious that there is an increased resources saving as the word length increases. For the architectures that utilize the DDS for CFO compensation, the MSA can achieve 35% resource saving in terms of slice LUTs for 8-bit word length while 42% saving can be obtained for 16-bit word length compared with the PSA as illustrated in Table 7.2. Moreover, it can be observed that increasing the word length imposes both architectures to use comparable number of BRAMs since the FFT cores also require some BRAMs to

Table 7.2: Hardware resources usage for the parallel-stream and multiplexed-stream architectures

Target Device:	**xc6vsx315t-3ff1156**			
	PSA		**MSA**	
	8-bit	**16-bit**	**8-bit**	**16-bit**
No. of slice registers	5,849	8,764	3,146	4,283
No. of slice LUTs	4,641	6,512	3,008	3,757
No. of occupied slices	1,386	1,800	846	1,042
No. of DSP48E1s	52	63	23	27
No. of of RAMB18E1	7	10	10	11
Max. Freq. (MHz)	110	111	111	117

store the input data, the phase factors and reorder buffer.

Table 7.3 shows the resource utilization for the proposed CORDIC based PSA and MSA compared with DDS based PSA and MSA for 12-bit word length. It is clear that the DDS based PSA and MSA consumes less fabric resources compared with CORDIC based implementation for the CFO compensation module which uses CORDIC IP cores configured with parallel word architecture to compensate for the trial CFOs. However, the CORDIC based architectures have the advantage of consuming fewer number of embedded multipliers since the CORDIC processor implements the rotation using only iterative add/shift microperation. Moreover, the CORDIC based architectures can achieve a higher frequency of operation when compared with DDS based architectures as illustrated in Table 7.3. The hardware resource utilization in terms of slice LUT for different word lengths and implementation alternatives is shown in Fig. 7.11. It can be observed that the overall resource saving that CORDIC based MSA can achieve is less than the DDS based implementation because of the CORDIC operations that dominating the number of utilized resources. For instance, as shown in Table 7.3, for 12-bit word length, the MSA based CORDIC can achieve 25% reduction in resources compared with PSA based CORDIC. However, 37% resource saving can be achieved by using MSA based DDS compared with PSA based DDS for the same word length.

Table 7.3: Hardware resources comparison between DDS and CORDIC based CFO compensation module for the parallel-stream and multiplexed-stream architecture

Target Device:	**xc6vsx315t-3ff1156**			
	PSA		**MSA**	
	DDS	**CORDIC**	**DDS**	**CORDIC**
No. of slice registers	6,906	8,462	3,581	5,117
No. of slice LUTs	5,222	7564	3,266	5,629
No. of occupied slices	1,492	2,066	913	1,508
No. of DSP48E1s	57	50	25	18
No. of RAMB18E1	10	9	11	10
Max. Freq. (MHz)	111	132	112	137

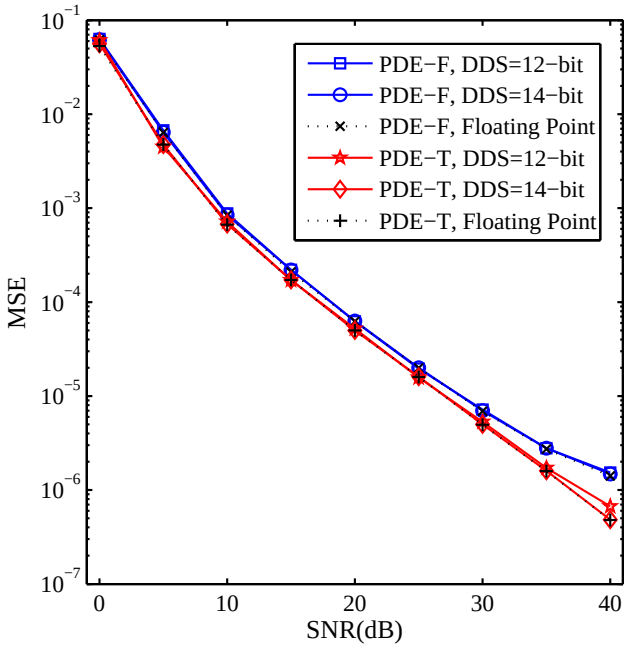

Figure 7.7: The MSE of the configurable PDE-F/T vs. SNR with different phase width for the DDS compared with floating point precision.

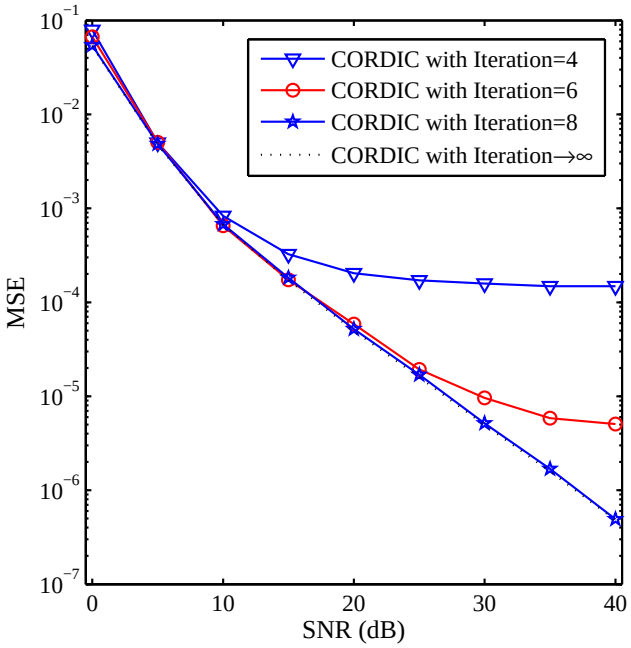

Figure 7.8: The MSE of the PDE-T scheme vs. SNR for different CORDIC iterations for the CFO compensation module compared with floating point precision.

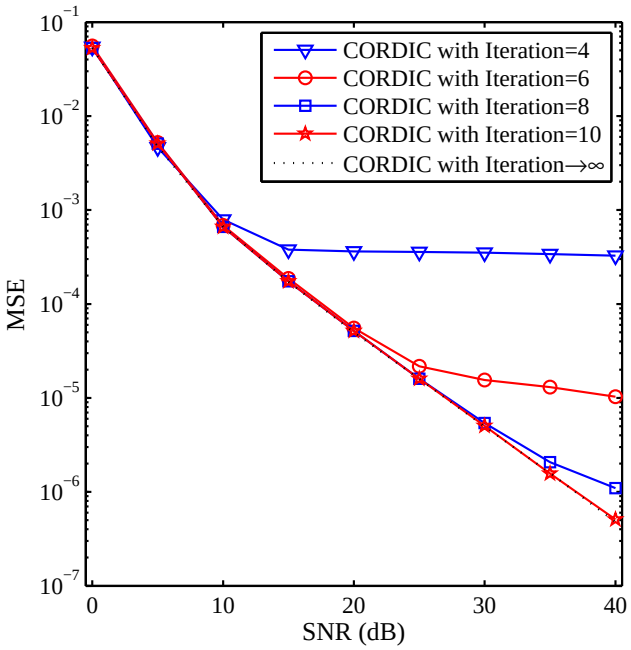

Figure 7.9: The MSE of the PDE-T scheme vs. SNR for different CORDIC iterations for the CFO estimation module compared with floating point precision.

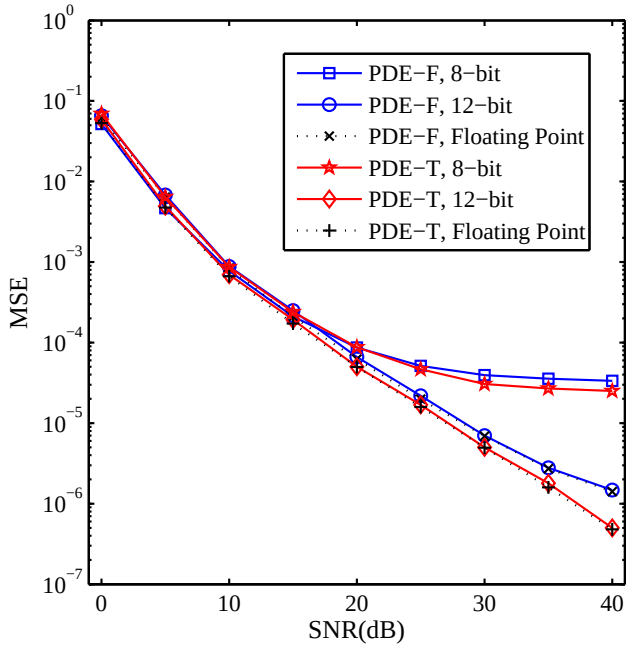

Figure 7.10: The MSE of the configurable PDE-F/T hardware module vs. SNR for different word length compared with floating point precision.

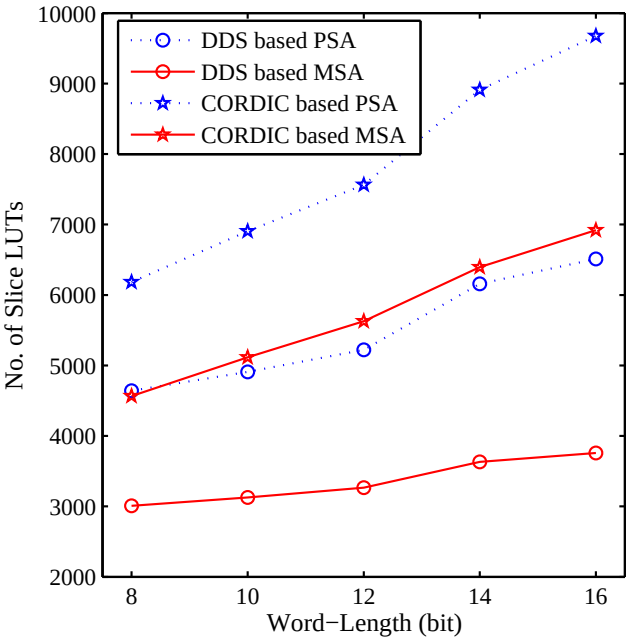

Figure 7.11: The number of slice LUTs for the proposed architectures with different implementation alternatives versus the word length.

7.5 Chapter Summary

This chapter investigated the architectural aspects of implementing the PDE CFO estimation technique for OFDM systems on a reconfigurable hardware platform. A configurable parallel and multiplexed-stream architectures for the PDE-F/T CFO estimator have been proposed and evaluated for FPGA prototyping using Xilinx DSP design flow. This methodology has demonstrated a wide range of flexibility to explore the design space and to analyse different IPs to trade-off the implementation results for the considered CFO estimation algorithm. The design parameters for the proposed architectures have been configured so that the performance loss due to the finite hardware precision is trivial. The prototyping results for the proposed architectures confirmed that the MSA results in a more resource efficient implementation in comparison to the PSA. However, the MSA requires more BRAM units in order to multiplex the CFO compensated samples into one stream for FFT processing. In addition, it was shown that the parallel-word CORDIC implementation for the CFO compensation module results in higher maximum frequency of operation for the proposed parallel and multiplexed stream architectures compared with the DDS implementation. On the other hand, it was confirmed the CORDIC based implementation consumes more hardware resources of the FPGA fabric.

Chapter 8

Conclusions and Further Work

In this thesis, we addressed the synchronization algorithms and architectures for OFDM based wireless communication systems. We started by discussing the effect of synchronization errors, classification of synchronization methodologies and reviewing some conventional synchronization designs for OFDM systems. Unfortunately, much of the non data-aided synchronization techniques in the OFDM literature are not totally blind in the sense that some information might be required to assist the synchronization, such as SNRs or the channel statistical information. In addition, the computational complexity of non data-aided algorithms are much higher than those that are data-aided. Furthermore, the performance of most blind schemes is severely deteriorates in frequency selective fading channels resulting into an inconsistent estimate for the synchronization parameters.

The motivation behind this research was to develop blind synchronization architectures, i.e. without the need for training sequences or pilots and that can perform robustly in frequency selective fading channels with reasonable computational complexity. The key objective was to design time and frequency synchronization for OFDM systems that are totally blind, by decoupling the synchronization from other estimation blocks such that the receiver design is simplified, and can produce consistent estimation for the synchronization parameters over short observation window.

To achieve this objective, two methods have been presented to improve the design of frequency synchronization for OFDM systems. The considered CFO estimators exploit the power and phase difference between the subcarriers in consecutive OFDM symbols. The cost function of the PDE-T estimator is constructed in the time direction, by accumulating the power difference between the subcarrier of constant

modulus signalling, taking advantage of the approximate channel response over two consecutive symbols. The IGVAV estimator is inspired from the efficient VAV phase estimator developed for single carrier systems. The iterative structure for the VAV algorithm has been proposed to tackle the problem of ICI limited performance and to expand the estimation range. In contrast to the other blind frequency synchronization methods that require one to perform a linear search over the interval of trial offsets, the PDE-T and IGVAV CFO estimators provide the estimate in a closed-form which significantly reduces the computational complexity. A comprehensive comparison for the performance of the PDE-T and IGVAV CFO estimators in the presence of timing uncertainty has been carried out and compared with the other methods. The simulation results have confirmed that a wide range of timing errors can be tolerated using the PDE-T and IGVAV frequency synchronization techniques.

For the timing synchronization, a new timing estimator has been proposed by exploiting the power difference measurements between the subcarriers of constant modulus constellation. The cost function of the proposed timing estimator is formulated either in the frequency or time direction depending on the channel conditions. The feedforward and feedback configurations for the proposed timing estimator have been investigated. The utilization of the CPE as pre-synchronizer has shown a vital role to reduce the complexity of the feedforward estimator and to allow the design of a self-noise free timing synchronization loop. Consequently, the performance of the ELG configuration has been enhanced significantly in terms of accuracy and acquisition time.

The proposed timing and frequency synchronization schemes are further extended to MIMO-OFDM systems employing space-time coding (STC). The cost functions of the proposed CFO and STO estimators are constructed by measuring the power difference between the subcarriers either in the frequency direction in one STC block or the time direction between two consecutive STC blocks. In addition, the adoption of the proposed synchronization technique for MIMO-OFDM with spatially multiplexed streams by exploiting the preambles has been discussed.

The performance of the proposed timing and frequency synchronization schemes is assessed in time invariant and time varying fading channels with different frequency selectivity conditions. In addition, the coupling effect between the two synchronization processes has been investigated. The performance is compared with other well-established blind synchronization methods reported in the literature. The

Monte Carlo simulation results obtained for various channel conditions have confirmed the robustness and superiority of the proposed synchronization algorithms with respect to the other estimators in moderate and severe frequency selective fading channels. The formulation of the cost function for PDE-T in the time direction has solved the problem of degraded performance of most blind synchronization techniques in wideband channels. However, it was observed that the PDE-F outperforms the PDE-T in time-varying narrowband channels. For the CFO synchronization using IGVAV, the iterative operation has demonstrated to be very efficient because it improves the accuracy by eliminating the ICI, reduces the complexity by using very few subcarriers in the first two iterations and helps to extend the unambiguous estimation range of the estimator.

The simulation results of the proposed timing estimator based on the power difference measurements have confirmed the superior performance of the power difference estimator without the need of channel statistical information. Compared with other ELG timing recovery systems, the novel design for the proposed ELG realization of the PDE timing metric has offered significant improvement in reducing the loop timing jitter and the acquisition time. Furthermore, the newly proposed performance assessment metric, denoted as deviation from the safe region (DSR), has shown to be more informative in comparing the performance of different timing synchronization algorithms, as the conventional MSE metric does not take into account the presence of the SR.

The architectural exploration and different design alternatives have been investigated to map the CFO synchronization algorithm using PDE on reconfigurable platforms. The proposed architectures can be configured in a dual-mode of operation to implement either the PDE-F or PDE-T depending on the channel conditions. The proposed multiplexed-stream architecture has demonstrated significant reduction in terms of the utilized hardware resources at the expense of little increase in the memory requirements of the system compared with parallel-stream architecture. In addition, the simulation results of the mapped architectures have illustrated that CORDIC based implementation of CFO compensation module would result into higher maximum frequency operation for the proposed architectures compared with DDS implementation, however at the expense of more resource utilization.

Further Work

This research project concentrated primarily on developing blind synchronization algorithms and architectures for OFDM systems, however, there is still room for improvement that can be considered in future work. In the proposed techniques, the timing and frequency synchronization are treated separately. However, future work should consider the joint estimation for the STOs and CFOs using a PDE approach to optimize the synchronization performance. The emphasis should be placed on techniques to reduce the complexity of the joint estimation problem. More efficient searching algorithms could be investigated for this purpose with some advanced FFT configurations.

Although the extension of proposed synchronization methods for MIMO-OFDM systems was considered in this thesis, more attention could be given to MIMO-OFDM systems with distributed antennas and spatial multiplexing where each antennas pair experiences different CFOs and STOs. In addition, for such problems, the correction of multi-CFOs should be treated. The minimization of the power difference or maximizing the SINR approaches could be considered to optimize the compensation process such that the system performance is improved.

From the architectural point of view, the architecture of the IGVAV algorithm could be studied where the iterative process adds more challenge to the design of the synchronization unit. The IGVAV architecture can be integrated with a filter to realize a hardware oriented carrier recovery loop. In addition, a hardware architecture for the proposed PDE-ELG timing estimator for OFDM systems can be examined. The architecture design could be incorporated with some advanced reconfigurable hardware aspects such as dynamic partial and run-time reconfiguration to construct variable structure timing recovery loop. The timing error detector can be implemented in hardware while the softcore processor implements the loop lock and updates the loop filter parameters. Furthermore, the timing and frequency synchronization architecture unit could be evaluated in a testbed OFDM system.

Appendix A

In this part we present the sinusoidal approximation for the cost function given in (4.18). In the following, we consider the noise free case of (4.5) and assume that no averaging is used, i.e. $L = 1$. By substituting (4.1) in (4.5) we obtain

$$s_k(l) = \frac{e^{j\frac{2\pi n}{N}\epsilon l(N+N_{CP})}}{N} \sum_{i=0}^{N-1} \tilde{s}_i(l) \sum_{n=0}^{N-1} e^{j\frac{2\pi n}{N}(i+\tilde{\epsilon}-k)}, \tag{A.1}$$

where $\tilde{\epsilon} \triangleq \epsilon - \hat{\epsilon}$ and $\tilde{s}_i(l) \triangleq H_i(l)d_i(l)$. Expanding (4.16) gives,

$$J(\tilde{\epsilon}) = \sum_{k=0}^{N-1} |s_k(l)|^4 + \sum_{k=0}^{N-1} |s_k(l+1)|^4 - 2\sum_{k=0}^{N-1} |s_k(l)|^2 |s_k(l+1)|^2. \tag{A.2}$$

Substituting (A.1) in the first terms of (A.2) gives,

$$\sum_{k=0}^{N-1} |s_k(l)|^4 = \frac{1}{N^4} \sum_{i_1,i_2,c_1,c_2=0}^{N-1} \tilde{s}_{i_1}(l)\tilde{s}^*_{i_2}(l)\tilde{s}_{c_1}(l)\tilde{s}^*_{c_2}(l) \sum_{n_1,n_2,m_1,m_2=0}^{N-1} e^{j\frac{2\pi\tilde{\epsilon}}{N}\lambda} e^{j\frac{2\pi}{N}(n_1 i_1 - n_2 i_2 + m_1 c_1 - m_2 c_2)} \sum_{k=0}^{N-1} e^{-j\frac{2\pi k}{N}\lambda} \tag{A.3}$$

where $\lambda = n_1 - n_2 + m_1 - m_2$. Noting that,

$$\sum_{k=0}^{N-1} e^{-j\frac{2\pi k}{N}\lambda} = \begin{cases} N, & \lambda = N, 0, -N \\ 0, & otherwise \end{cases} \tag{A.4}$$

Thus (A.3) can be simplified to

$$\sum_{k=0}^{N-1}|s_k(l)|^4 = \frac{2}{N^3}\mathrm{Re}\{e^{-j2\pi\tilde{\epsilon}}\sum_{i_1,i_2,c_1,c_2=0}^{N-1}\tilde{s}_{i_1}(l)\tilde{s}^*_{i_2}(l)\tilde{s}_{c_1}(l)\tilde{s}^*_{c_2}(l) \sum_{n_1=0}^{N-1}\sum_{n_2=n_1+1}^{N-1}\sum_{m_1=0}^{n_2-n_1-1} e^{j\frac{2\pi n_1}{N}(i_1-c_2)}e^{-j\frac{2\pi n_2}{N}(i_2-c_2)}e^{-j\frac{2\pi m_1}{N}(c_1-c_2)}\} + C_1(l) \quad \text{(A.5)}$$

where $C_1(l)$ is a real constant independent of $\tilde{\epsilon}$ and can be obtained by substituting $\lambda = 0$ in (A.3). Now define:

$$\Omega \triangleq \{i_1, i_2, c_1, c_2\}, \quad \Omega_1 \triangleq \{\Omega \,|i_1 = i_2 \; or \; c_1 = c_2\}, \quad \Omega_2 \triangleq \{\Omega \,|i_1 \neq i_2 \; and \; c_1 \neq c_2\}$$

the indices $i_1, i_2, c_1, c_2 \in \{0, 1, ..., N-1\}$, $\Omega = \Omega_1 \cup \Omega_2$ and $\Omega_1 \cap \Omega_2 = \oslash$. Therefore, (A.5) can be expressed as

$$\sum_{k=0}^{N-1}|s_k(l)|^4 = \frac{2}{N^3}\mathrm{Re}\left\{e^{-j2\pi\tilde{\epsilon}}B_{\Omega_1}(l)\right\} + \frac{2}{N^3}\mathrm{Re}\left\{e^{-j2\pi\tilde{\epsilon}}B_{\Omega_2}(l)\right\} + C_1(l) \quad \text{(A.6)}$$

where

$$B_\Psi(l) = \sum_{\substack{i_1,i_2,c_1,c_2=0 \\ i_1,i_2,c_1,c_2\in\Psi}}^{N-1}\tilde{s}_{i_1}(l)\tilde{s}^*_{i_2}(l)\tilde{s}_{c_1}(l)\tilde{s}^*_{c_2}(l) \sum_{n_1=0}^{N-1}\sum_{n_2=n_1+1}^{N-1}\sum_{m_1=0}^{n_2-n_1-1} e^{j\frac{2\pi n_1}{N}(i_1-c_2)}e^{-j\frac{2\pi n_2}{N}(i_2-c_2)}e^{-j\frac{2\pi m_1}{N}(c_1-c_2)} \quad \text{(A.7)}$$

and $\Psi \in \{\Omega_1, \Omega_2\}$. Similarly,

$$\sum_{k=0}^{N-1}|s_k(l+1)|^4 = \frac{2}{N^3}\mathrm{Re}\left\{e^{-j2\pi\tilde{\epsilon}}B_{\Omega_1}(l+1)\right\} + \frac{2}{N^3}\mathrm{Re}\left\{e^{-j2\pi\tilde{\epsilon}}B_{\Omega_2}(l+1)\right\} + C_1(l+1). \quad \text{(A.8)}$$

The last term can be expressed as,

$$\sum_{k=0}^{N-1}|s_k(l)|^2|s_k(l+1)|^2 = \frac{2}{N^3}\mathrm{Re}\left\{e^{-j2\pi\tilde{\epsilon}}D_{\Omega_1}(l)\right\} + \frac{2}{N^3}\mathrm{Re}\left\{e^{-j2\pi\tilde{\epsilon}}D_{\Omega_2}(l)\right\} + C_2(l), \quad \text{(A.9)}$$

where

$$D_{\Psi}(l) = \sum_{\substack{i_1,i_2,c_1,c_2=0 \\ i_1,i_2,c_1,c_2\in\Psi}}^{N-1} \tilde{s}_{i_1}(l)\tilde{s}^{*}_{i_2}(l)\tilde{s}_{c_1}(l+1)\tilde{s}^{*}_{c_2}(l+1) \sum_{n_1=0}^{N-1}\sum_{n_2=n_1+1}^{N-1}\sum_{m_1=0}^{n_2-n_1-1} e^{j\frac{2\pi n_1}{N}(i_1-c_2+1)}e^{-j\frac{2\pi n_2}{N}(i_2-c_2+1)}e^{-j\frac{2\pi m_1}{N}(c_1-c_2)}. \quad \text{(A.10)}$$

Substituting (A.6), (A.8) and (A.9) in (A.2) gives

$$J(\tilde{\epsilon}) = \frac{2}{N^3}\mathrm{Re}\left\{e^{-j2\pi\tilde{\epsilon}}(B_{\Omega_1}(l) + B_{\Omega_1}(l+1) - 2D_{\Omega_1}(l))\right\} + \frac{2}{N^3}\mathrm{Re}\left\{e^{-j2\pi\tilde{\epsilon}}(B_{\Omega_2}(l) + B_{\Omega_2}(l+1) - 2D_{\Omega 2}(l))\right\} + C_1(l) + C_1(l+1) - 2C_2(l). \quad \text{(A.11)}$$

Under the assumption in (4.15), $B_{\Omega_1}(l+1) + B_{\Omega_1}(l) \approx 2D_{\Omega_1}(l)$ [52]. Therefore, the cost function described in (4.16) can be simplified to,

$$J(\mu) \approx A\cos(2\pi\tilde{\epsilon}) + C, \quad \text{(A.12)}$$

where A and C are real constants,

$$A = -2\left[B_{\Omega_2}(l) + B_{\Omega_2}(l+1) - 2D_{\Omega_2}(l)\right]/N^3, \quad \text{(A.13)}$$

and

$$C{=}C_1(l) + C_1(l+1) - 2C_2(l). \quad \text{(A.14)}$$

Appendix B

The CFO estimate $\hat{\epsilon}$ using PDE-T estimator can be obtained by evaluating the cost function at three special trial points $(-1/4,\ 0,\ 1/4)$ as follows,

$$J_{PDE-T}(0) \approx A\cos[2\pi(\epsilon)] + C, \tag{B.1}$$

$$J_{PDE-T}(-1/4) \approx a\cos[2\pi(\epsilon - 1/4)] + C = A\sin[2\pi(\epsilon)] + C, \tag{B.2}$$

and

$$J_{PDE-T}(1/4) \approx A\cos[2\pi(\epsilon + 1/4)] + C = -A\sin[2\pi(\epsilon)] + C. \tag{B.3}$$

Thus, the constants A and C can be obtained,

$$C = \frac{1}{2}[J_{PDE-T}(1/4) + J_{PDE-T}(-1/4)], \tag{B.4}$$

$$A = \frac{J_{PDE-T}(0) - \frac{1}{2}[J_{PDE-T}(1/4) + J_{PDE-T}(-1/4)]}{\cos(2\pi\epsilon)}. \tag{B.5}$$

Substituting (B.4) and (B.5) into (B.3),

$$\tan(2\pi\epsilon) = \frac{\frac{1}{2}[J_{PDE-T}(1/4) - J_{PDE-T}(-1/4)]}{\frac{1}{2}[J_{PDE-T}(1/4) - J_{PDE-T}(-1/4)] - J_{PDE-T}(0)}. \tag{B.6}$$

Denoting,

$$a = \frac{1}{2}[J_{PDE-T}(1/4) + J_{PDE-T}(-1/4)] - J_{PDE-T}(0), \tag{B.7}$$

and

$$b = \frac{1}{2}[J_{PDE-T}(1/4) - J_{PDE-T}(-1/4)]. \tag{B.8}$$

The CFO estimate can be obtained as follows,

$$\hat{\epsilon} = \begin{cases} \frac{1}{2\pi}\tan^{-1}(b/a) & a \geq 0 \\ \frac{1}{2\pi}\tan^{-1}(b/a) + \frac{1}{2} & a < 0 \text{ and } b \geq 0 \\ \frac{1}{2\pi}\tan^{-1}(b/a) - \frac{1}{2} & a < 0 \text{ and } b \leq 0 \end{cases} \tag{B.9}$$

References

[1] I. Kuon, R. Tessier, and J. Rose, "FPGA architecture: Survey and challenges," *Foundations and Trends in Electronic Design Automation*, vol. 2, pp. 135–253, 2008.

[2] Xilinx, *Xilinx System Generator for DSP: Reference Guide, version 12.2*, 2010.

[3] ——, *Xilinx System Generator for DSP: Getting Started Guide, version 12.2*, 2010.

[4] S. Weinstein and P. Ebert, "Data transmission by frequency-division multiplexing using the discrete fourier transform," *IEEE Trans. Commun. Technol.*, vol. 16, pp. 628–634, 1971.

[5] L. Hanzo and C. H. Wong, *Adaptive Wireless Transceivers: Turbo-Coded, Turbo-Equalised and Space-Time Coded TDMA, CDMA, MC-CDMA and OFDM Systems*. New York, USA: John Wiley & Sons, Inc., 2002.

[6] *Radio broadcasting systems; Digital Audio Broadcasting (DAB) to mobile, portable and fixed receivers, European Telecommunication Standard 300 and 401*. Valbonne, France: 2nd ed., European Telecommunication Standard Institute, 1997.

[7] *Digital Video Broadcasting (DVB); Framing structure, channel coding and modulation for digital terrestrial television*. European Standard EN 300 744 V1.1.2, 1997-08.

[8] *IEEE P802.11n/D1.10 Wireless LAN Medium Access Control (MAC) and Physical Layer (PHY) specifications: Enhancements for Higher Throughput*. IEEE Std., Feb 2007.

[9] *Draft IEEE standard for local and metropolitan area networks Part 16: air interface for fixed and mobile broadband wireless access systems.* 802.16e-2005, December 2005.

[10] M. Baker, *LTE-Advanced physical layer.* Beijing, China: IMT-Advanced Evaluation Workshop, 2009.

[11] K. Fazel and S. Kaiser, *Multi-carrier and spread spectrum systems from OFDM and MC-CDMA to LTE and WiMAX.* Wiley press, 2008.

[12] J. G. Andrews, A. Ghosh, and R. Muhamed, *Fundamentals of WiMAX.* Prentice-Hall, 2007.

[13] T. Schmidl and D. Cox, "Robust frequency and timing synchronization for OFDM," *IEEE Trans. Commun.*, vol. 45, pp. 1613–1621, 1997.

[14] B. Seo, S. Kim, and J. Park, "Fast coarse estimation of carrier frequency offset for OFDM systems," *IET Elect. Lett.*, vol. 38, pp. 1520–1521, 2002.

[15] X. Yi, W. Shieh, and Y. Tang, "Phase estimation for coherent optical OFDM systems," *IEEE Photonics Technology Lett.*, vol. 19, pp. 919–921, 2007.

[16] M. Luise, M. Marselli, and R. Reggiannini, "Low-complexity blind carrier frequency recovery for OFDM signals over frequency-selective radio channels," *IEEE Trans. Commun.*, vol. 50, pp. 1182–1188, 2002.

[17] J. van de Beek, M. Sandell, and P. Borjesson, "ML estimation of timing and frequency offset in OFDM systems," *IEEE Trans. Signal Process.*, vol. 45, pp. 1800–1805, Jul. 1997.

[18] R. Mo, Y. Chew, and T. Tjhung, "A new blind joint timing and frequency offset estimator for OFDM systems over multipath fading channels," *IEEE Trans. Veh. Technol.*, vol. 57, pp. 2947–2957, 2008.

[19] L. Wu, X.-D. Zhang, P.-S. Li, and Y.-T. Su, "A blind CFO estimator based on smoothing power spectrum for OFDM systems," *IEEE Transactions on Communications*, vol. 57, no. 7, pp. 1924–1927, 2009.

[20] Y. Mostofi and D. Cox, "A robust timing synchronization design in OFDM systems-part I: low-mobility cases," *IEEE Trans. Wireless Commun.*, vol. 6, 2007.

[21] X. Dia, "Carrier frequency offset estimation for OFDM/SDMA systems using consecutive pilots," *IET Commun.*, vol. 152, pp. 624–632, 2005.

[22] A. J. Al-Dweik, "Robust non data-aided frequency offset estimation technique for OFDM systems in rayleigh fading channels," in *Proc. IEEE PIMRC*, 2004, pp. 1365–1369.

[23] Y. Yingwei and G. B. Giannakis, "Blind carrier frequency offset estimation in SISO, MIMO, and multiuser OFDM systems," *IEEE Trans. Commun.*, vol. 53, pp. 173–183, 2005.

[24] W.-L. Chin and S.-G. Chen, "A blind synchronizer for OFDM systems based on SINR maximization in multipath fading channels," *IEEE Trans. Veh. Technol.*, vol. 58, pp. 625–635, Feb. 2009.

[25] A. J. Al-Dweik, "A non-data-aided symbol timing recovery technique for OFDM systems," *IEEE Trans. Commun.*, vol. 1, pp. 37–40, Jan. 2006.

[26] J. G. Proakis, *Digital Communications.* McGraw Hill, Fourth edition, 2001.

[27] M. Petrov, "System components and design for OFDM-based broadcasting receivers," Ph.D. dissertation, TU Darmstadt, July 2008.

[28] T. S. Rappaport, *Wireless communications: principles and practice.* Prentice Hall, 2002.

[29] W. C. Jakes, *Microwave Mobile Communications.* John Wiley Sons, 1974.

[30] B. Sklar, "Rayleigh fading channels in mobile digital communication systems, part i: Characterization," *IEEE Commun. Mag.*, vol. 35, pp. 136–146, Sep. 1997.

[31] P. Murphy, "Design, implementation and characterization of a cooperative communications system," Ph.D. dissertation, Rice University, 2010.

[32] A. Al-Dweik, B. Sharif, and R. Shubair, "Robust frequency offset estimator for OFDM with general constellation," *IET Elect. Lett.*, vol. 44, pp. 980–981, 2008.

[33] A. AL-Dweik, A. Hazmi, S. Younis, B. S. Sharif, and C. C. Tsimenidis, "Iterative frequency offset estimator for OFDM systems," *IET Com.*, vol. 4, p. 2008 2019, 2010.

[34] M. Morelli, C. C. J. Kuo, and M. O. Pun, "Synchronization techniques for orthogonal frequency division multiple access (OFDMA): A tutorial review," *Proceedings of the IEEE*, vol. 95, pp. 1394–1427, 2007.

[35] R. D. Girolamo and T. Le-Ngoc, "Frequency independent nonlinear feedforward phase estimator," *Wireless Personal Communications*, vol. 5, pp. 19–50, 1997.

[36] A. Al-Dweik, R. Hamila, and M. Renfors, "Blind estimation of large carrier frequency offsets in wireless OFDM systems," *IEEE Trans. Veh. Technol.*, vol. 56, pp. 965–968, 2007.

[37] H. Meyr, M. Moeneclaey, and S. Fechteligital, *Communication Receivers, vol. 2: Synchronization, Channel Estimation, and Signal Processing.* NY: Wiley and Sons, 1998.

[38] M. Ghogho and A. Swami, *carrier frequency synchronization for OFDM systems.* Book Chapter in Signal Processing for Wireless Communication Handbook, Ed. Ibnkahla, CRC Press, 2004.

[39] A. Bo, Z. Zhang-Dui, Z. Gang, X. Rong-Tao, and D. Jian-Wen, "Patents on synchronization techniques in wireless OFDM systems," *Recent Patents on Electrical Engineering*, vol. 1, pp. 14–21, 2010.

[40] H. Minn, V. K. Bhargava, and K. B. Letaief, "A robust timing and frequency synchronization for OFDM systems," *IEEE Trans. Commun.*, vol. 2, pp. 822–839, 2003.

[41] M. Speth, S. Fechtel, G. Fock, and H. Myer, "Optimum receiver design for wireless broad-band systems using OFDM-part I," *IEEE Trans. Commun.*, vol. 47, pp. 1668–1677, 1999.

[42] M. Speth, F. Classen, and H. Meyr, "Frame synchronization of OFDM systems in frequency selective fading channels," in *Proc. IEEE VTC*, Arizona, USA, May 1997, pp. 1807–1811.

[43] S. Kim, Y. Choi, K. Kwak, K. Bang, and D. Hong, "A robust timing recovery algorithm for OFDM systems," in *Proc. IEEE GLOBECOM*, LA, USA, 2008, pp. 3215–3219.

[44] B. Yang, K. Letaief, S. Cheng, , and Z. Cao, "Timing recovery for OFDM transmission," *IEEE J. Sel. Areas Commun.*, vol. 18, pp. 2278–2289, 2000.

[45] M. Hsieh and C. Wei, "A low-complexity frame synchronization and frequency offset compensation scheme for OFDM systems over fading channels," *IEEE Trans. Veh. Technol.*, vol. 48, pp. 1596–1609, 1999.

[46] Y. Mostofi and D. Cox, "Timing Synchronization in High Mobility OFDM Systems," in *Proceedings of IEEE 39th International Conference on Communications (ICC)*, vol. 4, Paris, France, June 2004, pp. 2402–2406.

[47] Q. Zhu and Z. Liu, "Minimum interference blind time-offset estimation for OFDM systems," *IEEE Trans. Wireless Commun.*, vol. 5, pp. 2136–2142, 2006.

[48] A. Al-Dweik, A. Hazmi, and M. Renfors, "Joint symbol timing and frequency offset estimation for wireless OFDM systems," in *Proc. IEEE PIMRC*, Gannes, France, 2008, pp. 1–5.

[49] Y. Zeng, W. Leon, Y. Liang, and A. Leyman, "A new method for frequency offset and channel estimation in OFDM," in *Proc. IEEE ICC*, 2006, pp. 4606–4611.

[50] J. Chen, Y. Wu, S. Ma, and T. Ng, "Timing robust joint carrier frequency offset and channel estimation for OFDM systems," in *Proc. IEEE WCNC*, 2007, pp. 1025–1029.

[51] ——, "ML joint CFO and channel estimation in OFDM systems with timing ambiguity," *IEEE Trans. Wireless Commun.*, vol. 7, 2008.

[52] X. Zeng and A. Ghrayeb, "A blind carrier frequency offset estimation scheme for OFDM systems with constant modulus signaling," *IEEE Trans. Commun.*, vol. 56, pp. 1032–1037, Jul. 2008.

[53] U. Meyer-Baese, *Digital Signal Processing with Field Programmable Gate Arrays*, 3rd ed. Springer Publishing Company, Incorporated, 2007.

[54] S. Che, J. Li, J. Sheaffer, K. Skadron, and J. Lach, "Accelerating compute-intensive applications with GPUs and FPGAs," in *Proc. of IEEE SASP*, June 2008, pp. 101–107.

[55] R. Tessier and W. Burleson, "Reconfigurable computing for digital signal processing: A survey," *Journal of VLSI Signal Processing*, vol. 28, pp. 7–27, 2001.

[56] Xilinx, *Xilinx System Generator for DSP: User Guide, version 12.2*, 2010.

[57] M. Rice, *Digital Communications: A Discrete-Time Approach*. Earson Education, Inc., 2009.

[58] P. Meher, J. Valls, J. Tso-Bing, K. Sridharan, and K. Maharatna, "50 years of CORDIC: algorithms, architectures, and applications," *IEEE Trans. Circuits Syst. I*, vol. 56, pp. 1893–1907, 2009.

[59] M. Ercegovac and T. Lang, *Digital arithmetic*. Morgan Kaufmann, 2003.

[60] S. A. Khan, *Digital Design of signal processing systems: A practical approach*. John Wiley & Sons, Ltd., 2011.

[61] R. Andraka, "A survey of CORDIC algorithms for FPGA based computers," in *Proc. of ACM/SIGDA international symposium on FPGA*, New York, NY, USA, 1998, pp. 191–200.

[62] J. M. Palmer, "Real-time carrier frequency estimation using disjoint pilot symbol blocks," Ph.D. dissertation, Brigham Young University, 2009.

[63] ——, "The hybrid architecture parallel fast fourier transform (HAPFFT)," Master's thesis, Brigham Young University, 2005.

[64] R. S. Azad, "A custom FFT hardware accelerator for wave fields synthesis," Master's thesis, Delft University of Technology, 2009.

[65] P. Moose, "A technique for orthogonal frequency division multiplexing frequency offset correction," *IEEE Trans. Commun.*, vol. 42, pp. 2908–2914, 1994.

[66] L. Wu, X.-D. Zhang, P.-S. Li, and Y. Su, "A closed-form blind CFO estimator based on frequency analysis for OFDM systems," *IEEE Transactions on Communications*, vol. 57, no. 6, pp. 1634–1637, 2009.

[67] T. Roman and V. Koivunen, "Subspace method for blind CFO estimation for OFDM systems with constant modulus constellations," in *Proc. IEEE VTC*, Stockholm, Sweden, May 2005, pp. 1253–1257.

[68] A. Viterbi and A. Viterbi, "Nonlinear estimation of PSK modulated carrier phase with application to burst digital transmission," *IEEE Trans. Inf. Theory*, vol. 32, pp. 543–551, 1983.

[69] M. P. Fitz, "Nonlinear digital carrier synchronization for rician fading channels," in *Proc. IEEE Glob. Comm.*, San Diego, CA, 1990, pp. 623–628.

[70] S. Kay, "A fast and accurate single frequency estimator," *IEEE Trans. Acoust., Speech, Signal Process.*, vol. 37, pp. 1987–1990, 1989.

[71] A. AL-Dweik, A. Hazmi, S. Younis, B. S. Sharif, and C. C. Tsimenidis, "Carrier frequency offset estimation for OFDM systems over mobile radio channels," *IEEE Trans. Veh. Technol.*, vol. 59, pp. 974–979, 2010.

[72] S. Younis, A. Al-Dweik, B. Sharif, C. Tsimenidis, and A. Hazmi, "The effect of timing errors on frequency offset estimation in OFDM systems," in *Proc. IEEE ISSPIT*, Bilbao, Spain, Dec. 2011.

[73] J. Anderson, T. Aulin, and C. Sundberg, *Digital phase modulation*. New York: Plenum Press, 1986.

[74] P. Ciblat and M. Ghogho, "Blind NLLS carrier frequency-offset estimation for QAM, PSK, and PAM modulations: performance at low SNR," *IEEE Trans. Commun.*, vol. 54, pp. 1725–1730, 2006.

[75] R. Nee and R. Prasad, *OFDM Wireless Multimedia Communications*. Boston: CArtech House, 2000.

[76] T. Hwang, C. Yang, G. Wu, S. Li, and G. Y. Li, "OFDM and its wireless applications: A survey," *IEEE Trans. Veh. Technol.*, vol. 58, pp. 1673–1694, May 2009.

[77] Y. Mostofi and D. Cox, "Mathematical analysis of the impact of timing synchronization errors on the performance of an ofdm system," *IEEE Trans. Commun.*, vol. 54, pp. 226–230, Feb. 2006.

[78] B. Park, H. Cheon, C. Kang, and D. Hong, "A novel timing estimation method for OFDM systems," *IEEE Commun. Lett.*, vol. 7, pp. 239–241, May 2003.

[79] C. Li and W. Hu, "Super-imposed training scheme for timing and frequency synchronization in OFDM systems," *IEEE Trans. Broadcast.*, vol. 53, pp. 574–583, 2007.

[80] W.-L. Chin, "Channel length assisted symbol synchronization for OFDM systems in multipath fading channels," *EURASIP Journal on Wireless Communications and Networking*, vol. 68, 2011.

[81] S. Younis, A. Al-Dweik, A. Hazmi, C. Tsimenidis, and B. Sharif, "Symbol timing offset estimation scheme for OFDM systems based on power difference measurements," in *Proc. IEEE PIMRC*, Istanbul, Turkey, Sept. 2010.

[82] A. Al-Dweik, S. Younis, A. Hazmi, B. Sharif, and C. Tsimenidis, "Efficient timing estimator for OFDM systems using power difference measurements," Accepted for Publication in *IEEE Trans. Veh. Technol.*

[83] A. Al-Dweik and R. E. Khazali, "A modified early-late gate for blind symbol timing recovery of OFDM systems," *IEICE Trans. Commun.*, vol. E89-B, pp. 11–18, Jan. 2006.

[84] A. P. Liavas, P. A. Regalia, and J.-P. Delmas, "Blind channel approximation: effective channel order determination," *IEEE Trans. Signal Process.*, vol. 47, pp. 3336–3344, 1999.

[85] W. H. Gerstacker and D. P. Taylor, "Blind channel order estimation based on second-order statistics," *IEEE Signal Process. Lett.*, vol. 10, 2003.

[86] V. Torres, A. Perez-Pascual, T. Sansaloni, and J. Valls, "Design and FPGA-implementation of a high performance timing recovery loop for broadband communications," *J. Sign. Process. Syst.*, vol. 56, pp. 17–23, 2009.

[87] H. R. Anderson, *Fixed broadband wireless system design.* New York: Wiley press, 2008.

[88] H. Bolcskei, "MIMO-OFDM wireless systems: basics, perspectives, and challenges," *IEEE Trans. Wireless Commun.*, vol. 13, pp. 31–37, 2006.

[89] A. Gershman and N. Sidiropoulos, *Space-time processing for MIMO communications*. Wiley press, 2005.

[90] *3GPP TS 36.201: Evolved Universal Terrestrial Radio Access (E-UTRA): Long Term Evolution (LTE) physical layer: General description*. 3GPP Std., 2008.

[91] T. Schenk, *RF Imperfections in High-rate Wireless Systems: Impact and Digital Compensation*. Springer, 2008.

[92] S. Attallah, Y. Wu, and J. W. M. Bergmans, "Low complexity blind estimation of residual carrier offset in orthogonal frequency division multiplexing based wireless local area network systems," *IET Commun.*, vol. 1, pp. 604–611, 2007.

[93] A. Mody and G. Stuber, "Synchronization for MIMO OFDM systems," in *Proc. IEEE GLOBECOM*, USA, 2001, pp. 509–513.

[94] A. V. Zelst and T. Schenk, "Implementation of a MIMO OFDM-based wireless LAN system," *IEEE Trans. Signal Process.*, vol. 52, pp. 483–494, 2004.

[95] T. Schenk and A. van Zelst, "Frequency synchronization for MIMO OFDM wireless LAN systems," in *Proc. IEEE Fall VTC*, vol. 3, Orlando (FL), 2003, pp. 1521 –1525.

[96] E. Zhou, X. Zhang, H. Zhao, and W. Wang, "Synchronization algorithms for MIMO OFDM systems," in *Proc. IEEE WCNC*, vol. 1, LA (USA), 2005, pp. 18 –22.

[97] G. Stuber, J. Barry, S. McLaughlin, Y. Li, M. Ingram, and T. Pratt, "Broadband MIMO-OFDM wireless communications," *Proceedings of the IEEE*, vol. 92, no. 2, pp. 271 – 294, feb 2004.

[98] M. Xiaoli, C. Tepedelenlioglu, G. B. Giannakis, and S. Barbarossa, "Non-data-aided carrier offset estimators for OFDM with null subcarriers: identifiability, algorithms, and performance," *IEEE J. Sel. Areas Commun.*, vol. 19, pp. 2504–2515, 2001.

[99] M. Xiaoli, O. Mi-Kyung, G. B. Giannakis, and P. Dong-Jo, "Hopping pilots for estimation of frequency-offset and multiantenna channels in MIMO-OFDM," *IEEE Trans. Commun.*, vol. 53, pp. 162–172, 2005.

[100] Z. Yonghong, A. R. Leyman, and T. S. Ng, "Joint semi-blind frequency offset and channel estimation for multi-user MIMO-OFDM uplink," *IEEE Trans. Commun.*, vol. 55, pp. 2270–2278, 2007.

[101] J. Chen, Y. Wu, S. C. Chan, and T. S. Ng, "Joint maximum-likelihood CFO and channel estimation for OFDMA uplink using importance sampling," *IEEE Trans. Veh. Technol.*, vol. 57, pp. 3462–3470, 2008.

[102] W. Lu, Z. Xian-Da, and L. Pei-Sheng, "A low-complexity blind carrier frequency offset estimator for MIMO-OFDM systems," *IEEE Signal Process. Lett.*, vol. 15, pp. 769–772, 2008.

[103] A. Saemi, V. Meghdadi, J. Cances, M. Zahabi, and J.-M. Dumas, "ML time synchronization algorithm joint with channel estimation for MIMO-OFDM systems in frequency selective fading channel," in *Proc. IEEE CSNDSP*, Greece, 2006.

[104] T. C. W. Schenk, M. M. de Laat, P. P. M. Smulders, and E. R. Fledderus, "Symbol timing for multiple antenna OFDM systems," in *Proc. IEEE 63rd VTC*, vol. 3, Greece, May 2006, pp. 1521 –1525.

[105] J. S. Baek and J. S. Seo, "Effective symbol timing recovery based on pilot-aided channel estimation for MISO transmission mode of DVB-T2 system," *IEEE Trans. Broadcast.*, vol. 56, pp. 193 –200, 2010.

[106] S. Younis, B. Sharif, C. Tsimenidis, A. Al-Dweik, and A. Hazmi, "Blind scheme for carrier frequency offset estimation in MIMO-OFDM systems," in *Proc. IEEE ISSPIT*, Ajman, UAE, Dec. 2009.

[107] S. Younis, A. AL-Dweik, A. Hazmi, B. S. Sharif, and C. C. Tsimenidis, "Blind cfo estimator for MIMO-OFDM systems over frequency selective fading channels," *IET Commun.*, vol. 4, pp. 990–999, May. 2010.

[108] S. Younis, A. Al-Dweik, B. Sharif, C. Tsimenidis, and A. Hazmi, "Robust early-late gate system for symbol timing recovery in MIMO-OFDM systems," in *Proc. IEEE WiMob*, Shanghai, China, Oct. 2011.

[109] S. M. Alamouti, "A simple transmit diversity technique for wireless communications," *IEEE J. Sel. Areas Commun.*, vol. 16, pp. 1451–1458, 1998.

[110] H. Wang, Q. Yin, Y. Meng, and H. Deng, "Adaptive joint estimation of symbol timing and carrier frequency offset for OFDM systems," in *Proc. IEEE ICC*, Glasgow, UK, 2007, pp. 3034–3039.

[111] X. Li, Y. Zheng, and Z. Lai, "A low complexity sign ML detector for symbol and frequency synchronization of OFDM systems," *IEEE Trans. Consum. Electron.*, vol. 52, pp. 317–320, May 2006.

[112] H. Zheng, J. Tang, and B. Shen, "Low-complexity joint synchronization of symbol timing and carrier frequency for OFDM systems," *IEEE Trans. Consum. Electron.*, vol. 51, pp. 783–789, 2005.

[113] J. G. Bayon, C. Carreras, and O. Edfors, "A multistandard frequency offset synchronization scheme for 802.11n, 802.16d, LTE, and DVB-T/H systems," *EURASIP Journal of Computers Systems, Networks, and Communications*, vol. 2010, pp. 317–320, Article ID 628657, 9 pages 2010.

[114] J. Park, M. Sunwoo, P. Kim, and D. Chang, "Low complexity synchronizer using common autocorrelator for DVB-S2 system," *Journal of Semiconductor Technology and Science.*, vol. 10, Dec. 2009.

[115] J. Cho, J. Kim, and W. Cho, "VLSI implementation of auto-correlation architecture for synchronization of MIMO-OFDM WLAN systems," *Journal of Semiconductor Technology and Science.*, vol. 10, Sept. 2009.

[116] H. Liu and C. Lee, "A low-complexity synchronizer for OFDM-based UWB system," *IEEE Trans. Circuits Syst. II*, vol. 11, pp. 1269–1273, 2006.

[117] A. Troya, K. Maharatna, M. Krstic, E. Grass, U. Jagdhold, and R. Kraemer, "Low-power VLSI implementation of the inner receiver for OFDM-based WLAN systems," *IEEE Trans. Circuits Syst. I*, vol. 55, pp. 672–686, 2008.

[118] T. Kim and I. Park, "Low-power and high-accurate synchronization for IEEE 802.16d systems," *IEEE Trans. VLSI Syst.*, vol. 16, pp. 1620–1630, 2008.

[119] J. Lin, H. Yu, Y. Wu, and H. Ma, "A power efficient baseband engine for multiuser mobile MIMO-OFDMA communications," *IEEE Trans. Circuits Syst. I*, vol. 57, pp. 1779–1792, 2010.

[120] I. Diaz, L. Wilhelmsson, J. Rodrigues, J. Lofgren, T. Olsson, and V. Owall, "A sign-bit auto-correlation architecture for fractional frequency offset estimation in OFDM," in *Proc. IEEE ISCAS*, Gannes, France, 2010, pp. 3765–3768.

[121] I. Diaz, L. Wilhelmsson, J. Rodrigues, T. Olsson, and V. Owall, "Sign-bit based architecture for OFDM acquisition for multiple-standards," in *Proc. IEEE NORCHIP*, Gannes, France, 2009, pp. 1–4.

[122] C. Chang, C. Su, and J. Wu, "A low power baseband OFDM receiver IC for fixed WiMAX communication," in *Proc. IEEE ASSCC*, 2007, pp. 292–295.

[123] T. Brack, U. Wasenmuller, and N. Wehn, "A configurable IP core for combined blind frequency and phase synchronization of MPSK bursts," in *Proc. of 1st Mobile and Wireless Communications Summit*, 2005.

[124] D. Schmidt, T. Brack, U. Wasenmuller, and N. Wehn, "From algorithm to implementation: a case study on blind carrier synchronization," *Adv. Radio Sci.*, vol. 4, pp. 313–318, 2006.

[125] A. Sghaier, S. Areibi, and R. Dony, "Implementation approaches trade-offs for Wimax OFDM functions on reconfigurable platforms," *ACM Trans. on Reconfigurable Technology and Systems*, vol. 3, 2010.

[126] R. Woods, J. McAllister, Y. Yi, and G. Lightbody, *FPGA-based Implementation of Signal Processing Systems.* John Wiley & Sons, 2008.

[127] S. Younis, A. Al-Dweik, B. Sharif, C. Tsimenidis, and A. Hazmi, "CORDIC based architecture for blind CFO estimation in OFDM systems," in *Proc. IEEE ISSPIT*, Bilbao, Spain, Dec. 2011.

[128] S. T. Pérez, J. B. Alonso, C. M. Travieso, M. A. Ferrer, and J. F. Cruz, "Design of a synchronous FFHSS modulator on a FPGA with system generator," *WSEAS Trans. Cir. and Sys.*, vol. 8, no. 8, pp. 641–650, Aug. 2009.